Design and Syntheses of Functional MOFs for Environmental Applications

A Thesis

Submitted in Partial Fulfillment of the Requirements for the

Degree of

Doctor of Philosophy

by

Shivani Sharma

ID: 20132012



Indian Institute of Science Education and Research (IISER), Pune

2020

Dedicated to

Mummy, Papaji, Bhaiya and Rover

Indian Institute of Science Education and Research (IISER), Pune

Certificate

It is hereby certified that the work described in this thesis entitled *"Design and Syntheses of functional MOFs for Environmental Applications"* submitted by *Ms. Shivani Sharma* was carried out by the candidate, under my supervision. The work presented here or any part of it has not been included in any other thesis submitted previously for the award of any degree or diploma from any other university or institution.



Date: 31st July, 2020

Prof. Sujit K. Ghosh

Research Supervisor

Email: sghosh@iiserpune.ac.in

Contact No.: +91 (20) 25908076

Declaration

I declare that this written submission represents my ideas in my own words and wherever other's ideas have been included; I have adequately cited and referenced the original sources. I also declare that I have adhered to all principles of academic honesty and integrity and have not misrepresented or fabricated or falsified any idea/data/fact/source in my submission. I understand that violation of the above will cause for disciplinary action by the Institute and can also evoke penal action from the sources which have thus not been properly cited or from whom proper permission has not been taken when needed.



Date: 31st July, 2020

Shivani Sharma
ID: 20132012

Acknowledgement

I am deeply grateful to Prof. Sujit K. Ghosh for mentoring me during the tenure of my doctoral thesis. His constant encouragement and guidance helped me a lot to charter unknown dimensions with an unwavering faith, a quintessential skill to develop as a budding researcher. I thank him for believing in me and providing me freedom to explore my ideas and build my confidence. I am also grateful to him for pushing me to develop and learn variety of skills which will be very helpful in future. The experience I have gained under your supervision will serve as stepping stone. Thankyou sir.

I would like sincerely like to thank Indian Institute of Science Education and Research, Pune and the director's (present as well as past) Prof. Jayant B. Udgaonkar and Prof. Krishna N. Ganesh for providing cutting edge research technology and facilities. I am sincerely grateful to my Research Advisory Committee members (RAC) (Dr. Benudhar Punji, National Chemical Laboratory, Pune and Dr. Moumita Majumdar, Indian Institute of Science Education and Research, Pune) for their valued inputs and suggestions during the annual review meetings.

I would like to thank Prof. H. N. Gopi, Prof. M. Jaykannan (Present and Past Chair, Department of Chemistry) for maintaining a healthy and conducive environment in the department. I would like to thank all the IISER Pune faculty for their constant motivation during this time especially Dr. Nirmalya Ballav, Dr. Pramod Pillai, Dr. Angshuman Nag, Dr. R. Vaidyanathan, Prof. R. G. Bhat, Prof. R. Boomishankar. Dr. Anirban Hazra. I am grateful to the faculty who have taught me during my master's coursework and would like to express my sincere thanks to the faculties who supervised my lab rotations – Prof. H. N. Gopi, Prof. R. Boomishankar, Dr. Partha Hazra. I am grateful to Dr. Gyana Ranjan Tripathy for letting me use ICP-MS facility in his laboratory. I would like to acknowledge all the collaborators Dr. Ravichandar Babarao (RMIT, Australia), Dr. Mandar M. Shirolkar (Symbiosis Deemed University) for their invaluable inputs to my research work.

I very thankful to Mr. Parveen Nasa, Ms. Archana, Ms. Swati, Mr. Mahesh Jadhav, Mr. Nilesh Dumre, Mr. Anil, Mr. Yatish, Mr. Vikrant (ECS department) for their help during various instrumental analyses. I would especially thank Mrs. Reshma Deshpande, Mrs. Vinita Shetty from Indian Institute of Technology, Bombay (SAIF Facility) for their help with ICP analyses. I would also like to thank Mr. Mayuresh, Mr. Tushar, Mr. Mahesh, Mr. Nitin, Mr. Prabhas for their administrative and official support during my research period at IISER, Pune. I want to extend my sincere thanks to Anupam (Doctoral Student, ECS Department) for his support during ICP analysis.

I would like to extend my warm regards to Dr. Sudarshana Mukherjee. Ma'am, your words of encouragement, your ever-positive outlook and advice helped me a lot. I wish Suvan and Suyash a

wonderful life ahead.

I want to also acknowledge Dr. Sushma Bhan (Associate Professor, Gargi College, Delhi University) for believing in me and pushing me to realise my potential. I am also grateful to all the other teachers who have taught me in during my years at Gargi College, Delhi University. I am very deeply indebted to all my school (Dayawati Modi Academy-I) teachers for building the foundations of my learnings in life.

The overall research experience at IISER-Pune was made special by various members of the 'Microporous Materials Lab' group (Dr. Sanjog Nagarkar, Dr. Biplab Joarder, Dr. Biplab Manna, Dr. Soumya Mukherjee, Dr. Avishek Karmakar, Dr. Aamod V. Desai, Dr. Partha Samanta, Samraj Mollick, Yogeshwar More, Prateek Agrawal, Arunabha Sen, Subhajit Dutta, Sumanta Let, Sahel Fajal, Writakshi Mandal, Gourab Kumar Dam, Debanjan Mahato, Dr. Tarak Nath Mandal, Dr. Sreenu Bhanoth, Arif Inamdar, Shilpa Sonar, Naveen Kumar, Priyanshu Chandra, Arkendu Roy). Thank you all for being a part of this journey. I would like to thank seniors (Sanjog, Biplab J, Biplab M, Somu da, Avishek da) for their guidance and mentoring during the early days of my research. I would extend my deepest gratitude to Aamod and Partha for their support, mentorship, discussions during my formative years. Special thanks to Aamod for motivating, mentoring, and helping me solve exciting problems. In addition to this, I have learnt life lessons from Aamod and have found an amazing friend in him. I am also grateful to my juniors (Sumanta, Subhajit, Gourab) for their support, help, discussions in the last phase of my work. I would also like to acknowledge Arunabha Sen for some challenging discussions that were always followed by lots of thinking. I would like to thank Samraj, Tarak Da, Yogesh, Sahel, Writakshi, Debanjan for their valuable inputs. I am grateful to Ashwini Jadhav, BSMS student who helped me gain insights into the world of mentoring and worked enthusiastically with me. I would like to acknowledge Ms. Kriti Gupta for her constant support.

My time at IISER-Pune was made memorable by "Integrated Ph.D. 2013 Batch" (Bharat, Anish, Mehak, Aditi, Sandip, Neeladri, Ron, Divya, Dhriti, Akhila, Amar, Jay, Kashyap, Deepak, Adarsh, Anshul, Harpreet, Swati, Charu). I shared some amazing experiences with this bunch of people who are kind, inspiring, loving, hilarious, unimaginably weird and witty at the same time and these individuals have become a part of my extended family. I am so grateful that our paths crossed and these seven years laid the foundations of lifelong friendships. The support, endless laughter, fun and joking after a long tiring day of work made me go through even the toughest of the times. Bharat, Anish, Mehak, I will be forever grateful to you guys for believing in me in the darkest of the times. I want to thank Bharat for being with me in this long journey of ups and downs. Special mention to (Bharat, Neel, Sandy, Anish, Jay, Ron, Mehak, Dhriti) for all the fun filled saturdays, sunday, late night coffee, that I have spent with you guys. Some of the most cherishing memories came from during these times as well as from the uncountable number of trips that I took with you guys. I am also grateful to Tomin macha for his presence and his

ever-enthusiastic persona that was such joy to witness. I will always cherish the memories especially the K2S trek. I whole heartedly would like to thank Ankitha (Anku Di), Mukul (Mukku Bhaiya), Neha (Panku), Aamod for their heaps of support, love and guidance for my time at IISER. You guys are really special. I want to thank all my school and college friends (Sonali, Richa, Juhi, Shikha, Salma, Divyansh, Gazal, Srishti) for being with me through this journey.

I am grateful to IISER Pune and CSIR-SRF for the providing the research funding. I sincerely thank American Chemical Society (ACS), Royal Society of Chemistry (RSC), John Wiley & Sons, and Springer for publishing several research articles, reviews and book chapters during my tenure at IISER Pune.

At last, I want to extend my deepest gratitude towards my family especially Mummy, Papaji, Bhaiya and Rover, Amma, Bittoo Bhaiya whose support stood tall and their unwavering confidence in me helped me a lot. The last soul whom I would extend my heartfelt gratitude and love would be Rover, one of the brightest stars of my life (you will always be alive in my memories).

Contents

1.	**Introduction**	
1.1	Porous Coordination Polymers/Metal-Organic Frameworks	1.1
1.2	Classification of MOFs	1.2
1.3	Neutral N-donor based MOFs	1.4
1.4	Applications of N-donor linker derived MOFs	1.6
1.5	Objectives and Overview of thesis	1.10
1.6	References	1.12
2.	**Toxic Aromatics Induced Responsive Facets for a Pore Surface Functionalized Luminescent Coordination Polymer**	
2.1	Introduction	2.1
2.2	Experimental	2.2
2.3	Results and discussion	2.4
2.4	Conclusions	2.10
2.5	Appendix Section	2.11
2.6	References	2.36
3.	**Specific recognition of toxic allyl alcohol by pore-functionalized metal–organic frameworks**	
3.1	Introduction	3.1
3.2	Experimental	3.3
3.3	Results and discussion	3.5
3.4	Conclusions	3.9
3.5	Appendix Section	3.10
3.6	References	3.27

4. A Water-Stable Ionic MOF for the Selective Capture of Toxic oxoanions of Se(VI) and As(V) and Crystallographic Insight into the Ion-Exchange Mechanism

4.1	Introduction	4.1
4.2	Experimental	4.2
4.3	Results and discussion	4.6
4.4	Conclusions	4.11
4.5	Appendix Section	4.12
4.6	References	4.35

5. Rapid, selective capture of toxic oxo-anions of Se(IV), Se(VI) and As(V) from water by an ionic metal-organic framework (iMOF)

5.1	Introduction	5.1
5.2	Experimental	5.3
5.3	Results and discussion	5.9
5.4	Conclusions	5.17
5.5	Appendix Section	5.19
5.6	References	5.61

List of Abbreviations:

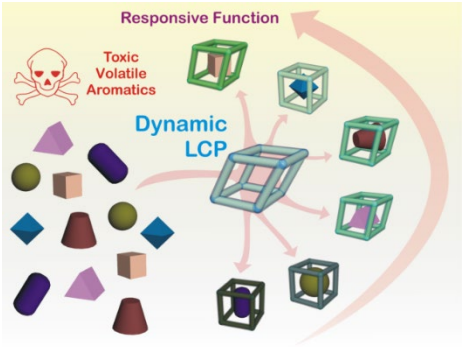
AAS	Atomic Absorption Spectroscopy
AES	Atomic Emission Spectroscopy
Anal.	Analysis
Å	Angstrom
α	Alpha
Calc	Calculated
cm^{-1}	centimeter Inverse
CCDC	Cambridge Crystallographic Data Centre
CP	Coordination Polymer
CT	Charge Transfer
°C	Degree Celsius
DNA	Deoxyribonucleic acid
DMF	Dimethylformamide
DFT	Density Functional Theory
DMSO-d6	Dimethylsulfoxide-d6
EDS	Energy Dispersive X-ray spectroscopy
eV	electron volt
ESR	Electron Spin Resonance
FESEM	Field Emission Scanning Electron Microscopy
g	gram
h	hour(s)
HSAB	Hard Soft Acid Base theory
HOMO	Highest Occupied Molecular Orbital
Hz	Hertz
^{1}H-NMR	Proton Nuclear Magnetic Resonance
H_2O	Water
ICP	Inductively Coupled Plasma
iMOFs	ionic MOFs
IP	Ionization Potential
K_d	Distribution Coefficient
λ	Lambda
LDHs	Layered Double Hydroxides

LCP	Luminescent Coordination Polymer
LUMO	Lowest Unoccupied Molecular Orbital
MOFs	Metal-organic Frameworks
MS	Mass Spectroscopy
mM	millimole(s)
mg	milligram(s)
mol	mole(s)
mL	milliliter(s)
min	minute(s)
N2	Nitrogen
NBz	Nitrobenzene
PXRD	Powder X-ray diffraction
ppb	parts per billion
ppm	parts per million
PCPs	Porous Coordination Polymers
PL	Photoluminescence
SC-XRD	Single-Crystal X-ray diffraction
TEM	Transmission Electron Microscopy
TGA	Thermogravimetric Analysis
US-EPA	United States- Environmental Protection Agency
UV-Vis	Ultraviolet-visible
VOC	Volatile Organic Compound
WHO	World Health Organization
XPS	X-ray Photoelectron spectroscopy

Synopsis:

The present work explores the design and syntheses of neutral nitrogen-donor linker-based MOFs targeted as hosts for the selective recognition and sequestration of hazardous and toxic analytes. In this respect, the rationale choice of utilizing MOFs built from neutral nitrogen donor linkers offered prospects to impart peculiar functionalities viz. specific recognition sites, shape memory effect that propelled the emergence of selectivity in these extended coordination compounds. In the first section of the work, the development of neutral nitrogen linker-based MOFs was pursued for toxic analyte sensing such as volatile organic compounds (VOCs), allyl alcohol which are categorized by the EPA in the category of priority pollutants. While in the subsequent chapters, ionic MOFs were explored for the capture of toxic oxoanions of arsenic and selenium.

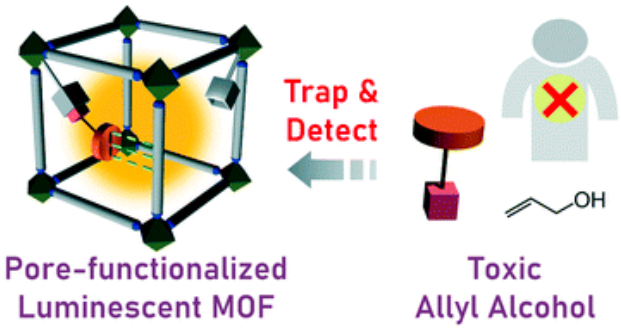
In **chapter 2**, an interpenetrated luminescent MOF was designed that served as a molecular decoder toward hazardous volatile organic compounds (VOCs). The material afforded soft-dynamism with its reversible nature that led to formulation of distinct photoluminescent response in synergism with the exciplex formation between the host-guest systems. The experiments revealed that the energetics of the host-guest complex were perturbed via multiple factor's including the electronic nature as well as the ionization potential of the analytes. In addition to this photoluminescence response, a colorimetric response was also observed specifically for dimethylaniline which was attributed to the formation of radical cations within the voids of MOF. LCP-100 serves as a striking example of MOF's ability to stabilize radicals within the voids of the channels. (Scheme 1) (*Inorg. Chem*. 2017, **56**, 6864-6869)



Scheme 1: Schematic representation showing analyte responsive dynamic host coordination polymer.

Further in the next **chapter 3**, efforts were dedicated towards developing a sensor for highly toxic and flammable allyl alcohol. In this regard, we rationally designed two neutral MOF appended with functional sites viz. metal-chloride along the porous channels of the network. The solids were screened as a sensor for alcohols and the materials showed a distinct response towards allyl alcohol as compared to congener alcohols. The selective recognition was ascribed to the multiple factors including the π-π

interaction, similar LUMO energy levels of the coordination polymers with the allyl alcohol. The properties were investigated thoroughly in detail. Notably, this is the first MOF explored towards the detection of allyl alcohol and this will propel the design of MOFs for this application. (Scheme 2) (*Mol. Syst. Des. Eng.* 2020, **5**, 469-476.)



Scheme 2: Schematic highlighting the design strategy in a functionalized MOF for allyl alcohol sensing.

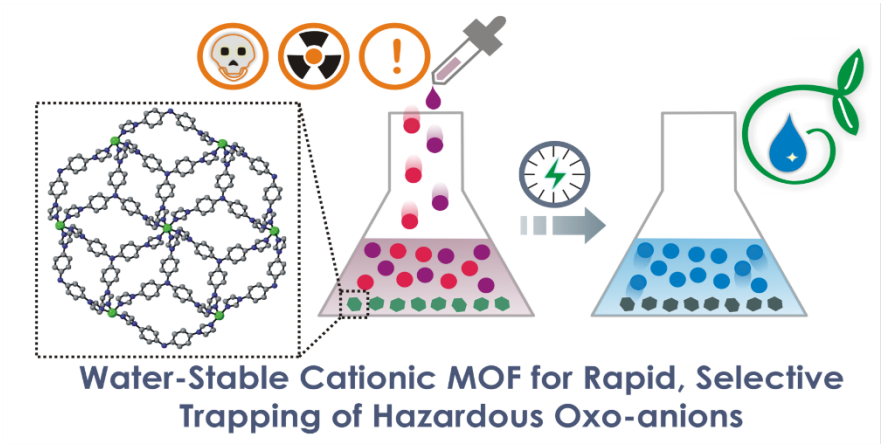
In the next section of the work, the focus was towards the development of cationic MOFs as scavengers for the sequestration of oxoanions of arsenic and selenium which has not been previously explored in literature. The interesting feature of these oxoanions include weak binding affinity as well as high solubility in water that renders their sequestration very arduous in nature. In **chapter 4**, the solution to this problem was approach through a rationale choice of a water stable ionic MOF, iMOF-1C, owing to the presence exchangeable SO_4^{2-} anions that imparted the shape memory effect. The material was thoroughly investigated in detail for its behaviour to sequester oxoanions of Se(VI) and As(V) in terms of kinetics, uptake capacity as well as for recyclability and the results obtained were quite promising. The selective uptake was rationalized on the basis of shape memory effect offered by SO_4^{2-} anions as well as the hydration energy difference between the oxoanions and framework.



Scheme 3: Schematic design illustrating the utilizing of ionic MOFs as scavenger towards oxoanions of arsenic and selenium.

Further, the ion-exchange mechanism was confirmed by single crystal diffraction analysis that also revealed variable modes of binding of oxoanions of arsenic and selenium as well as crucial role of hydrogen bonding interaction in the stabilization of these weakly bound oxoanions. This study served as the first example of ionic MOF explored for this application. (Scheme 3) (*Angew. Chem. Int. Ed.*, 2020, **59**, 7788-7792)

Learning from the previous study, the development of cationic MOF for the capture of oxoanions of arsenic and selenium was pushed via rationally designing a novel cationic MOF, iMOF-3C in **chapter 5**. The cationic network wad knitted with features such as shape template effect, chemical stability in water as well as basic media along with the presence of one-dimensional porous channels that facilitated the ion-exchange. (Scheme 4)



Scheme 4: Schematic representing rapid capture of oxoanions of arsenic and selenium by a cationic network.

As a consequence, the material exhibited a rapid and selective uptake behaviour towards oxoanions of Se(IV), Se(VI) and As(V) with one the highest maximum uptake capacity. In detail analysis revealed the corresponding distribution coefficient values as the highest in the field of MOFs. Moreover, iMOF-3C was able to reduce the concentrations of arsenic and selenium in river water to yield drinking quality water that met the US-EPA criteria. The excellent experimental results were supported by theoretical investigation that provided insights regarding the stabilization sites as well as the high binding energies. These reports will further the design of ionic MOFs for capture of oxoanion of arsenic and selenium. (*Manuscript Submitted*)

In summary, this thesis will help propel the development of neutral nitrogen donor MOFs in the domain of sensing as well as sequestration of toxic analyte which is crucial for the sustainable development.

RIGHTS AND PERMISSIONS

Chapter – 2

Adapted with permission from (*Inorg. Chem.*, 2017, **56**, 6864-6869). Copyright (2017) American Chemical Society.

Chapter – 3

Reproduced with permission from (*Mol. Syst. Des. Eng.*, 2020, **5**, 469-476). Copyright (2020) The Royal Society of Chemistry

Chapter – 4

Reproduced with permissions from (*Angew. Chem. Int. Ed.*, 2020, **59**, 7788-7792) Copyright (2020) John Wiley and Sons.

Publications:

(† - indicates equal contribution)

Included in thesis

1. **S. Sharma**, † A. V. Desai, † B. Joarder and S. K. Ghosh. *Angew. Chem. Int. Ed.*, 2020, **59**, 7788-7792
2. **S. Sharma**, S. Let, A. V. Desai, S. Dutta, M. M. Shilorkar, R. Babarao and S. K. Ghosh. (*Manuscript Submitted*).
3. B. Manna, † **S. Sharma**, † S. Mukherjee, A. V. Desai and S. K. Ghosh. *Inorg. Chem*. 2017, **56**, 6864-6869.
4. A. V. Desai,† **S. Sharma**, † A. Roy and S. K. Ghosh. *Mol. Syst. Des. Eng.*, 2020, **5**, 469-476.

Not included in thesis

5. **S. Sharma**, A. Karmakar and S. K. Ghosh. (Book Chapter) *World Scientific Publishers*, 2018, 325-375, doi: 10.1142/9789813226739_0008.
6. A. Sen, † **S. Sharma**, † S. Dutta and S. K. Ghosh *(Manuscript under preparation)*
7. **S. Sharma** and S. K. Ghosh. *ACS Omega*, 2018, **3**, 254-258.
8. B. Manna, † **S. Sharma**† and S. K. Ghosh. *Crystals*, 2018, **8**, 37.
9. A. V. Desai, †**S. Sharma**, † S. Let and S. K. Ghosh. *Coord. Chem. Rev.* 2019, **395**, 146-192.
10. A. V. Desai, † **S. Sharma**, † A. Roy and S. K. Ghosh. *Cryst. Growth Des*. 2019, **19**, 7046-7054.
11. S. Mukherjee, **S. Sharma** and S. K. Ghosh. *APL Mater.* 2019, **7**, 050701.
12. A. V. Desai, **S. Sharma** and S. K. Ghosh. *Elsevier*, 2019, 95-140, doi: 10.1016/B978-0-12-814633-0.00006-5.
13. R. Bakthavatsalam, M. P. U. Haris, S. R. Shaikh, A. Lohar, A. Mohanty, D. Moghe, **S. Sharma**, C. Biswas, S. S. K. Raavi, R. G. Gonnade, J. Kundu. *J. Phys. Chem. C.* 2020, **124**, 3, 1888-1897.
14. P. Samanta, A. V. Desai, **S. Sharma** and S. K. Ghosh. *Inorg. Chem.* 2018, **57**, 2360-2364.
15. T. N. Mandal, A. Karmakar, **S. Sharma** and S. K. Ghosh. *The Chemical Record*, 2018, **18**, 154-164.
16. B. Manna, S. Mukherjee, A. V. Desai, **S. Sharma**, R. Krishna and S. K. Ghosh. *Chem. Commun.*, 2015, **51**, 15386-15389.
17. **S. Sharma**, † S. Mukherjee, † M. Vandichel, A. V. Desai, A. Jadhav, G. Kociok-Köhn, M. J. Zaworotko and S. K. Ghosh* (Manuscript under preparation)

Chapter 1

Introduction

1.1 Porous Coordination Polymers/ Metal-organic Frameworks:

Porous Coordination Polymers (PCPs)/ Metal-organic Frameworks (MOFs) are a class of crystalline, hybrid organic-inorganic coordination polymers.[1] They are assembled via coordination bonds between organic ligand(s) and metal ion(s)/cluster(s) while the extended coordination prompts the formation of a framework structure with potential voids, generally occupied by guest solvent molecules, counterions, unreacted linkers (Figure 1.1).[2] MOFs are differentiated from coordination polymer (CPs) based on dimensionality as well as potential porosity.[1a] The research interest in the field of MOFs escalated toward the end of the 20th century. Nevertheless, the past two decades have unraveled the vast potential of MOFs in several fields ranging from adsorption, toxic analyte chemical sensing, environmental pollutant capture, catalysis (Figure 1.2).[3] An excellent understanding of self-assembly processes and coordination chemistry is critical for the rational design of such supramolecular framework solids. The fine tunability emanating from the hybrid nature of MOFs plays a crucial role in distinguishing them from other classes of porous sorbent materials such as zeolites, porous carbons. The tuneable nature provided researchers a platform to play with solid-state materials in terms of aperture size, functionality, and so-on that lacked in literature before the realization of MOFs.[4] The wide range of organic linkers, as well as large scale availability of numerous metal ions, bestows the possibility of infinite combinations. Hitherto, since the advent of MOFs, > 70000 novel structures have been discovered and with few possessing remarkably large surface areas > 10000 m^2/g.[5] This fine-tuning has been explored thoroughly and led to the realization of multi-variate MOFs, isostructural MOFs, hierarchal MOFs, multi-functional MOFs.[6] Additionally, MOFs can be modulated based on the pore size with the voids ranging from ultramicropores (aperture size < 0.7 nm), micropores (aperture size 0.7 nm - < 2 nm), mesopores (aperture size > 2 nm to < 5 nm) to macropore (> 5 nm) according per IUPAC notation which is not feasible in conventional porous solids.[7]

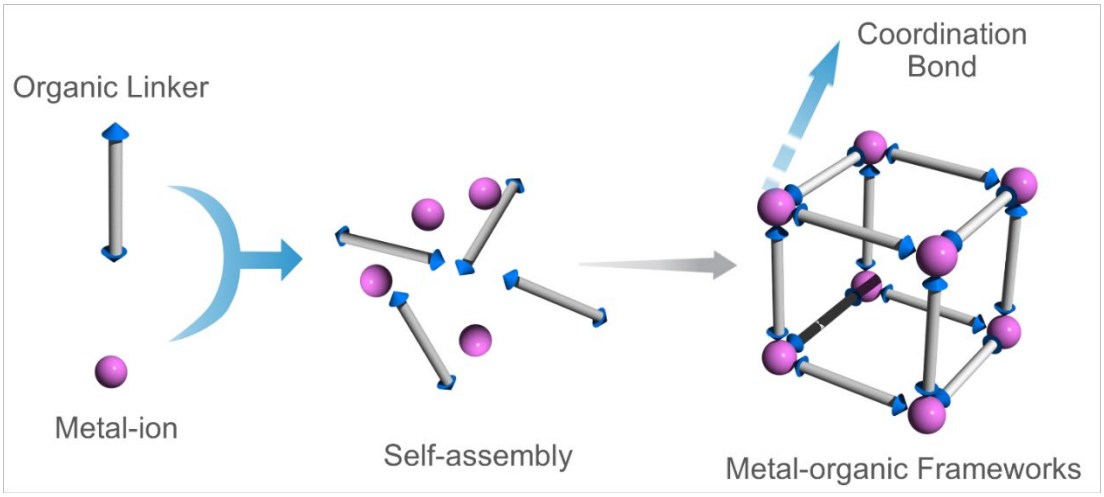


Figure 1.1: Representation showing the generic approach for the synthesis of metal-organic frameworks (MOFs).

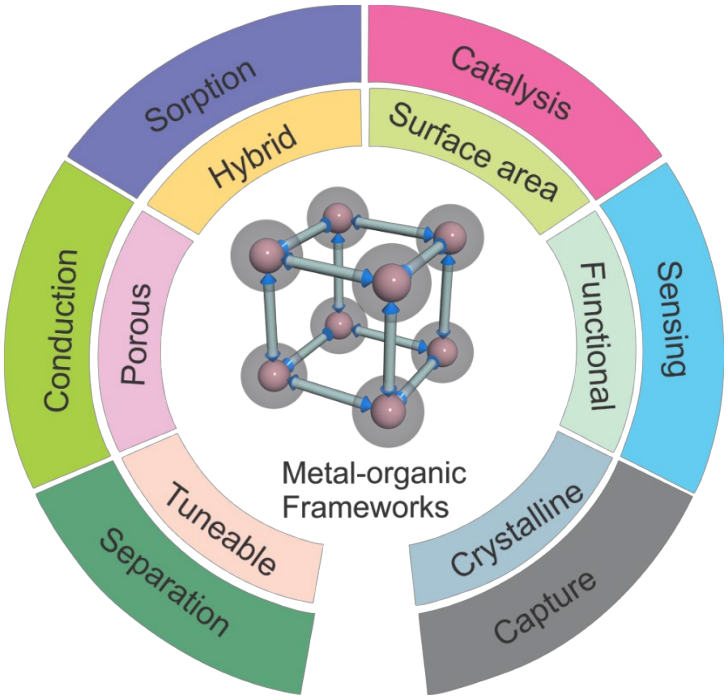


Figure 1.2: Schematic diagram showing peculiar features of MOFs and its applications.

1.1.1 Building Units and Synthesis of MOFs

As already mentioned in section 1.1, MOFs are composed of the organic linker(s), metal ion(s) with guest molecules occupying the porous space. Typically, the organic linkers can be either di/multi-topic in nature. Moreover, the broad spectrum of organic linkers can be classified based on terminal donor moiety as (i) Oxygen donor, (ii) Nitrogen donor.[8] These include various functional groups, including carboxylates (R-COOH) and sulfonates (R-SO_3H), neutral/charged nitrogen donor linkers viz. pyridine, azolates, etc. MOFs can be fabricated from a variety of metal ions, such as transition metal ions like Cr(III), Ni(II), Zn(II); alkali metals and alkaline earth metals, lanthanoids etc. thereby providing plenty of opportunity for a rationale choice according to the targeted application.Various syntheses pathways for the fabrication of MOFs have been realized including methods such as solvothermal synthesis, hydrothermal synthesis, slow diffusion, electrodeposition, microwave synthesis.[9] Generally, the coordination environment of the metal ion center in MOF depends on several parameters, including the choice of a metal atom, type of donor atom in the linker, crystal field stabilization energy, pKa of the linker, the reaction conditions, etc.[10]

1.2 Classification of MOFs

1.2.1 Neutral MOFs and ionic-MOFs.

MOFs can be classified depending on the charge of the framework backbone into two categories: (i) Neutral MOFs and (ii) Ionic MOFs (iMOFs).[11] The fabrication of neutral/ionic MOFs is performed by variable pathways, and the syntheses are guided by the principles of coordination chemistry, which directly highlights the importance of the choice of linkers as well as metal ions. Neutral MOFs require the presence of charge balancing moieties at the metal center, for instance, negatively charged counter anions from the metal salts or charged linkers (Figure 1.3b). While for the case of ionic MOFs, the framework is associated with a residual positive or negative charge, thereby yielding anionic/cationic network whose charge is typically offset by the guest anions/cations (Figure 1.3a, c). The probability resulting in the formation of either kind of network comes down to several parameters viz. charge of metal ion, denticity of the linker, size of metal ion, the donor atom of the linker, reaction temperature, concentrations, pressure and so-on.[10] In view of the interest of this thesis focus, the fabrication strategy for cationic MOFs derived from neutral nitrogen donor linker has been explained herein. Cationic MOFs are constructed majorly via a combination of neutral nitrogen donor-based linkers with metal ions having weakly coordinating counter anions (Figure 1.3c).[11] Few more strategies viz. post-synthetic modification of organic functional groups such as pyridyl have also been reported. [12]

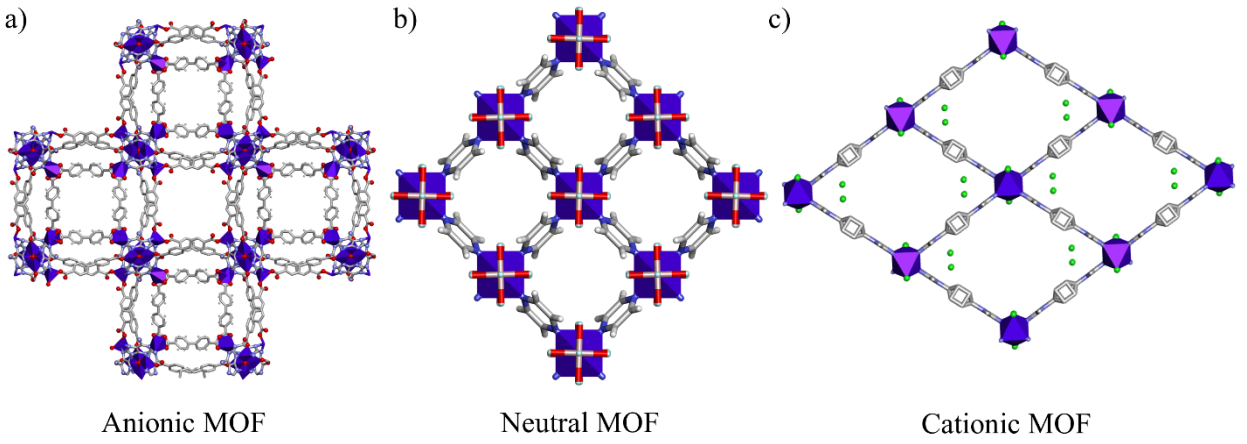


Figure 1.3: Representative figure showing different kinds of MOFs (a) Anionic MOF, (b) Neutral MOF and (c) Cationic MOF. Ref Code: (a) NUDLAA, (b) DAXNOI, (c) SUCNUC01.

1.2.2 Classification based on structural aspect: Rigid and flexible MOFs and various generations of MOF

MOFs can be broadly classified as flexible/rigid depending on the framework features. Flexible MOFs exhibit peculiar structural transition, with respect to an external stimulus, while maintaining the crystalline nature of molecular solids. In this respect, numerous chemical and physical stimuli, including chemicals,

light, temperature, pressure, electric, and magnetic fields, have been explored to drive such structural transitions.[13] In this respect, the classical concept of soft porous crystals, as discussed by Kitagawa and co-workers, highlights the various concepts involved in the fabrication of a flexible network.[14] The MOFs constructed from neutral nitrogen donor linkers feature prominently in that category.[15] These flexible networks can exist in a multi-stable state and can be converted from one phase to another easily when triggered via stimuli. In sharp contrast to flexible MOFs, certain MOFs are known for the extremely rigid nature and even maintain the structural characteristics in the presence of any external stimulus. These stimuli-responsive structural transitions directly impact the characteristic properties of the MOFs. This behaviour has been explored well in literature with some flexible MOFs yielding unique results in the field of sensing, separation, catalysis, capture, conduction.[16] Hitherto, flexibility in MOFs is highly sought after and especially has high relevance for molecular decoding applications as well (Discussed further in Section 1.4.1).

Additionally, MOFs can be classified among different generations viz. 1st generation, 2nd generation, 3rd generation, and 4th generation based on the type of network.[14] The first-generation MOFs disassemble after the removal of guest solvent molecules in contrast to the second-generation MOFs which are quite known to maintain their structural integrity. Further, the third generation MOFs can alter their structure depending upon a stimulus, and a new crystalline phase is achieved via structural transformation. Lastly, fourth-generation MOFs are relatively novel and encompass frameworks wherein the long-range order remains intact to impart robustness whilst the flexibility is introduced via displacement of counter anions, guest solvent molecules, introduction of flexible groups, defect creation, post-synthetic modification etc.[17]

1.3 Neutral N-donor linker based MOFs

Neutral nitrogen donor linker based MOF stands tall among the earliest examples of extended framework structures. The end of the 20th century and early 21st century has witnessed the rise of nitrogen donor linker for MOF fabrication. However, the in-depth investigations pushing for real-time applications are catching up more so in the past decade.[18] These MOFs are fabricated utilizing organic linkers such as bipyridyl, pyrazine, imidazole, cyanide, triazole (Figure 1.4) and so-on. In combination with a suited metal-ion/counter anion these linkers yield either a neutral/cationic network depending on the properties of the co-reactants present during the crystallization process. These networks can be easily fine-tuned in terms of functionality, pore size, guest anion. Typically, neutral nitrogen donor linker based MOFs are constructed from substituted six-membered pyridyl linkers, substituted five-membered aromatic heterocycles and so-on. The peculiar size of the organic donor moiety significantly affects the product formation. For instance, six coordination from pyridine type linker is untenable, which favors anion binding at the vacant metal sites. While on the other hand, five-membered nitrogen linkers do not have any such steric constraints, thereby

allowing crowding of the metal center that imparts stability to the metal-nitrogen bond. Moreover, the stability of neutral nitrogen-based MOFs revolves around (i) The metal-linker bond that includes factors such as pKa of the linker, charge of the metal ion, HSAB principles, denticity of the linker.[19] Generally, pyridine substituted linkers have relatively lower pKa values, while the azolates are quite known for high pKa. Notably, the pka values of the linker is direct proportional to the tendency of electron donation to M-L bond and has a direct impact on the strength of the metal-nitrogen bond as elucidated from the literature. Additionally, multi-dentate nitrogen donor linkers possess higher kinetic stability, as has been reported in the literature. (ii) Structural factors inclusive of the interpenetration as well as the formation of SBU or metal clusters. These are relevant for imparting high resilience to the network and seldom induced guest mediated structural transitions pertaining to the interpenetration of the network. (iii) Lastly Hydrophobicity of the linker, Steric crowding at the metal center. Introducing hydrophobic groups viz. fluorine atoms, alkyl chains in the linker have been trialled for increasing the water contact angle, therefore, enhancing the resistance towards moisture, chemicals for MOFs built from neutral nitrogen donor linkers. Apart from that, the crowding around the metal center also plays a crucial role in enhancing the protective armor around the coordination bond, thereby providing stability. Metal-nitrogen bond in neutral nitrogen donor linker based MOFs are relatively weak, and the guest-species present within the voids influence the bond strength and overall stability of the frameworks.[20] These host-guest interactions are quite relevant, and even the slightest tweaking of the non-covalent interactions can induce a response, which is a desirable feature. Additionally, cationic MOFs display several prominent features including shape memory effect, electrostatic interactions with the guest species thereby prevent leaching.[21] Encompassing such attractive features nitrogen donor-based MOFs are an intriguing subclass of MOFs. Herein, this thesis concerns with the development of neutral nitrogen donor-based functional MOFs and subsequent applications.

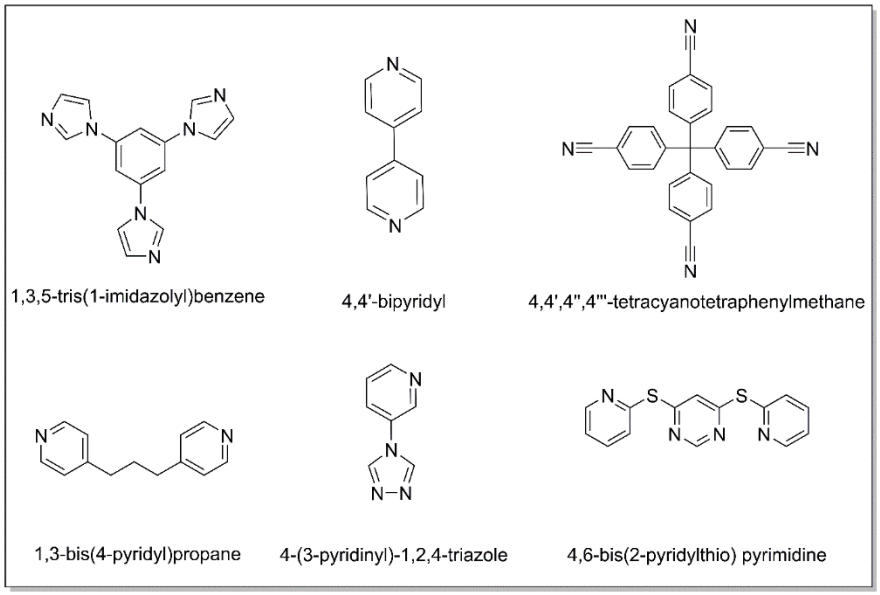


Figure 1.4: Representative examples of neutral nitrogen based organic linkers.

1.4 Applications of neutral N-donor linker based MOFs

Neutral nitrogen donor-based MOFs have seen commendable progress during the past decade with emerging applications in several fields, including catalysis, separation, conduction, magnetism, capture, sensing, and so-on.[18] In particular, research interest in the field of toxic analytes sensing and sequestration has gained tremendous attention lately owed to the close overlap between the anthropogenic polluting sources and the living spaces.[22] The direct influence of this overlap has caused severe contamination of air, groundwater that needs to be monitored as well mitigated. In this regard, the United Nations Sustainable Development Goals and targets initiative ensures the availability of basic needs such as clean air, safe drinking water. [23]A key factor to achieve this goal would be to develop suited materials that can selectively detect presence of such toxic compounds. Neutral nitrogen donor linker-based MOFs are at the forefront among solid-state materials investigated for this application as they offer features such as host-guest interactions crucial for imparting selectivity, pre-concentration of the guest moiety to maximize the interactions, ionic nature to attract the charged toxic analytes via electrostatic interactions to prevent leaching, template effect for selectivity.[18] To acknowledge and prioritize hazardous pollutants, the United States EPA has come up with a list of pollutants based on toxicity and hazardous nature. It encompasses various inorganic and organic pollutants like oxoanions, dyes, antibiotics; gaseous pollutants like VOCs, amines, $SO_{x;}$ explosives, hazardous air contaminants etc. Developing materials that exhibit selective detection as remediation tendency toward these aforementioned pollutants is imment in order to contribut

towards sustainable development goals. In this regard, neutral nitrogen donor MOFs were rationally designed and explored for various environmental applications and further details are mentioned below.

1.4.1 Toxic analyte sensing

Selective sensing and adsorption of toxic compounds by solid-state materials viz. MOFs is an emerging research field.[24] MOFs score over as highly suited candidates owed to tuneable features afforded these hybrid compounds. Several MOFs have shown immense potential towards toxic analyte sensing through different response pathways, including colorimetric detection, electrochemical detection, change in conductivity, photoluminescence, and so-on. Among these methods, the photoluminescence response mediated signal transduction in MOFs has gained much attention lately due (i) fast response time, (ii) detection possible for minuscule amounts even in the ppb range, (iii) high selectivity and sensitivity, (iv) heterogeneous phase.[25] The photoluminescent/colorimetric response is generated via numerous mechanisms such as metal to linker charge transfer, linker to linker charge transfer, guest induced luminescence etc.

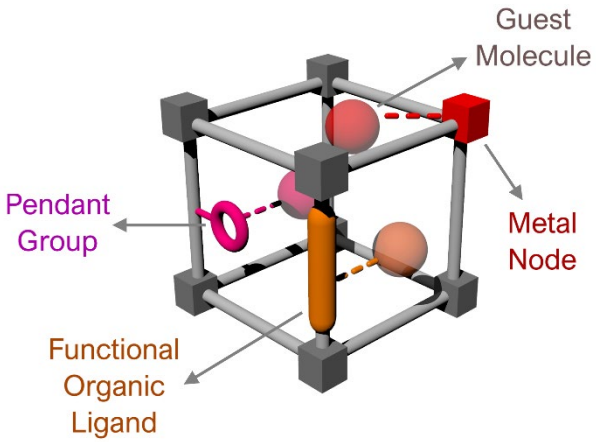


Figure 1.5: Schematic representation illustrating the various components of MOFs responsible for photoluminescence.

These analytes are detected via generation of a readout signal that typically involves either change in the associated intensity of the chromophore, shift in wavelength, or emergence of new peaks in the spectrum. Furthermore, depending on the electronic spin states involved during the radiative deacy, for instance, singlet to singlet transition affords luminescence. In contrast, singlet to triplet transition promotes phosphorescence. Neutral nitrogen donor-based MOFs can be easily tuned and imparted with functional sites for toxic analyte sensing and detection, for instance, functional sites, guest molecule, pendant functionality (Figure 1.5). Additionally, the intrinsic flexible nature imparts another level of dimensionality to enhance specificity, selectivity, and sensitivity of response. The selective non-covalent interactions of the framework backbone with the analyte forces energy-driven structural transitions to maximize such

interactions hence enhancing the sensitivity and selectivity of the solid host. Notably, these structural transformations are highly dependent on the electronic nature of the host and guest toxic analyte, the functional groups, shape, and size of toxic guests, pore aperture therefore providing a differential response. Hence, the development of MOF materials investigated for the toxic analyte(s) such as volatile organic compounds, hazardous industrial chemicals that pose huge risks are highly relevant. In this regard, several research groups have shown utility of luminescent MOFs for VOC sensing in both liquid as well as vapor phase. Prof. Kitagawa and co-workers studied a napthalenedimide based entangled PCP namely $[Zn_2(bdc)_2(dpNDI)]_n$ wherein (dpNDI= N,N'-di(4-pyridyl)-1,4,5,8-naphthalenediimide; bdc = 1,4-benzenedicarboxylate;). This material exhibited molecular decoding applications towards aromatic volatile organic compounds.[26] Prof. Li and co-workers fabricated luminescent entangled network $[\{(CuCN)_3L\cdot(guest)_x]_n$ (L= 2,6-bis((3,5-dimethyl-1*H*-pyrazol-4yl)methyl)pyridine; x=1,2). The material afforded structural dynamism in synergy with the changes in the photoluminescent signature emission profile towards VOC. Prof. Chen and co-workers synthesized $[Zn_7(ip)_{12}](OH)_2$ (MAF-34) from HIP = 1*H*-Imidazo[4,5-f][1,10]phenanthroline and it showed luminescent change towards toxic solvent vapors. There are few more reports of MOFs exhibiting VOC sensing, [29] however, novel MOFs exhibiting peculiar response in vapour phase are desired.

1.4.2 Ion capture

Water is an essential resource to all facets of life and according to a recent report by the united nations, the consumption of water is projected to increase by 20-55% by the year 2050.[30]In conjunction with this, according to the United Nations Sustainable Development Goals (SDG: 6), an initiative has been rolled in order to make clean water available to everyone. One solution proposed involves bridging the gap between the fresh water resources and the contaminated water as an efficient way to restore the degrading fresh water resources.[31] The various contaminants have been enlisted by United States-Environmental Protection Agency (US-EPA) that majorly categorizes as organic and inorganic moieties. Some of the organic pollutants include organic dyes, mycotoxins, antibiotics while the inorganic pollutants contain Hg^{2+}, Cd^{2+}, Pb^{2+}, Cs^{+}, UO_2^{2+}, I^{-}, SeO_4^{2-}, CrO_4^{2-}, $HAsO_4^{2-}$ and so-on.[32] Among these pollutants, oxoanions based of p-block elements viz. arsenic and selenium feature prominently but the research is still limited for the sequestration of these oxoanions. Arsenic poisoning is affecting millions of people across the globe.[33] At present the materials being utilized to sequester oxoanions of arsenic lack in terms of selectivity, uptake capacity, kinetics.[34] Additionally, selenium is a toxic element > 400 ppb and also selenium features a radioactive isotope (^{79}Se) which is produced in the nuclear power plant as a by-product of ^{235}U fission.[35]This necessitates the development of novel materials including the in-depth studies for kinetics, stability, uptake

capacity etc. In this regard, cationic MOFs have distinct advantages as already discussed in section 1.3. The unique shape template effect/shape memory effect can be easily imparted to such systems by careful selection of anion/cation precursors. The similarity in the shape and size of anions/cations with respect to the incoming toxic anions plays a critical role in maximising the interactions of the framework backbone with the incoming toxic guests. Additionally, the mode of capture i.e. via ion-exchange is governed by the electrostatic interaction between the positively charged network and the negatively charged anions plays a major role in the selective capture.[34] Moreover, non-covalent interactions viz. hydrogen bonding, electrostatic interactions, lewis acid-base pair interactions as well as key physical parameters like hydrophobicity affect the stabilization of toxic anion (Figure 1.6).[34,36] In this regard, cationic MOFs offer tremendous potential especially in the field of capture of toxic and hazardous ions attributed to the aforementioned features.

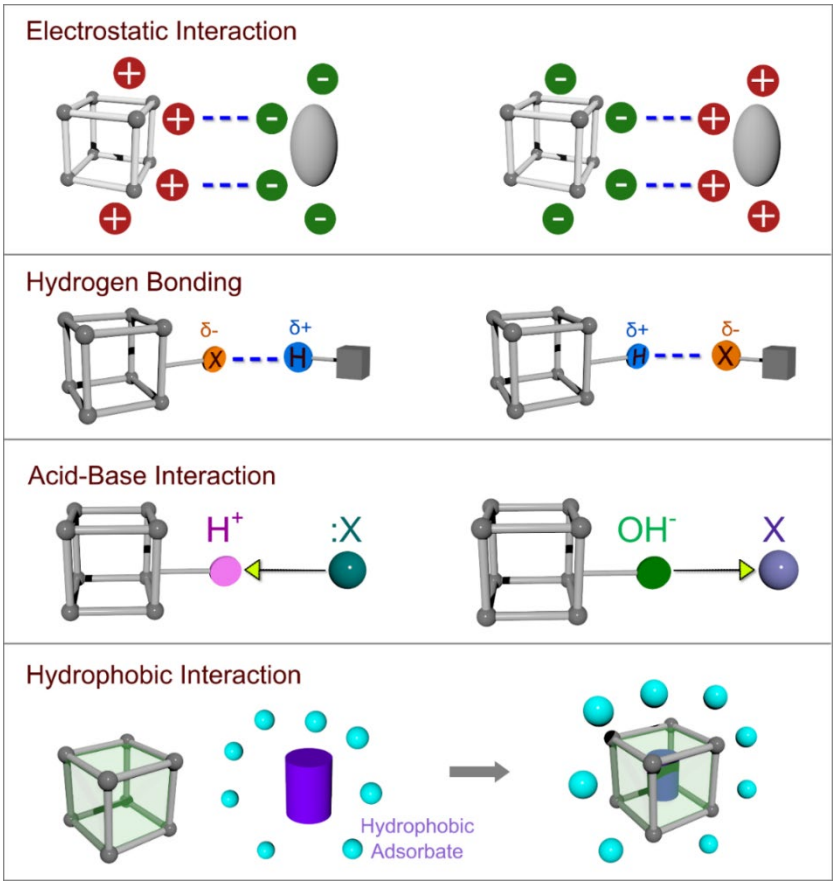


Figure 1.6: Various non-covalent interactions exhibited by MOFs for stabilization of toxic compounds.

Surprisingly, such cationic scaffolds have not been explored previously for the sequestration of oxoanions exhibiting extremely weak binding affinity for instance oxoanions of arsenic and selenium. In the field of MOFs, various neutral MOFs have been trialled for capture of these oxoanions. Farha and co-workers screened several MOFs viz. NU-1000, UiO-66, UiO-66-NH_2 encompassing zirconium clusters as SBU.[37] These linker replacement at the zirconium cluster served as the driving force for the capture of toxic anions of selenate and selenite. Further, Yang and co-workers synthesized bismuth based MOF namely CAU-17 that showed capture of selenite oxoanions via irreversible binding.[38] For arsenic oxoanions capture there are few reports wherein neutral MOFs have been investigated via adsorption.[34] However, ionic MOFs are yet to be explored for the capture of oxoanion of selenium and arsenic therefore in order to push the development of ionic MOFs in this respect, capture of these aforementioned oxoanions was studied. The focus was to utilize water stable cationic MOFs constructed via variety of strategies including utilization of multi-dentate linkers, using Ni(II) as metal ions to further enhance the stability of solids via increasing crystal field stabilization energy.

1.5 Objectives and Overview of thesis

With this brief background, the focus of the present thesis is towards the development of neutral nitrogen donor based MOF materials that can selectively detect and capture hazardous and toxic compounds selectively. Though MOFs have exhibited huge potential at this front, however, there is plenty of room for improvement in order to arrive at an ideal solution applicable in real-time. The main objectives of this work include:

(a) Development of novel sensors and to study the structure-property correlation.

(b) To employ targeted functional sites and analyze their effect on the host-guest interactions.

(c) Develop and design sorbents materials for weakly binding oxoanions.

(d) Understanding the role of shape template effect, non-covalent interactions for stabilization of such ions.

This thesis explores neutral nitrogen donor derived MOFs for toxic analyte sensing and capture based applications. In the first two chapters, luminescent MOFs were explored as solid-state sensors for toxic analyte sensing as well as detection. While in the last two chapters, cationic MOFs were studied as scavengers for toxic oxoanions of arsenic and selenium which is not reported in literature previously.

Chapter Two describes design, synthesis and characterization of a luminescent coordination polymer from neutral nitrogen donor linker and Cd(II) metal ion, termed as LCP-100. The reactants in combination with the nitrobenzene solvent molecules (template) yielded a flexible interpenetrating MOF. The desolvated phase LCP-100a exhibited reversible nature with characteristic affinity towards aromatic toxic VOCs. The strong host-guest interactions in synergy with the photoluminescent nature yielded variable response for toxic VOCs viz. N, N'-dimethylaniline, anisole, cyanobenzene, benzene etc. This was elucidated from photoluminescent as well as solids-state absorption studies and the contribution from charge transfer and variable ionization potential played a critical role. Additionally, some colorimetric response was observed for N, N'-dimethylaniline exposed phase which was thoroughly investigated by electron paramagnetic resonance that indicated presence of radical species.

Chapter Three focusses on the design, synthesis and characterization of two rationally designed metal-organic frameworks. A luminescent coordination polymer that exhibited decoding property selectively for highly toxic and hazardous VOC viz. Allyl alcohol was designed rationally. The network was appended with specific recognition site for facile host-guest interaction in addition to the conjugated linker as site for stabilization of allyl alcohol molecules via π-π interaction. The photoluminescence spectroscopy revealed selective sensing of allyl alcohol by both the networks and theoretical modelling further revealed rationale behind the selective performance of these solids.

Chapter Four presents the first attempt in MOF literature wherein a cationic MOF, viz. iMOF-1C was studied for its efficacy towards sequestration of oxoanions of arsenic and selenium. The network was rationally selected owed to the features such as water stability, one dimensional porous channel and most importantly sulphate as the exchangeable ions. The critical choice of sulphate anion (tetrahedral geometry) has been discussed and signifies the importance of shape template effect in ion-exchange process. iMOF-1C showed selective uptake behaviour towards oxoanion of Se(VI) and As(V), with among the highest uptake capacity. Additionally, the single crystals exposed to toxic oxoanions were discerned via single-crystal X-ray diffraction analysis and the mechanism of toxic anion capture has been discussed in detail.

Chapter Five presents the synthesis, characterization and application of a novel cationic MOF, termed as iMOF-3C. Improving the limitations of the previous chapter i.e slow kinetics, stability limited to water medium, via rationale design a novel chemically stable cationic MOFs for rapid sequestration of oxoanions of Se(IV), Se(VI) and As(V) was targeted. The choice of tripodal neutral nitrogen donor linker, Ni(II) metal centers coupled with solvothermal synthetic pathway was crucial to the design strategy. Structural insights revealed a porous two-dimensional network with sulphate anions present within the voids. The material

afforded a rapid kinetics, selective uptake and among the highest uptake capacities in the field of MOFs. Additionally, the material produced potable drinking water from a river water sample spiked with arsenic and selenium oxoanions thereby meeting the EPA and WHO criteria. Theoretical studies supported the experimental data and high binding energies were unvieled.

1.6 References

1. (a) S. Kitagawa, R. Kitaura and S.-i. Noro, *Angew. Chem. Int. Ed.* 2004, **43**, 2334-2375, (b) S. R. Batten, N. R. Champness, X.-M. Chen, J. Garcia-Martinez, S. Kitagawa, L. Öhrström, L.; M. O'Keeffe, M. P. Suh and J. Reedijk, *Pure Appl. Chem*., 2013**, 85***,* 1715-1724.

2. (a) H. C. Zhou, J. Long and O. M. Yaghi, *Chem. Rev*., 2012, *2*, 673-674.

3. B. Li, H.-M. Wen, Y. Cui, W, Zhou, G. Qian and B. Chen, *Adv. Mater*., 2016, **28**, 8819-8860.

4. (a) M. O'Keeffe and O. M. Yaghi, *Chem. Rev.*, 2012**, 112***,* 675-702, (b) A. Dhakshinamoorthy, A. M. Asiri and H. Garcia, *Chem. Comm*., 2017, **53**, 10851-10869. (c) S. T. Meek, J. A. Greathouse and M. D. Allendorf, *Adv. Mater.*, 2011, *23*, 249-267.

5. (a) P. Z. Moghadam, A. Li, A. B. Wiggin, A. Tao, A. G. P. Maloney, P. A. Wood, S. C. Ward and D. Fairen-Jimenez, *Chem. Mater.*, 2017, **29**, 2618-2625, (b) H. Furukawa, K. E. Cordova, M. O' Keefe and O. M. Yaghi, *Science*, 2013, **341**, 1230444.

6. (a) L. Feng, K.-Y. Wang, G. S. Day and H.-C. Zhou, *Chem. Soc. Rev.*, 2019, **48**, 4823-4853. (b) K. K. Tanabe and S. M. Cohen, *Chem. Soc. Rev.*, 2011, 40, 498-519.

7. K. S. W. Sing, D. H. Everett, R. A. W. Haul, L. Moscou, R. A. Pierotti, J. Rouquerol and T. Siemieniewska, *Pure and Applied Chemistry*, 1985**, 57***,* 603-619.

8. W. Lu, Z. Wei, Z.-Y. Gu, T.-F. Liu, J. Park, J. Park, J. Tian, M. Zhang, Q. Zhang, T. Gentle III, M. Boscha and H.-C. Zhou, *Chem. Soc. Rev.*, 2014, **43**, 5561-5593.

9. (a) S. Biswas and N. Stock, *Chem. Rev.*, 2012, **112**, 933-969. (b) S. Yuan, L. Feng, K. Wang, J. Pang, M. Bosch, C. Lollar, Y. Sun, J. Qin, X. Yang, P. Zhang, Q. Wang, L. Zou, Y. Zhang, L. Zhang, Y. Fang, J. Li and H.-C. Zhou, *Adv. Mater.*, 2018, **30**, 1704303. (c) M. Rubio-Martinez, C. Avci-Camur, A. W. Thornton, I. Imaz, D. Maspoch and M. R. Hill, *Chem Soc. Rev.*, 2017, **46**, 3453-3480.

10. A. J. Howarth, Y. Liu, P. Li, Z. Li, T. C. Wang, J. T. Hupp and O. K. Farha, *Nat. Mater. Rev.*, 2016, 1, 15018.

11. A. Karmakar, A. V. Desai and S. K. Ghosh, *Coord. Chem. Rev.*, 2016, 307, 313-341.

12. S. Sharma, A. Karmakar, and S. K. Ghosh, Elaboration and Applications of Metal-Organic Frameworks; World Scientific Publications, 2018; pp 325−375; DOI: 10.1142/ 9789813226739_0008.

13. A. Schneemann, V. Bon, I. Schwedler, I. Senkovska, S. Kaskel and R. A. Fischer, *Chem. Soc. Rev.*, 2014, **43**, 6062-6096.

14. S. Horike, S. Shimomura and S. Kitagawa, *Nat. Chem.*, 2009, **1**, 695-704.

15. B. Manna, A. V. Desai and S. K. Ghosh, *Dalton Trans.*, 2016, 45, 4060-4072.

16. Z. Chang, D.-H. Yang, J. Xu, T.-L. Hu and X.-H. Bu, *Adv. Mater*., 2015, **27**, 5432-5441.

17. (a) S. Kitagawa, New Dimensions of Porous Coordination Polymers/Metal-Organic Frameworks. Presented at the 43rd International Conference on Coordination Chemistry, Sendai, Japan, July 30−August 4, 2018; Abstract A00584-SK. (b) S.-Y. Zhang, S. Jensen, K. Tan, L. Wojtas, M. Roveto, J. Cure, T. Thonhauser, Y. J. Chabal, and M. J. Zaworotko, *J. Am. Chem. Soc.*, 2018, **140**, 12545-12552. (c) B. Liu, *ACS Materials Lett.*, 2019, **1**, 564-567.

18. A. V. Desai, S. Sharma, S. Let and S. K. Ghosh, *Coord. Chem. Rev.*, 2019, **395**, 146-192.

19. N. Li, J. Xu, R. Feng, T.-L. Hu and X.-H. Bu, *Chem. Comm.*, 2016, **52**, 8501-8513.

20. A. Karmakar, P. Samanta, A. V. Desai and S. K. Ghosh, *Acc. Res. Chem.*, 2017, **50**, 2457-2469.

21. (a) A. V. Desai, B. Manna, Avishek Karmakar, Amit Sahu and S. K. Ghosh, *Angew. Chem. Int. Ed.*, 2016, **55**, 7811-7815.

22. (a) T. Islamoglu, Z. Chen, M. C. Wasson, C. T. Buru, K. O. Kirlikovali, U. Afrin, M. R. Mian and O. K. Farha, *Chem. Rev.*, 2020, DOI: 10.1021/acs.chemrev.9b00828. (b) P. Samanta, A. V. Desai, Sumanta Let and S. K. Ghosh, *ACS Sustainable Chem. Eng.*, 2019, **7**, 7456–7478. (c) N. S. Bobbitt, M. L. Mendonca, A. J. Howarth, T. Islamoglu, J. T. Hupp, O. K. Farha and R. Q. Snurr, *Chem. Soc. Rev.*, 2017,**46**, 3357-3385. (d) Metal-organic Frameworks for Environmental Applications, 2019, Eslevier, DOI: 10.1016/B978-0-12-814633-0.00018-1

23. UN General Assembly, *Transforming our world : the 2030 Agenda for Sustainable Development*, 21 October 2015, A/RES/70/1.

24. (a) H. Wang, W. P. Lustig and J. Li, *Chem. Soc. Rev*., 2018, **47**, 4729-4756.

25. (a) M. D. Allendorf, C. A. Bauer, R. K. Bhakta and R. J. T. Houk, *Chem. Soc. Rev.*, 2009, **38**, 1330-1352. (b) Y. Cui, Y. Yue, G. Qian and B. Chen., *Chem. Rev.*, 2012, **112**, 1126-1162.

26. Y. Takashima, V. M. Martínez, S. Furukawa, M. Kondo, S. Shimomura, H. Uehara, M. Nakahama, K. Sugimoto and S. Kitagawa, *Nat. Comm*., 2011, **2**, 168.

27. J.-H. Wang, M. Li and D. Li, *Chem. Sci.*, 2013, **4**, 1793.

28. X.-L. Qi, R.-B. Lin, Q. Chen, J.-B. Lin, J.-P. Zhang and X.-M. Chen, *Chem. Sci.*, 2011, **2**, 2214-2218.

29. W. P. Lustig, S. M. Mukherjee, N. D. Rudd, A. V. Desai, J. Li and S. K. Ghosh, *Chem. Soc. Rev.*, 2017, 46, 3242-3285.

30. R. P.Schwarzenbach, B. I.Escher,K.Fenner, T. B. Hofstetter, C. A. Johnson, U. v. Gunten and B. Wehril, *Science*, 2006, **313**, 1072-1077; (*b*)The United Nations World Water Development Report 2019. [ISBN: 978-92-3-100309-7]; (*c*) OECD Environmental Outlook to 2050: The Consequences of Inaction - ISBN 978-92-64-122161; (*d*) A. Boretti and L. Rosa, *npj Clean Water*, 2019, **2**, 15; (*e*) United States Environmental Protection Agency. National Primary Drinking Water Regulations. EPA, 816-F-09-004, MAY 2009.

31. UN General Assembly, *Transforming our world : the 2030 Agenda for Sustainable Development*, 21 October 2015, A/RES/70/1. **Ref:;23**

32. (a) P. B. Tchounwou, C. G. Yedjou, A. K. Patlolla and D. J. Sutton, *EXS*, 2012, 133–164. (b) J. Li, X. Wang, G. Zhao, C. Chen, Z. Chai, A. Alsaedi, T. Hayat and X. Wang, *Chem. Soc. Rev.,* 2018, **47**, 2322-2356. (c) S. N. Groudev, S. G. Bratcova and K. Komnitsas, *Miner. Eng.*, 1999, **12**, 261–270. (d) Q. Gao, J. Xu and X. -H. Bu, *Coord. Chem. Rev.*, 2019, DOI:10.1016/j.ccr.2018.03.015.

33. J. Podgorski and M. Berg, *Science*, 2020, **368**, 845-850.

34. P. Kumar, A. Pournara, K.-H. Kim, V. Bansal, S. Rapti and M. J. Manos, *Prog. Mater. Sci.*, 2017, **86**, 25-74.

35. (*a*) J.-Y. Chung, S.-D. Yu and Y. S. Hong, *J. Prev. Med. Public Health*, 2014, **47**, 253-257; (*b*) Y. He, Y. Xiang, Y. Zhou, Y. Yang, J. Zhang, H. Huang, C. Shang, L. Luo, J. Gao and L. Tang, *Environ. Res.*, 2018, **164**, 288-301.

36. L. Zhu, D. Sheng, C. Xu, X. Dai, M. A. Silver, J. Li, P. Li, Y. Wang, Y. Wang, L. Chen, C. Xiao, J. Chen, R. Zhou, C. Zhang, O. K. Farha, Z. Chai, T. E. Albrecht-Schmitt and S. Wang, *J. Am. Chem. Soc.,* 2017, **139**, 14873-14876
37. A. J. Howarth, M. J. Katz, T. C. Wang, A. E. Platero-Prats, K. W. Chapman, J. T. Hupp and O. K. Farha, *J. Am. Chem. Soc.*, 2015, **137**, 7488-7494
38. H. Ouyang, N. Chen, G. Chang, X. Zhao, Y. Sun, S. Chen, H. Zhang and D. Yang, *Angew. Chem. Int. Ed.*, 2018, 57, 13197-13201.

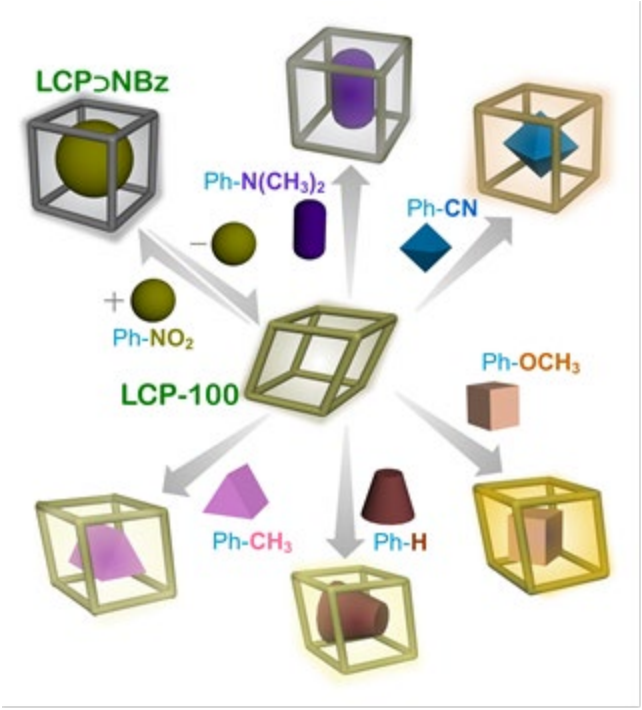
Chapter 2

Toxic Aromatics Induced Responsive Facets for a Pore Surface Functionalized Luminescent Coordination Polymer

2.1 Introduction

Recognition of environmentally toxic aromatics is of great concern. Severe air pollution, an aftermath of global development, has led to the escalation of levels for toxic aromatic species present in the environment. The United States Environmental Protection Agency (EPA) continually monitors the levels of these toxic species. These compounds react with nitrogen oxides and lead to the formation of toxic ozone at the ground level, resulting in photochemical smog with adverse effects such as lung cancers, gene toxicity, carcinogenicity, etc.[1,2] State-of-the-art sophisticated techniques involving chromatographic separation bearing high input cost and difficult on-field availability limits their usage.[3,4] The situation demands development of materials with highly selective and specific sensing of these toxic analytes with quick response time accompanied by easy readout transduction mechanism. Of late, the fluorescence-based technique has emerged, offering the unique amalgamation of dual facets of high sensitivity and selectivity.[5] Optimization of host−guest chemistry in coordination nanospace and preconcentration of the aromatic species play a vital role in enhanced signal readout.[6,7] In the past decade, coordination polymers (CPs) have emerged as a class of supramolecular crystalline materials.[8,9] The supramolecular coordination architectures of such CPs involve mono- or multidentate linker struts linked to the metal centers/clusters via multivariate coordination bonds. Tuning functional groups at the linker struts imparts tailorability at the molecular level, hence leading to diversified potential applicability in the fields of chemical separation,[10,11] molecular recognition and sensing,[12,13] heterogeneous catalysis,[14] conduction, [15] etc. Luminescent CPs (LCPs) have drawn tremendous attention in the arena of functional CPs and, owing to their easy fabrication, have potential applicability in sensing of diverse pollutant toxins, gas, and explosive organics with fast response time and unmatched convenience of signal processability.[16,17] As an omnipresent facet to such exciting host −guest chemistry within the coordination nanospace, guest confinement effect resulting in enhanced interactions of the framework and analytes leads to a better response mechanism. The corresponding readout is highly specific to the electronic nature of guest analyte and resultant analyte−framework interactions, rendering LCPs apposite for luminescence-based sensing purposes.[18,19] Fabrication of LCPs involves highly conjugated organic chromophores, as the organic linkers in conjugation with d^{10}/4f metal ions generally lead to luminescence signatures.[19] Interdigitation/interpenetration of LCPs can also play a decisive role in the luminescence response mechanism, resulting in multivariate emission profiles, exciting from the aspect of serving application frontiers. The dislocation of two entangled framework nets may, in fact, lead to enhancement in signal output because of manifestation of dual mechanisms, as pioneered by Kitagawa et al.[19] These two are induced-fit structural transformation and cooperative accommodation, each of them illustrating distinctive pathways leading to enhanced framework interactions with the targeted guest pollutant(s).[20] The inherent dynamism within a framework provides selective recognition sites, wherein the

favorable interactions between the functional sites lining the pores and the inclusion solvent analyte molecules may lead to characteristic signal generation.[21] Therefore, the dynamism of the framework may indeed play a pivotal role in the overall recognition process. Aimed at the syntheses of luminescent coordination polymers, π-electronically rich conjugated linkers have been well-harnessed as building blocks.[22] In this context, strategic utilization of highly conjugated linker with π-electronically enriched alkene functionality with electron deficient guest template might accelerate the crystallization of a CP. Hence, targeted at differential recognition patterns for the volatile aromatics, a π-electron-rich linker (L = 1,2-di(pyridyl-4-yl)ethene) was used to synthesize the studied coordination polymer, bearing a strongly emissive luminescence signature upon guest removal (Scheme 2.1).



Scheme 2.1. Schematic Illustration of the Toxic Aromatics' Induced Responsive Function by Dynamic Coordination Polymer Host

2.2 Experimental

2.2.1 Materials

All the reagents and solvents were commercially available and used without further purification. Ligand L was used as received.

2.2.2 Synthesis of LCP-100⊃NBz Compound LCP-100⊃NBz was synthesized by slow diffusion of a solution of 1 mL of 1,2-di(pyridyl-4-yl)ethene (0.0182 g, 0.1 mmol in DCM), 1 mL of nitrobenzene, and 1 mL of $Cd(ClO_4)_2 \cdot xH_2O$ (0.0311 g, 0.1 mmol in MeOH) in a glass tube. X-ray quality rod shaped pale yellow single crystals were obtained within 10 days with a yield of 72%. Elemental analysis (%) calculated for $\{[Cd(L)_2(ClO_4)_2] \cdot 2PhNO_2\}_n$: C 46.85, H 3.25, N 9.11. Found: C 46.10, H 3.48, N 8.89.

2.2.3 Activated phase LCP-100: LCP-100⊃NBz was activated by heating crystals in vacuum at 255 ºC for about 48 h to get LCP-100. The activated phase as obtained was well- characterised using TGA and PXRD, FT-IR and fluorescence spectroscopy.

2.2.4 Preparation of solvent exposed compounds: Each compound were prepared by putting desolvated compound in a vial which was kept in large screw capped vial consisting 2 mL of each solvent respectively for 6 days at RT. They were further characterized using PXRD, TGA and fluorescence spectroscopy.

2.2.5 Fluorescence Measurement. Approximately 30 mg of each solid polycrystalline powder samples was put separately in a sample holder to record emission profiles at room temperature.

2.2.6 Molecular Formula calculated from TGA: TGA suggested the formulae as $[\{Cd(L)_2(ClO_4)_2\}]n$ for LCP-100; $[\{Cd(L)_2(ClO_4)_2\}.x(DMA)]_n$ for LCP-100⊃DMA where $1.3<x<1.5$; $[\{Cd(L)_2(ClO_4)_2\}.x(PhCN)]_n$ for LCP-100⊃PhCN where $1.3<x<1.5$; $[\{Cd(L)_{2(}ClO4)_2\}.x(PhOMe)]_n$ for LCP-100⊃PhOMe where $0.9<x<1$.

2.2.7 NMR sample preparation: 15mg sample of each compound LCP-100⊃NBz and LCP-100 were separately digested using few drops of NaOD and further dissolved in DMSO-d6 under sonication. DMSO-d^6 layer was separated and ^{13}C and ^{1}H NMR spectroscopy was performed[23,24] .

2.2.8 Band gap calculation: Band gap calculations for PhOMe and DMA were performed using Density functional theory (DFT) with DMol3[25] module in Material Studio v.8. Generalized-gradient approximation (GGA) exchange correlation function[26] has been applied with the DNP (double-numeric quality with polarization functions) basis Set[27] for these calculations.

2.2.9 Quantum yield: Using relative method quantum yield of solid samples were measured. The results are depicted in the following table;

2.2.10 Measurements:

Powder X-ray diffraction (PXRD) patterns were measured on Bruker D8 Advanced X-ray diffractometer at room temperature using Cu Kα radiation (λ = 1.5406 Å) with a scan speed of 0.5° min^{-1} and a step size

of 0.01° in 2θ. Thermogravimetric analysis results were obtained in the temperature range of 30−800 °C on PerkinElmer STA 6000 analyzer under N_2 atmosphere at a heating rate of 10 °C min^{-1}. Fourier transform infrared (FT-IR) spectra were recorded on NICOLET 6700 FT-IR spectrophotometer using KBr pellets. The solid-state fluorescence spectra were recorded on a Horiba Fluorolog3 instrument.

2.2.11 X-ray Structural Studies. Single-crystal X-ray data of compound LCP-100⊃NBz were collected at 150 K on a Bruker KAPPA APEX II CCD Duo diffractometer (operated at 1500 W power: 50 kV, 30 mA) using graphite-monochromated Mo Kα radiation (λ = 0.71073 Å) mounted on nylon CryoLoops (Hampton Research) with Paraton-N (Hampton Research) oil. The data integration and reduction were processed with SAINT[28] software. A multiscan absorption correction was applied to the collected reflections. The structure was solved by the direct method using SHELXTL[29] and refined on F2 by full-matrix least-squares technique using the SHELXL-97[30] program package within the WINGX[31] program. All non-hydrogen atoms were refined anisotropically. All hydrogen atoms were located in successive difference Fourier maps and were treated as riding atoms using SHELXL default parameters. The structure was examined using the Adsym subroutine of PLATON[32] to ensure that no additional symmetry could be applied to the models. Appendix Table 2.3 contains crystallographic data for the compound LCP-100⊃NBz. CCDC 1525758 contains the supplementary crystallographic data for LCP-100⊃NBz. These data can be obtained free of charge from Cambridge Crystallographic Data Centre via www.ccdc.cam.ac.uk/data_request/cif.

2.3 Results and discussion

Slow diffusion of L with $Cd(ClO_4)_2 \cdot xH_2O$ in the presence of nitrobenzene and solvent combination of DCM/MeOH (1:1) yielded pale yellow colored crystals of LCP-100⊃NBz (Appendix 2.1). SC-XRD analysis revealed that the compound crystallized in orthorhombic crystal system with space group Pna21 (Appendix Table 2.3). The asymmetric unit of LCP-100⊃NBz involves one Cd(II) and two linkers (L) and two ClO_4^- and two nitrobenzene as guest solvent molecules (Appendix 2.2). Each metal ion is six coordinated with a distorted octahedral geometry having N_4O_2 as the donor set of atoms (four nitrogen atoms from four ligands and two oxygen atoms from two ClO_4^-) (Figure 2.1b). Extension of such coordination via both ends of the ditopic ligand leads to the formation of a two dimensional (2D)-layered structure. Overall, three-dimensional (3D) packing of the compound was found to contain two-fold interpenetrating networks with nitrobenzene guests occupying channels (Figures 2.1c, Appendix 2.3, and 2.4). Use of electron deficient nitrobenzene as guest coupled with highly conjugated linker favored the crystallization of LCP-100⊃NBz.

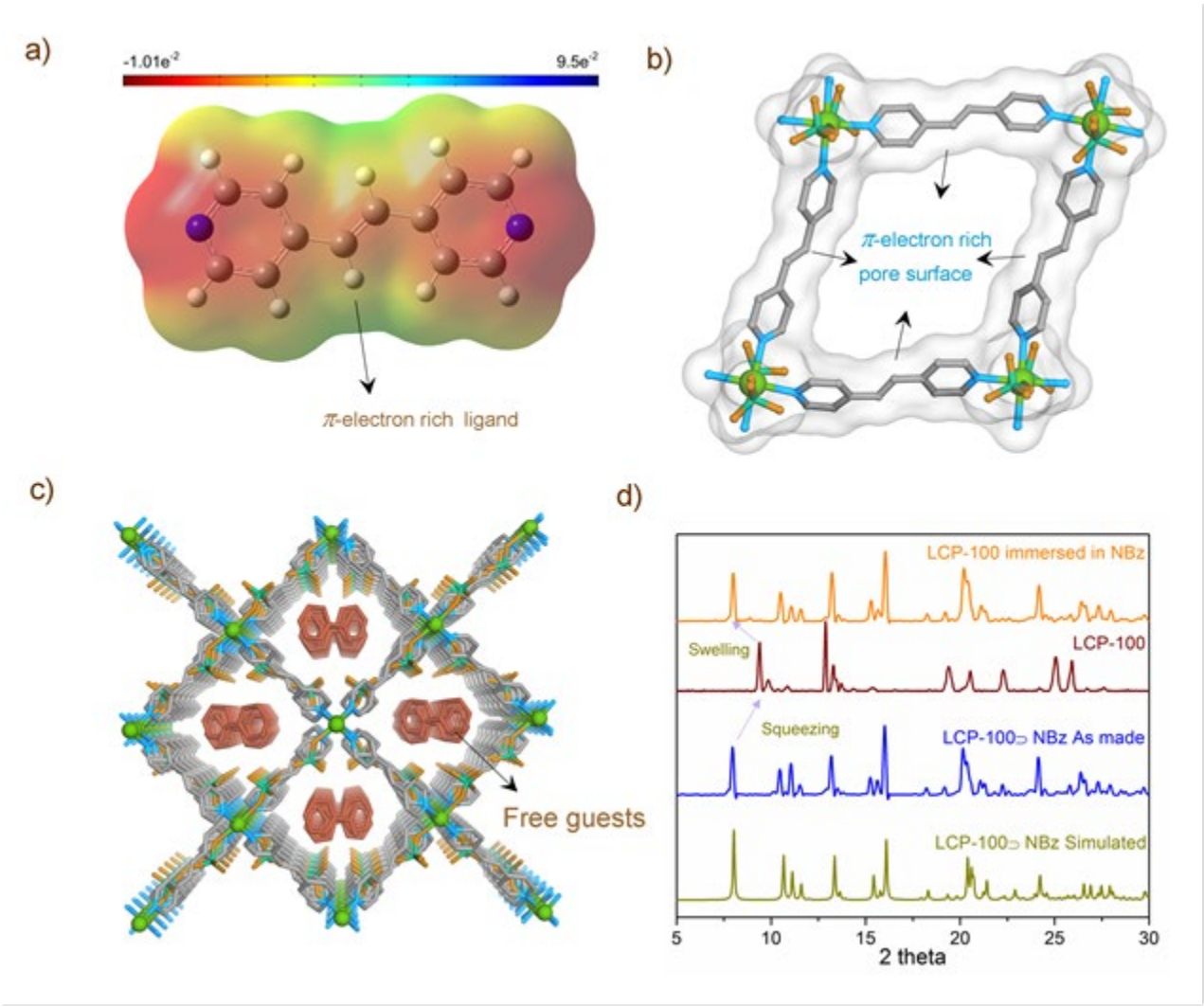


Figure 2.1. (a) Electrostatic surface potential plot for the linker (L) representative of the π-electron-rich electron density map. (b) Single pore view of the guest-accessible Connolly surface of LCP-100⊃NBz decorated with π-electron-rich linkers. (c) Guest nitrobenzene molecules accommodated within LCP-100⊃NBz framework viewed along the a-axis. (d) PXRD patterns of LCP-100⊃NBz for simulated, as-made, desolvated LCP-100, and resolvated LCP-100 (reimmersed in nitrobenzene) phases, suggesting the reversible dynamic nature of the framework (O and C atoms are shown by orange and gray sticks, respectively, while H atoms are omitted for clarity).

This can be attributed to the favorable π–π interactions between electronically enriched linker (Figure 2.1a) and electron-deficient guests, hence providing the requisite template effect, a very crucial aspect for crystallization in these supramolecular CPs (Figures 2.2a, Appendix 2.5, and 2.6).[33]

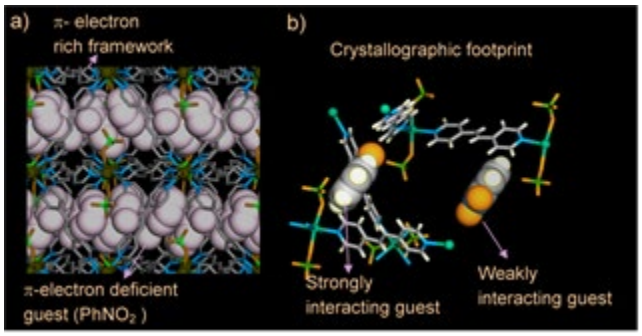


Figure 2.2. a) Perspective view of overall packing arrangement of electron-deficient nitrobenzene molecules stacked inside the π electron-rich host **LCP-100⊃NBz** ; b) Two crystallographically different nitrobenzene molecules, both flanked by distinct host-guest interactions in **LCP-100⊃NBz .**

^{1}H and ^{13}C NMR spectra (Appendix 2.13 and 2.14) of digested LCP-100⊃NBz also showed the respective peaks for nitrobenzene guests. Among the two nitrobenzene molecules, one was observed to interact via strong supramolecular interactions with the framework, while the other nitrobenzene moiety is lying freely within the undulated channels of the interdigitated framework (Figures 2.2b and Appendix 2.7). Bulk phase purity of LCP-100⊃NBz was confirmed by overlapping PXRD patterns (Figures 2.1d and Appendix 2.8) and elemental analysis. Thermogravimetric analysis (TGA) revealed that LCP-100⊃NBz showed ~26% weight loss at around 255 °C owing to the loss of two nitrobenzene guests occupying the pores of the framework (Appendix 2.10). Guest-free phase LCP- 100 was obtained by heating crystals of LCP-100⊃NBz in vacuum at 255 °C, resulting in removal of nitrobenzene guests, as confirmed by the TGA analysis (Appendix 2.10). ^{1}H and ^{13}C NMR spectra (Appendix 2.15 and 2.16) of digested LCP-100 showed no characteristic peaks for free nitrobenzene, indicative of guest-free nature of LCP-100. Characterization of LCP-100 by PXRD analyses showed a crystalline pattern with a considerable right shift, which might be ascribed to solvent loss mediated framework squeezing (Figure 2.1d). Interestingly, LCP-100 swelled back to the original phase (LCP-100⊃NBz) when soaked in nitrobenzene solvent (for ~4 days), as confirmed by the PXRD and TGA patterns, which is indicative of the soft porous crystallinity/reversible dynamism of the framework (Figures 2.1d, Appendix 2.8, 2.11).[34,35] To get structural insights of the dried phase, several attempts were made to obtain the single crystal structure of LCP-100, but due to lack of X-ray quality single crystallites, the clear single crystallographic picture of the guest-free desolvated phase LCP-100 could not be realized. Photophysical properties of the original and dried phases of the framework were carried out by measuring photoluminescence (PL) emission profiles of well-ground powder at room temperature. Upon photoexcitation at 353 nm, LCP-100 was found to be highly luminescent in nature as compared to LCP-100⊃NBz (Appendix 2.20). Such drastic enhancement in PL intensity might be directly correlated to the absence of nitrobenzene as fluorescence quencher in the LCP-100.[36] Owing to the presence of π-electron-

rich linker along with intrinsic interdigitation in the framework, it was hypothesized that volatile aromatics bearing variant electronic nature would promote strong host−guest interactions. This formed the basis for the experiment that involved exposing LCP-100 to various volatile aromatics and understanding the influence of functional groups, template effects, electronic nature of analyte. In a typical experiment, well-ground polycrystalline sample of LCP-100 kept in a saturation chamber was separately exposed to vapors of benzene (Bz), toluene (Tol), anisole (PhOMe), cyanobenzene (PhCN), dimethylaniline (DMA) (Experimental Section 2.2.5) at room temperature. Occlusion of each of these guests inside the LCP-100 can be evidenced from the respective weight loss of included guests in their corresponding TGA profiles (Appendix 2.12). LCP-100⊃DMA and LCP-100⊃PhCN showed ∼20 wt% (at ∼247°C) and ∼18 wt % (at ∼206 °C) losses, respectively, which indicates guest content of each guest as $1.3 < x < 1.5$ (x denotes number of guest per formula unit) (Experimental Section 2.2.6). Approximately 15 wt % (at 176 °C) loss was observed for LCP-100⊃PhOMe, which resembles the guest content as $0.9 < x < 1$ (Experimental Section 2.2.6). However, the loading of benzene and toluene were very low, as observed in their TGA profiles (Appendix 2.12), which can be attributed to the similar electronic nature of guest and host framework. PXRD analyses of guest included phases revealed structural alteration in the framework, which is due to the differential guest responsive behavior of the framework (Appendix 2.8 and Appendix 2.9). In-depth analysis of the corresponding PXRD profiles illustrated three different kinds of diffraction patterns. LCP-100⊃Bz and LCP-100⊃Tol showed very similar and slightly left-shifted (with respect to LCP-100) diffraction patterns, indicative of only slight opening of the porous channels. On the other hand, LCP-100⊃PhCN and LCP-100⊃DMA exhibited patterns similar to those of LCP-100⊃NBz, therefore demonstrating complete opening of the pores, whereas slight left shifted PXRD patterns (with respect to LCP-100⊃Bz and LCP-100⊃Tol) of LCP-100⊃PhOMe might indicate opening of the channel in an extent greater than that of LCP-100⊃Bz and LCP-100⊃Tol. Such inequality in pore opening can be correlated to the extent of guest loadings (as observed in the TGA profiles; Appendix 2.12) and differential host−guest interactions, and the latter can be elucidated on the basis of the varying electronic natures of the guest species (Appendix 2.9). FT-IR analyses of the aforementioned guest introduced phases showed the presence of characteristic bands associated with the incorporated guest functionalities within the framework (Appendix 2.17). All the guest-occluded compounds exhibited guest-responsive luminescent behavior. Solid-state reflectance spectra of all the compounds were recorded at room temperature with minimum reflectance appearing in the range 350−360 nm (Appendix 2.18). PL spectra of the different vapor exposed solid phase samples were comprehensively recorded. Photo excitation of LCP-100 at λ_{ex} ∼ 353 nm resulted in λ_{em} ∼ 429 nm. Characteristic emission maxima of LCP-100⊃PhCN, LCP-100⊃PhOMe, and LCP-100⊃DMA were observed at λ_{em} ∼412, ∼465, and ∼583 nm, respectively (Figure 2.3a). A mixture of ligand

to metal charge transfer (LMCT) and interligand charge transfer (ILCT) interactions are considered to be responsible for the emission signature of LCP-100 (Appendix 2.21).

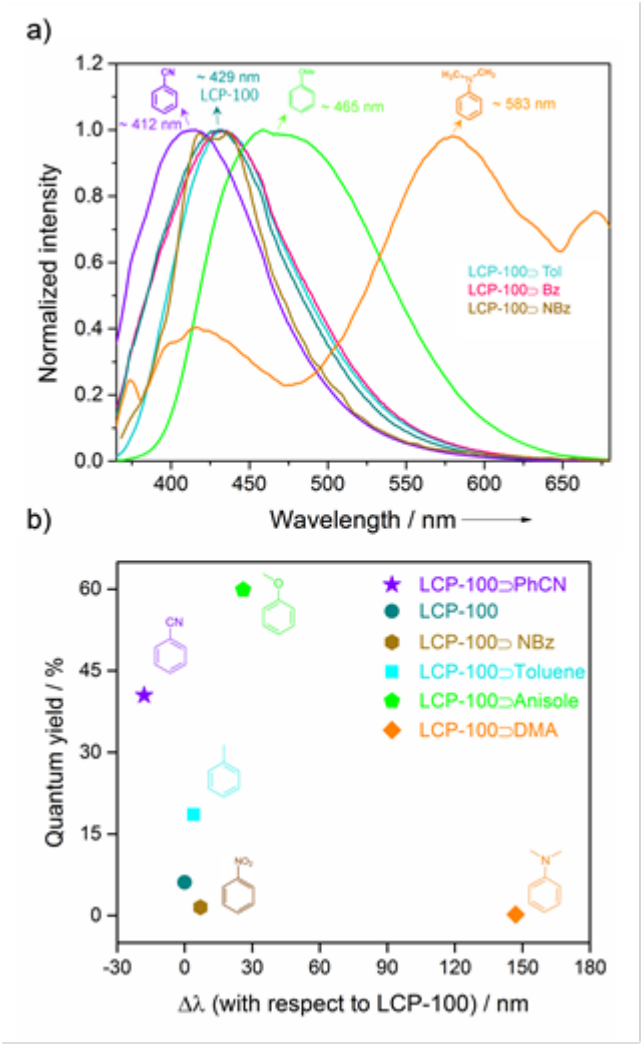


Figure 2.3. a) Normalized emission profile for the **LCP-100** and different guest exposed phases with their respective emission maxima; b) 2D-plot of quantum yields and their corresponding peak shifts for the solid-state emission bands.

Such CT interactions are perturbed with the inclusion of guests. The differential emission profiles of various guest exposed phases might be attributed to the varying nature of host−guest interactions, which can be coherently linked to the electronic nature of guest species associated with their respective ionization potentials (IP).[19,35] In case of volatile aromatics with higher IP such as for electron-withdrawing species, emission profiles with blue shift might be observed (LCP-100⊃PhCN). For electron-rich species with low IP, facile electron transfer occurs, resulting in low HOMO−LUMO band gap (Appendix 2.17 and Appendix

Table 2.2) of the framework, consequently resulting in red shift of the emission profiles (LCP-100⊃PhOMe and LCP-100⊃DMA).19 LCP-100⊃Bz and LCP-100⊃Tol do not show much difference in emission profiles. This might be attributed to weaker or reduced host− guest interactions between the framework and the guest species, which can be correlated to lower loadings of the respective guests. PL intensity profiles for various guest incorporated phases exhibited variations in luminescence profiles, which can be precisely corroborated with electronic nature of the guest volatile organic compounds (VOCs). In addition, quantum yield measurements (Appendix Table 2.1) of the samples could revalidate the observed trend in luminescent intensities (Figures 2.3b and Appendix 2.21).

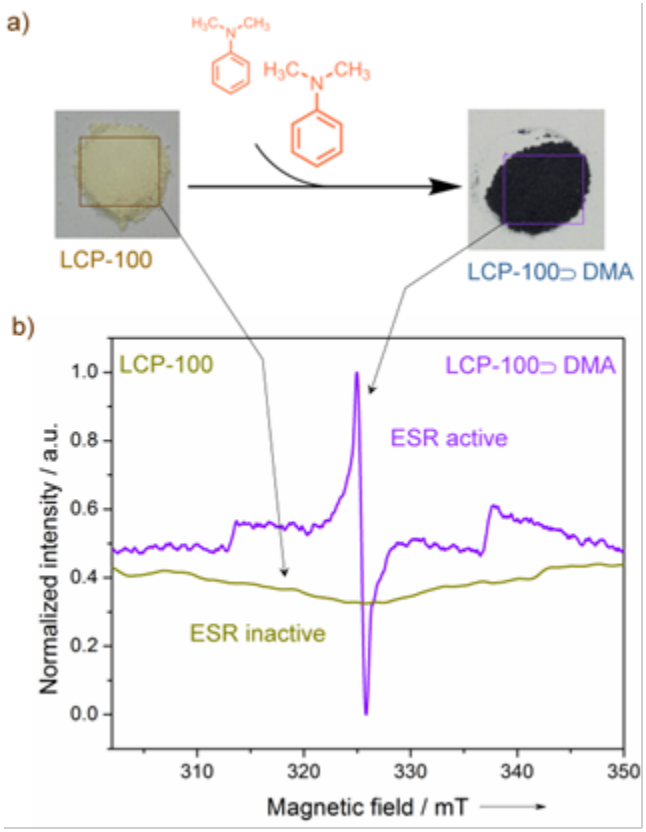


Figure 2.4. a) Guest accommodation leading to drastic color change in ambient condition; b) ESR profiles of LCP-100 and LCP-100⊃DMA at low temperature showing signal *on* and *off* behavior respectively.

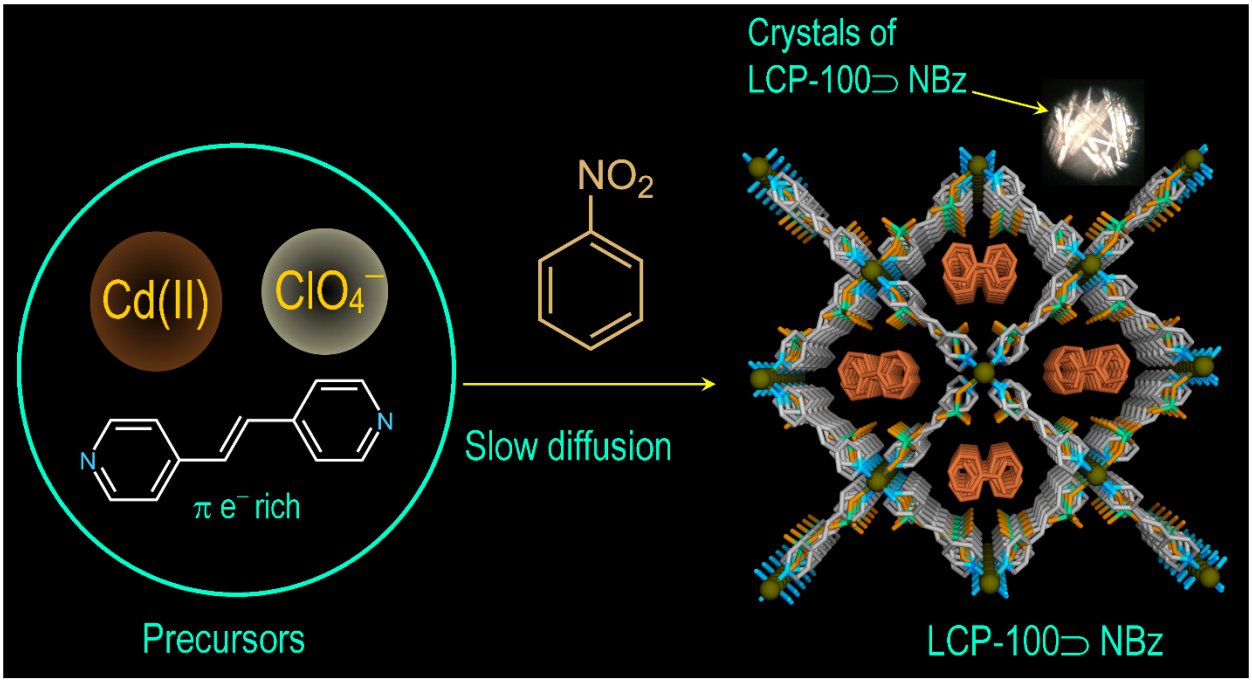
LCP-100⊃PhOMe showed the highest intensity of luminescence. This may be due to the mesomeric nature of methoxy unit, which increases the charge density of the benzene ring by participating with the framework via pronounced charge transfer (CT) interactions. LCP-100⊃DMA showed a substantial luminescence quenching irrespective of a low IP (Appendix 2.23). This may be because of the facile formation of a radical-ion pair state triggered by very strong host−guest interactions.[37] For efficient recognition of various

toxic aromatics, the differences in emission maxima might be very useful. An amalgamation of intensity profile (in terms of quantum yield) and peak shift of various aromatics (embedded into LCP-100) is presented in Figure 2.3b, wherein LCP-100⊃DMA registered a massive red shift with respect to that of LCP-100, and LCP-100⊃PhCN showed a slight blue shift. When LCP-100 was exposed to DMA, a significant color change from pale yellow to dark purple was observed (Figures 2.4a and Appendix 2.24). In fact, this is consistent with the recorded broad absorption profile in the range of 530−600 nm of LCP-100⊃DMA (Appendix 2.21). Such broad absorption characteristic cogently associated with the hypothesis of radical ion-pair state is experimentally consolidated by a sharp band in the electron spin resonance (ESR) spectrum of the corresponding sample (Figure 2.4b). LCP-100⊃PhCN led to enhancement in the PL intensity, even though PhCN possesses high IP value. However, the reason behind such enhancement in emission intensity is not very obvious. This is probably due to feasible energy transfer interactions between PhCN and the framework, leading to an increase in population of the corresponding LUMO state, in turn increasing the luminescence intensity. LCP-100⊃Bz and LCP-100⊃Tol have almost similar emission intensity profiles due to their similar CT interactions (Appendix 2.23).

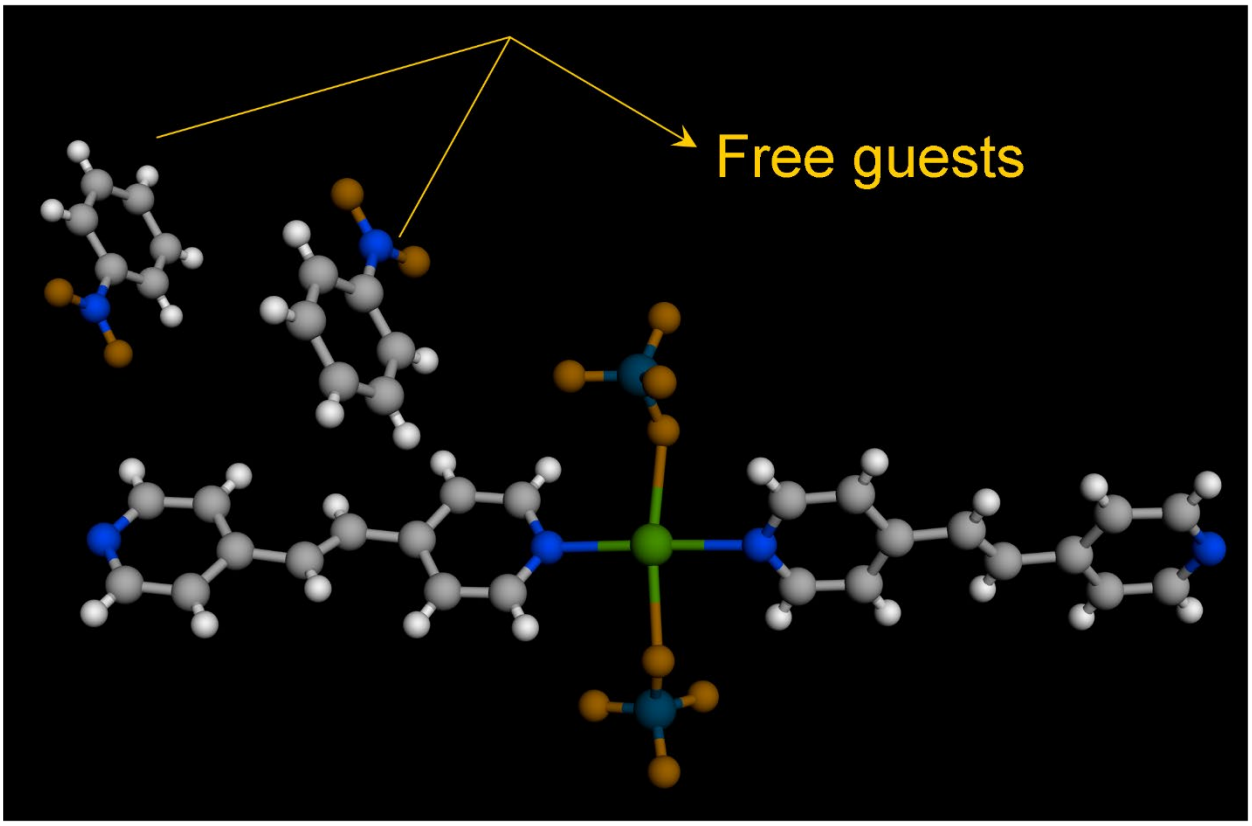
2.4 Conclusions

In conclusion, following the linker prefunctionalization rationale-based synthesis and structural characterization, a π-electron rich luminescent coordination polymer has been comprehensibly exploited for guest switchable framework breathing. Harmful vapors of active pollutant toxins, nonmethane VOCs, which play a crucial role in tropospheric ozone formation, can be well-recognized by luminescence-based read out signaling protocol with the aid of guest-free phase (LCP-100). This may be due to anticipated CT interactions between the framework and toxic aromatic pollutants, accordingly leading to a highly specific response. Framework entanglement may also be recognized as a major prerequisite in designing materials for recognition purposes as it leads to sliding of the framework, hence rendering maximum interactions between the pollutant toxins and constrained framework nanospace. Such soft coordination polymers show promising prospects within the realm of designed chemosensors, and the ensuing study will help in the further development of environmental toxin sensors with better sensitivity and selectivity.

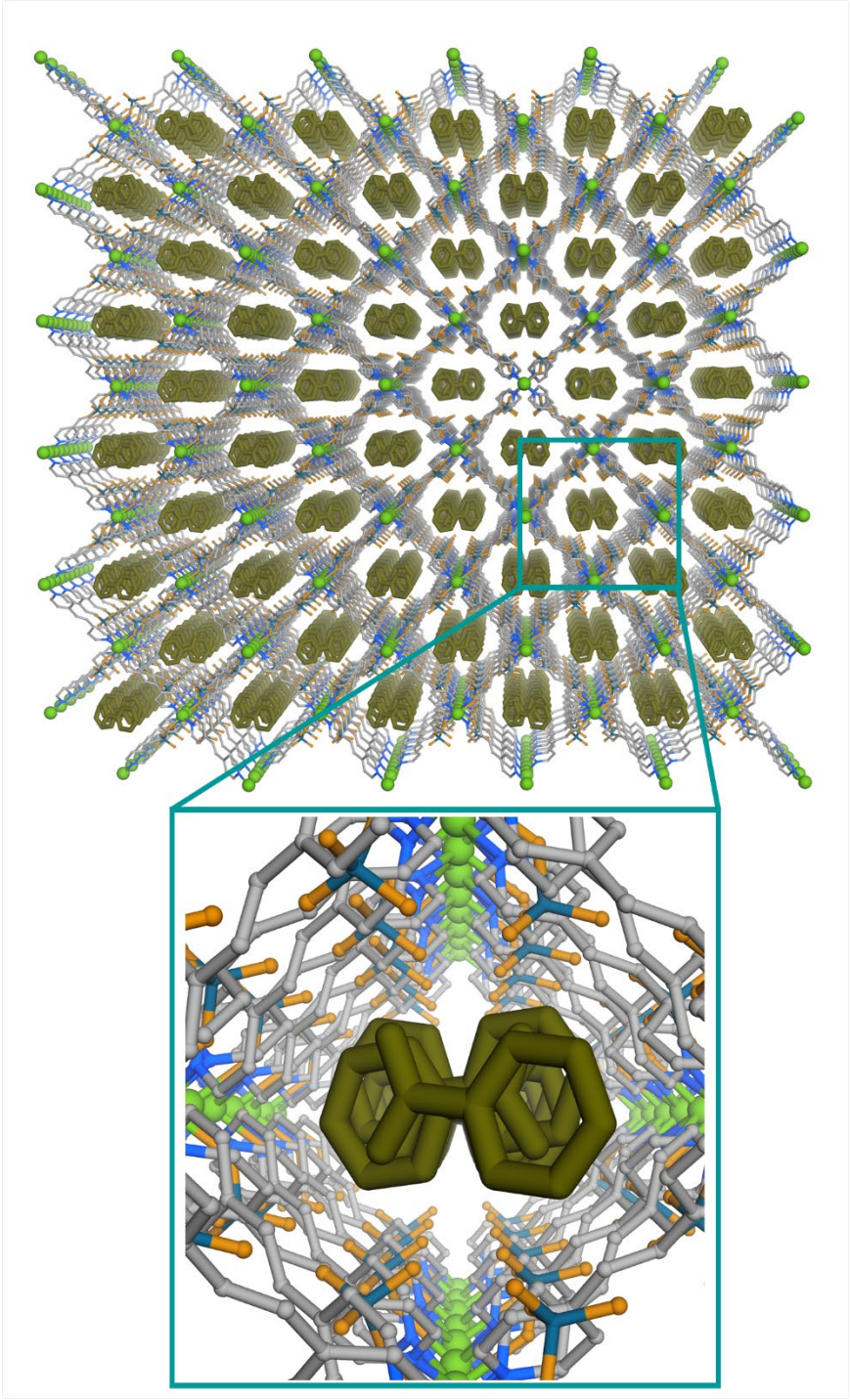
2.5 Appendix Section



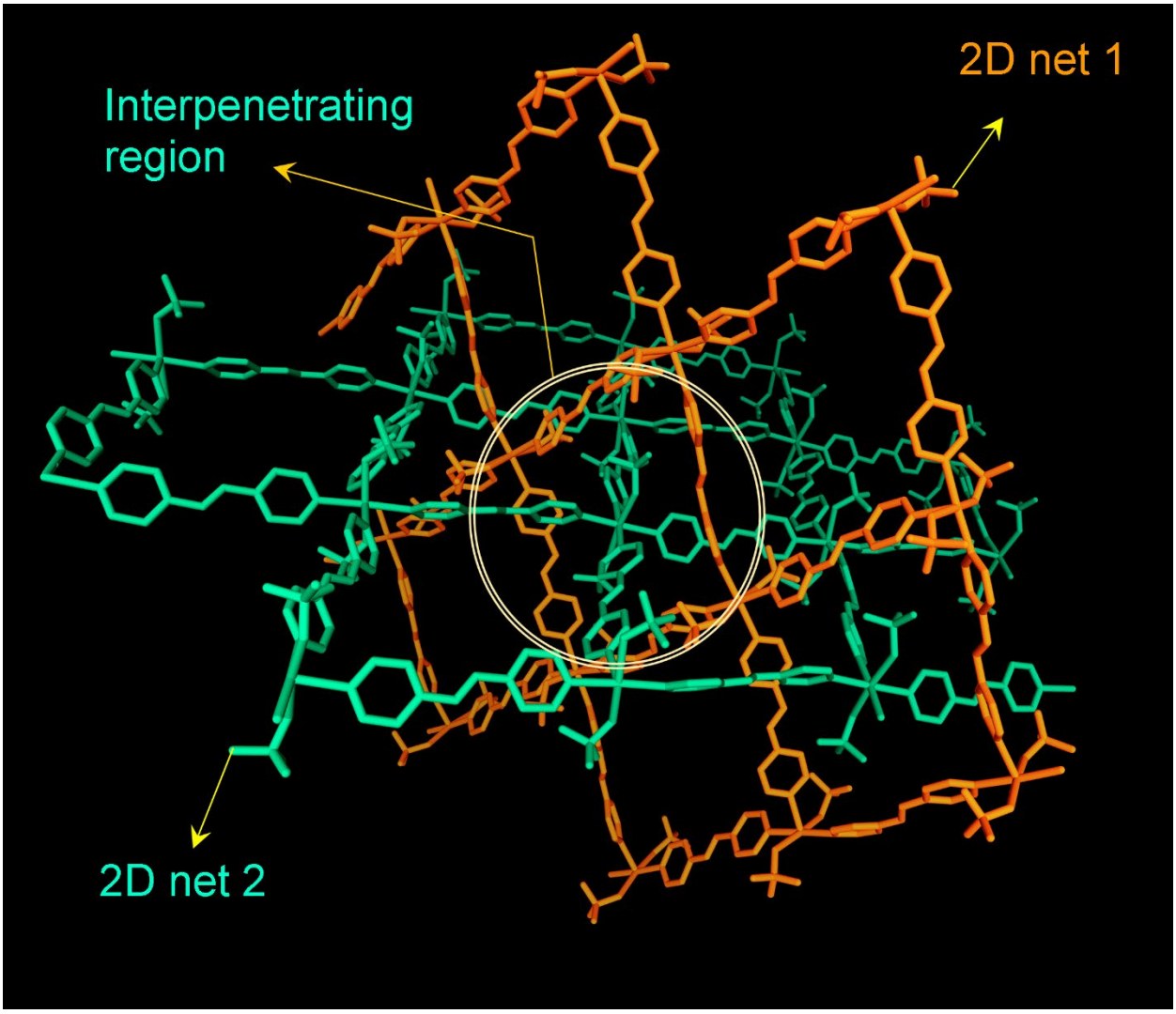
Appendix 2.1: Reaction scheme of synthesis of **LCP-100⊃ NBz** (Color code; Carbon: gray, oxygen: Orange, nitrogen: blue, cadmium: Dark green, chlorine: light blue, Guest: light brown).



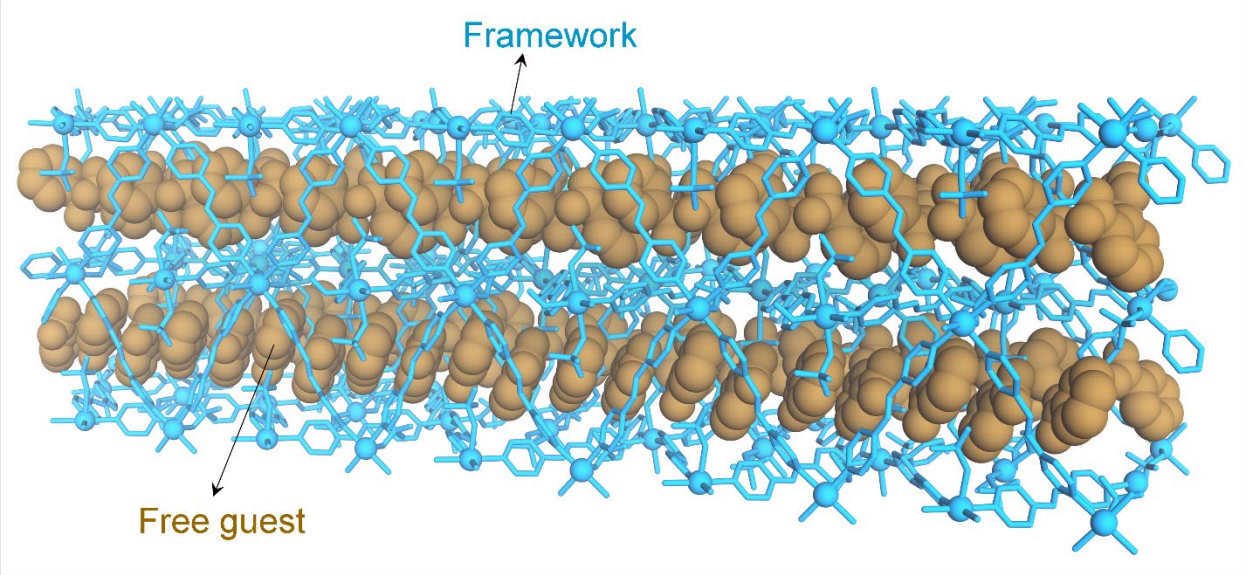
Appendix 2.2: Asymmetric unit of **LCP-100⊃ NBz** (Color code; Carbon: gray, oxygen: Brown, nitrogen: blue, cadmium: Dark green, chlorine: Dark blue).



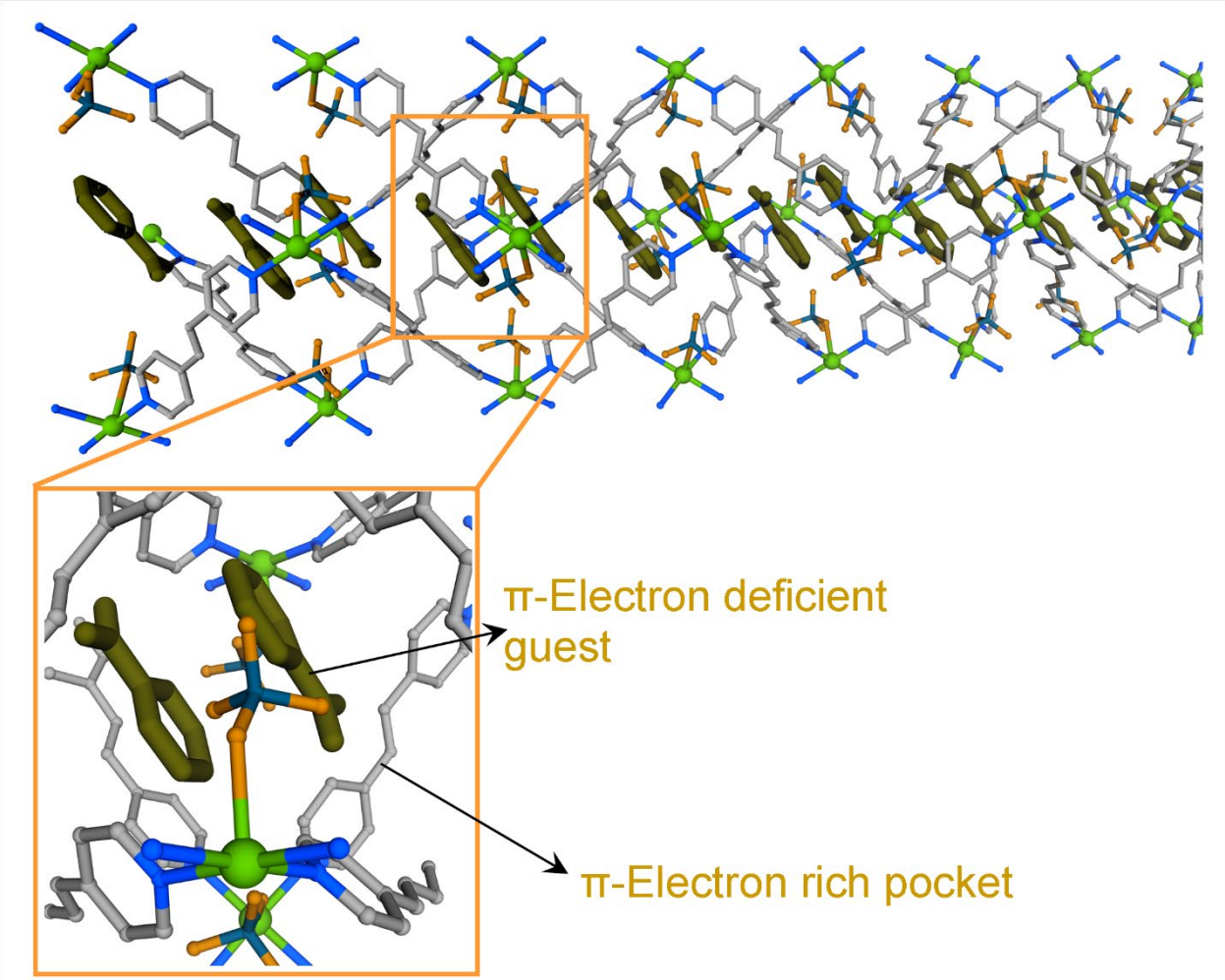
Appendix 2.3: Perspective view of overall packing along *a* axis for **LCP-100⊃ NBz** (top).Zoomed view showing guest accommodation in the channel(below) (Color code; Carbon: gray, oxygen: Brown, nitrogen: blue, cadmium: green, chlorine: Dark blue, G: Brown).



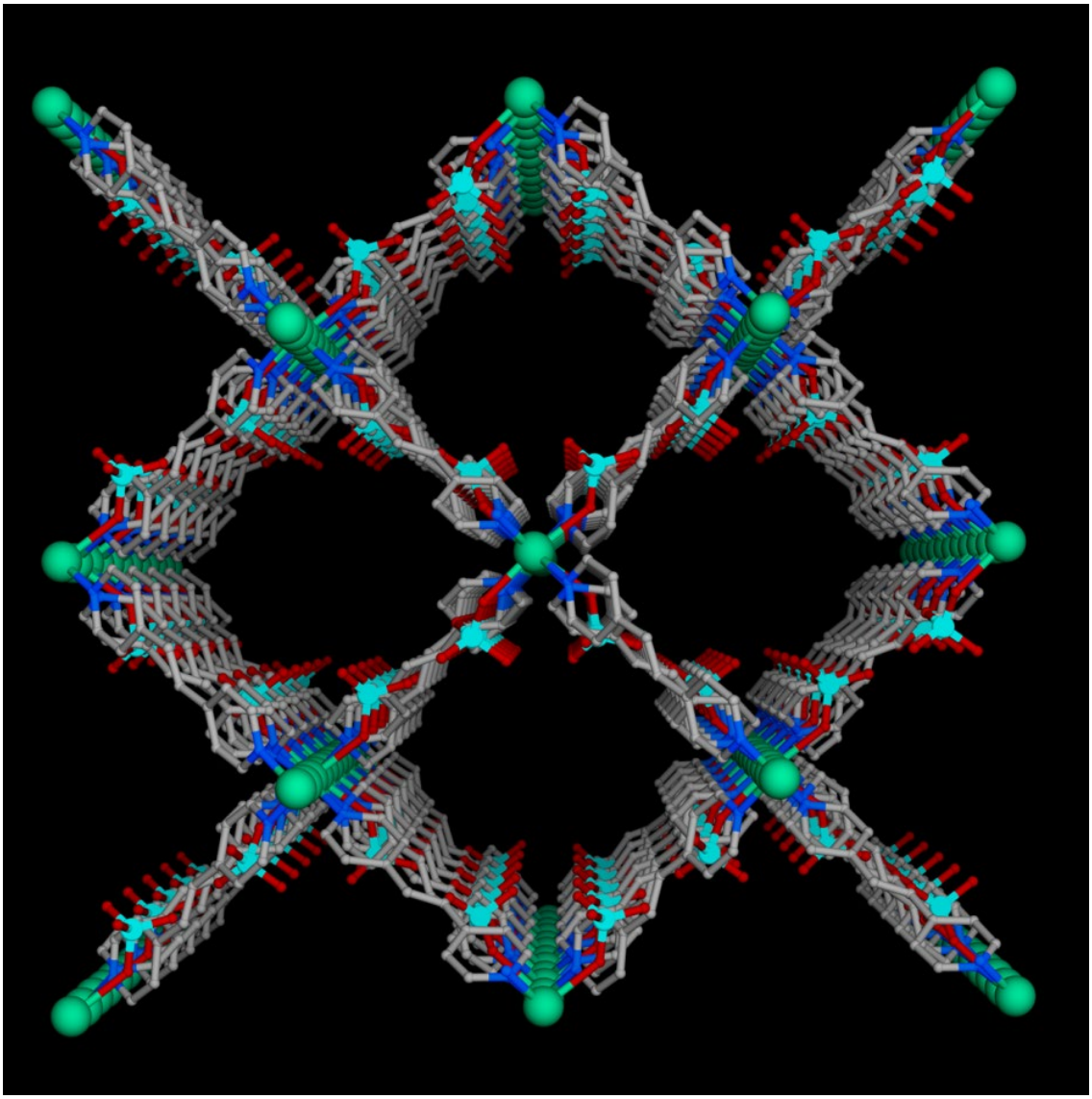
Appendix 2.4: Two fold interpenetration in the framework of **LCP-100⊃ NBz** showing nets and interpenetrating region.



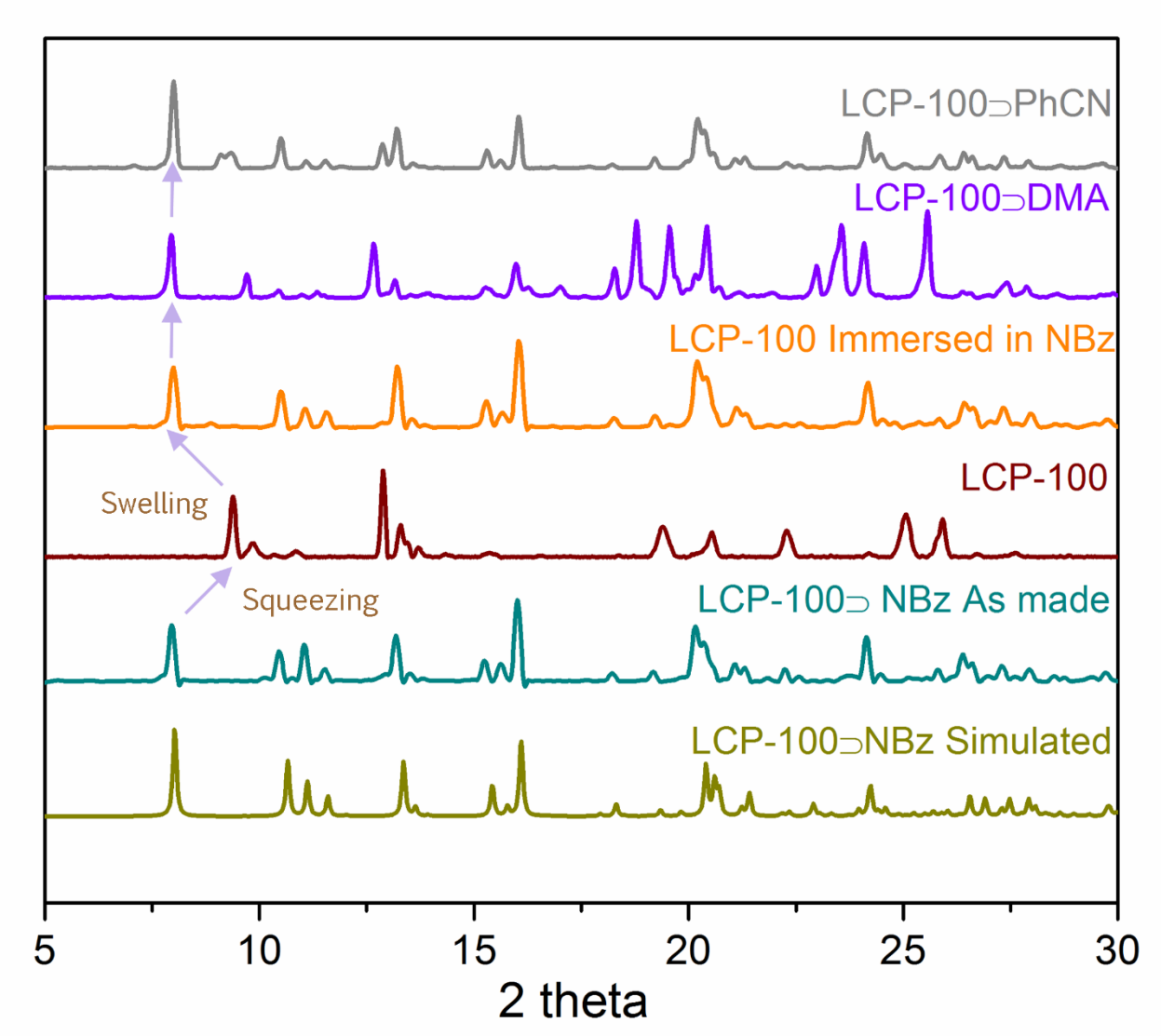
Appendix 2.5: Perspective view of overall packing along a side showing 1D array of free guest(shown in brown CPK model) within the pores of the framework (shown in light blue ball and stick model).



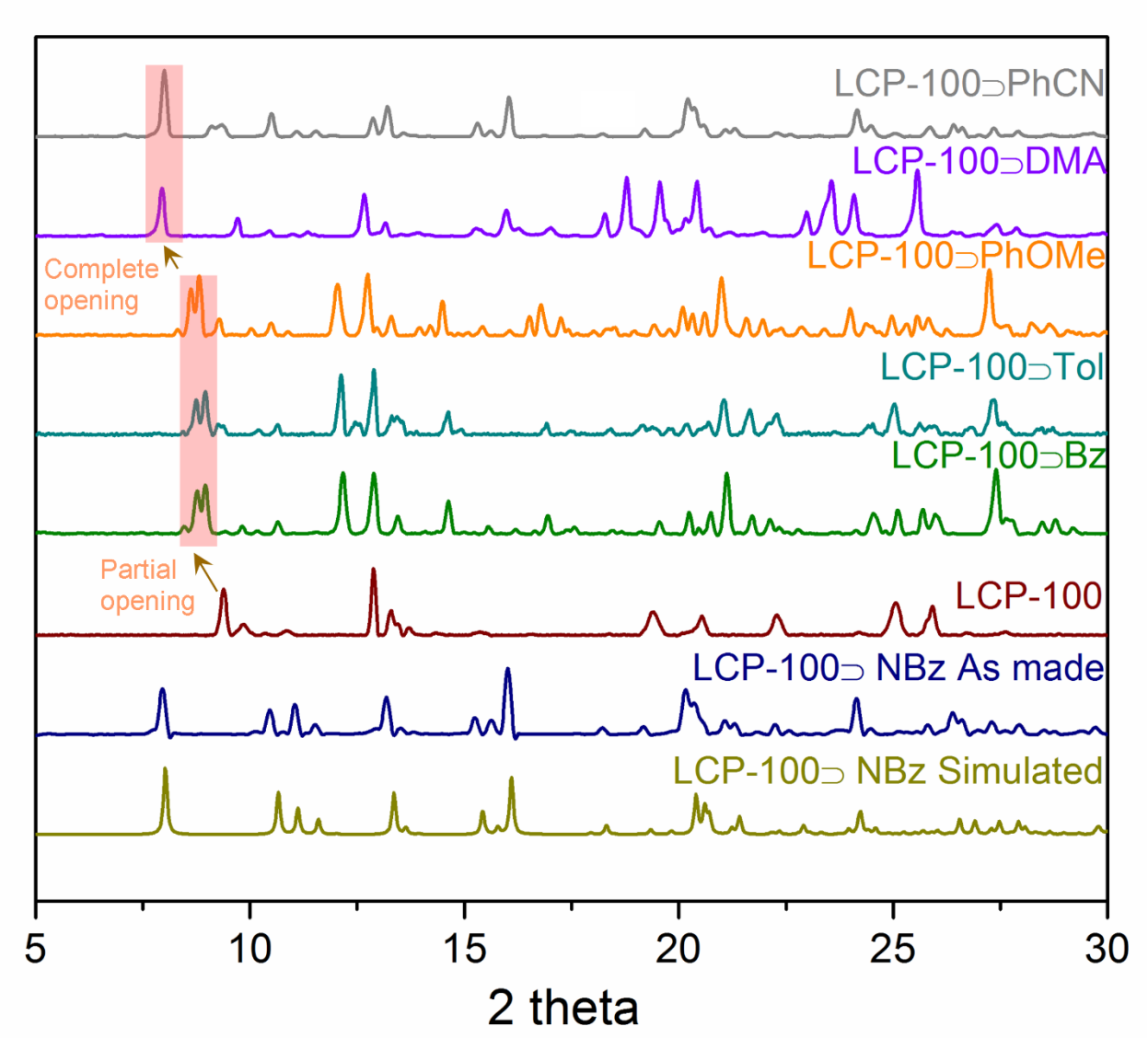
Appendix 2.6: Magnified view showing the inclusion π-electron deficient guest molecules in the π-electron rich pocket. (Color code; Carbon: Gray, oxygen: Orange, nitrogen: Blue, cadmium: Green, chlorine: Dark blue, G: yellow green).



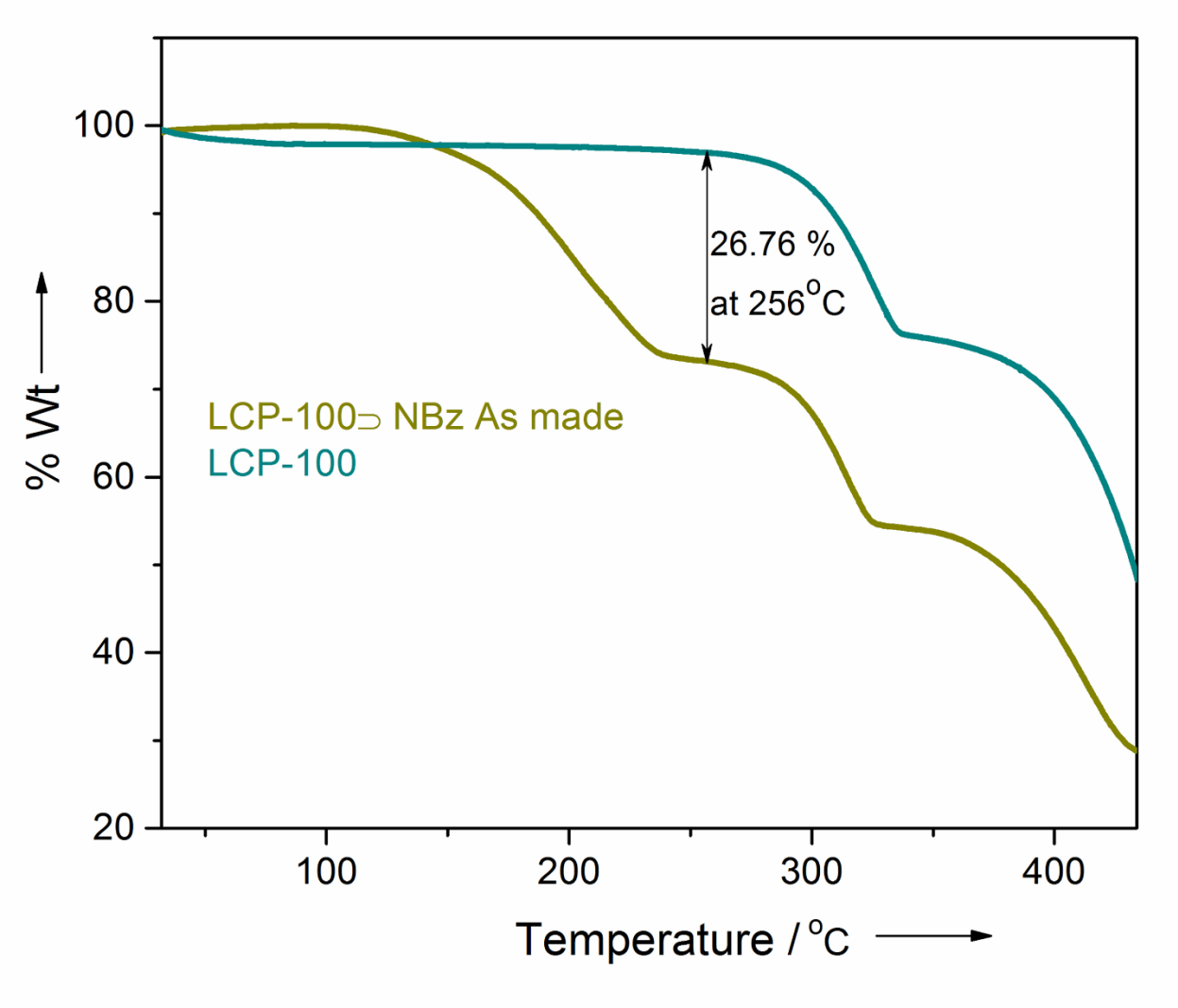
Appendix 2.7: Guest omitted depiction of framework along *a* axis**.**(Color code; Carbon: gray, oxygen: red, nitrogen: blue, cadmium: green, chlorine: light blue).



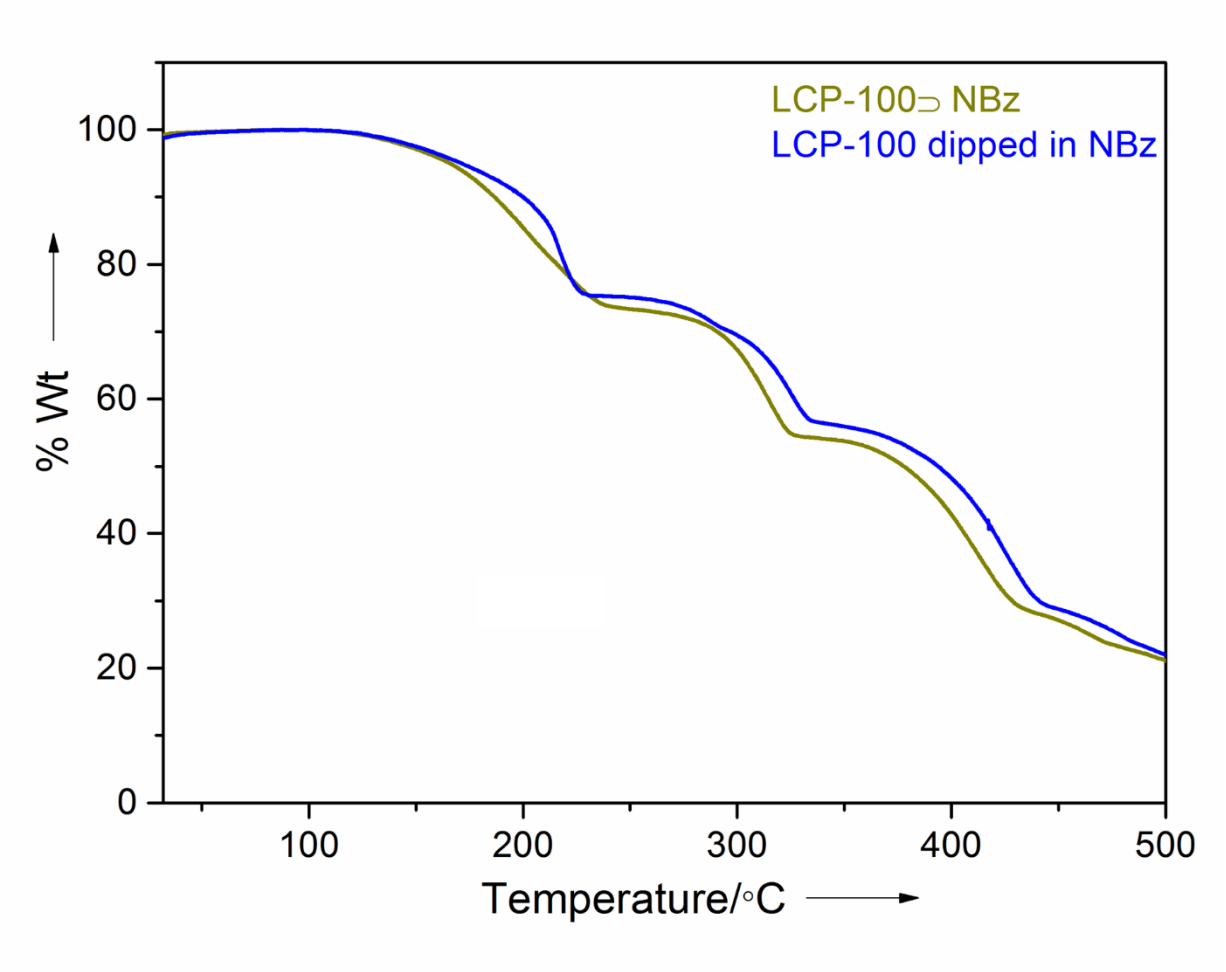
Appendix 2.8: PXRD patterns of different exposed samples.



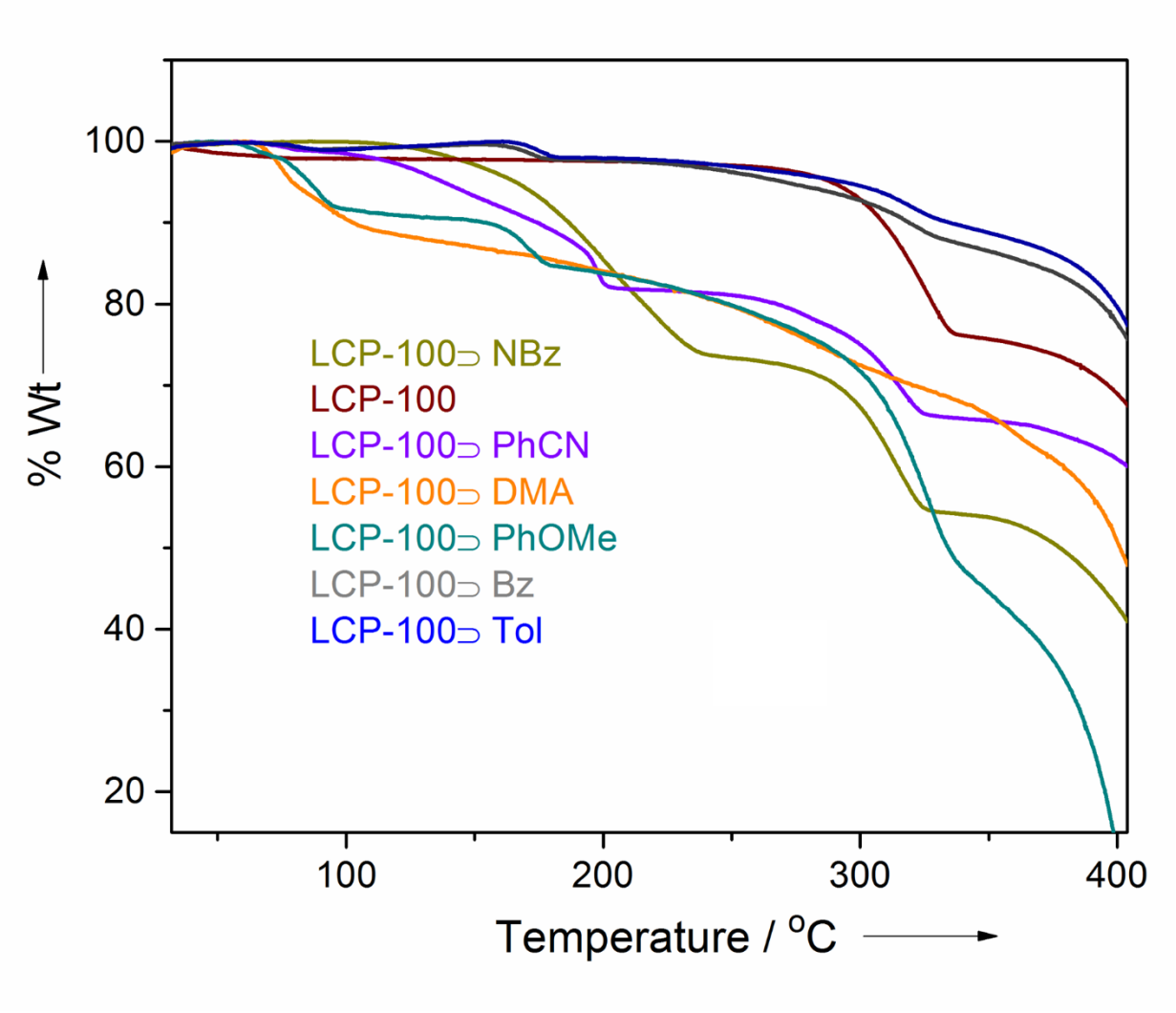
Appendix 2.9: PXRD patterns of different exposed samples indicating guest responsive nature.



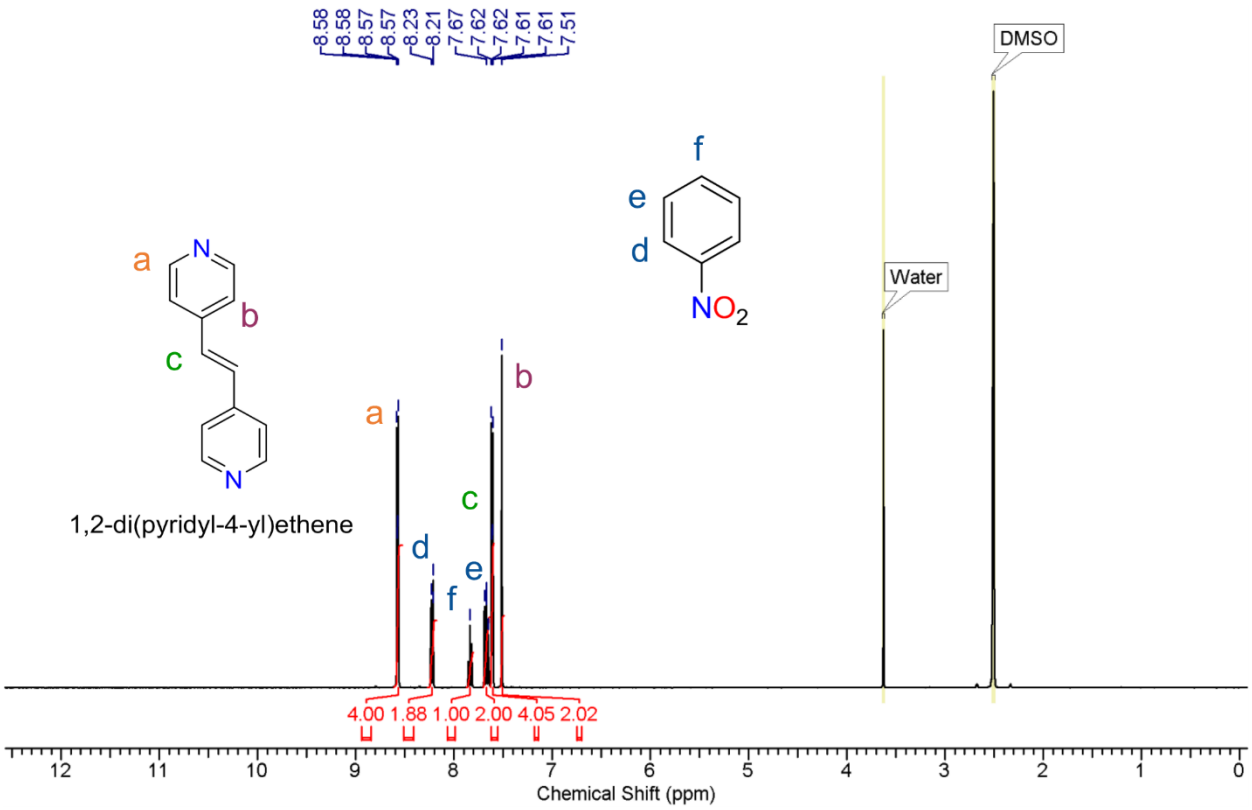
Appendix 2.10: TGA data of **LCP-100⊃ NBz** and **LCP-100**.



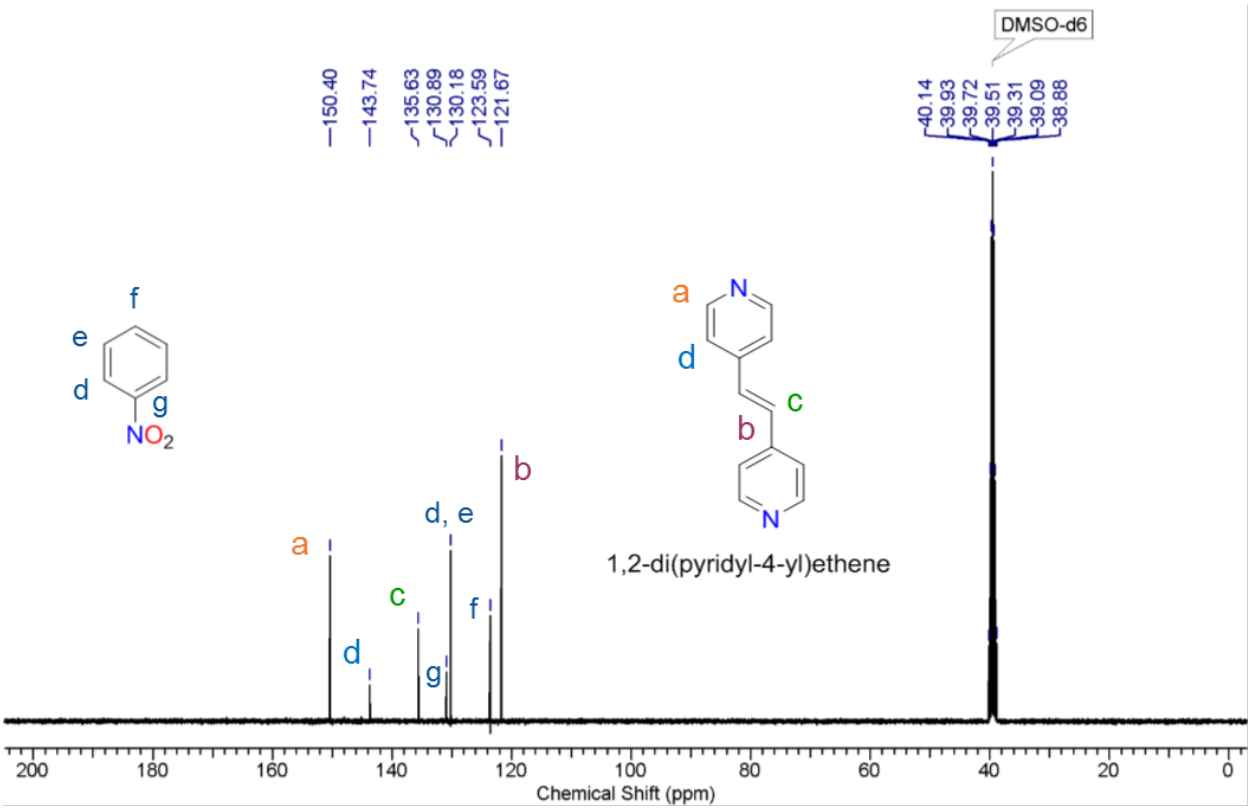
Appendix 2.11: TGA data of **LCP-100⊃ NBz** and **LCP-100** dipped in NBz.



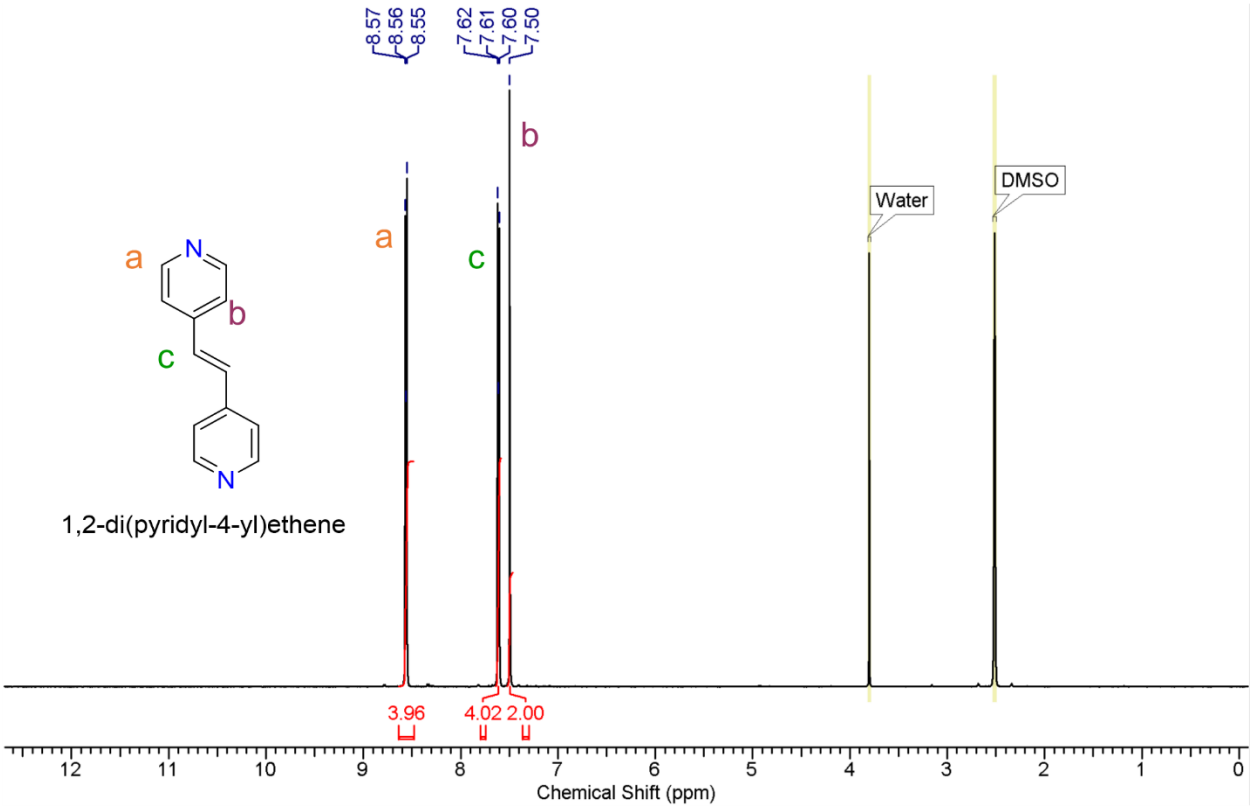
Appendix 2.12: TGA data of **LCP-100**, **LCP-100⊃ NBz** and all other guest exposed phases.



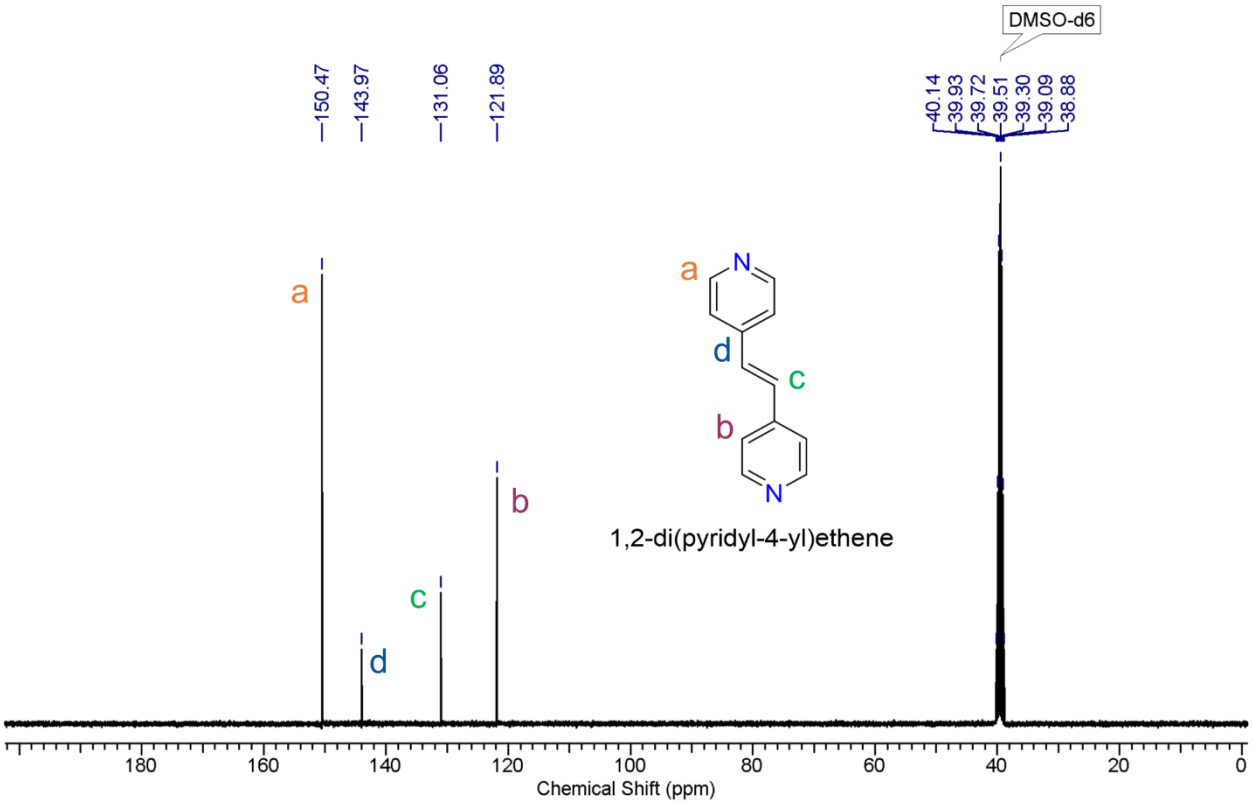
Appendix 2.13: ^{1}H NMR spectra of digested **LCP-100⊃NBz** showing the presence of free guest(NBz).



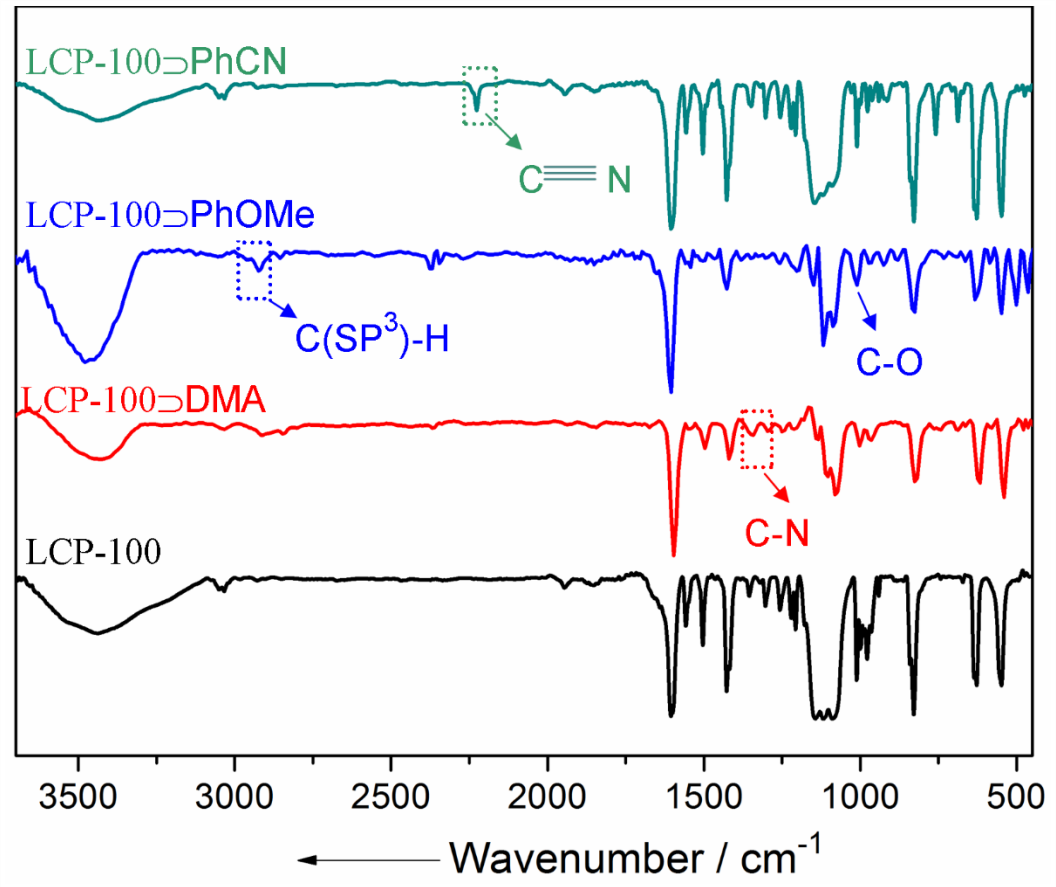
Appendix 2.14: ^{13}C NMR spectra of digested **LCP-100⊃ NBz** showing the presence of free guest(NBz).



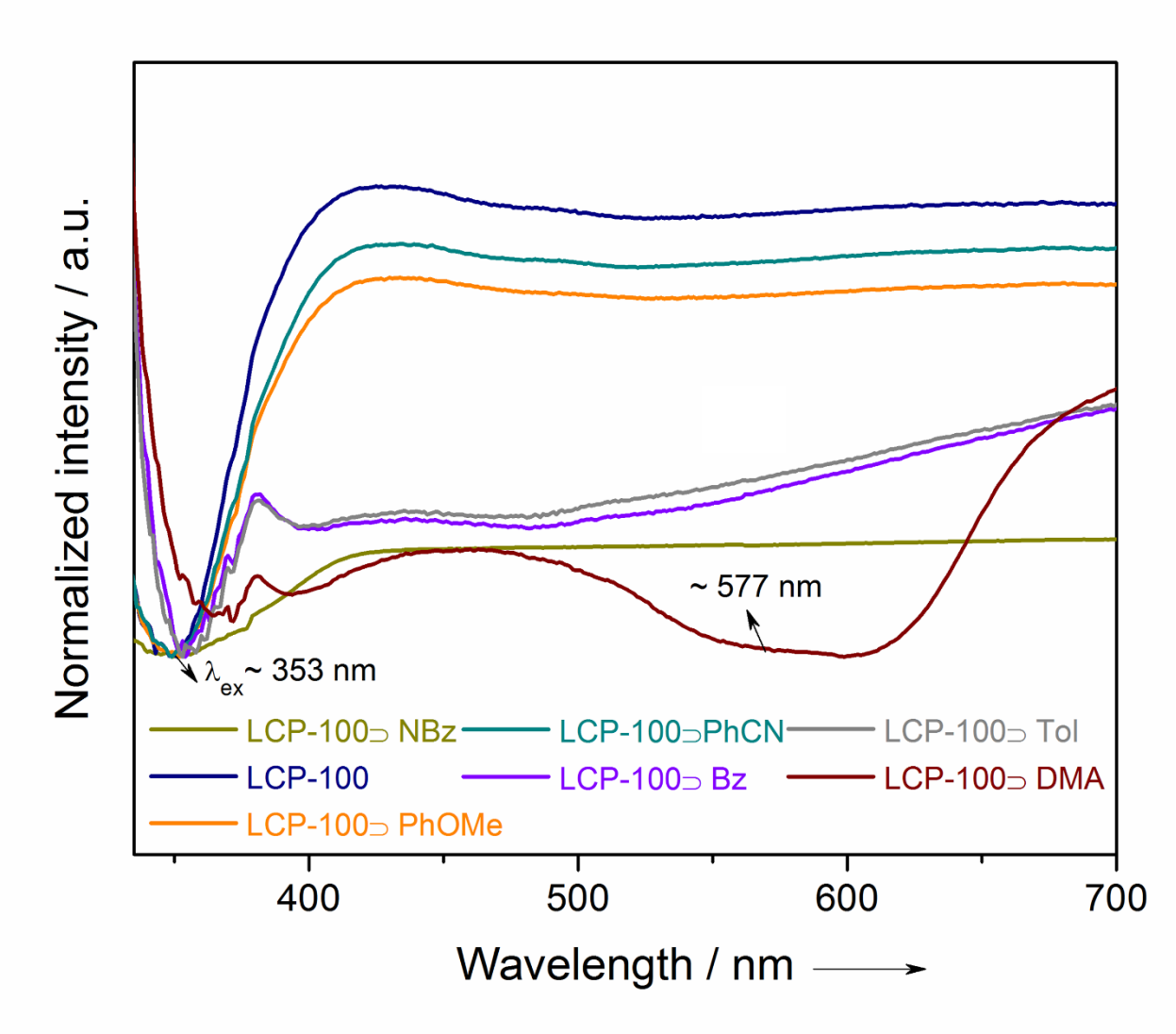
Appendix 2.15: ^{1}H NMR spectra of digested **LCP-100** showing the absence of free guest.



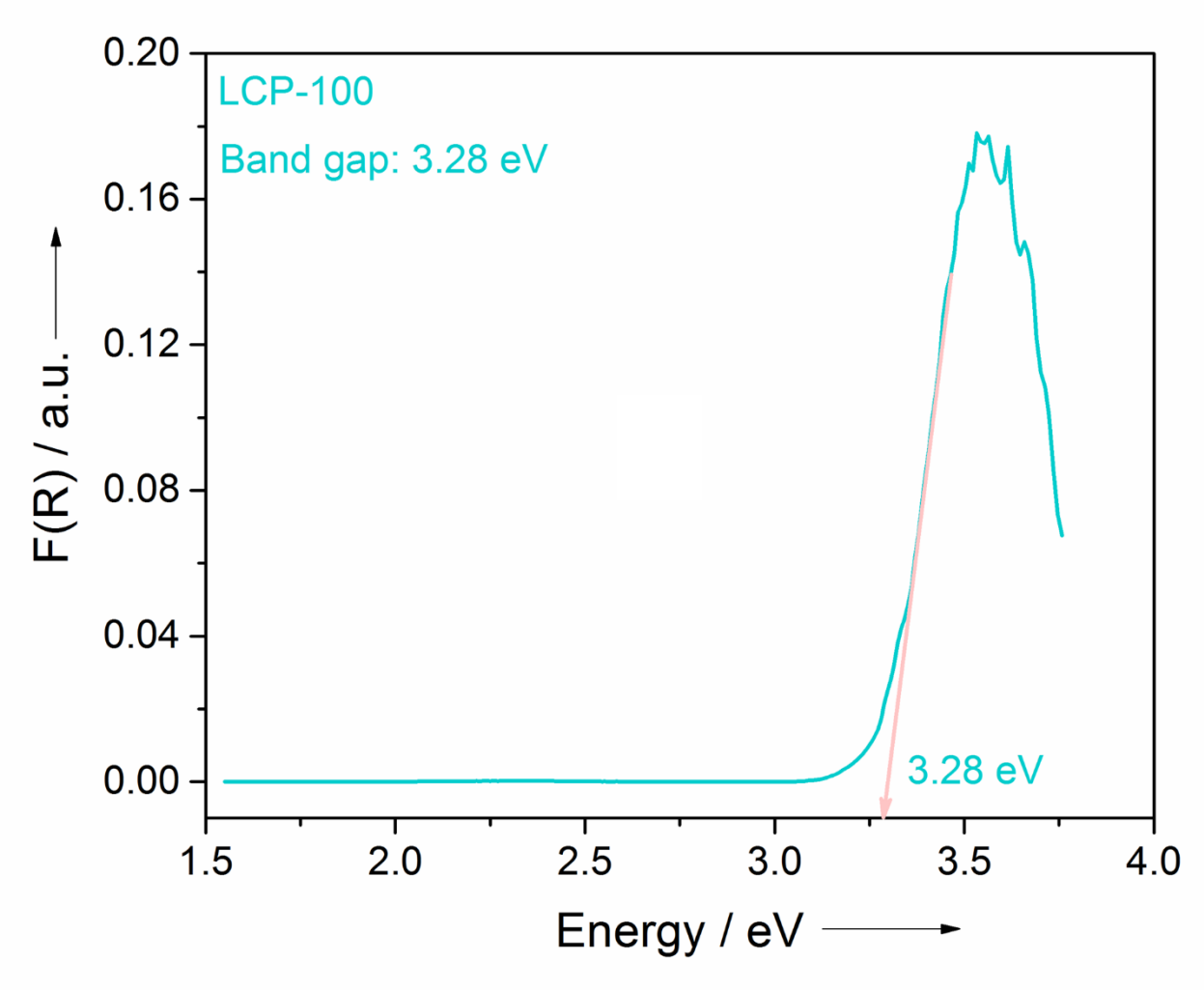
Appendix 2.16: ^{13}C NMR spectra of digested **LCP-100** showing the absence of free guest.



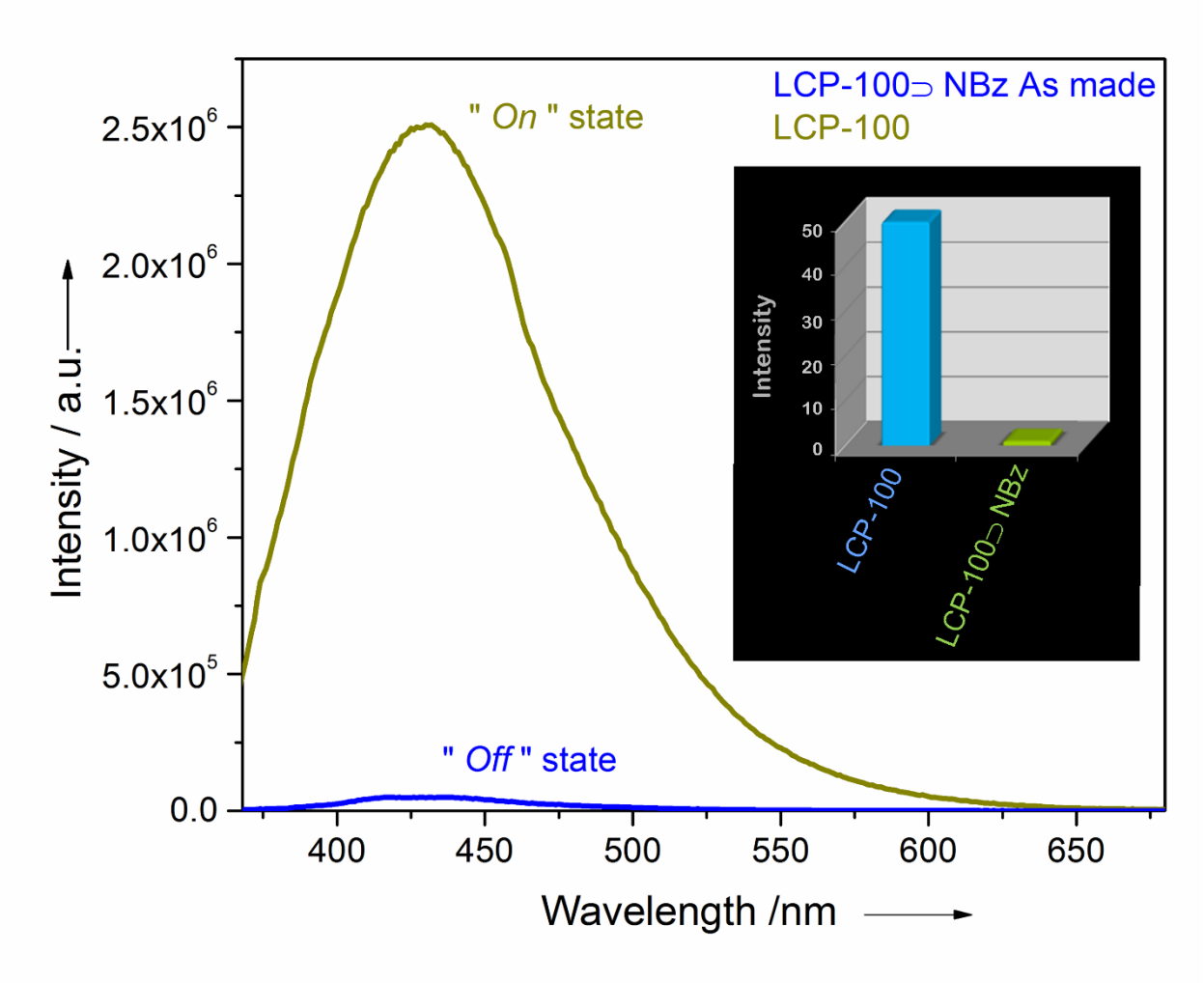
Appendix 2.17: FT-IR spectra of different solvent exposed compounds at RT.



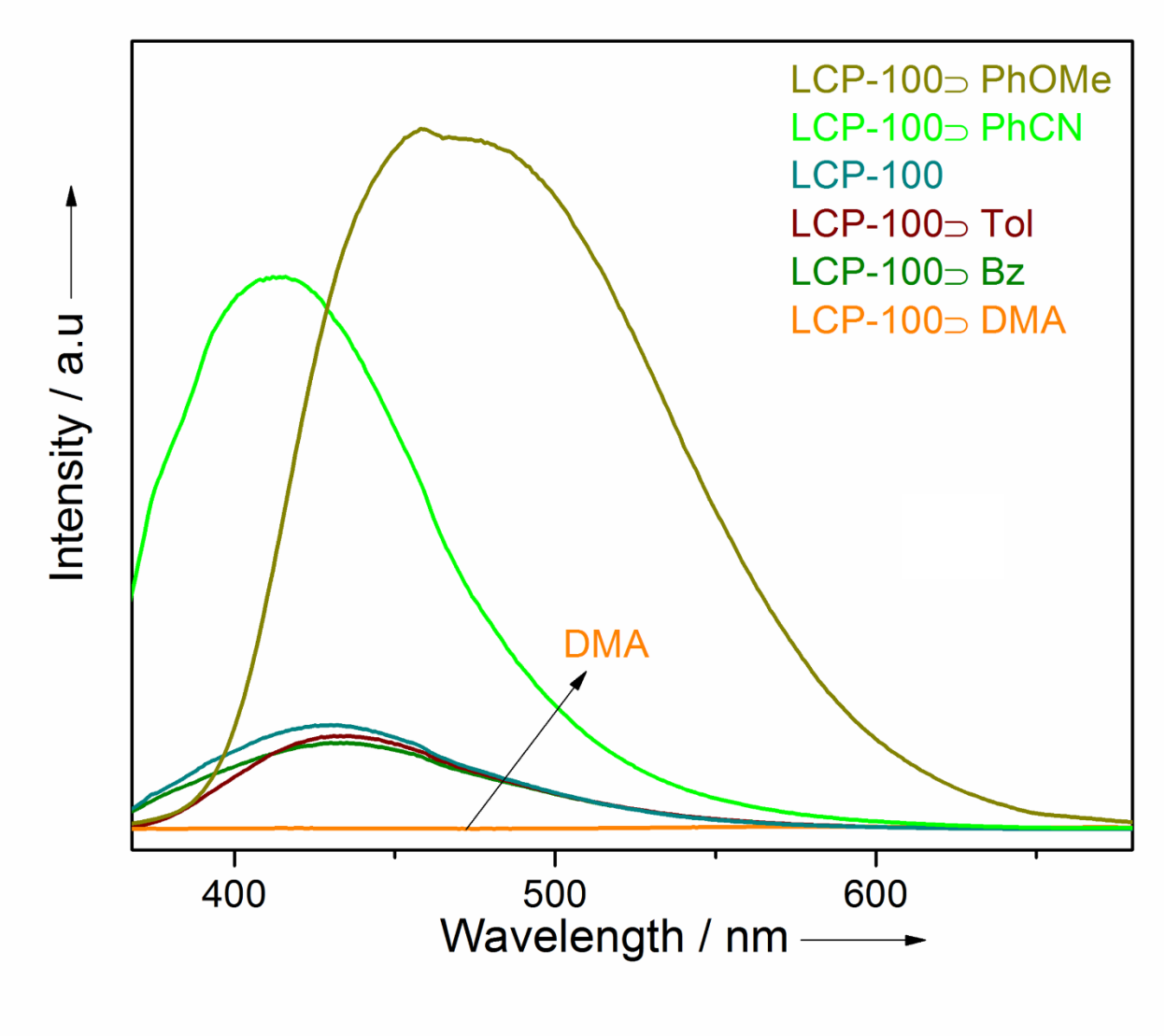
Appendix 2.18: Solid state reflectance spectra of **LCP-100⊃ NBz**, **LCP-100** and all other guest exposed phases.



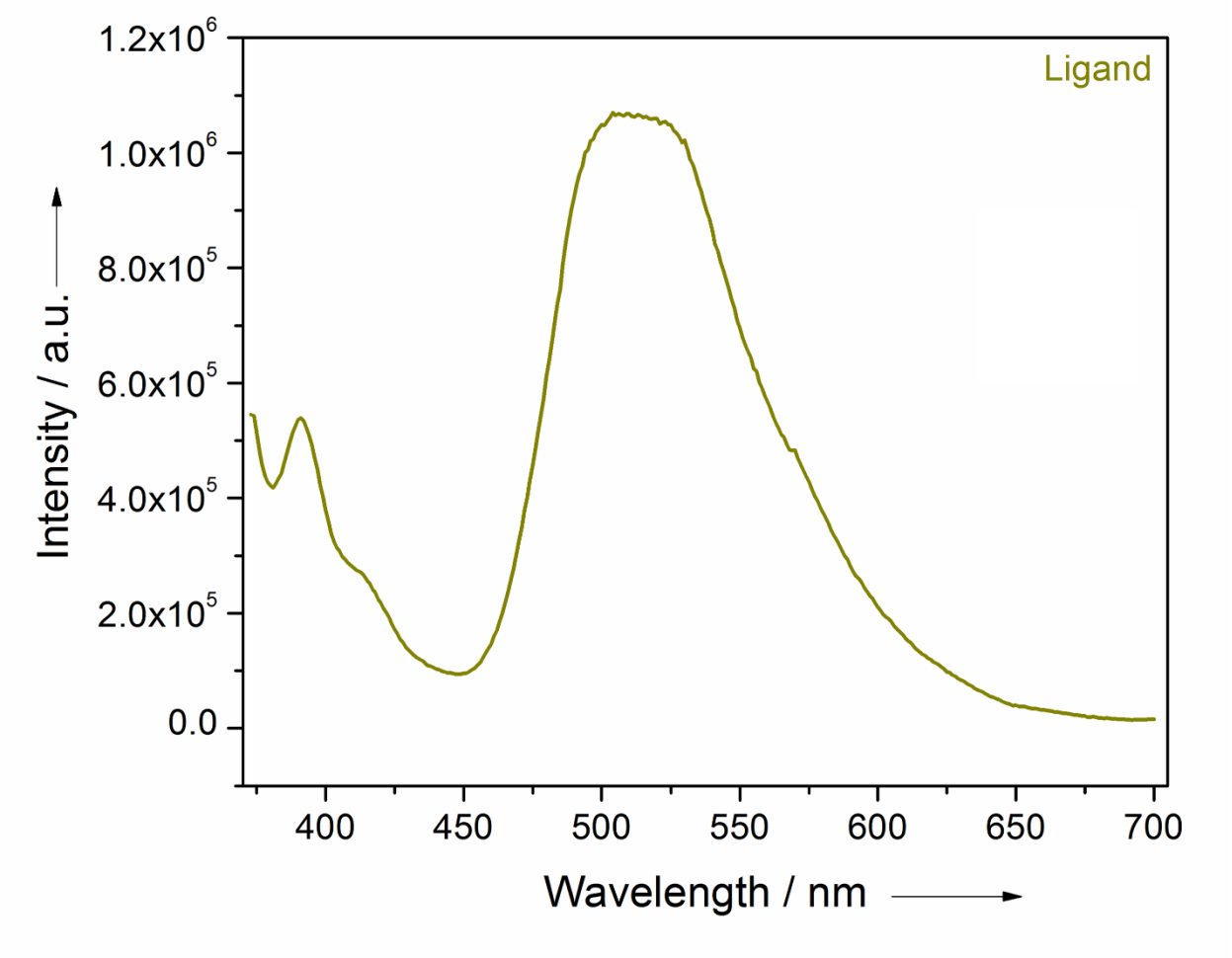
Appendix 2.19: Kubelka-Munk function of **LCP-100** showing the respective band gap.



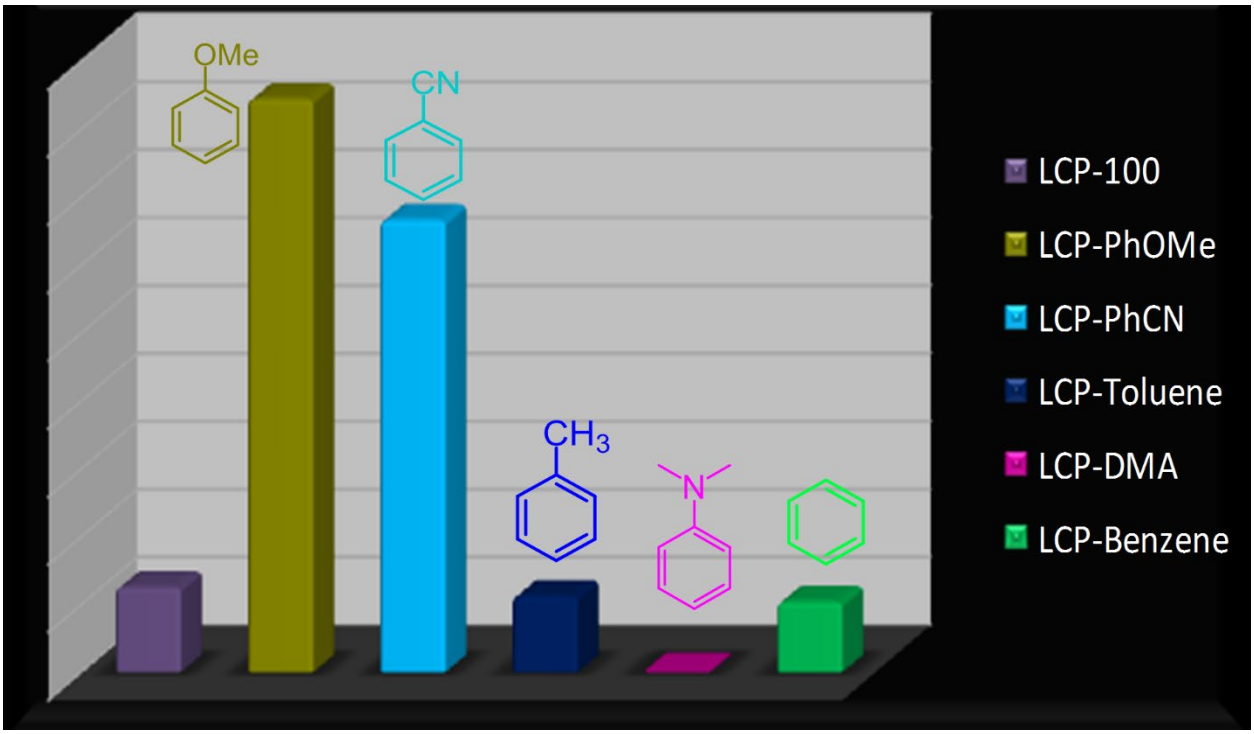
Appendix 2.20: Fluorescence intensity comparison plot between **LCP-100⊃ NBz** and **LCP-100**.



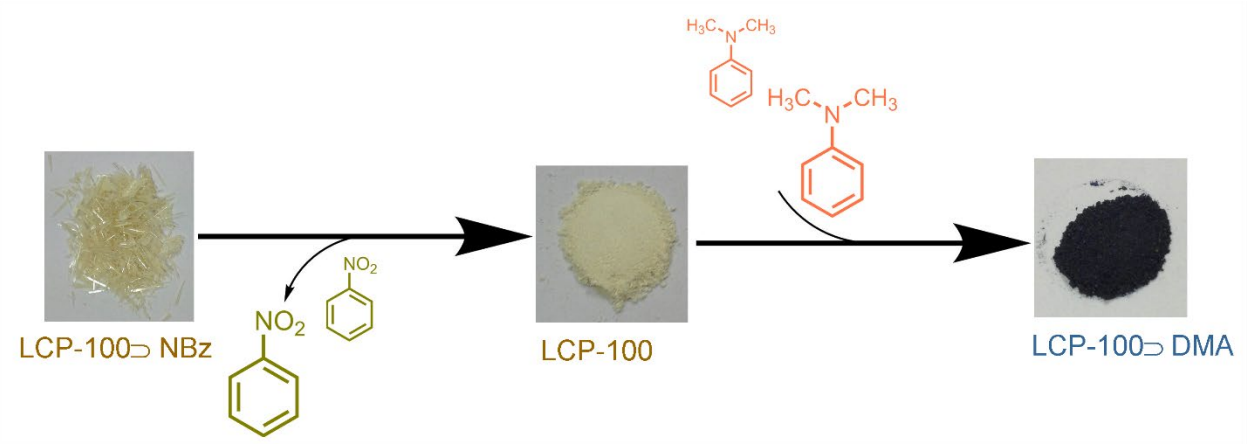
Appendix 2.21: Fluorescence intensity plot for different solvent exposed samples at RT.



Appendix 2.22: Fluorescence intensity plot for free ligand at RT.



Appendix 2.23: Bar diagram depicting the variation in fluorescence intensity of different solvent exposed samples.



Appendix 2.24: Photographs of various phases while losing / accommodating guest molecules of different nature.

Appendix Table 2.1. Quantum yield measurement table:

Quantum yield (%)	
LCP-100⊃ NBz	1.5
LCP-100	6.1
LCP-100⊃Tol	18.6
LCP-100⊃PhOMe	59.9
LCP-100⊃PhCN	40.5
LCP-100⊃DMA	0.2

Appendix Table 2.2: Band gap table of **LCP-100** and all other guests[36].

Band gap(in eV)	
LCP-100	3.28
Benzene	4.50
Tolune	4.40
Anisole	3.54
Benzonitrile	3.41
N,N-dimethylaniline	2.89
Nitrobenzene	2.27

Appendix Table 2.3 : Crystal data table of **LCP-100⊃NBz**.

Identification code	LCP-100⊃NBz	
Empirical formula	C36 H30 Cd Cl2 N6 O12	
Formula weight	921.96	
Temperature	150(2) K	
Wavelength	0.71073 Å	
Crystal system	Orthorhombic	
Space group	P n a 21	
Unit cell dimensions	a = 16.581(2) Å	a= 90°.
	b = 15.248(2) Å	b= 90°.
	c = 15.900(2) Å	g = 90°.
Volume	4019.8(10) $Å^3$	
Z	4	
Density (calculated)	1.523 Mg/m^3	
Absorption coefficient	0.744 mm^{-1}	
F(000)	1864	
Crystal size	0.160 x 0.130 x 0.100 mm^3	
Theta range for data collection	1.814 to 28.528°.	
Index ranges	-19<=h<=22, -20<=k<=20, -21<=l<=20	
Reflections collected	73985	
Independent reflections	10020 [R(int) = 0.0559]	
Completeness to theta = 25.242°	100.0 %	
Refinement method	Full-matrix least-squares on F^2	
Data / restraints / parameters	10020 / 1 / 515	
Goodness-of-fit on F^2	1.073	
Final R indices [I>2sigma(I)]	R1 = 0.0395, wR2 = 0.1008	
R indices (all data)	R1 = 0.0427, wR2 = 0.1032	
Absolute structure parameter	0.38(4)	
Extinction coefficient	n/a	
Largest diff. peak and hole	2.128 and -0.481 e.$Å^{-3}$	

2.6 References

1. T. B. Ryerson, M. Trainer, J. S. Holloway, D. D. Parrish, L. G. Huey, D. T. Sueper, G. J. Frost, S. G. Donnelly, S. Schauffler, E. L. Atlas, W. C. Kuster, P. D. Goldan, G. Hübler, J. F. Meagher and F. C. Fehsenfeld, *Science*, 2001, **292**, 719−723.

2. B. J. Finlayson-Pitts and J. N. Pitts, *Science*, 1997, **276**, 1045−1051.

3. A. C. Lewis, N. Carslaw, P. J. Marriott, R. M. Kinghorn, P. Morrison, A. L. Lee, K. D. Bartle and M. J. Pilling, *Nature*, 2000, **405**, 778−781.

4. Y. Zhang, D. Wu, X. Yan, K. Ding and Y. Guan, *Talanta*, 2016, **154**, 548−554.

5. Z. Zhang, D. S. Kim, C.-Y. Lin, H. Zhang, A. D. Lammer, V. M. Lynch, I. Popov, O. Š. Miljanić, E. V. Anslyn and J. L. Sessler, *J. Am. Chem. Soc*., 2015, **137**, 7769−7774.

6. Y. Cui, Y. Yue, G. Qian and B. Chen, *Chem. Rev*., 2012, **112**, 1126−1162.

7. F.-Y. Yi, D. Chen, M.-K. Wu, L. Han and H.-L. Jiang, *ChemPlusChem*, 2016, **81**, 675−690.

8. M. L. Foo, R. Matsuda and S. Kitagawa, *Chem. Mater*., 2014, **26**, 310−322.

9. S. Kitagawa, R. Kitaura and S.-i. Noro, *Angew. Chem., Int. Ed*., 2004, **43**, 2334−2375.

10. Z. Zhang, Z.-Z. Yao, S. Xiang and B. Chen, *Energy Environ. Sci*., 2014, **7**, 2868−2899.

11. D. Banerjee, C. M. Simon, A. M. Plonka, R. K. Motkuri, J. Liu, X. Chen, B. Smit, J. B. Parise, M. Haranczyk and P. K. Thallapally, *Nat. Commun*., 2016, **7**, 11831.

12. Z. Hu, K. Tan, W. P. Lustig, H. Wang, Y. Zhao, C. Zheng, D. Banerjee, T. J. Emge, Y. J. Chabal, and J. Li, *Chem. Sci*., 2014, **5**, 4873−4877.

13. N. Yanai, K. Kitayama, Y. Hijikata, H. Sato, R. Matsuda, Y. Kubota, M. Takata, M. Mizuno, T. Uemura and S. Kitagawa, *Nat. Mater*., 2011, **10**, 787−793.

14. J. Huo, J. Aguilera-Sigalat, S. El-Hankari and D. Bradshaw, *Chem. Sci*., 2015, **6**, 1938−1943.

15. P. Ramaswamy, N. E. Wong, B. S. Gelfand and G. K. H. Shimizu, *J. Am. Chem. Soc*., 2015, **137**, 7640−7643.

16. M. Zhang, G. Feng, Z. Song, Y.-P. Zhou, H.-Y. Chao, D. Yuan, T. T. Y. Tan, Z. Guo, Z. Hu, B. Z. Tang, B. Liu and D. J. Zhao, *J. Am. Chem. Soc*., 2014, **136**, 7241−7244.

17. Y. Guo, X. Feng, T. Han, S. Wang, Z. Lin, Y. Dong and B. J. Wang, *J. Am. Chem. Soc*., 2014, **136**, 15485−15488.

18. K. C. Stylianou, R. Heck, S. Y. Chong, J. Bacsa, J. T. A. Jones, Y. Z. Khimyak, D. Bradshaw and M. J. Rosseinsky, *J. Am. Chem. Soc*., 2010, **132**, 4119−4130.

19. Y. Takashima, V. M. Martínez, S. Furukawa, M. Kondo, S. Shimomura, H. Uehara, M. Nakahama, K. Sugimoto and S. Kitagawa, *Nat. Commun*., 2011, **2**, 168.

20. R. Kitaura, K. Seki, G. Akiyama and S. Kitagawa, *Angew. Chem., Int. Ed*., 2003, **42**, 428−431.

21. N. Yanai, T. Uemura, M. Inoue, R. Matsuda, T. Fukushima, M. Tsujimoto, S. Isoda and S. Kitagawa, *J. Am. Chem. Soc*., 2012, **134**, 4501−4504.

22. M. E. Foster, J. D. Azoulay, B. M Wong, and M. D. Allendorf, *Chem. Sci*., 2014, **5**, 2081−2090.

23. M. Savonnet, E. Kockrick, A. Camarata, D. Bazer-Bachi, N. Bats, V. Lecocq, C. Pinela and D. Farrusseng, *New J. Chem*., 2011, **35**, 1892–1897.

24. M. A. Nasalevich, R. Becker, E. V. Ramos-Fernandez, S. Castellanos, S. L. Veber, M. V. Fedin, F. Kapteijn, J. N. H. Reek, J. I. van der Vlugt and J. Gascon, *Energy Environ. Sci*., 2015, **8**, 364–375.

25. B. Delley, *Phys.: Condens. Matter,* 2010, **22**, 384208.

26. M. D. Patey and C. E. H. Dessent, *J. Phys. Chem. A,* **2002**, *106*, 4623-4631.

27. Y. Inada and H. Orita, *J. Comput. Chem*., 2008, **29**, 225-232.

28. SAINT Plus, v 7.03; Bruker AXS Inc.: Madison, WI, 2004.

29. G. M. Sheldrick, SHELXTL, Reference Manual, v 5.1; Bruker AXS: Madison, WI, 1997.

30. G. M. Sheldrick, *Acta Crystallogr., Sect. A: Found. Crystallogr*. 2008, **64**, 112−122.

31. L. Farrugia, WINGX, v 1.80.05; University of Glasgow: Glasgow,Scotland, 2013.

32. A. L. Spek, PLATON, A Multipurpose Crystallographic Tool; Utrecht University: Utrecht, The Netherlands, 2005.

33. J.-P. Zhang, X.-C. Huang and X.-M. Chen, *Chem. Soc. Rev*., 2009, **38**, 2385−2396.

34. S. Horike, S. Shimomura and S. Kitagawa, *Nat. Chem*., 2009, **1**, 695−704.

35. X. Shi, W. Wang, H. Hou and Y. Fan, *Eur. J. Inorg. Chem*., 2010, **2010**, 3652.

36. S. Pramanik, C. Zheng, X. Zhang, T. J. Emge, J. Li, *J. Am. Chem. Soc*., 2011, **133**, 4153−4155.

37. G. Andric, J. F. Boas, A. M. Bond, G. D. Fallon, K. P. Ghiggino, C. F. Hogan, J. A. Hutchison, M. A. Lee, S. J. Langford, J. R. Pilbrow, G. J. Troup and C. P. Woodward, *Aust. J. Chem*., 2004, **57**, 1011−1019.

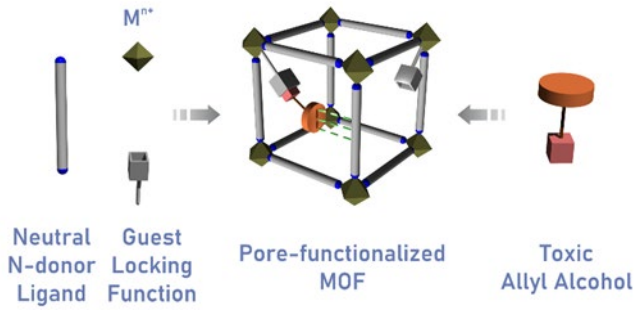
Chapter 3

Specific recognition of toxic allyl alcohol by pore-functionalized metal–organic frameworks

3.1 Introduction

Allyl alcohol (AA) is a systematic toxicant according to US based Environmental Protection Agency (EPA), which is readily absorbed via skin tissues, the respiratory tract, and mucous membranes.[1] Severe intoxication signs include pulmonary edema, inflammation, and severe eye irritation with exposure levels as low as ~5 ppm. According to EPA, the odour recognition concentration for allyl alcohol is much less, i.e., ~0.78 ppm while the air borne disabling/lethal concentration for 10 minutes of exposure is 11 ppm/87 ppm.[2] Allyl alcohol toxicity is due to the formation of an endogenous metabolite, acrolein, by alcohol dehydrogenase.[3,4] The electrophillic nature of acrolein leads to a reaction with nucleophilic moieties viz. guanine in DNA. Acrolein is potentially carcinogenic in nature and is linked with several diseases. Allyl alcohol is present as a water-soluble, colorless liquid, which has significant environmental hazards.[5,6] Owing to its utility, allyl alcohol is widely utilized across several industries as a resourceful raw material such as for the preparation of glycerols, plasticizers, flame-resistant materials, textile auxiliaries, pesticides, medicines, and cosmetics.[7–10] Allyl alcohol is highly flammable in nature and has a high vapour pressure, which makes its transportation difficult, as it can catch fire when their content in the air is greater than 2.5%. Thus, it has become vital, in the pursuit of minimizing harmful effects to living beings, to identify the presence of such toxic species and ensure their safe storage and disposal. Usually allyl alcohol is determined by chromatographic methods or reaction-based processes,[11–14] which prompts the examination by other analytical techniques for rapid, in-field applications. In this regard, the exploration of novel materials as the receptors of such toxic species, either for recognition, storage, or disposal, are highly demanded and their research is of topical interest. Among the different methods investigated for molecular recognition, fluorescence-based techniques are commanding greater attention owing to several benefits such as portability, simplicity, fast analyte response, and low detection limits.[15,16] To tap into these advantages, several artificial probes have been developed to detect different toxic species or biologically relevant molecules. In this regard, metal–organic frameworks (MOFs) have drawn significant research attention as luminescent probes for a range of species, including neurotransmitters, toxic molecules, volatile organic compounds (VOCs), and environmental pollutants.[17–35] Metal–organic frameworks (MOFs) or porous coordination polymers (PCPs) are a rapidly emerging domain of porous materials that are built from organic linkers and metal ions and extended via coordination bonds.[36–43] The characteristics of the system afford a distinct advantage to maximize the probe-analyte interaction via the selection of appropriate building blocks. More specifically, the feasibility of a specific probe-analyte interaction affords the response with a distinct signal generation.[17–35] The porous nature of MOFs yields another interesting effect, viz., the pore confinement effect, which has been linked to a better response mechanism. Owing to the plethora of building blocks, the electronic and related physical features of the compound can be tuned to

suit the demands of the targeted species. Although MOFs have been proven to be quite useful in the field of toxic analyte sensing or capture,[44–61] there still remains plenty of room to expand the scope and examine other relevant species that have not been profoundly explored, such as highly toxic allyl alcohol. With this background, efforts were dedicated to test the possibility of using MOFs for the recognition of toxic allyl alcohol through rationale design. To recognize the target molecule specifically, the probe needs to interact strongly with the guest and the process should have a read-out with a distinct signal. Literature suggested that chloride ions bound to metal ions pose high affinity towards the hydroxyl group.[62] For MOFs, the anchoring of recognition sites on building units have been employed as an affirmative approach to immobilize specific guest molecules.[17–35] Hence, as a primary design step, the influence of metal-bound chloride moiety in MOFs was examined toward allyl alcohol (Scheme 1). Owing to the benefits of luminescence-based pathways, luminescent MOFs were chosen to evaluate this interaction. Neutral N-donor linker based MOFs require the presence of additional entities to satisfy the electronic charge.[63–75] Thus, to anchor specific anionic sites in the polymeric network, these neutral linkers were well suited.[67,68,71,73] In addition, the possibility of having fluorescence properties with conjugated aromatic groups make them favorable for designing molecular probes.[17,20,21] For this reason, highly conjugated tridentate linker (L-tris(4-(1H-imidazol-1-yl)phenyl)amine) with neutral imidazole binding groups was selected, as they have higher binding tendencies among neutral donor groups.[75]



Scheme 3.1. Schematic illustration showing synthesis outline for the preparation of functional MOFs towards detection of allyl alcohol.

To accommodate the coordination assemblies with specific building blocks, linkers with flexible cores were well suited. This further supported the choice of the ligand (L), which had a flexible central moiety. Also, the ligand (L) was known to exhibit luminescence features, which was the primary target of the current study. Apart from having a luminescent linker that contributed to the emission properties via ligand-based emissions, the choice of the metal ion also influenced the overall emissive features of the compound in the charge-transfer interactions with the ligand.[17–35] To accommodate the necessity of having metal bound chloride ions, chloride salt of a hard Lewis acid viz. In(III) was chosen, that also fulfilled the requirement

of a metal center with a d^{10} electronic configuration. It was hypothesized that this preinstalled antenna (M–Cl) may pick up allyl alcohol and the presence of π-electrons in the guest can promote signal transduction via a change in host luminescence features, whereas other alcohols without π-electrons may not perturb the readout.[17–35] Herein, the synthesis of two rationally designed MOFs was conducted and also their ability to selectively detect the presence of toxic allyl alcohol over other small alcohols was studied.

3.2 Experimental

3.2.1 Materials:

All solvents and reagents were commercially available and used without further purification. The ligand, [L-tris4-(1Himidazol-1-yl)phenyl)amine], was synthesized according to the reported protocol.[76]

3.2.2 Synthesis of compound IPM-303

A mixture of the ligand (8.86 mg, 0.02 mmol), $InCl_3 \cdot 4H_2O$ (5.86 mg, 0.02 mmol), N, N-dimethylformamide (2 mL), and ethanol (1 mL) was placed in a glass vial and heated at 90 °C for 48 hours, followed by slow cooling to room temperature. The crystals were filtered off and washed with methanol several times. The compound, IPM-303 viz. $\{[In(L)(Cl)_3] \cdot xG\}_n$, was isolated in ~45% yield. These crystals were dipped in a MeCN solution for the exchange, and heated under vacuum at 75 °C to obtain the guest free phase. The guest solvent molecules were found to be highly-disordered during analysis. The formula for the guest-free phase was estimated to be $\{[In(L)(Cl)_3\}_n$. Anal. Calcd. (guest free phase): C/N, 3.31; C/H, 15.34. Found: C/N, 2.87; C/H, 15.93.

3.2.3 Synthesis of compound IPM-304

This compound was synthesized similarly as mentioned above, except that $MnCl_2 \cdot 4H_2O$ (4.0 mg) was used as the metal salt. The formula for the guest-free phase was estimated to be $[\{Mn_2(L)_2(Cl)_4\}]_n$. Anal. calcd. (guest free phase): C/N, 3.31; C/H, 15.31. Found: C/N, 3.39; C/H, 15.85.

3.2.4 Fluorescence measurements

Powdered crystals of IPM-303 (2 mg) were dispersed in the respective organic solvents (2 mL) and kept for equilibration overnight before measuring the excitation and emission spectra. The same protocol was followed for IPM-304.

3.2.5 Physical measurements

Powder X-ray diffraction patterns were recorded on a Bruker D8 Advanced X-ray diffractometer using Cu Kα radiation (λ = 1.5406 Å) in the 5° to 40° 2θ range with a scan speed of 1.2° min^{-1}. All of the fluorescence

measurements were performed on a Jobin Yvon Fluoromax-4 spectrofluorometer. The SEM images & EDX data were obtained using a FEI Quanta 3D dual beam ESEM. The thermogravimetric analysis profiles were recorded on a Perkin-Elmer STA6000, TGA analyser under N_2 atmosphere with a heating rate of 10 °C min^{-1}. The FT-IR spectra were recorded on a Bruker spectrometer.

3.2.6 X-ray structural studies

Single-crystal X-ray data of compound IPM-303 and IPM-304 were collected at 100 K on a Bruker D8 Venture Duo X-ray diffractometer equipped with a Microfocus X-ray source (operated at 50 W; 50 kV/1 mA) and graded multilayer optics for monochromatic Mo Kα radiation (λ = 0.71073 Å) with a focused X-ray beam and a Photon 100 CMOS chip based detector system. The crystal was mounted on nylon CryoLoops (Hampton Research) with Paraton-N (Hampton Research). The data integration and reduction were processed with SAINT software.[77] A multi-scan absorption correction was applied to the collected reflections.[78] The structure was solved by a direct method using SHELXTL[79,80] and was refined on F^2 with a full-matrix least-squares technique using the SHELXL-2014/7 [81] program package within the WINGX[82] programme. All of the non-hydrogen atoms were refined anisotropically. All of the hydrogen atoms were located in successive difference Fourier maps and they were treated as riding atoms using SHELXL default parameters. The structures were examined using the Adsym subroutine in PLATON to assure that no additional symmetries could be applied to the models. The SQUEEZE option[83] was used to eliminate the contribution from the disordered guest molecules. CCDC 1922524 and 1922527, for IPM-303 and IPM-304, respectively, contains the supplementary crystallographic data for this paper.

3.2.7 Structure simulation studies

The Materials Studio software suite 2017 (Accelrys)[84] was used to perform the structural simulations. First, the molecular structure of the MOF unit cell was fully relaxed using a DMOL^3 code. Generalized gradient approximations (GGA), Perdew–Burke–Ernzerhof (PBE)[85,86] and PBE-GGA were employed as the exchange correlation functions with All Electron Core treatment, hexadecapole multipolar expansion, and DNP+ Basis set with a medium quality global orbital cutoff scheme. During the relaxation process, the energy, force, and displacement parameters were set to 2 × 10−5 Ha, 0.004 Ha $Å^{-1}$, and 0.005 Å, respectively. An additional structural simulation on the relaxed structure was performed using a universal force field at a fine-quality calculation level. A Connolly surface was created for the model using the Atom, Volumes and Surface tool in the Materials Studio with a fine grid resolution (0.25 Å). The Connolly radius was set to 1.0 Å. The sorption isotherms for the different guest molecules introduced in the MOF structure were modelled using the Sorption module, which was available within the Materials Studio. The calculations were performed using the Metropolis algorithm with a fine quality grid calculation at 298 K

on a single unit cell and 3 × 3 × 3 supercell. In order to quantify the interactions of the allyl alcohol molecules with the molecular structure, a sketch module was employed to calculate the bond parameters. The calculations were performed using a universal force field at a fine-quality calculation level and at 298 K. The discovery studio suite 2016 (Accelrys) was used to calculate the HOMO–LUMO (HOMO: highest occupied molecular orbital; LUMO: lowest unoccupied molecular orbital) energy levels for a single MOF unit and the interactions for the guest molecules. A single MOF unit was geometry optimized using a DMOL3 code with the same parameters as those explained above. Then, a specific molecule was introduced into the relaxed MOF unit. The HOMO–LUMO energy levels were calculated with a PBE-GGA exchange correlation function and dispersion correction. The optical properties were calculated using a CASTEP code.[87] The calculations were performed on the above obtained geometry optimized MOF unit cell along with guest molecules. In this regard, a 3 × 3 × 3 supercell was constructed with this MOF unit cell. Thereafter, generalized gradient approximations (GGA), Perdew–Burke–Ernzerhof (PBE) and PBE-GGA0 were used as exchange correlation functions with norm conserving pseudopotentials, Koelling–Harmon relativistic treatment, a 600 eV energy cut-off, a self – consistent dipole correction, and a 2 × 2 × 2 Monkhorst-Pack grid.

3.3 Results and discussion

Bearing consideration from the aforementioned hypothesis, a novel In(III) based neutral MOF viz. IPM-303 was fabricated (where IPM stands for IISER Pune Materials). IPM-303 was synthesized as a block shaped crystal in a solvothermal reaction of $InCl_3 \cdot 4H_2O$ and the ligand (L) in a solvent mixture of DMF/EtOH (1 : 1) at 90 °C. From the single crystal X-ray diffraction (SC-XRD) analysis, IPM-303 was found to crystallize in the P21/n space group. The asymmetric unit comprises 1 In(III) cation, 1 ligand unit, and 3 chloride anions (Appendix 3.1). Each metal center is octahedral in coordination with the bonds, along with N-atoms of 3 independent linkers and 3 chloride anions (Fig. 3.1a and Appendix 3.2). All three imidazole terminal sites of each linker are coordinated to a In(III) center. The coordination of the 3 chloride anions blocked the growth of the coordination entities along the two axes and the coordination polymer was extended only along the crystallographic *a*-axis (Appendix 3.3). A careful analysis revealed that the adjacent one-dimensional polymers were strongly held by non-covalent interactions (Appendix 3.4). This led to the formation of a strongly-packed, higher-dimensional, supramolecular architecture based on non-covalent interactions. The uniqueness of the structure was emphasized in the building blocks employed in the reaction medium as evidenced by the Cambridge Structural Database (CSD) screening approach. In(III) was a hard Lewis acid. Therefore, the coordination polymers with neutral N-donor linkers were less likely to form. A CSD search highlighted the lack of reports on the preparation of such compounds. The ability of the higher-dentate linkers to propagate the formation of the polymers is well understood in the literature.

Thus, the current example further underscores this thought, wherein there is only one kind of donor group (neutral N-donor) in the tridentate ligand.

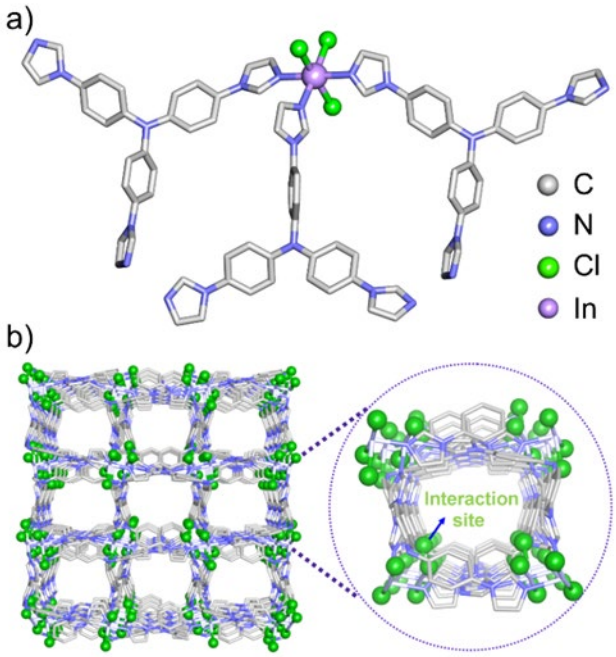


Figure 3.1. Structural representation of IPM-303 showing a) coordination environment and b) presence of chloride ions along porous channels (H-atoms have been omitted for clarity).

However, a coordination polymer was formed with a hard Lewis acidic cation. Further investigations using this approach will lead to the formation of coordination polymers with neutral donor linkers and hard Lewis acids. In addition, it will also lead to the exploration of an untapped scope in the domain of coordination polymers. The packing of IPM-303 showed a one-dimensional narrow pore channel, which was accessible to the guest molecules (Fig. 3.1b and Appendix 3.5). The void volume of the packing was 1032.50 $Å^3$ (29.1%), and the diagonal of the rectangular pore had a length of ~5.5 Å (considering the van der Waals radii of the concerned atoms). Interestingly, as desired, the pore walls had metal-coordinated chloride anions, thus presenting a polar site for guest adsorption. Also, the restricted pore permitted the loading of only guest molecules with relatively smaller sizes. A bulk phase characterization was performed using a powder X-ray diffraction analysis (Appendix 3.6). The overlap of the peaks with a simulated pattern validated the bulk-phase crystallinity of the product. The thermo-gravimetric analysis (TGA) suggested the presence of guest molecules that were occluded in the pores during the synthesis (Appendix 3.7). A conventional activation protocol was applied by dipping the crystals of the compound in acetonitrile over 24 hours and subsequently drying under vacuum. The crystalline activated phase (Appendix 3.14) was further used for all fluorescence studies. The SEM images revealed the presence of a crystalline morphology

(Appendix 3.9). The FT-IR spectra confirmed the inclusion of peaks present in the ligand (Appendix 3.10). The presence of a fluorescent linker and d^{10} metal center, along-with the presence of a metal-bound chloride served as basis to further probe the compound for the sensing of allyl alcohol. Initially the solid-state absorption was checked (Appendix 3.11). To test the photophysical properties, ground crystals of IPM-303 that were initially dipped in acetonitrile were recorded. Upon excitation at 320 nm, the emission was found to peak at 391 nm (Appendix 3.12). Enthused by these basic features, the compound was then screened for its sensing ability towards several alcoholic molecules such as methanol, ethanol, 1-propanol, 1-butanol, and allyl alcohol. In a typical experiment, crystals of IPM-303 were dispersed in the respective solvents and left overnight to equilibrate. This was followed by recording the fluorescence emission spectrum. Interestingly, a significant shift in the emission maxima for allyl alcohol was observed, which was exclusive in the set of chosen analytes (Fig. 3.2b and Appendix 3.13). Additionally, there was a change in the luminescence intensities for different solvents, but the shift was observed only in the case of allyl alcohol. There was no loss of crystallinity in the presence of allyl alcohol or the mixture of other solvents (Appendix 3.14). The SEM images confirmed the retention of the morphology (Appendix 3.9) and the FT-IR spectra validated the presence of allyl alcohol (Appendix 3.15). It was speculated that the presence of the polar pendant sites (Fig. 3.1b) was actuating the inclusion of the protic alcoholic guest molecules, owing to the favoured interaction of chloride with hydroxyl moieties.[62] Seemingly, the presence of π-electrons in allyl alcohol led to a distinguishable host–guest read-out signal unlike that for other guest molecules, which did not have π-electrons. The presence of CH–π interactions was reported in literature,[88–90] wherein the acidity of the C–H bond was found to have a strong influence on the interaction energetics. In addition, this CH–π bonding has been found to have a significant interaction, leading to orbital reformation.[90] In the present case, owing to the presence of the ligand-based emission, any perturbation to the electronic character of the ligand may have had a direct influence on the emissive character, which may have been brought about by the presence of acidic C–H bonds in the confined environments of the MOF. To extend this investigation and test the hypothesis further, another luminescent compound viz. IPM-304 was prepared. The compound was prepared in an analogous manner as above. The SC-XRD studies revealed that the crystallization of IPM-304 was in the $P\bar{1}$ space group. The asymmetric unit comprises 2 metal centers, 2 ligands, and 4 chloride anions (Appendix 3.16). Each Mn(II) center is octahedral with coordination from 3 independent linkers. 2 chloride ions bridged adjacent Mn(II) cations, while another chloride ion coordinated singularly (Appendix 3.17). Two linkers were coordinated to the same two Mn_2Cl_2 nodes, which led to the overall packing being a 2-dimensional MOF. The compound was found to have a 1D porous channel (Appendix 3.18) and the void volume was estimated to be 1568.33 Å3 (40.3%). Similar to the case for IPM-303, the porous channels for IPM-304 comprise the presence of chloride ions aligned along the pore walls. A bulk phase characterization was performed using PXRD, FT-IR spectroscopy, SEM, and TGA profiles

(Appendix 3.19–Appendix 3.22). Similar to the previous case, the compound was activated and used for further experiments. The basic photophysical features of IPM-304 were tested by exciting ground crystals of IPM-304 in acetonitrile at 320 nm, as observed from the solid-state absorption spectrum (Appendix 3.23). Upon excitation, an emission spectrum peaking at 389 nm was observed (Appendix 3.24). As described earlier, the emission spectra were recorded for several analytes (Fig. 3.2 and Appendix 3.25). As observed earlier, the emission spectrum was remarkably perturbed only in the case of allyl alcohol. PXRD patterns confirmed the retention of crystallinity (Appendix 3.26). FT-IR spectra confirmed the inclusion of allyl alcohol in the framework (Appendix 3.27).

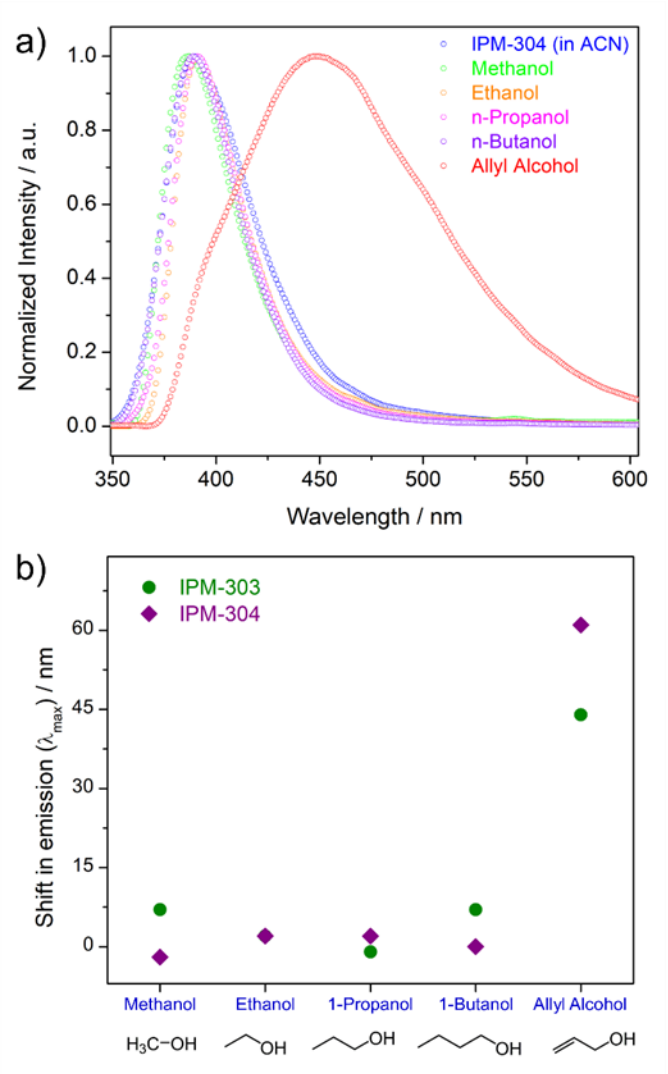


Figure 3.2. a) Normalized emission profiles for IPM-304 dispersed in different solvents (λ_{exc} = 320 nm). b) Plot showing change in emission maxima position of IPM-303 and IPM-304 upon dipping in different alcoholic solvents and allyl alcohol.

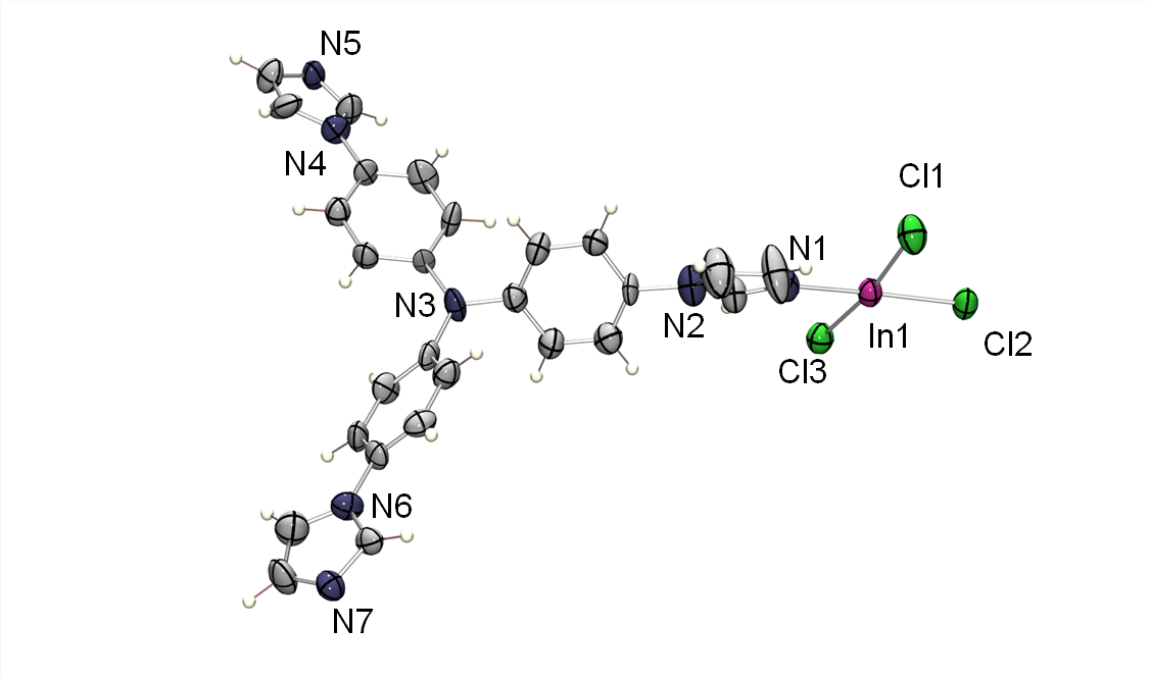
To delve deeper into insights at the molecular level and the mechanism, DFT calculations with IPM-303 and other solvents used in this study was conducted. The electron density map showed a differential electronic density (Appendix 3.28a). The framework was found to present accessible sites for all of the guest molecule inclusions (Appendix 3.28b and Appendix 3.28c). The M–Cl bond distance and the C–H aromatic bonds were found to be perturbed upon the inclusion of the guest allyl alcohol within the voids of the framework (Appendix 3.28d and Appendix 3.28e). The estimated binding energies (Appendix 3.28f) and uptakes were found to be different (Appendix 3.28g), which was attributed to the size and shape of the different guest molecules. The involvement of the non-covalent interactions for the unsaturated C–H bonded entities was previously found to be involved in orbital energy changes.[88–90] Therefore, estimation of the orbital energies of the MOF when loaded with different guest molecules was quite crucial to this study (Appendix 3.28h). The HOMO– LUMO gaps corroborated with the experimental observations, wherein the LUMO of the MOF and LUMO of allyl alcohol were found to be in close proximity. This suggested a strong orbital overlap leading to a differential response in the estimated emission features for the MOF–allyl alcohol complex (Appendix 3.28i). Also, the predicted emission pattern was found to have a close resemblance to the experimentally observed pattern (Appendix 3.13). For all of the other solvents, the LUMO was found to be much higher, thus excluding the possibility of perturbation in the emission properties of the framework. The pronounced effect in the experimental spectrum for the MOF–allyl alcohol complex was attributed to the bulk solvent effects, which were not accounted for in the DFT calculations. This theoretical evidence strongly supported the experimental observations, which further endorsed the design approach of the MOFs for the specific detection of allyl alcohol over other small alcohols.

3.4 Conclusions

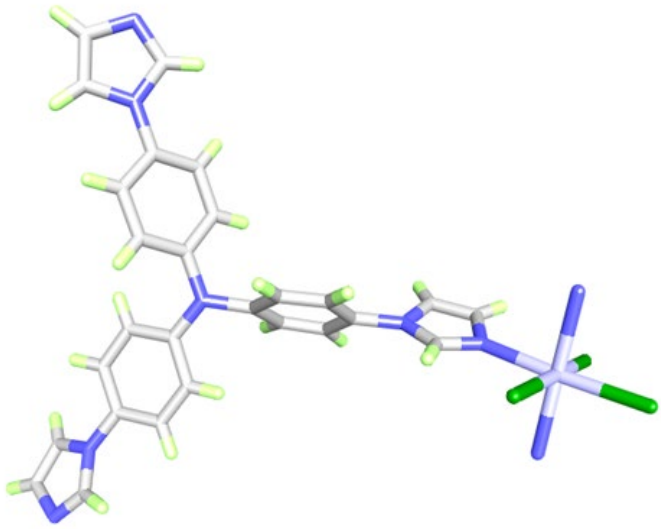
In summary, this study reports the synthesis and characterization of two luminescent porous coordination polymers based on chloride salts of In(III) and Mn(II) and a tridentate neutral N-donor ligand viz. IPM-303 and IPM-304. The two MOFs allowed for the presence of the coordinated chloride ions, which were aligned along the pore channels. IPM-303 presented a rare example of a MOF constructed by the coordination bonding of a neutral N-donor ligand with hard In(III) cations. The presence of the functional site in conjunction with the close proximity of the organic fluorophore (organic linker) was tapped for the fluorescence recognition of toxic, volatile allyl alcohol. The response was sharp and selective over other small alcohols and was similar for both the MOFs. The experimental findings were endorsed by theoretical calculations. Although MOFs have been sought for sensing applications involving several analytes, hitherto, MOFs have not been explored for the detection of allyl alcohol. The present findings will

contribute significantly to the development of MOFs and other materials as solid-state sensors for toxic organic compounds and other environmental contaminants.

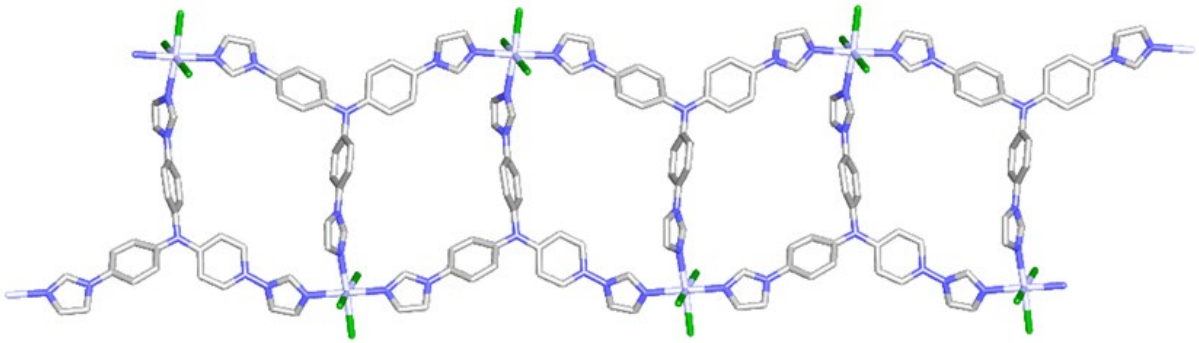
3.5 Appendix Section



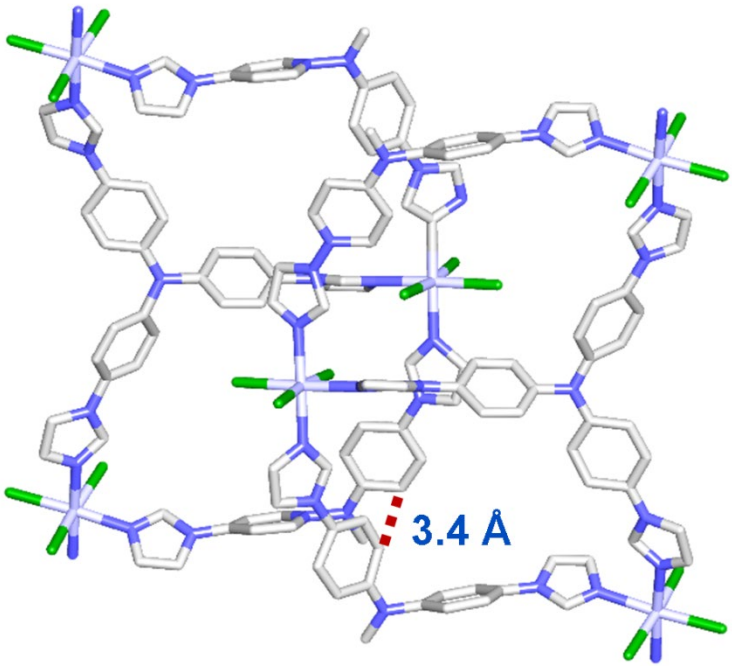
Appendix 3.1: ORTEP diagram for **IPM-303** in thermal ellipsoids.



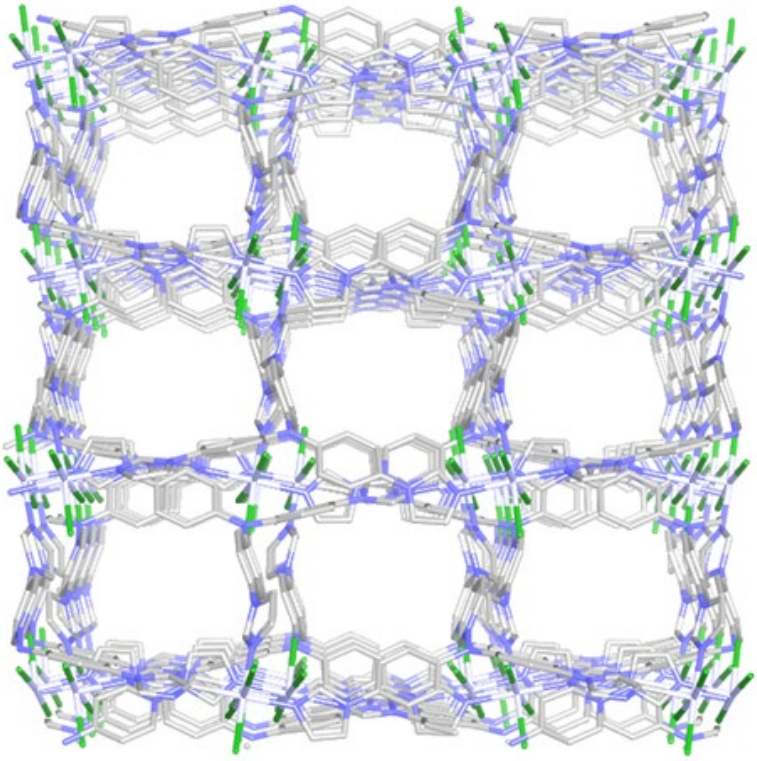
Appendix 3.2: Coordination environment of **IPM-303**. (Colour code: C, grey; N, blue; In, pale violet; Cl, green; H, pale green).



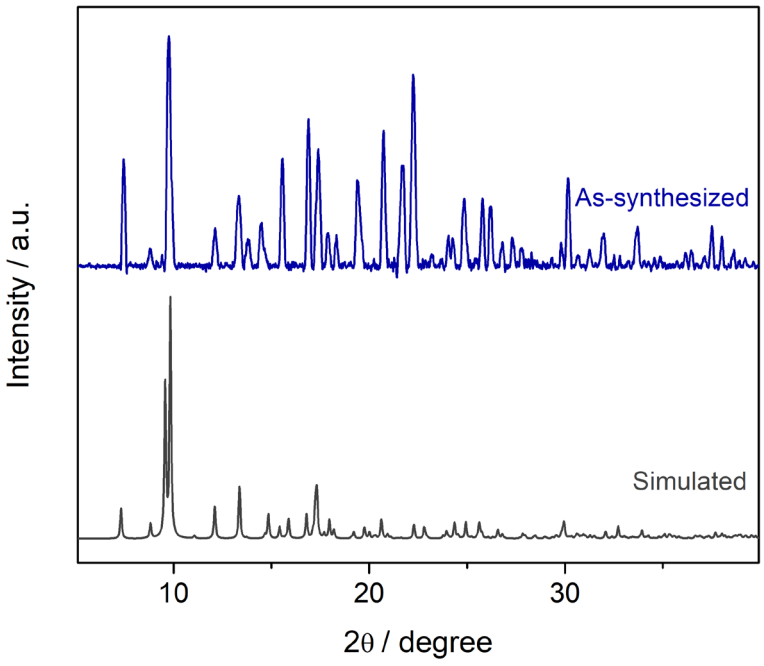
Appendix 3.3: Packing in **IPM-303** showing 1D extension of coordination polymer. (Hydrogen atoms have been omitted for clarity, colour: Gray - C, Blue - N, Light purple - In, Green - Cl).



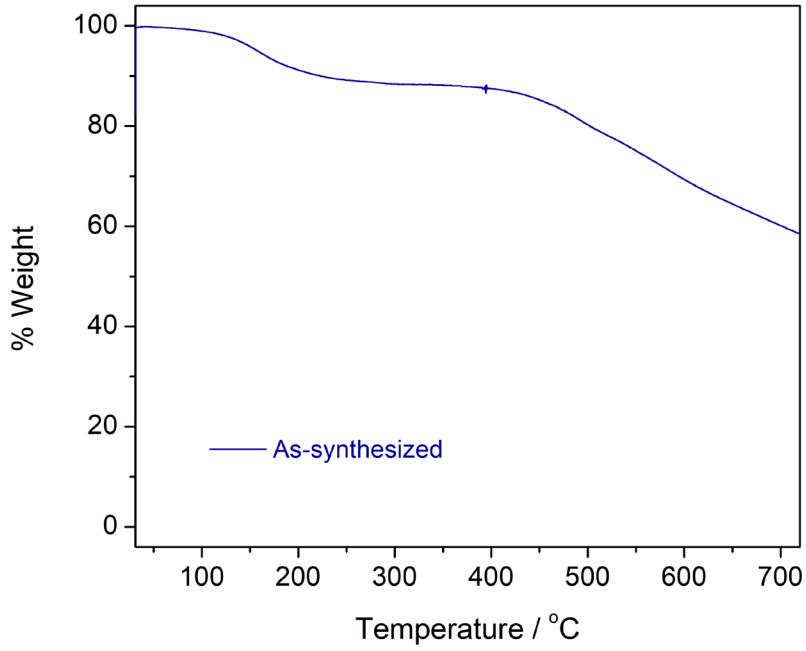
Appendix 3.4: Packing diagram of **IPM-303** showing interaction between adjacent 1D layers. (Hydrogen atoms have been omitted for clarity, colour: Gray - C, Blue - N, Light purple - In, Green - Cl).



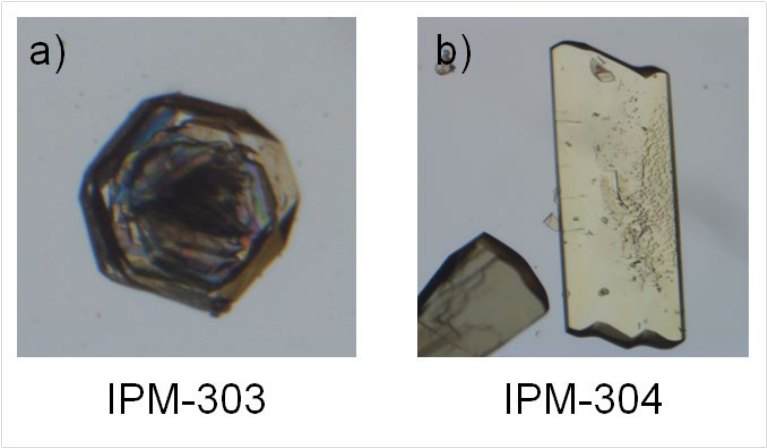
Appendix 3.5: Packing diagram of **IPM-303** showing porous channel. (Hydrogen atoms have been omitted for clarity, colour: Gray - C, Blue - N, Light purple - In, Green - Cl).



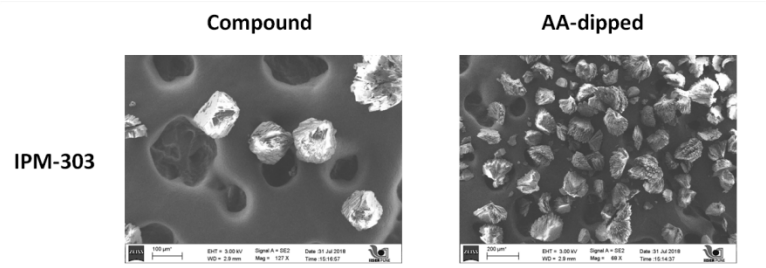
Appendix 3.6: Powder X-ray diffraction patterns of **IPM-303** - Simulated (gray), as-synthesized (blue).



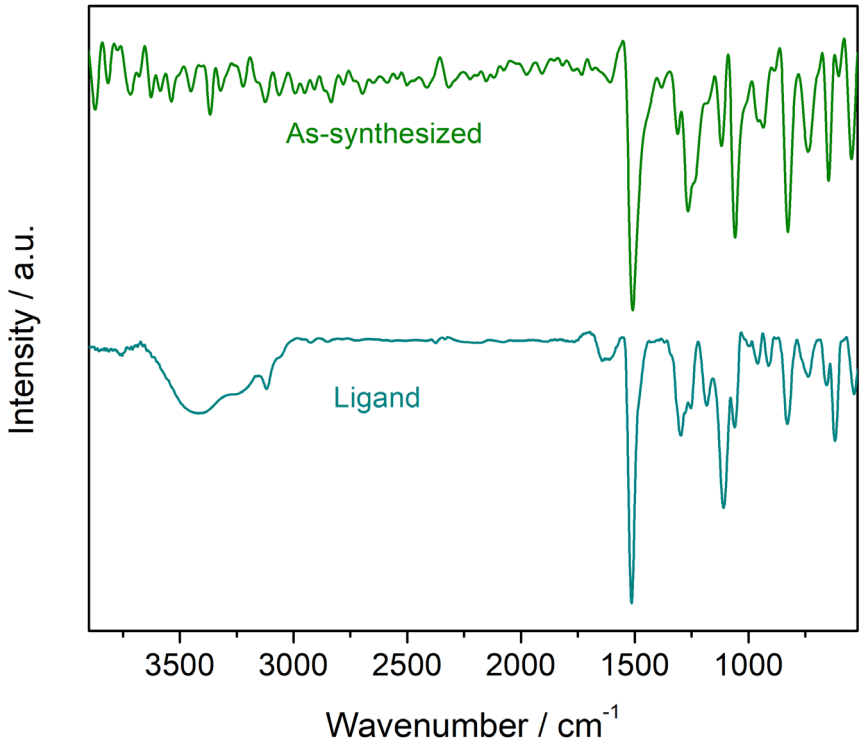
Appendix 3.7: TGA profile for compound **IPM-303**.



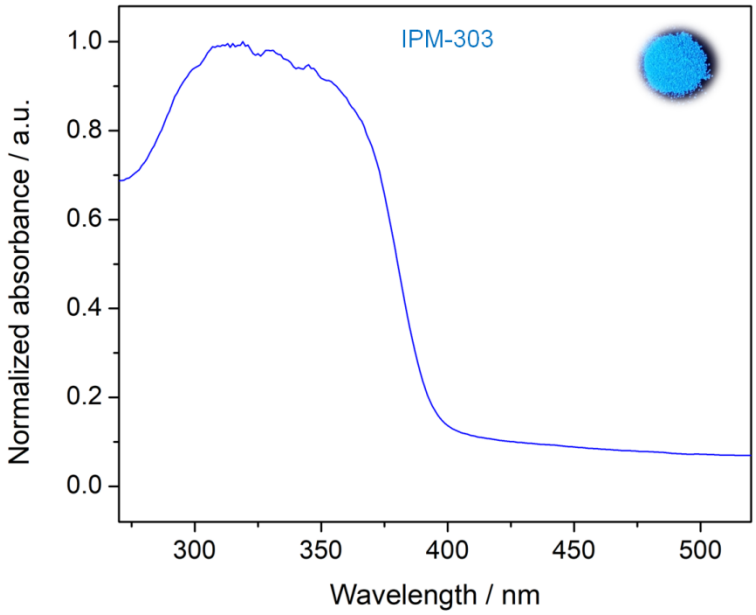
Appendix 3.8: Photographs of crystals of a) **IPM-303** and b) **IPM-304** taken under optical microscope.



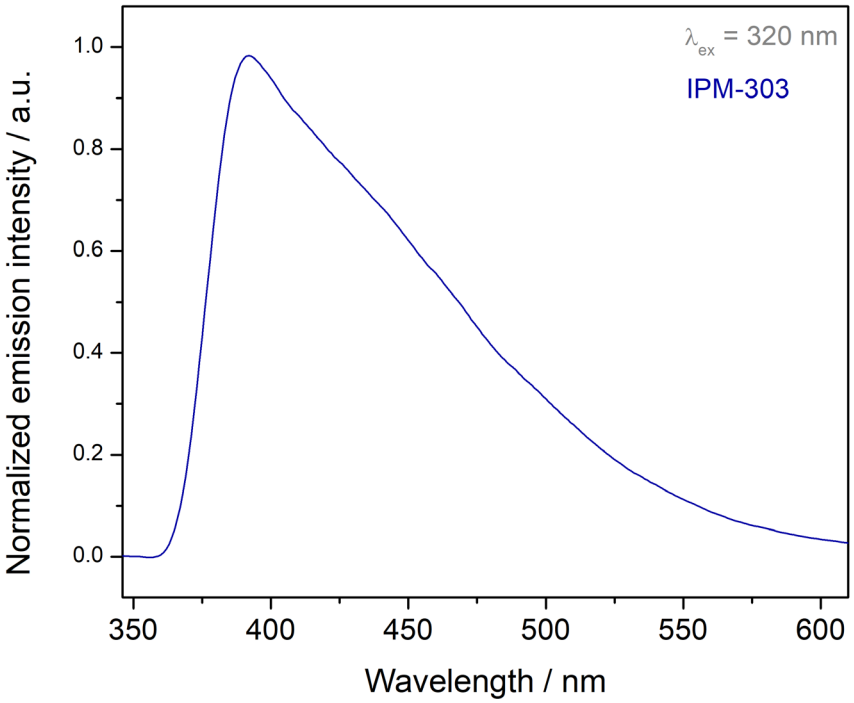
Appendix 3.9: FESEM images for compound **IPM-303** - (left) as-synthesized phase, (right) crystals upon dipping in allyl alcohol. The images were recorded for the solid samples on carbon tape.



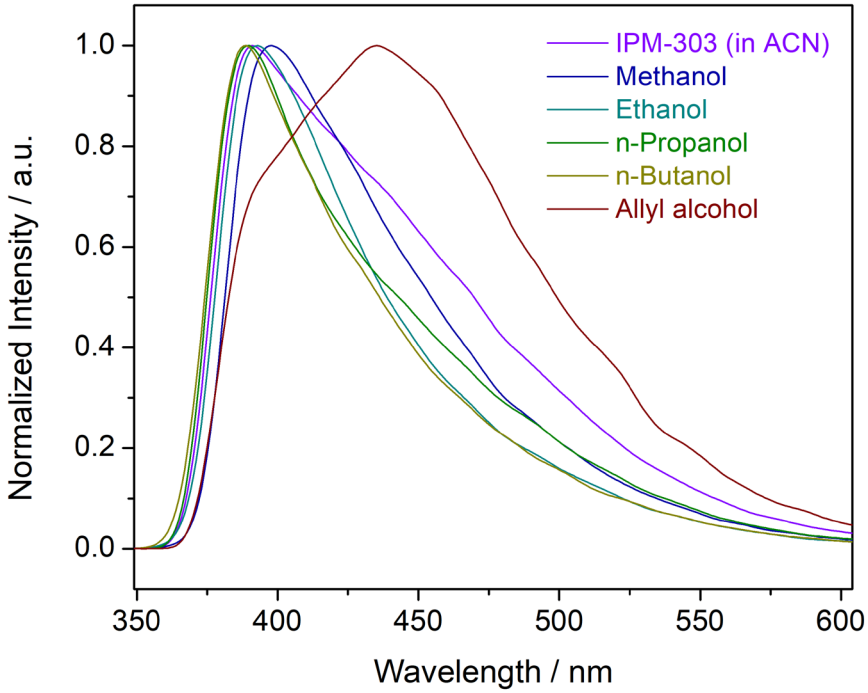
Appendix 3.10: FT-IR spectra for the ligand and compounds **IPM-303**.



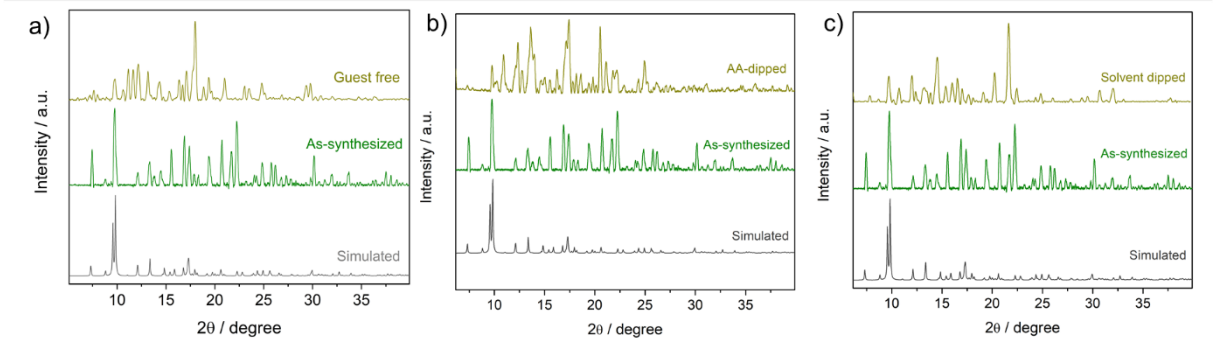
Appendix 3.11: Solid-state UV absorbance profile for **IPM-303**. (Inset) image of illuminated MOF powder under UV lamp (365 nm).



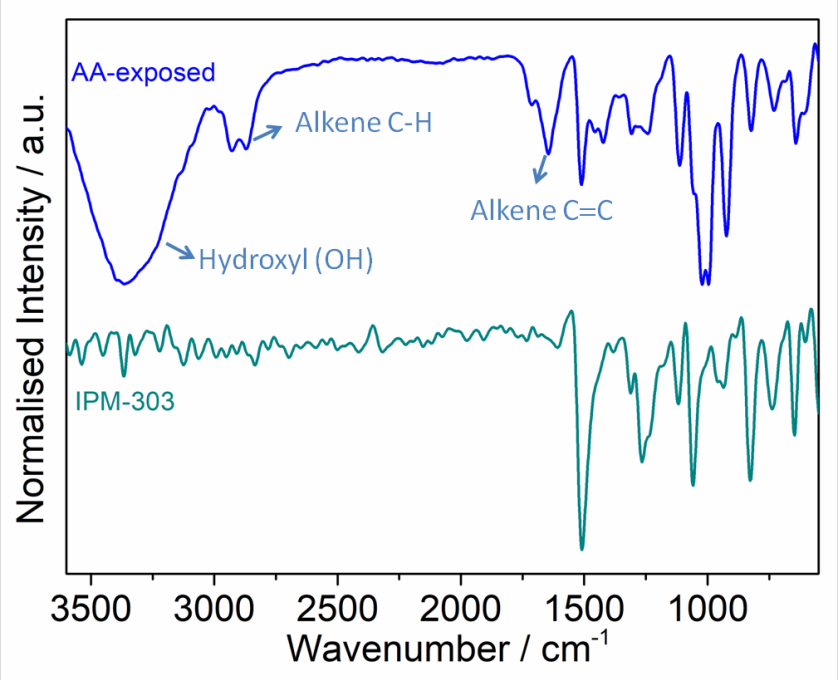
Appendix 3.12: Fluorescence emission profile for **IPM-303** dispersed in acetonitrile (λ_{exc} = 320 nm).



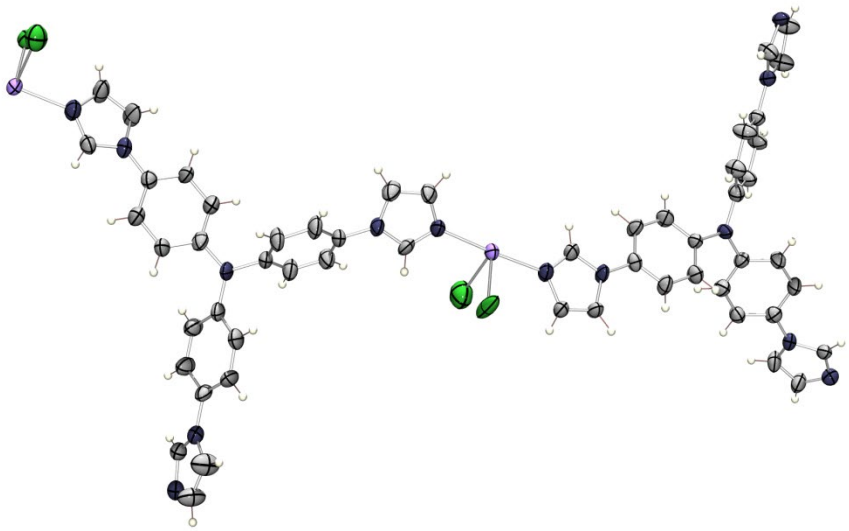
Appendix 3.13: Normalized emission profiles for **IPM-303** when dipped in different solvents.



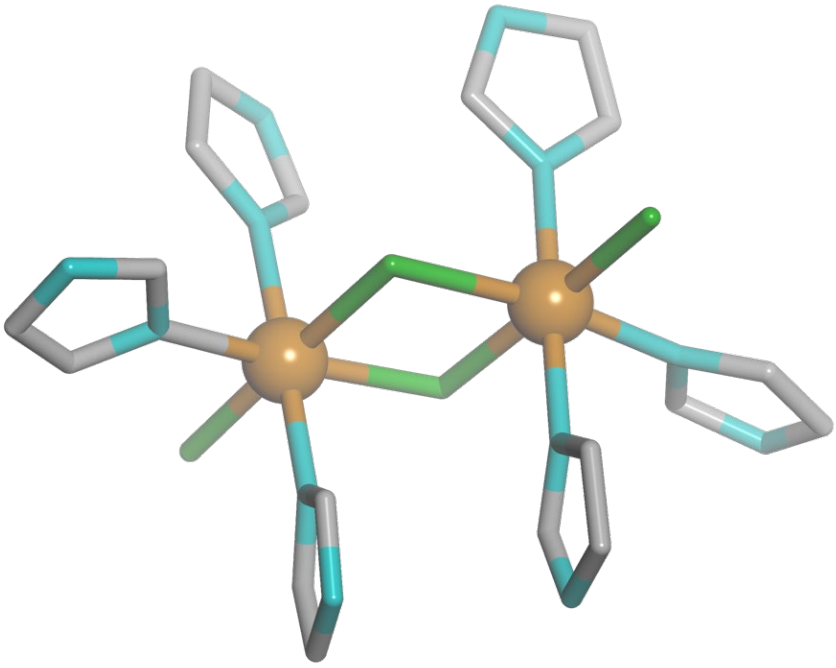
Appendix 3.14: PXRD for **IPM-303** of a) guest free phase, b) AA-dipped phase and c) phase dipped in mixture of all other solvents used in this study.



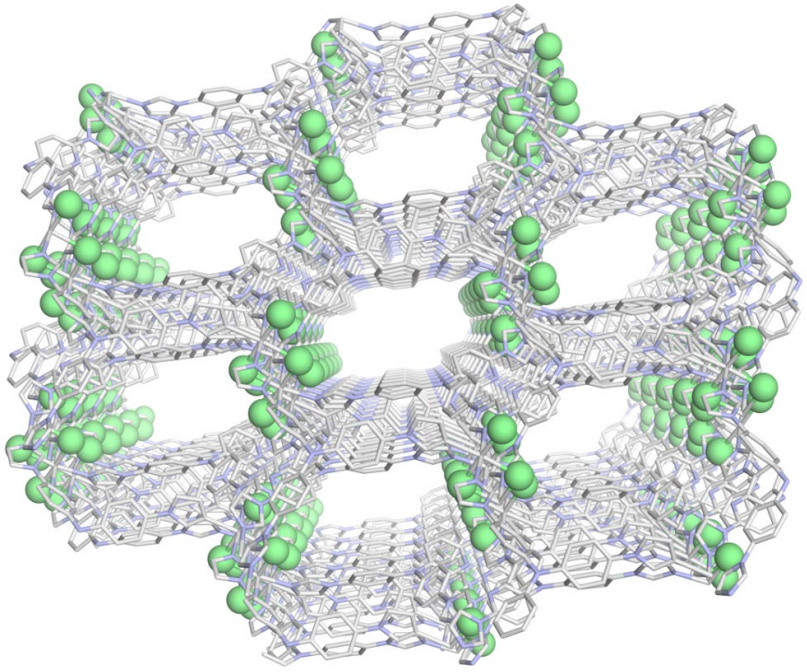
Appendix 3.15: FTIR for the as-synthesized phase (cyan) and AA-exposed (blue).



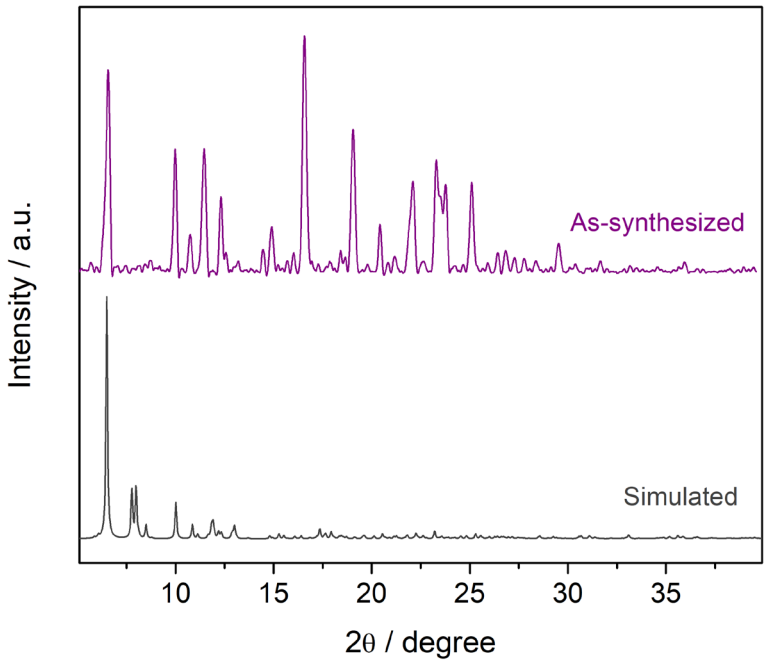
Appendix 3.16: ORTEP diagram for **IPM-304** in thermal ellipsoids.



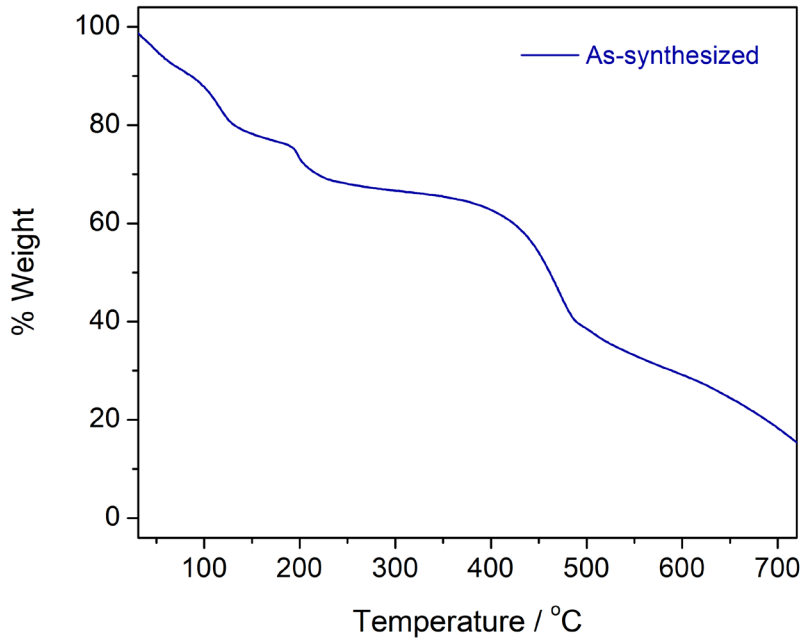
Appendix 3.17: Coordination environment in **IPM-304** (H-atoms omitted for clarity. Colour code: C, grey; N, blue; Cl, green; Mn, orange).



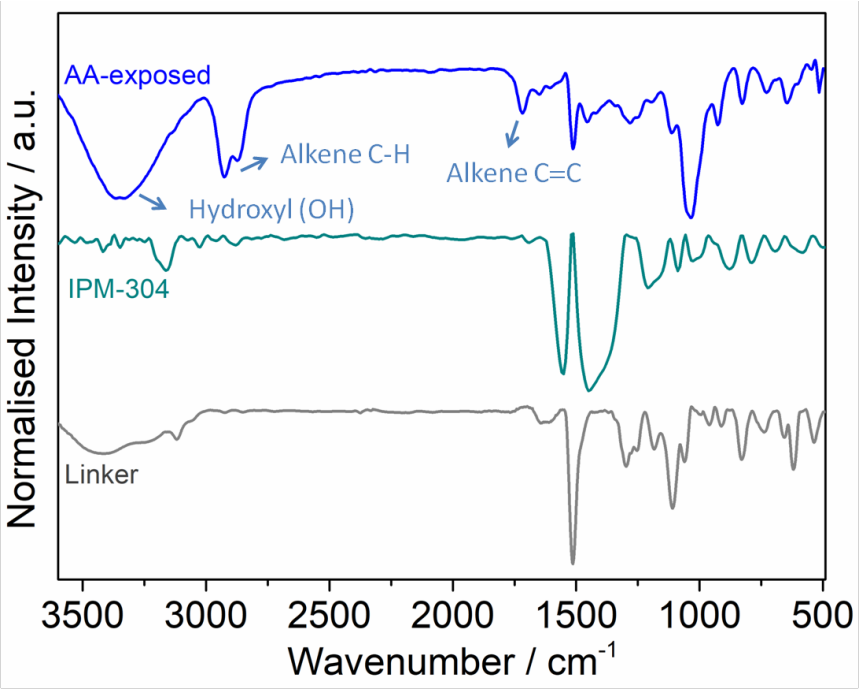
Appendix 3.18: Packing diagram for **IPM-304** showing porous channel (H-atoms have been omitted for clarity. Colour code: C, grey; N, blue; Cl, green; Mn, light purple).



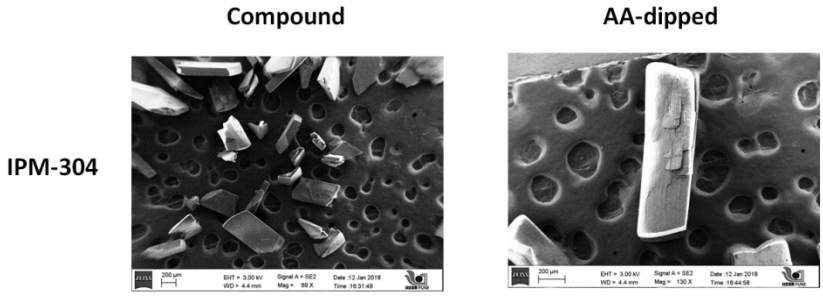
Appendix 3.19: PXRD pattern for **IPM-304**.



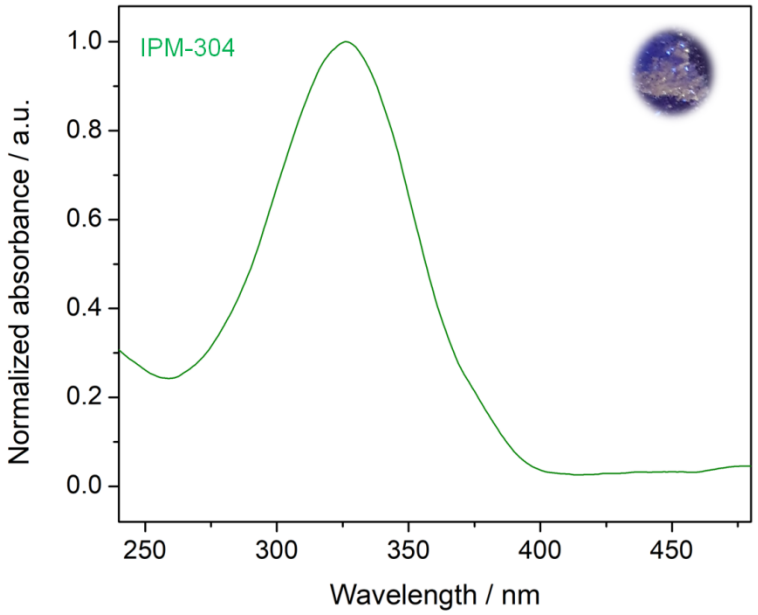
Appendix 3.20: TGA profile for **IPM-304**.



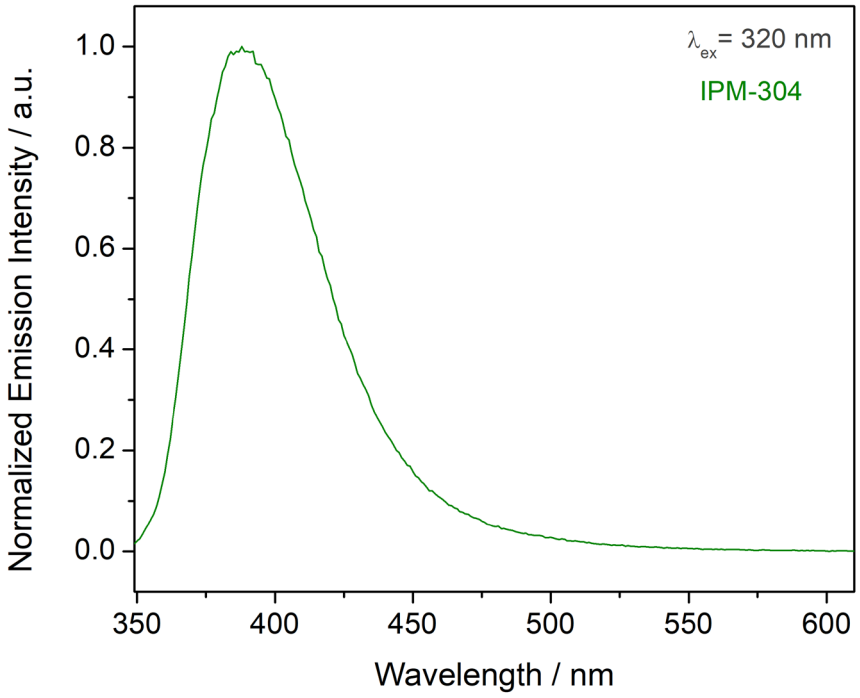
Appendix 3.21: FTIR spectra for ligand and **IPM-304**.



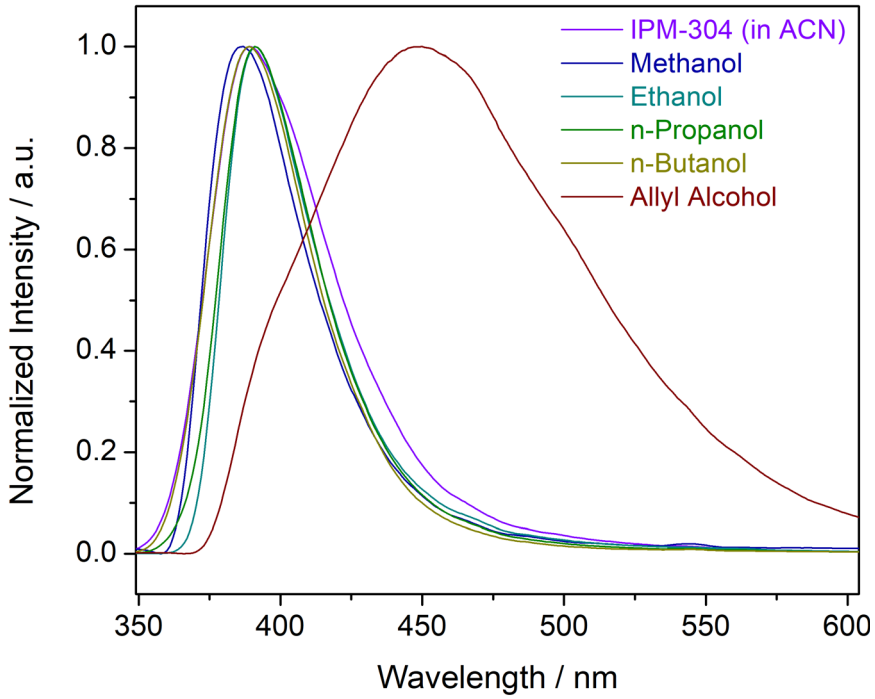
Appendix 3.22: FESEM images **IPM-304**, (left) as-synthesized phase (right) crystals upon dipping in allyl alcohol.



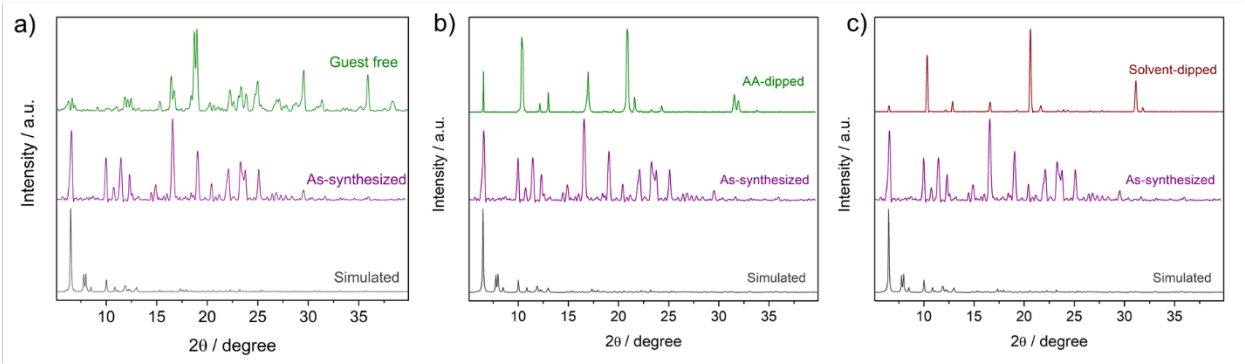
Appendix 3.23: Solid-state UV absorbance for **IPM-304**. (Inset) Image of MOF powder illuminated under UV lamp (365 nm).



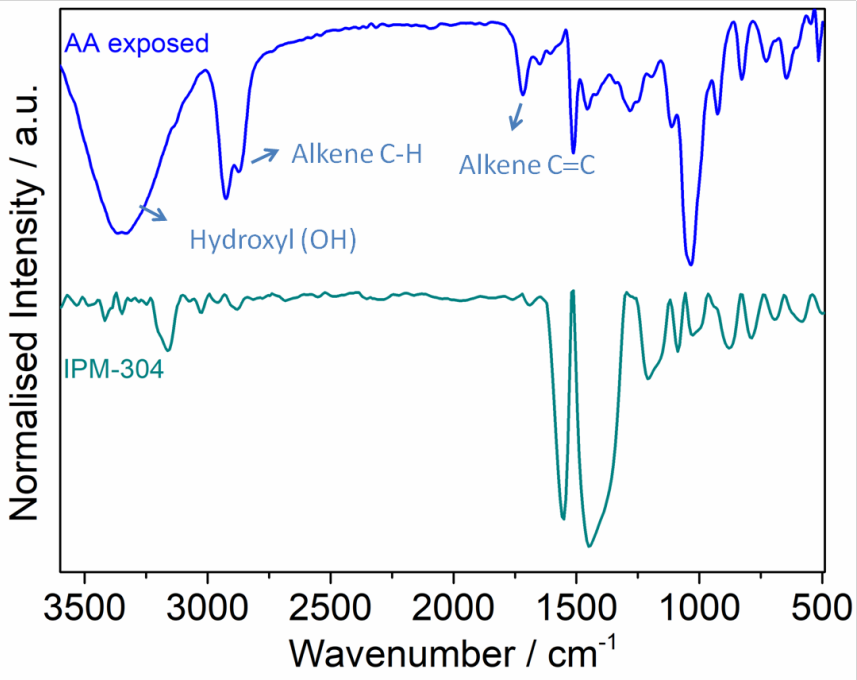
Appendix 3.24: Fluorescence emission profile for **IPM-304** upon dispersing in acetonitrile (λ_{exc} = 320 nm).



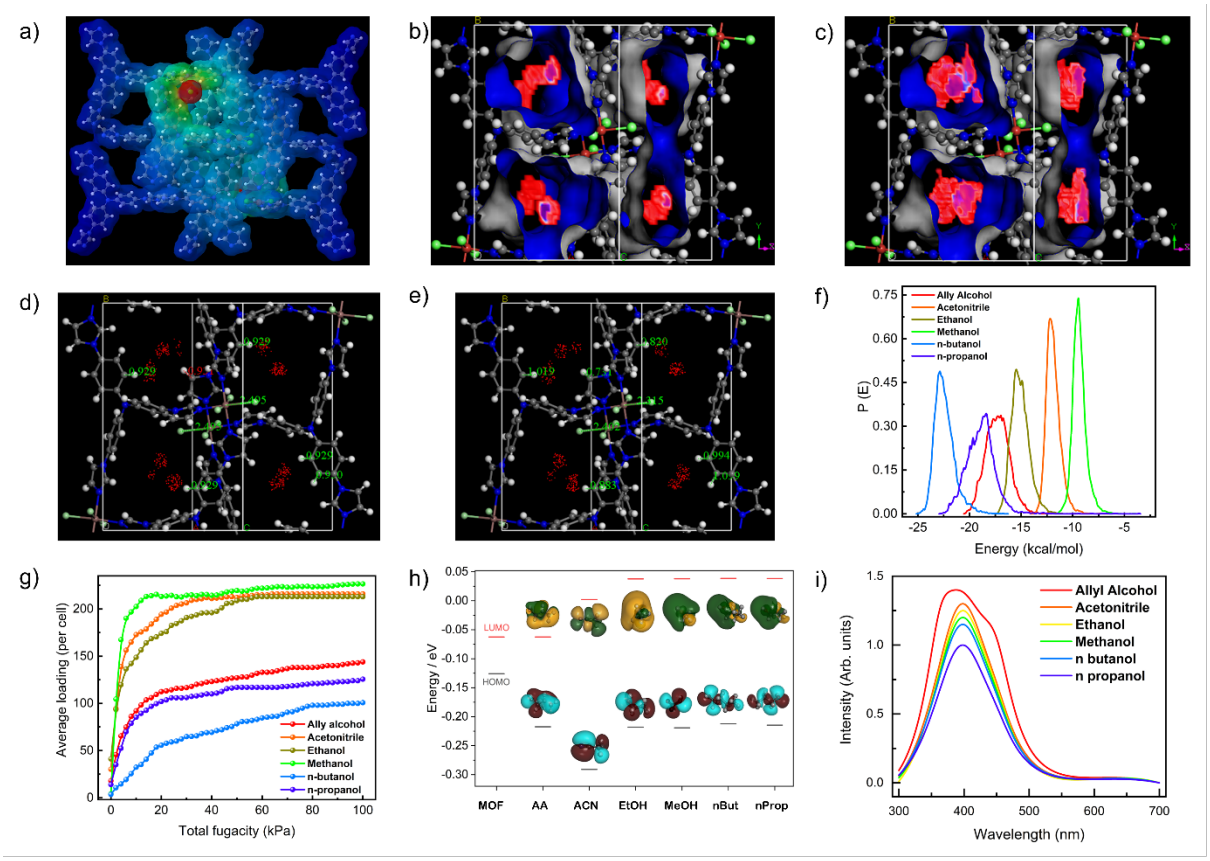
Appendix 3.25: Normalized emission profiles for **IPM-304**, when dipped in different solvents.



Appendix 3.26: PXRD for **IPM-304** of a) guest-free phase, b) AA-dipped phase and c) phase dipped in mixture of all other solvents used in this study.



Appendix 3.27: FTIR spectra for **IPM-304** (Cyan) and AA-exposed phase (blue).



Appendix3.28: a) Electron density map for **IPM-303**. Figure showing Connolly surface in **IPM-303** and presence of void (represented in blue) and guest b) AA molecules (represented in red) and c) Methanol, in pore of single unit cell dimension. Change in bond distances upon interaction of AA with **IPM-303** d) before interaction and e) after interaction. f) Estimated binding energy profiles for the different molecules used in the study. g) Theoretical adsorption profile of solvents by **IPM-303** (obtained on MOF 3 x 3 x 3 supercell) in fugacity range of 0.01 kPa to 100 kPa. h) Comparative plot of HOMO-LUMO energies of MOF (single unit) and different solvents (AA – allyl alcohol, ACN – acetonitrile, EtOH – ethanol, MeOH – methanol, nBut – n-butanol, nProp – n-Propanol) . i) Theoretically predicted emission profiles for the MOF (**IPM-303**)-Guest complexes based on DFT-calculations on single unit.

Appendix Table 3.1. Crystal data and structure refinement for **IPM-303**.

Identification code	IPM-303	
Empirical formula	C_{27} H_{21} Cl_3 In N_7	
Formula weight	664.68	
Temperature	150(2) K	
Wavelength	0.71073 Å	
Crystal system	Monoclinic	
Space group	*P* 2_1/n	
Unit cell dimensions	a = 12.037(3) Å	α= 90°.
	b = 18.466(5) Å	β= 97.790(10)°.
	c = 16.103(4) Å	γ = 90°.
Volume	3546.1(15) $Å^3$	
Z	4	
Density (calculated)	1.245 Mg/m^3	
Absorption coefficient	0.916 mm^{-1}	
F(000)	1328	
Crystal size	0.10 x 0.08 x 0.06 mm^3	
Theta range for data collection	2.266 to 26.418°.	
Index ranges	-15<=h<=15, -23<=k<=22, -20<=l<=20	
Reflections collected	57173	
Independent reflections	7252 [R(int) = 0.1172]	
Completeness to theta = 25.242°	99.9 %	
Refinement method	Full-matrix least-squares on F^2	
Data / restraints / parameters	7252 / 0 / 343	
Goodness-of-fit on F^2	1.261	
Final R indices [I>2sigma(I)]	R_1 = 0.1410, wR_2 = 0.2718	
R indices (all data)	R_1 = 0.1980, wR_2 = 0.3030	
Extinction coefficient	n/a	
Largest diff. peak and hole	1.172 and -1.063 $e.Å^{-3}$	

Appendix Table 3.2. Crystal data and structure refinement for **IPM-304**.

Identification code	IPM-304	
Empirical formula	C_{54} H_{42} Cl_4 Mn_2 N_{14}	
Formula weight	1138.69	
Temperature	150(2) K	
Wavelength	0.71073 Å	
Crystal system	Triclinic	
Space group	*P*-1	
Unit cell dimensions	a = 15.848(9) Å	α= 86.911(17)°.
	b = 16.338(9) Å	β= 66.305(16)°.
	c = 16.560(10) Å	γ = 82.791(17)°.
Volume	3895 (4) $Å^3$	
Z	2	
Density (calculated)	0.971 Mg/m^3	
Absorption coefficient	0.497 mm^{-1}	
F(000)	1164	
Crystal size	0.16 x 0.15 x 0.14 mm^3	
Theta range for data collection	2.305 to 26.027°.	
Index ranges	-18<=h<=18, -19<=k<=19, -20<=l<=19	
Reflections collected	104477	
Independent reflections	13730 [R(int) = 0.1047]	
Absorption correction	Semi-empirical from equivalents	
Max. and min. transmission	0.0258 and 0.0106	
Refinement method	Full-matrix least-squares on F^2	
Data / restraints / parameters	13730 / 0 / 668	
Goodness-of-fit on F^2	1.143	
Final R indices [I>2sigma(I)]	R_1 = 0.1194, wR_2 = 0.3149	
R indices (all data)	R_1 = 0.1597, wR_2 = 0.3372	
Extinction coefficient	n/a	
Largest diff. peak and hole	1.776 and -0.909 $e.Å^{-3}$	

3.6 References

1. U.S. Environmental Protection Agency, EPA/600/X-65/396 (NTIS PB88170857), Washington, D. C., 1985.

2. National Research Council, Acute Exposure Guideline Levels for Selected Airborne Chemicals, The National Academies Press, Washington, DC, 2014, vol. 16, DOI: 10.17226/18707.

3. Allyl alcohol [MAK Value Documentation, 2001], in The MAKCollection for Occupational Health and Safety, Wiley, 2001, vol. 15, pp. 32–40, DOI: 10.1002/3527600418.mb10718e0015.

4. U. Golla, G. Bandi and R. S. Tomar, *Chem. Res. Toxicol.*, 2015, **28**, 1246–1264.

5. S. W. Toennes, K. Schmidt, A. S. Fandino and G. F. Kauert *J. Anal. Toxicology*, 2002, **26**, 55–57.

6. M. Tobiszewski, J. Namiesnik and F. Pena-Pereira, *Green Chem.*, 2018, **19**, 1034–1042.

7. M. Sutter, E. D. Silva, N. Duguet, Y. Raoul, E. Metay and M. Lemaire, *Chem. Rev.*, 2015, **115**, 8609–8651.

8. H. A. Wittcoff, B. G. Reuben and J. S. Plotkin in Industrial Organic Chemicals, John Wiley & Sons, Inc., 2nd edn, 2004, DOI: 10.1002/0471651540.

9. F. Bauer and C. Hulteberg, *Biofuels Bioprod. Biorefin.*, 2013, **7**, 43–51.

10. L. Krahling, J. Krey, G. Jakobson, J. Grolig and L. Miksche in Ullmann's Encyclopedia of Industrial Chemicals, 2000, DOI:10.1002/14356007.a01_425.

11. D. Bose, K. N. Ramachandran and V. K. Gupta, *Chem. Anal.*, 1993, **38**, 645–648.

12. J.-Y. Lee, S.-H. Chung, M.-J. Kim and J.-H. Chung, *Toxicol. Methods*, 1995, **5**, 153–159.

13. J. H. Choi and K. H. Kyung, *J. Food Sci*., 2005, **70**, M305–M309.

14. U.S. Environment Protection Agency, Hazardous Waste Test Methods, SW-846 Test Method 8260D Rev. 4, 2018.

15. M. E. Jun, B. Roy and K. H. Ahn, *Chem. Commun.*, 2011, **47**, 7583–7601.

16. J. Wu, W. Liu, J. Ge, H. Zhang and P. Wang, *Chem. Soc. Rev*., 2011, **40**, 3483–3495.

17. M. D. Allendorf, C. A. Bauer, R. K. Bhakta and R. J. T. Houk, *Chem. Soc. Rev*., 2009, **38**, 1330–1352.

18. Y. Takashima, V. Martinez Martinez, S. Furukawa, M. Kondo, S. Shimomura, H. Uehara, M. Nakahama, K. Sugimoto and S. Kitagawa, *Nat. Commun.*, 2011, **2**, 168.

19. L. E. Kreno, K. Leong, O. K. Farha, M. Allendorf, R. P. Van Duyne and J. T. Hupp, *Chem. Rev.*, 2012, **112**, 1105–1125.

20. Y. Cui, Y. Yue, G. Qian and B. Chen, *Chem. Rev.*, 2012, **112**, 1126–1162.

21. Z. Hu, B. J. Deibert and J. Li, *Chem. Soc. Rev.*, 2014, **43**, 5815–5840.

22. W. P. Lustig, S. Mukherjee, N. D. Rudd, A. V. Desai, J. Li and S. K. Ghosh, *Chem. Soc. Rev.*, 2017, **46**, 3242–3285.

23. A. Karmakar, P. Samanta, A. V. Desai and S. K. Ghosh, *Acc. Chem. Res.*, 2017, **50**, 2457–2469.

24. X. Xie, S. Yu, C. Yang, J. Zhang, Z. Li and G. Li, *New J. Chem.*, 2018, **42**, 20197–20204.

25. K. Vikrant, D. C. W. Tsang, N. Raza, B. S. Giri, D. Kukkar and K.-H. Kim, *ACS Appl. Mater. Interfaces*, 2018, **10**, 8797–8817.

26. K. Guo, L. Zhao, S. Yu, W. Zhou, Z. Li and G. Li, *Inorg. Chem.*, 2018, **57**, 7104–7112.

27. Z.-J. Li, X.-Y. Li, Y.-T. Yan, L. Hou, W.-Y. Zhang and Y.-Y. Wang, *Cryst. Growth Des.*, 2018, **18**, 2031–2039.

28. S. Chand, A. Pal, S. C. Pal and M. C. Das, *Eur. J. Inorg. Chem.*, 2018, **24**, 2785–2792.

29. M. Jiang, P. Li, P. Wu, F. Zhang, X. Tian, C. Deng and J. Wang, *Chem. Commun.*, 2018, **54**, 9131–9134.

30. X. Zhang, Z. Zhan, X. Liang, C. Chen, X. Liu, Y. Jia and M. Hu, *Dalton Trans.*, 2018, **47**, 3272–3282.

31. S. Chand, S. Hota, S. M. Elahi and M. C. Das, *Polyhedron*, 2018, **153**, 115–121.

32. W.-Q. Tong, W.-N. Liu, J.-G. Cheng, P.-F. Zhang, G.-p. Li, L. Hou and Y.-Y. Wang, *Dalton Trans.*, 2018, **47**, 9466–9473.

33. L. Xia, J. Ni, P. Wu, J. Ma, L. Bao, Y. Shi and J. Wang, *Dalton Trans.*, 2018, **47**, 16551–16557.

34. J. Hao, X. Xu, H. Fei, L. Li and B. Yan, *Adv. Mater.*, 2018, **30**, 1705634.

35. Z. Zhan, X. Liang, X. Zhang, Y. Jia and M. Hu, *Dalton Trans.*, 2019, **48**, 1786–1794.

36. S. Kitagawa, R. Kitaura and S.-i. Noro, *Angew. Chem., Int. Ed.*, 2004, **43**, 2334–2375.

37. S. Kitagawa and R. Matsuda, *Coord. Chem. Rev.*, 2007, **251**, 2490–2509.

38. S. Horike, S. Shimomura and S. Kitagawa, *Nat. Chem.*, 2009, **1**, 695–704.

39. H.-C. Zhou, J. R. Long and O. M. Yaghi, *Chem. Rev.*, 2012, **112**, 673–674.

40. S. R. Batten, N. R. Champness, X.-M. Chen, J. GarciaMartinez, S. Kitagawa, L. Ohstrom, M. O'Keeffe, M. P. Suh and J. Reedijk, *Pure Appl. Chem.*, 2013, **85**, 1715–1724.

41. H. Furukawa, K. E. Cordova, M. O'Keeffe and O. M. Yaghi, *Science*, 2013, **341**, 1230444.

42. R. Ohtani and S. Kitagawa in Handbook of Solid State Chemistry, Wiley-VCH Verlag GmbH & Co. 2017, DOI:10.1002/9783527691036.hsscvol4015.

43. S. Yuan, L. Feng, K. Wang, J. Pang, M. Bosch, C. Lollar, Y. Sun, J. Qin, X. Yang, P. Zhang, Q. Wang, L. Zou, Y. Zhang, L. Zhang, Y. Fang, J. Li and H.-C. Zhou, *Adv. Mater.*, 2018, **30**, 1704303.

44. J. B. DeCoste and G. W. Peterson, *Chem. Rev.*, 2014, **114**, 5695–5727.

45. H. Y. Gao, L. Zhang, C. S. Yan, L. N. Meng, J. Q. Li, P. P. Meng, L. L. Gong and F. Luo, *CrystEngComm*, 2016, **18**, 5429–5433.

46. L. L. Gong, X. F. Feng, F. Luo, X. F. Yi and A. M. Zheng, *Green Chem.*, 2016, **18**, 2047–2055.

47. Y. Chen, B. Wang, X. Wang, L.-H. Xie, J. Li, Y. Xie and J.-R. Li, *ACS Appl. Mater. Interfaces*, 2017, **9**, 27027–27035.

48. N. S. Bobbitt, M. L. Mendonca, A. J. Howarth, T. Islamoglu, J. T. Hupp, O. K. Farha and R. Q. Snurr, *Chem. Soc. Rev.*, 2017, **46**, 3357–3385.

49. L.-H. Xie, X.-M. Liu, T. He and J.-R. Li, *Chem*, 2018, **4**, 1911–1927.

50. H. Wang, W. P. Lustig and J. Li, *Chem. Soc. Rev.*, 2018, **47**, 4729–4756.

51. T. He, Y.-Z. Zhang, X.-J. Kong, J. Yu, X.-L. Lv, Y. Wu, Z.-J.Guo and J.-R. Li, *ACS Appl. Mater. Interfaces*, 2018, **10**, 16650–16659.

52. S. K. Mostakim, S. Banesh, V. Trivedi and S. Biswas, *Inorg. Chem.*, 2018, **57**, 14574–14581.

53. D. Tian, X.-J. Liu, R. Feng, J.-L. Xu, J. Xu, R.-Y. Chen, L. Huang and X.-H. Bu, *ACS Appl. Mater. Interfaces*, 2018, **10**, 5618–5625.

54. P. Samanta, A. V. Desai, S. Let and S. K. Ghosh, *ACS Sustainable Chem. Eng.*, 2019, **7**, 7456–7478.

55. J. Zhang, L. Chen, X. Dai, L. Zhu, C. Xiao, L. Xu, Z. Zhang, E. V. Alekseev, Y. Wang, C. Zhang, H. Zhang, Y. Wang, J. Diwu, Z. Chai and S. Wang, *Chem*, 2019, **5**, 977–994.

56. D. Sheng, L. Zhu, X. Dai, C. Xu, P. Li, C. I. Pearce, C. Xiao, J. Chen, R. Zhou, T. Duan, O. K. Farha, Z. Chai and S. Wang, *Angew. Chem., Int. Ed.*, 2019, **58**, 4968–4972.

57. A. Mallick, A. M. El-Zohry, O. Shekhah, J. Yin, J. Jia, H. Aggarwal, A.-H. Emwas, O. F. Mohammed and M. Eddaoudi, *J. Am. Chem. Soc.*, 2019, **141**, 7245–7249.

58. C. Xiao, A. Khayambashi and S. Wang, *Chem. Mater.*, 2019, **31**, 3863–3877.

59. B. Wang, P. Wang, L.-H. Xie, R.-B. Lin, J. Lv, J.-R. Li and B. Chen, *Nat. Commun*., 2019, **10**, 3861.

60. J. Lv, B. Wang, Y. Xie, P. Wang, L. Shu, X. Su and J.-R. Li, *Environ. Sci.: Nano*, 2019, **6**, 2759–2766.

61. B. Wang, J.-H. Liu, J. Yu, J. Lv, C. Dong and J.-R. Li, *J. Hazard. Mater.*, 2020, **382**, 121018.

62. G. Aullon, D. Bellamy, L. Brammer, E. A. Bruton and A. G. Orpen, *Chem. Commun.*, 1998, 653–654.

63. Y. Inokuma, T. Arai and M. Fujita, *Nat. Chem.*, 2010, **2**, 780–783.

64. S.-S. Liu, S. Yuan, T.-P. Hu and D. Sun, *Z. Anorg. Allg. Chem.*, 2014, **640**, 2030–2034.

65. J. E. Clements, J. R. Price, S. M. Neville and C. J. Kepert, *Angew. Chem., Int. Ed.*, 2014, **53**, 10164–10168.

66. H.-R. Fu, Y. Kang and J. Zhang, *Inorg. Chem.*, 2014, **53**,4209–4214.

67. S. K. Elsaidi, M. H. Mohamed, H. T. Schaef, A. Kumar, M. Lusi, T. Pham, K. A. Forrest, B. Space, W. Xu, G. J. Halder, J. Liu, M. J. Zaworotko and P. K. Thallapally, *Chem. Commun.*, 2015, **51**, 15530–15533.

68. A. Karmakar, A. V. Desai and S. K. Ghosh, *Coord. Chem. Rev.*, 2016, **307**, 313–341.

69. B. Manna, A. V. Desai and S. K. Ghosh, *Dalton Trans.*, 2016, **45**, 4060–4072.

70. L.-X. Hu, M. Gao, T. Wen, Y. Kang and S. Chen, *Inorg. Chem.*, 2017, **56**, 6507–6511.

71. G. Zhang, G. Wei, Z. Liu, S. R. J. Oliver and H. Fei, *Chem. Mater.*, 2016, **28**, 6276–6281.

72. L. Zhu, D. Sheng, C. Xu, X. Dai, M. A. Silver, J. Li, P. Li, Y. Wang, Y. Wang, L. Chen, C. Xiao, J. Chen, R. Zhou, C. Zhang, O. K. Farha, Z. Chai, T. E. Albrecht-Schmitt and S. Wang, *J. Am. Chem. Soc.*, 2017, **139**, 14873–14876.

73. L. Yang, X. Cui, Y. Zhang, Q. Yang and H. Xing, *J. Mater. Chem. A*, 2018, **6**, 24452–24458.

74. E. Loukopoulos and G. E. Kostakis, *Coord. Chem. Rev.*, 2019, **395**, 193–229.

75. A. V. Desai, S. Sharma, S. Let and S. K. Ghosh, *Coord. Chem. Rev.*, 2019, **395**, 146–192.

76. A. V. Desai, B. Manna, A. Karmakar, A. Sahu and S. K. Ghosh, *Angew. Chem., Int. Ed*., 2016, **55**, 7811–7815.

77. SAINT Plus, Bruker AXS Inc., Madison, WI, 2004.

78. L. Krause, R. Herbst-Irmer, G. M. Sheldrick and D. Stalke, *J. Appl. Crystallogr.*, 2015, **48**, 3–10.

79. G. M. Sheldrick, SHELXTL, Reference Manual, version 5.1, Bruker AXS Inc., Madison, WI, 1997.

80. G. M. Sheldrick, *Acta Crystallogr., Sect. A: Found. Crystallogr.*, 2008, **64**, 112–122.

81. G. M. Sheldrick, *Acta Crystallogr., Sect. C: Struct. Chem.*, 2015, **71**, 3–8.

82. L. Farrugia, WinGX, University of Glasgow, Glasgow, Scotland.

83. A. L. Spek, *Acta Crystallogr., Sect. C: Struct. Chem.*, 2015, **71**, 9–18.

84. BIOVIA Dassault Systèmes, Materials Studio, San Diego, Dassault Systèmes, 2017.

85. J. P. Perdew, K. Burke and M. Ernzerho, *Phys. Rev. Lett.*, 1996, **77**, 3865–3868.

86. H. Peng and J. P. Perdew, *Phys. Rev. B*, 2017, **95**, 081105.

87. S. J. Clark, M. D. Segall, C. J. Pickard, P. J. Hasnip, M. J. Probert, K. Refson and M. C. Payne, *Z. Kristallogr.*, 2005, **220**, 567–570.

88. S. Tsuzuki, K. Honda, T. Uchimaru, M. Mikami and A. Fujii, *J. Phys. Chem. A*, 2006, **110**, 10163–10168.

89. K. Shibasaki, A. Fujii, N. Mikami and S. Tsuzuki, *J. Phys. Chem. A*, 2007, **111**, 753–758.

90. J.-F. Li and R.-Q. Zhang, *Sci. Rep.*, 2016, **6**, 22304.

Chapter 4

A Water-Stable Ionic MOF for the Selective Capture of Toxic oxoanions of Se(VI) and As(V) and Crystallographic Insight into the Ion-Exchange Mechanism

4.1 Introduction

Strategic tackling of radionuclide threat and freshwater crisis is among priority concerns for the global community. Among various pollutants, selenium has been listed as a toxic and priority pollutant by the United States Environmental Protection Agency (US EPA).[1] Although an essential element for living species, it becomes severely toxic above a threshold concentration of > 400 μg per day. The stringent guidelines by the World Health Organization (WHO) emphasizes the issue by restricting the concentration limit of selenium in drinking water as 50ppb (parts per billion).[2,3] Encompassing high mobility and high solubility in water, the oxoanionic species of selenium viz. SeO_4^{2-}, SeO_3^{2-} $HSeO_3^-$ etc. pose a challenge for containment.[4] The widespread sources of selenium discharge include industrial production, mining, coal and nuclear power plants. In particular, the discharge from nuclear power plant contains a radioactive isotope of selenium (^{79}Se) with an extensive half-life of 3.77×10^5 years, thus demanding immediate containment to avoid lethal problems such as gene mutation, respiratory and neurological defects etc.[5] Another noxious pollutant i.e Arsenic is a severe water contaminant and a "class A" human carcinogen. Arsenic poisoning leads to harmful diseases such as cancer, skin diseases, neurological disorders etc.[6] Global emphasis on arsenic poisoning can be understood from the strict regulation by WHO stating < 10 ppb of arsenic as the safe permissible limit in drinking water.[3] The release of arsenic into the environment includes both natural as well as artificial sources such as mining, industrial waste etc.[7] Generally, in water medium arsenic is converted to its oxoanionic form under oxidative conditions, and in the pH range of 6.7 to 13.4, mono hydrogen arsenate ($HAsO_4^{2-}$) is the dominant form of As(V).[8] Pertaining to this oxo-anionic chemistry, multiple pathways for sequestration of these oxo-anions have been explored via ion-exchange, adsorption, etc. Diverse materials have been trialled aiming toward the capture of oxo-anions of selenium and arsenic including metal-oxides, magnetite nanoparticles, activated carbon, zeolites, etc.[9] but lower surface area, weaker binding, leaching, poor selectivity or production of secondary pollutant species are the limiting factors for efficient and selective capture in the aforementioned materials. Also, conventional approaches are ineffective for sequestration of certain oxoanions of such toxic elements. For instance, metal-oxides have unfavourable complexation behaviour towards SeO_4^{2-} necessitating exploration of alternate materials with robust capture mechanism.[10] Thus, the topical research efforts are devoted for the realization of scalable host materials to entrap oxo-anion pollutants which exhibit high capture performance, fast kinetics, selectivity and facile regeneration.

Metal-organic frameworks (MOFs) have evolved as a class of multifunctional materials posing concurrent precision and flexibility to engineer desired systems exhibiting plethora of applications including environmental remediation.[11] Cationic MOFs, a subclass of ionic-MOFs (iMOFs) have been realised as exceptional host systems for capture of hazardous toxic oxo-anions.[12] Cationic MOFs render various levels of tunability in designing host systems with high selectivity via mimicking molecular geometry, hydrophobic character of toxic oxo-anions etc.[13] Additionally, the inherent ionic nature of cationic MOFs presents an elegant route to entrap toxic oxo-anionic species via ion-exchange pathway to tackle leaching issue.[14] Though having a robust capture mechanism, cationic

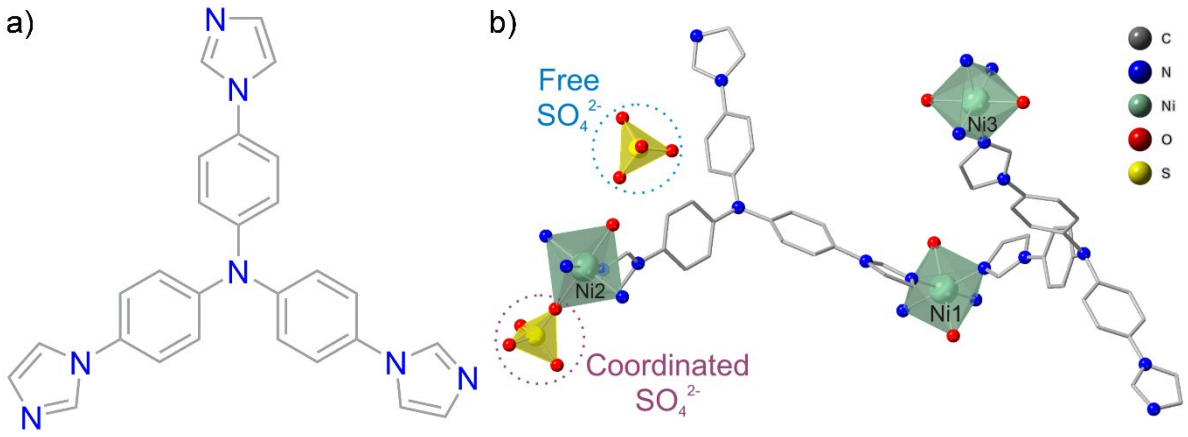
MOFs have not been explored hitherto for sequestrating toxic oxoanions of selenium and arsenic, however few neutral MOFs have been investigated for the same.[10b,11f,11i,11k,11l,11o] In the present study, cationic MOFs were explored as toward sequestration of oxo-anions of selenium and arsenic via ion-exchange approach, for the first time. An important aspect of ion-exchange phenomenon viz. shape memory effect of template anion has been utilized to provide selectivity, which can be realised efficiently in cationic MOFs wherein facile tuning of template is feasible via synthetic pathway.[13k] Additionally, with the trapped oxo-anions being an integral part of framework as charge balancing ions, potential leaching is ruled out. Cationic MOFs with the aforementioned attributes present an effective alternative in capturing oxo-anions in a desired selective manner. The preliminary criteria of water stability of cationic MOFs have hindered exploration of different applications in an aqueous medium.[15] Based on this background, consideration of aforementioned criteria was crucial while selecting a cationic MOFs targeting capture of oxo-anions of selenium (SeO_4^{2-}) and arsenic ($HAsO_4^{2-}$) from aqueous medium to extend the scope of porous crystalline solids. For an efficient ion-exchanger, the similarity of charge, shape and size of the anion in the host framework with the target anions viz. SeO_4^{2-} and $HAsO_4^{2-}$ would seemingly favour the process. Thus, our interest narrowed on cationic MOFs having sulphate (SO_4^{2-}) as the exchangeable anion, as it is divalent, the geometry around the central atom is tetrahedral and has similar shape and size as of target anions. Further, Ni(II) based cationic MOFs were rationally selected as Ni(II) based MOFs offer enhanced stability in water medium.[11g,11n,13h,13j] Combining all the desired features, a water-stable cationic MOF which meets all the above-mentioned requirements viz. $\{[Ni_2(L)_3(SO_4)(H_2O)_3]\cdot(SO_4)\cdot xG$ (hereafter referred as iMOF-1C), where L= tris(4-(1H-imidazol-1-yl)phenyl)amine, G = guest solvent molecules and C= Cationic , previously reported by our group was selected (Scheme 4.1a).[13g] Compound iMOF-1C is a 3D MOF having Ni(II) metal nodes extended via a tridentate neutral linker having imidazole as terminal donor moiety. The asymmetric unit constitutes two sulphate anions; one of which is coordinated to the Ni(II) node while the other remains free in the void space (Scheme 4.1b). The superior feature of the framework includes pre-aligned and readily exchangeable uncoordinated SO_4^{2-} anions within the porous channels, having weak non-covalent interactions with framework backbone (Figure 4.1a). Herein, capture of toxic oxoanions of Se(VI) and As(V) via utilization of cationic MOF by judicious selection of iMOF-1C as a selective sorbent posing high capacity and fast kinetics along with a rare crystallographic evidence for the ion-exchange process.

4.2 Experimental

4.2.1 Materials: All solvents and reagents were commercially available and used without further purification. Ligand (L) and bulk scale iMOF-1C was synthesized via a slightly modified protocol than used in previous literature.[13g]

4.2.2 Bulk scale synthesis: Bulk scale synthesis was performed by mixing 0.886 g of Ligand (L) and 0.560 g of $NiSO_4.xH_2O$ in a solvent combination of DMF:Water (1:1) (total volume = 300 mL) in a teflon capped jar. The

mixture was heated at 90 °C for 48 h and cooled to room temperature. Compound was filtered and bulk phase characterization were performed. The activated phase was obtained as per the previous report.[13g] Yield ~ 996 mg, % yield ~58.9 %.w.r.t linker.



Scheme 4.1: (a) Chemical diagram of ligand (L). (b) Schematic showing coordination environment of linker L and metal center in iMOF-1C.

4.2.3 Anion Exchange Studies: Single crystals of iMOF-1C were dipped in aqueous solutions (0.1 M/4 mL) of Na_2SeO_4 and $Na_2HAsO_4.7H_2O$ separately for 72 h at room temperature to yield the respective anion-exchanged products viz. iMOF-1C-SeO_4^{2-} and iMOF-1C-$HAsO_4^{2-}$. For structural analysis, suitable single crystals were separated.

For the bulk phase studies, the similar protocol was repeated by dipping 25 mg of iMOF-1C in aqueous solutions of respective anions (100 ppm, 5 mL). After anion exchange the compounds were washed with deionized water several times and air-dried. The air-dried compounds were characterized by FT-IR spectroscopy, PXRD FESEM-EDX, XPS. For CHN analysis, 10 mg compound was dipped in 1500 ppm solution of selenium for 72 h and the compound was filtered and air dried.

Anal Calcd for iMOF-1C: C/S, 15.19. Found: C/S, 15.30.

Anal Calcd. for iMOF-1C-SeO_4^{2-} exchange (1 anion): C/S, 30.36. Found: C/S, 27.11.

4.2.4 Anion Uptake studies:

ICP-AAS/MS analysis was performed during the anion-exchange process to understand the anion-exchange kinetics and capacities. All experiments were conducted at room temperature (25 °C) and in milliQ water.

Kinetic studies

For kinetics, iMOF-1C (2 mg) was dipped in 2 mL of 20 ppm/100 ppm solution of Na_2SeO_4 and $Na_2HAsO_4.7H_2O$. The solutions were kept for desired time and aliquots were separated and further diluted with 2-3% HNO_3. These samples were analyzed using ICP-AAS/ICP-MS and concentration of selenium and arsenic were monitored. Comparison with concentration of known solution was used to calculate uptake at different intervals. The data were fit to pseudo-Second order kinetic profile using the following equation:

$q(t)= (K_2q_e^2t)/(1+K_2q_et)$ where t is time in hours, q_e is the adsorption amount at time (t) and equilibration respectively and K_2 is the pseudo second order rate constant.[13e]

Maximum Uptake studies

For saturation uptake capacity, 2 mg of iMOF-1C was dipped in 2 mL of 100-1500 ppm solution of Se(VI) and As(V) for equilibration. Aliquots were removed after 72 h and these samples were analyzed using ICP-AAS and concentration of Se and As were monitored. Comparison with concentration of known solution was used to calculate uptake at different concentration and isotherms. The data acquired was used for calculating sorption isotherms.

Langmuir Analysis

Adsorption capacity as a function of time at different concentrations (q) is given in Figure S8, S17. The calculation was performed according to the following equation:

$q= [(C_i-C_f)\times V]/m$

wherein q= Adsorption capacity in mg/g of iMOF-1C, C_i = initial concentration, C_f = final concentration, V = volume of solution exposed to iMOF-1C, and m = mass of iMOF-1C in grams. These were further analyzed as per reported protocol.[10b]

4.2.5 Anion Selectivity Studies: Single crystals of iMOF-1C were dipped in an aqueous mixture of (1 mM/2 mL) of Na_2SeO_4 and (1 mM/2 mL) $NaNO_3$, NaCl for 2 days at room temperature to yield the anion-exchanged products. After anion exchange the compounds were washed with deionized water several times and air-dried. The compounds were characterized by FT-IR spectroscopy and PXRD. The same procedure was followed for SeO_4^{2-}/Cl^-. Similarly anion selectivity experiments were performed for $HAsO_4^{2-}$ exchange as well. For ICP analysis, 2 mg iMOF-1C was dipped in 1:1 (200 ppm) (2 mL) solution of SeO_4^{2-}/Cl^-, SeO_4^{2-}/NO_3^- each for 24 h and then centrifuged. The solutions were analyzed using ICP technique. Similar experiments were performed for $HAsO_4^{2-}$.

4.2.6 Reversibility Studies: Crystals of iMOF-1C-SeO_4^{2-} (15 mg) and iMOF-1C-$HAsO_4^{2-}$ (15 mg) were dipped in separate aqueous solutions of Na_2SO_4 (1 mM/2 mL) for 2 days at room temperature. Upon completion, the

compound was collected by filtration and washed with water several times. FT-IR spectroscopy and PXRD were used for characterization. The retrieved compounds were dipped again in aqueous solutions of Na_2SeO_4 and $Na_2HAsO_4.7H_2O$ separately. For checking the adsorption features for upto 3 cycles, the same experiment was repeated.

For ICP analysis, 2 mg of iMOF-1C was soaked in 100ppm solution of SeO_4^{2-}/ $HAsO_4^{2-}$ for 12 h and then centrifuged. The solution was analyzed with ICP while the residue was exposed to 1000 ppm SO_4^{2-} for 12 h and centrifuged. The experiment was repeated again for three consecutive cycles. To check the stability of compound during recycling experiment, the supernatant during the uptake experiment was filtered via syringe filter (200 μm) and the solution was analyzed for Ni(II) content by ICP-MS. (Table S4)

4.2.7 Physical Measurements: Powder X-ray diffraction patterns were recorded on Bruker D8 Advanced X-Ray diffractometer using Cu Kα radiation (λ= 1.5406 Å) in 5° to 40° 2θ range with a scan speed of 1.2 $^o min^{-1}$. The IR Spectra were acquired by using NICOLET 6700 FT-IR spectrophotometer using KBr pellet in 400-4000 cm^{-1} range. UV spectra were recorded on Shimadzu UV 2600 Spectrophotometer having stirring attachment. The SEM images & EDX data were obtained using FEI Quanta 3D dual beam ESEM. Thermogravimetric analysis profiles were recorded on Perkin-Elmer STA6000, TGA analyser under N_2 atmosphere with heating rate of 10 ^{o}C/min. ICP-AAS analysis were performed on Thermo Scientfific iCE 3000 Series.ICP-MS was performed on Quadrupole inductively coupled plasma mass spectrometry(Q-ICP MS; Thermo Scientific iCAP Q) instrument. Multielement standards were purchased from inorganic ventures. XPS studies was performed using K-Alpha+model (Thermo Fischer Scientific, UK) with Al Kα source.

4.2.8 X-ray Structural Studies: Single-crystal X-ray data of compound iMOF-1C-SeO_4 and iMOF-1C-$HAsO_4$ was collected at 100 K on a Bruker D8 Venture Duo X-ray diffractometer equipped with Microfocus X-ray source (operated at 50 W; 50 kV/1 mA), graded multilayer optics for monochromatic Mo Kα radiation (λ = 0.71073 Å) focused X-ray beam and Photon 100 CMOS chip based detector system. Crystal was mounted on nylon CryoLoops (Hampton Research) with Paraton-N (Hampton Research). The data integration and reduction were processed with SAINT software. [16] A multi-scan absorption correction was applied to the collected reflections. [17] The structure was solved by the direct method using SHELXTL[18,19] and was refined on F^2 by full-matrix least-squares technique using the SHELXL-2014/7[20] program package within the WINGX[21] programme. All non-hydrogen atoms were refined anisotropically. All hydrogen atoms were located in successive difference Fourier maps and they were treated as riding atoms using SHELXL default parameters. The structures were examined using the Adsym subroutine of PLATON to assure that no additional symmetry could be applied to the models. The SQUEEZE option[22] was used to eliminate the contribution of disordered guest molecules. In case of iMOF-1C -SeO4, the free anions (SeO_4^{2-}) were highly disordered due to sub-optimal data quality.

CCDC 1959440 (iMOF-1C-SeO_4), CCDC 1959430 (iMOF-1C-$HAsO_4$) contains the supplementary crystallographic data for this paper. These data can be obtained free of charge from The Cambridge Crystallographic Data Centre via www.ccdc.cam.ac.uk/data_request/cif.

4.3 Results and discussion

The bulk scale synthesis (gram scale) of iMOF-1C was realised via slight modification to reported procedure.[13g] This synthetic advancement is relevant towards targeting large scale applications; especially owing to the lack of such synthetic approaches in the domain of cationic MOFs. The bulk phase crystallinity and purity was corroborated via powder X-ray diffraction (PXRD) patterns (Appendix 4.1). Initially, to test the stability and crystallinity of the compound, crystals of iMOF-1C were dipped in an aqueous solution of selenate (SeO_4^{2-}) and mono hydrogen arsenate ($HAsO_4^{2-}$). Analysis under optical microscope revealed no changes to the shape and texture of crystals (Appendix 4.2). Further, energy dispersive X-ray (EDX) mapping confirmed the presence of selenium and retention of morphology (Figure 4.1b). Enthused from these observations, detailed studies were performed for selenate anion wherein microcrystalline powder of iMOF-1C were soaked in 100 ppm solution of selenate anion and characterized the obtained compound using various techniques.

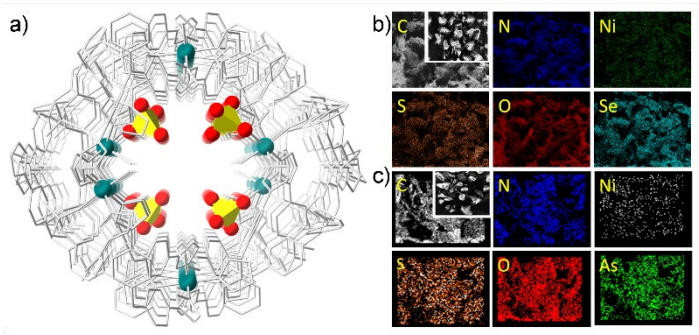


Figure 4.1: a) Packing diagram of iMOF-1C showing presence of exchangeable SO_4^{2-} anions (shown in tetrahedral). EDX spectra of iMOF-1C exposed to an aqueous solution of b) SeO_4^{2-} and c) $HAsO_4^{2-}$.

PXRD patterns revealed a similar profile as simulated pattern for iMOF-1C confirming retention of framework integrity (Appendix 4.1b). Field emission scanning electron microscopy (FESEM) analysis confirmed retention of block shaped morphology (Appendix 4.4a). EDX mapping analysis showed homogenous distribution of both selenium (Se) and sulfur (S) content (Figure 4.1b, Appendix 4.4b-4.4c). Fourier transform infrared spectroscopy (FT-IR) showed peaks corresponding to the SeO_4^{2-} anion (Appendix 4.6). Elemental analysis confirmed the ion-exchange mechanism as the S- content decreased post ion-exchange corresponding to exchange of ~1 sulphate anion (SI). These observations suggest primarily the exchange of sulphate anions from the porous voids. X-ray photoelectron spectroscopy (XPS) also validated this observation peaks for both sulphate and selenate at ~ 167.4 eV and ~ 59 eV were observed respectively (Appendix 4.3, 4.5). Further, iMOF-1C was soaked in 100 ppm

aqueous solution of selenate (SeO_4^{2-}) and the supernatant was analysed by performing inductively coupled plasma (ICP) measurements at various time intervals. The data analysis revealed significant uptake within 60 mins of contact time of iMOF-1C to the selenate stock solution (Figure 4.2b, Appendix 4.7, 4.10). The data indicates that the kinetics is rapid for SeO_4^{2-} uptake and a pseudo-second order kinetic model fits well to the experimental data.

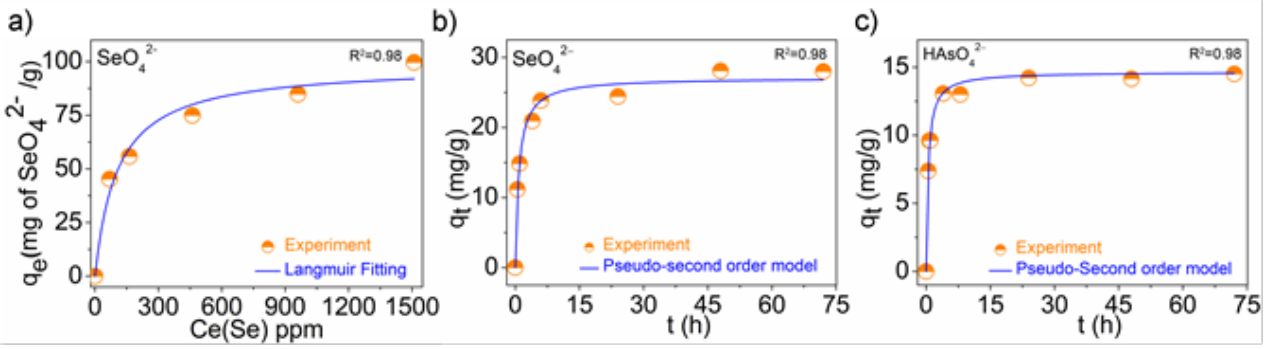


Figure 4.2: a) Concentration dependent isotherms representing SeO_4^{2-} uptake by iMOF-1C. Pseudo-second order kinetics for selenate sorption by iMOF-1C for b) SeO_4^{2-} and c) $HAsO_4^{2-}$

Further, to find out the maximum adsorption capacity of iMOF-1C, the compound was exposed to varied concentration of SeO_4^{2-} solution ranging from 100 ppm to 1500 ppm (Figure 4.2a, Appendix 4.8). From this data, the adsorption capacity was estimated to be 100 mg of SeO_4^{2-}/g of iMOF-1C, in accordance to the Langmuir adsorption model which matched well to the experimental value. (Appendix 4.8). It is noteworthy to mention that this uptake value is among the highest in the domain of MOFs for selenate capture (Appendix Table 4.1). Additionally, for any sorbent, selectivity is a crucial aspect for practical implementation, thus selectivity experiments was performed by exposing MOF to binary mixture of solution of anions viz. chloride (Cl^-), nitrate (NO_3^-), bicarbonate (HCO_3^-), sulfate (SO_4^{2-}), carbonate (CO_3^{2-}) and selenate (SeO_4^{2-}), as they are commonly encountered in waste water streams and groundwater.[9e, 23] The solid powder retrieved was investigated using FT-IR (NO_3^-/SeO_4^{2-}),(CO_3^{2-}/SeO_4^{2-}) and EDX analysis for (Cl^-/SeO_4^{2-}). FTIR analysis exhibited no peaks for the competing NO_3^- and CO_3^{2-} anion (Appendix 4.12) while EDX mapping profile also revealed homogenous distribution of selenium through the samples with the absence of peak for chloride (Appendix 4.23).The supernatant solution was analysed by ICP measurements and similar uptake performance even in presence of competing ions was

observed therefore rendering selectivity which is a crucial for assessing sorbent's performance under for practical scenario (Appendix 4.11). This highlights the efficacy of ion-exchange approach for trapping oxo-anions of weakly adsorbing elements. As a step towards seeking practical applicability, compound iMOF-1C was exposed to low concentration (20 ppm) and uptake behaviour was investigated. Fast kinetics with significant uptake was observed within an hour of exposure (Appendix 4.9). These observations indicated that iMOF-1C can serve affirmatively towards selenium oxoanion mitigation, and demonstrated the judicious choice of the MOF for affording selective trapping. Apart from selectivity, recyclability of a material is quite important for the practical consideration of a sorbent. Compound iMOF-1C was soaked alternately in 100 ppm solution of selenate salt for uptake and in 1000 ppm solution of sulphate salt for release. The supernatant was analyzed via ICP measurements for quantifying the uptake amounts while the sorbent material was characterized via PXRD and EDX mapping. ICP experiments revealed similar uptake amount for three consecutive uptake and release cycles (Appendix 4.22). EDX mapping confirmed the absence of selenium in the regenerated phase (Appendix 4.30). PXRD patterns also confirmed that the framework retained during multiple cycle of adsorption-desorption of anion (Appendix 4.28). Thus, this compound can be utilized towards effective mitigation of hazardous and/or radioactive isotopes of selenium with long half life which have similar chemical and physical properties.

Similarly, capture performance was investigated for the extremely toxic oxoanions of arsenic i.e. $HAsO_4^{2-}$. For preliminary investigation, crystals of iMOF-1C were soaked in 100 ppm solution of mono hydrogen arsenate and characterized using viz. PXRD, SEM, EDX, IR, ICP, XPS analysis. The PXRD pattern matched with the pristine MOF sugesting retention of framework integrity (Appendix 4.1b). FESEM analysis revealed block shape morphology while EDX mapping revealed a homogenous distribution of arsenic throughout the crystals along with the presence of sulfur (Figure 4.1c). The presence of sulfur is indicative of exchange of only free sulfate anions present within the voids. Further, the presence of the mono hydrogen arsenate was confirmed via FTIR with peaks at 823 cm^{-1} (Appendix 4.6). XPS spectra displayed peaks at ~45 eV corresponding to 3d orbitals of arsenic (Appendix 4.15). Enthused from this, the preliminary sorption experiment was performed to assess the uptake kinetics by exposing 2 mg of MOF to 100 ppm solution of mono hydrogen arsenate and the supernatant was analyzed by ICP measurements. The analysis revealed a steep uptake profile indicative of fast exchange behaviour (Figure 4.2c) which fitted well with pseudo-second order kinetics model (Appendix 4.16-4.19). To quantify maximum uptake amount, concentration dependent experiment was performed. Microcrystalline powder of iMOF-1C was exposed to

varying concentrations (100 ppm-1500 ppm) and the supernatant was evaluated by ICP measurements (Appendix 4.17). The maximum uptake was calculated as 85 mg of $HAsO_4^{2-}$/g of iMOF-1C and the experimental data fitted well to Langmuir model (Appendix 4.17). Further, selectivity was checked for the uptake of the $HAsO_4^{2-}$ in presence of interfering ions such as chloride (Cl^-), nitrate (NO_3^-), bicarbonate (HCO_3^-), sulfate (SO_4^{2-}), carbonate (CO_3^{2-}) in equimolar ratio. After exposing, the solid residue was characterized using FTIR (for NO_3^-/SeO_4^{2-}), (CO_3^{2-}/SeO_4^{2-}) and EDX analysis (for Cl^-/SeO_4^{2-}). FT-IR measurements revealed the presence of peaks corresponding to the oxoanion $HAsO_4^{2-}$ and no peaks due to competing anions(NO_3^-) (Appendix 4.21) while EDX analysis revealed the homogeneous distribution of arsenic throughout the compound (Figure S23) with no peak for Cl^-. Further, supernatant solution was analysed using ICP measurements and an appreciable uptake performance in presence of other common anions was observed (Appendix 4.20). Thereafter, reversibility was tested for upto three uptake-release cycles by soaking 2 mg of iMOF-1C in mono hydrogen arsenate solution and eluted with sodium sulfate solution (1000 ppm). The supernatant was characterized by ICP while the solids were evaluated via PXRD and EDX mapping. ICP measurements revealed similar uptake amounts (Appendix 4.22). Further, post release characterization via PXRD analysis showed retention of framework integrity (Figure S28). No arsenic was detected from the EDX profile (Appendix 4.30). Like the previous case, sorption behaviour at low concentration (20 ppm) was investigated and a similar trend was observed(Appendix 4.18). These results suggests the ability of the approach to work under real-time conditions.

Cationic MOFs seldom render structure-property correlation post ion-exchange, a quintessential feature sought after in material chemistry aiding fundamental understanding to the design principles.[12a,13h,13j] Single crystal analysis post ion-exchange is limited to a handful of reports due to rupturing of crystals during ion-exchange process.[12b,12d,13c,13f,13i] To study the encapsulation of oxo-anions crystallographically, crystals of the parent compound were exposed to an aqueous solution of $HAsO_4^{2-}$ and SeO_4^{2-} (Appendix 4.2). Unit cell refinement exhibited similar unit cell parameters as the parent framework (Appendix Table 4.3). Structural refinements revealed presence of mono hydrogen arsenate anion along the 1D channel of framework with a subtle shift in positioning of mono hydrogen arsenate oxo-anion with respect to sulfate anion which could be attributed to the larger size of anion thereby offering insight into variable modes of host-analyte interaction in a cationic framework (Figure 4.3, Appendix 4.27).

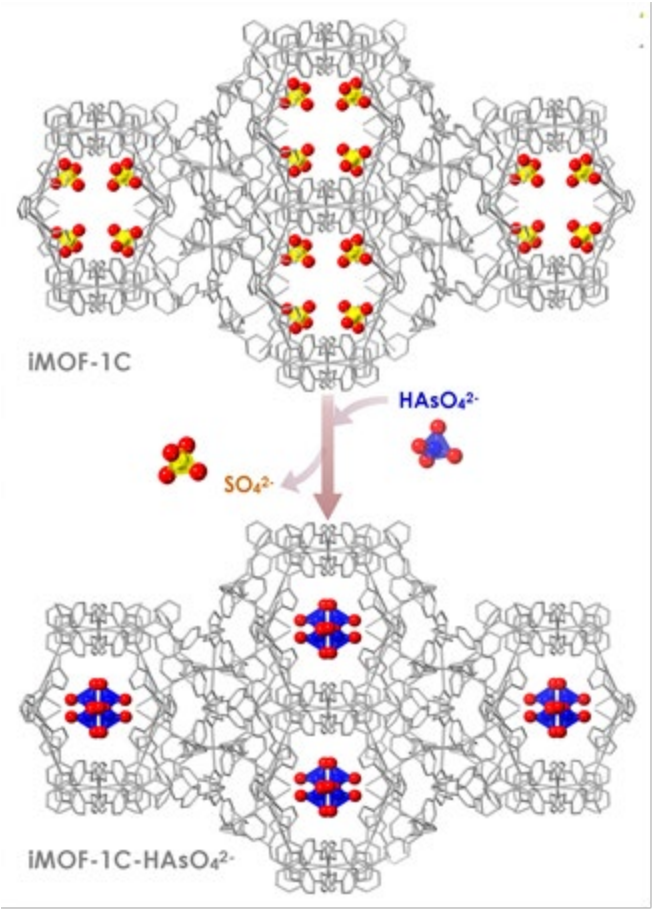


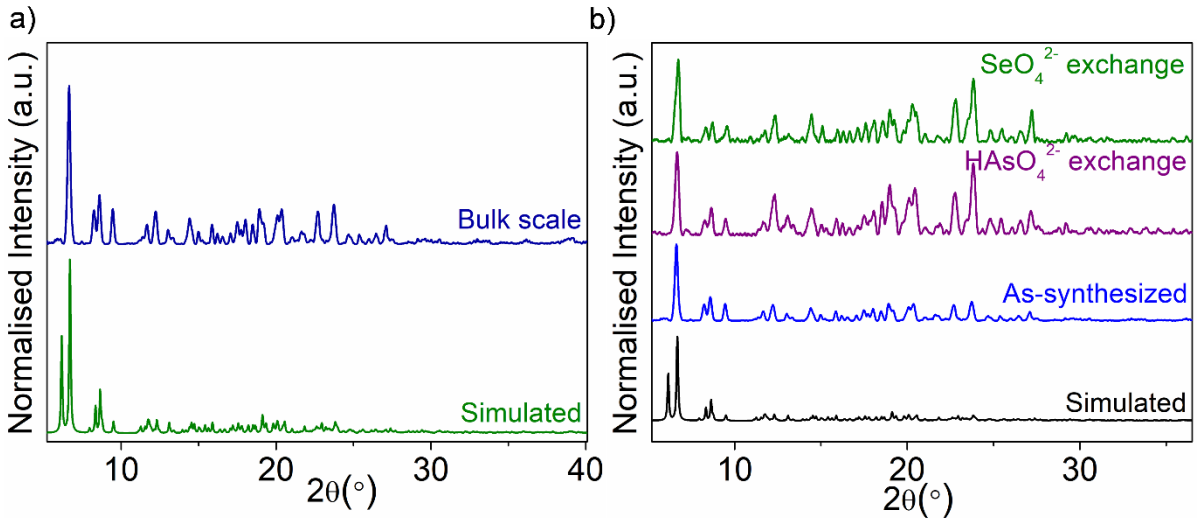
Figure 4.3: a) Packing diagram representing SC-SC transformation of parent cationic MOF viz. iMOF-1C to $HAsO_4^{2-}$ encapsulated phase.

The bond lengths of As-O bond in mono hydrogen arsenate anion were found to be within the range 1.65-1.75 Å, comparable to As(V) based anion.[24] In addition, detailed analysis revealed a different interacting site of the mono hydrogen arsenate anion with water molecule present at the Ni(II) metal node via hydrogen bonding interaction at a distance of 2.72 Å which may play a key role in overall stabilization of guest anion (Appendix 4.25-4.26). Further, the selenate exchanged crystal was also successfully analysed crystallographically. Even though selenate anions were found to be highly disordered in nature, but the positional occupancy within the voids was comparable to initial free sulfate anion (Appendix 4.13).

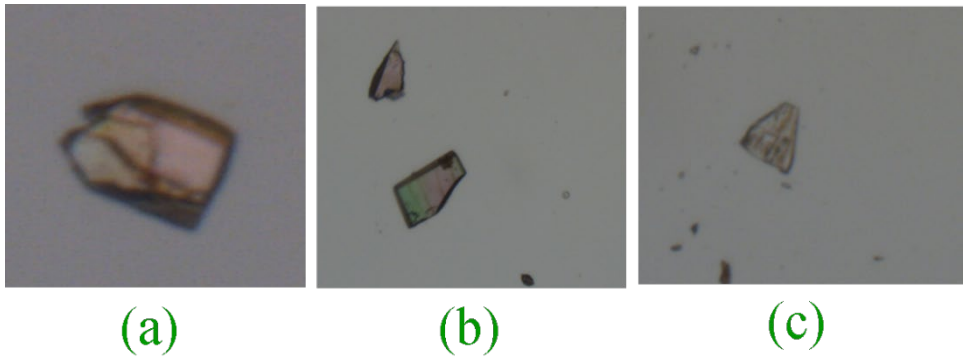
4.4 Conclusions

In conclusion, successful demonstration of bulk scale synthesis of a water stable cationic MOF viz. iMOF-1C was reported with simultaneous capture of toxic anions of SeO_4^{2-} and $HAsO_4^{2-}$.The framework exhibits fast kinetics and high sorption capacity i.e 100 mg/g and 84 mg/g for SeO_4^{2-} and $HAsO_4^{2-}$ respectively, which are among the highest values reported in the domain of MOFs. In addition, selective capture towards SeO_4^{2-} and $HAsO_4^{2-}$ anions was also exhibited in presence of concurrent anions such as Cl^- and NO_3^- which is crucial for practical applications. The regeneration of the framework viz. iMOF-1C was facile and multiple release-uptake cycles exhibited similar uptake amounts. Additionally, single crystal analysis provided a rare molecular insight between toxic anions and framework which could be correlated to nature and geometry of the guest anion. The present study opens new avenues for ionic MOFs to study the sequestration of oxoanions of less explored elements viz. selenium and arsenic, which are a potent hazard, and the insights gained from molecular level analysis could propel development of MOFs towards remediation of priority environmental pollutants.

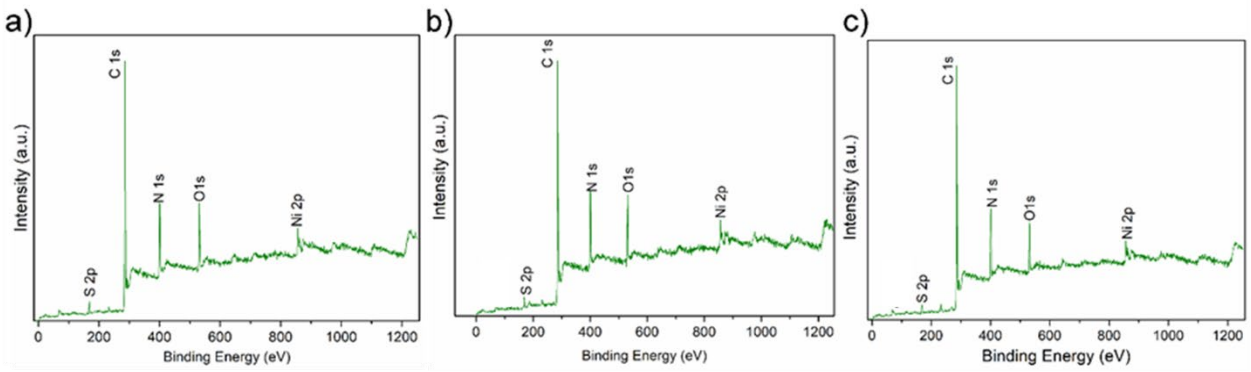
4.5 Appendix Section



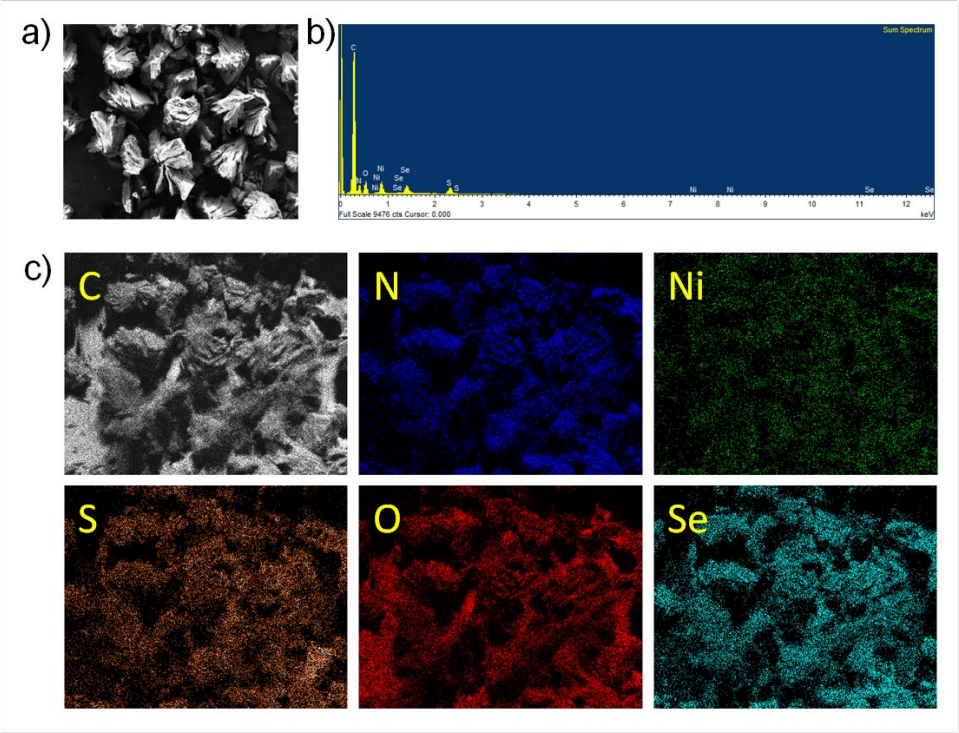
Appendix 4.1: (a) Simulated and bulk-phase PXRD patterns for iMOF-1C. (b) iMOF-1C simulated, As-synthesized, $HAsO_4^{2-}$ exchanged phase and SeO_4^{2-} exchanged phase.



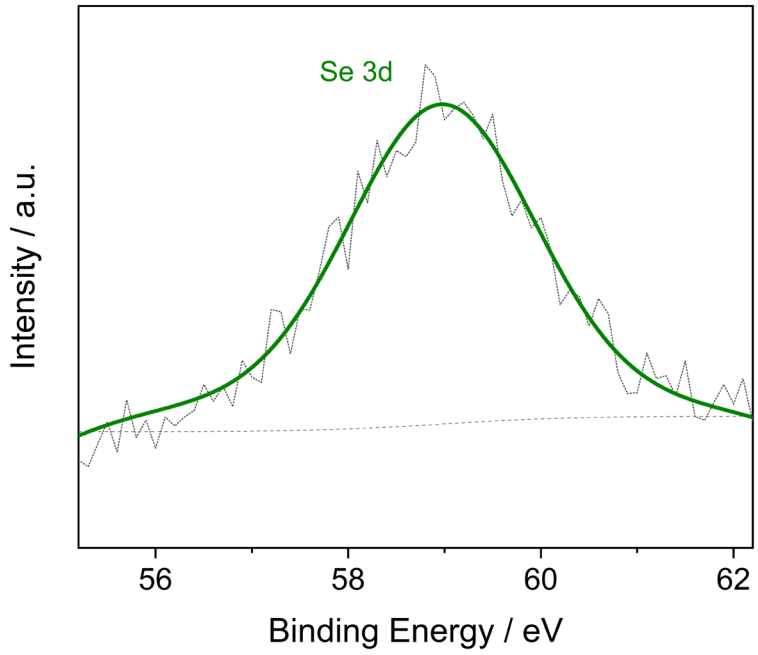
Appendix 4.2: Photographs of parent framework (a) iMOF-1C, b) SeO_4^{2-} and c) $HAsO_4^{2-}$ exposed phases taken under optical microscope.



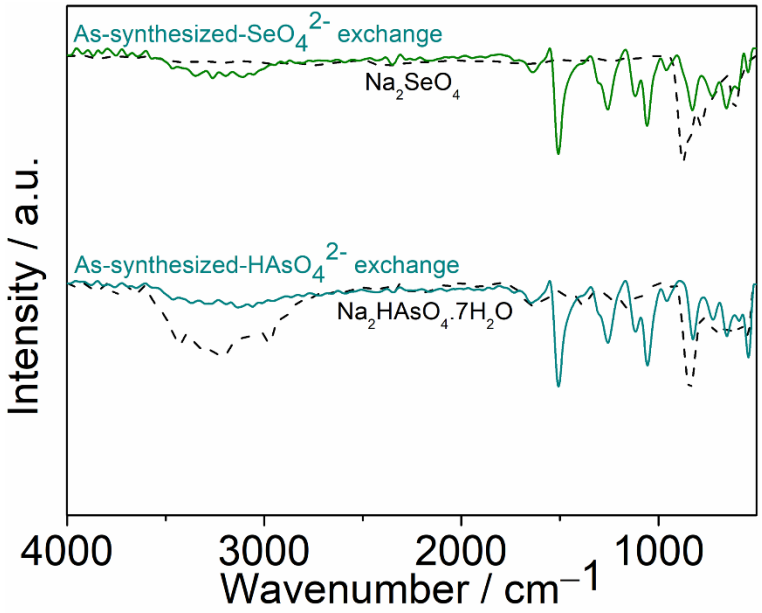
Appendix 4.3: Survey XPS spectra for bulk phase a) iMOF-1C, b) SeO_4^{2-} and c) $HAsO_4^{2-}$ exposed phase. (Note: The intensity peaks corresponding to selenium and arsenic was very weak/almost negligible, in survey spectra however this spectrum was needed to perform C1s corrections. To further detect arsenic and selenium more scans were given for a specific energy range dedicated to these elements and thjs data can be found in Appendix 4.5 and 4.15.



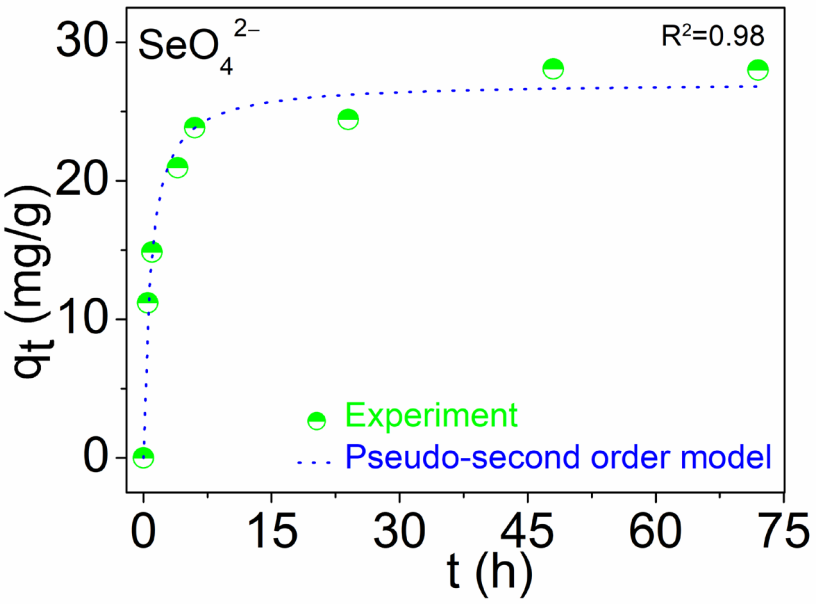
Appendix 4.4: a) FESEM images, b) EDX spectra and c) EDX mapping profile for iMOF-1C exposed to an aqueous solution of SeO_4^{2-}.



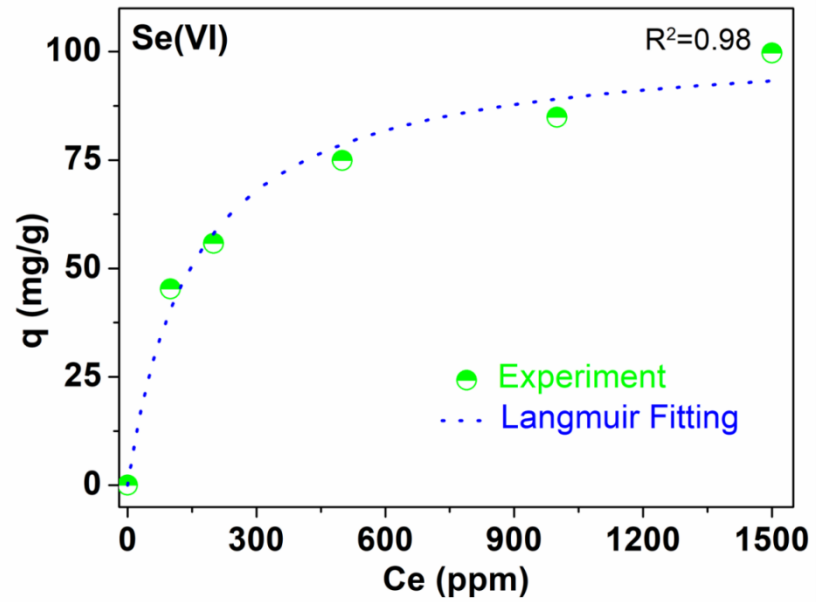
Appendix 4.5: XPS spectra of iMOF-1C after dipping in aqueous solution of SeO_4^{2-} anion



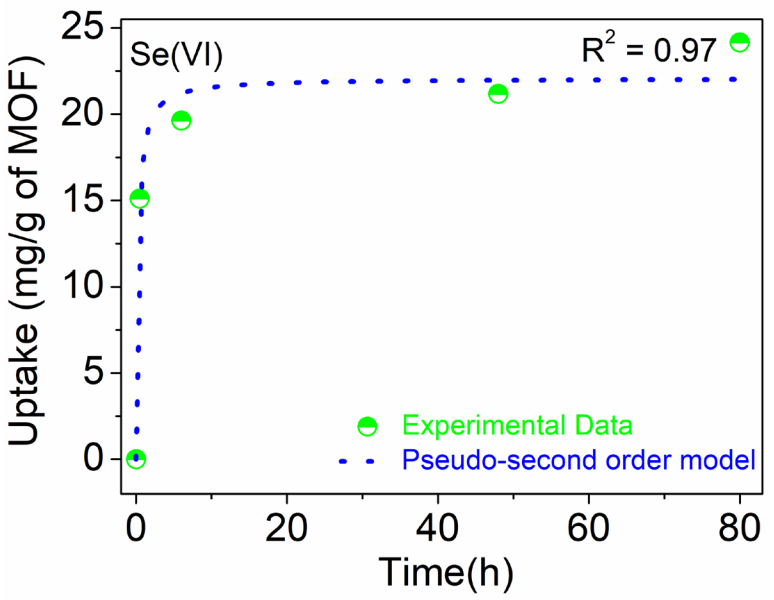
Appendix 4.6: FT-IR spectra for the anion exchanged phases along-with the corresponding spectrum for respective sodium salts.



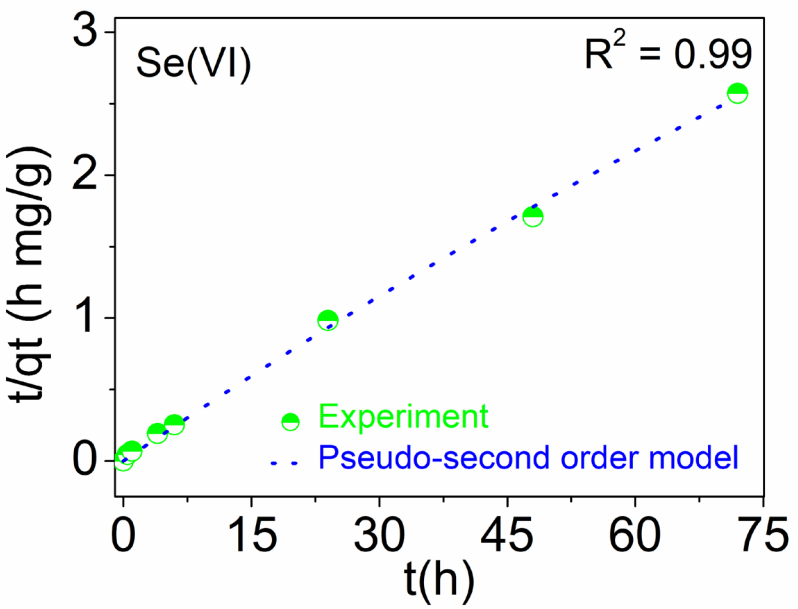
Appendix 4.7: Time dependent uptake profile of SeO_4^{2-} oxoanion by iMOF-1C at concentration (100 ppm, Se(VI)).



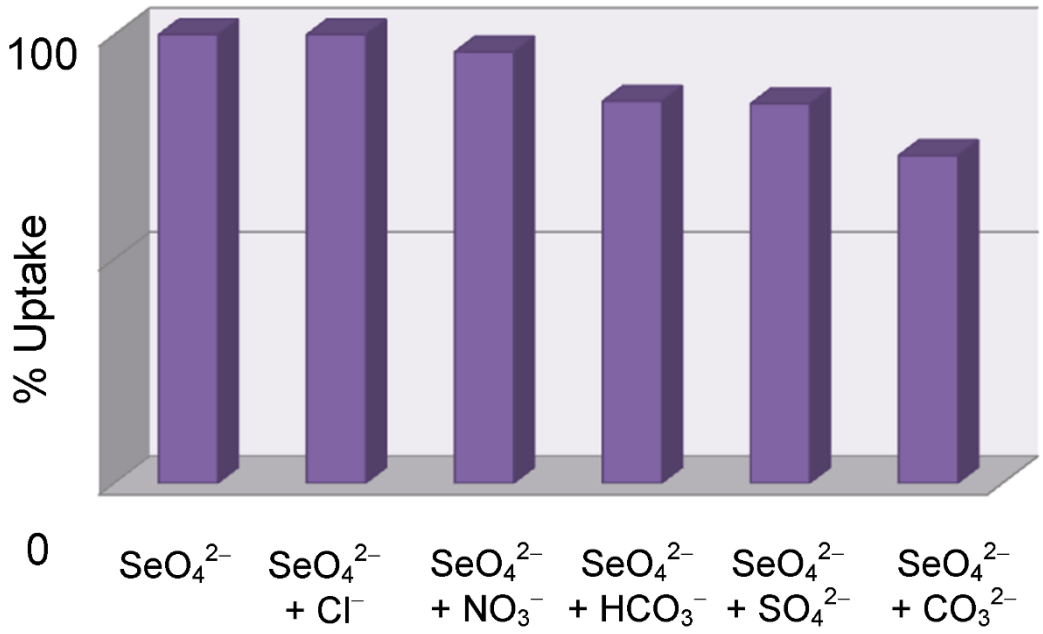
Appendix 4.8: Concentration dependent sorption isotherm for SeO_4^{2-} oxoanion capture by iMOF-1C fit with Langmuir model.



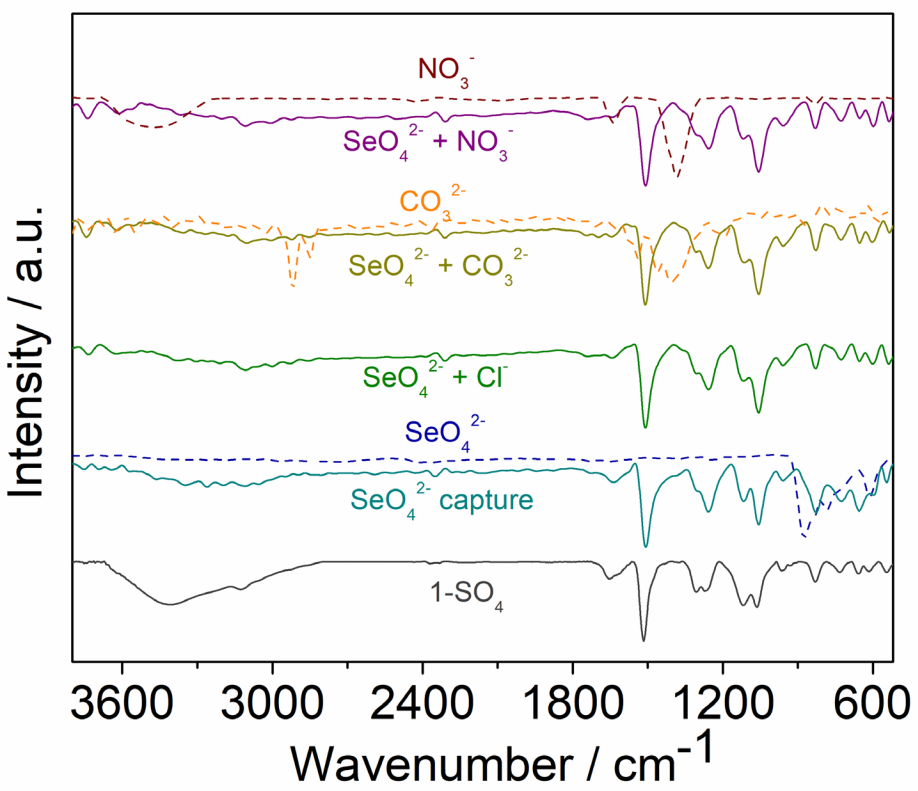
Appendix 4.9: Time dependent uptake profile for SeO_4^{2-} capture by iMOF-1C at low concentration (20 ppm of Se(VI)).



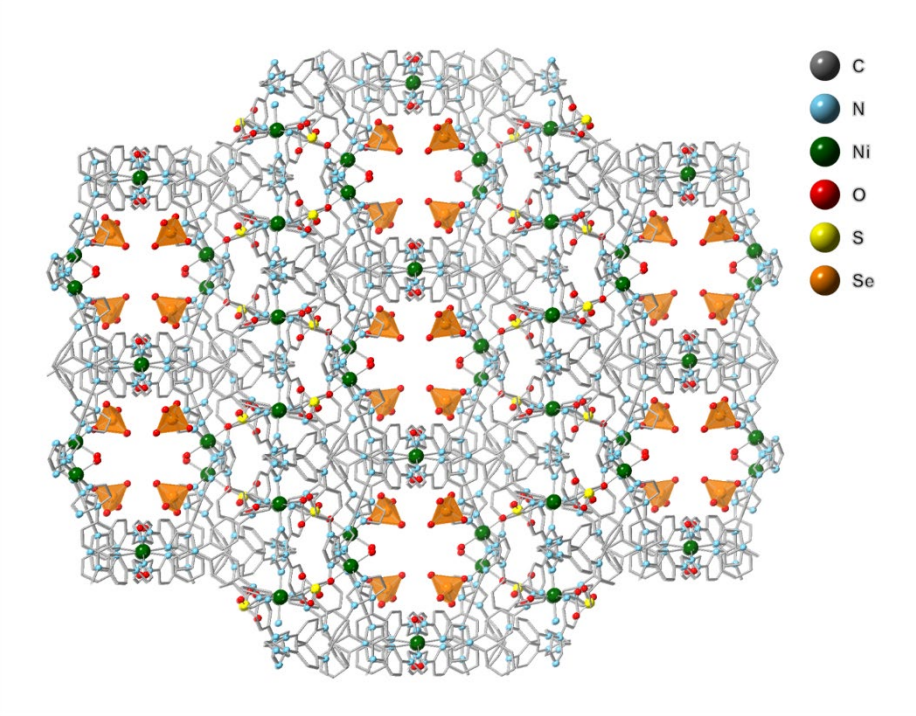
Appendix 4.10: Pseudo-second order kinetics profile for uptake of SeO_4^{2-} by iMOF-1C at higher concentration of 100 ppm of Se(VI).



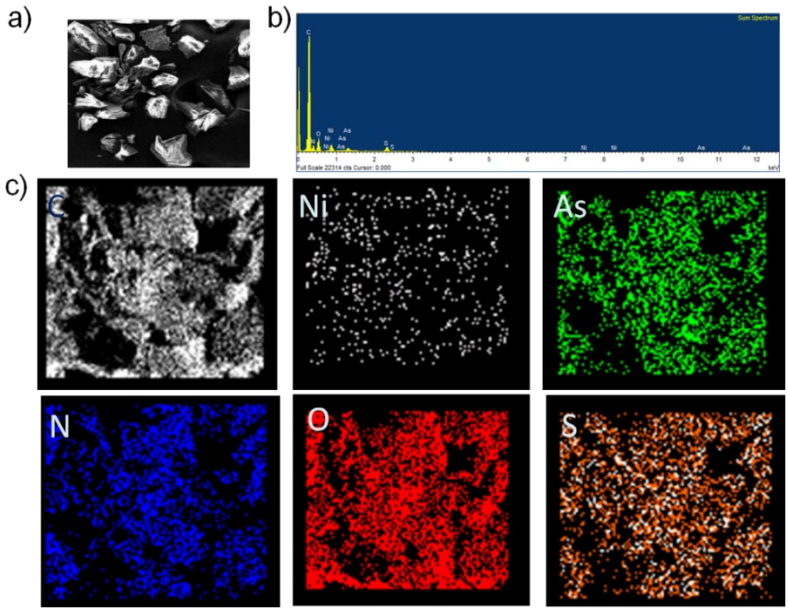
Appendix 4.11: Comparative percentage uptake profiles for SeO_4^{2-} by iMOF-1C in presence of equimolar ratio of NO_3^- ,Cl^-, HCO_3^-, SO_4^{2-}, CO_3^{2-}.



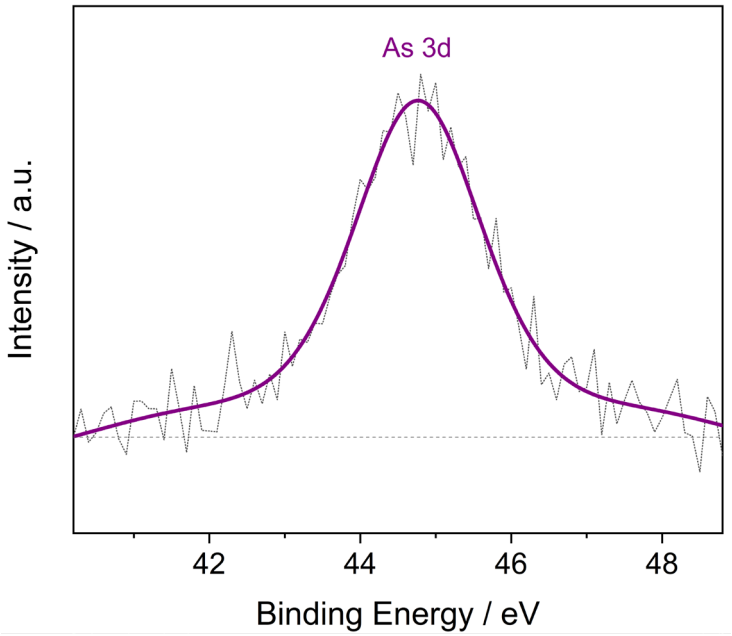
Appendix 4.12: FT-IR spectra for as-synthesized (iMOF-1C), iMOF-1C exposed to SeO_4^{2-} oxoanion, binary mixture of anions (continuous line) and individual anions (dotted line).



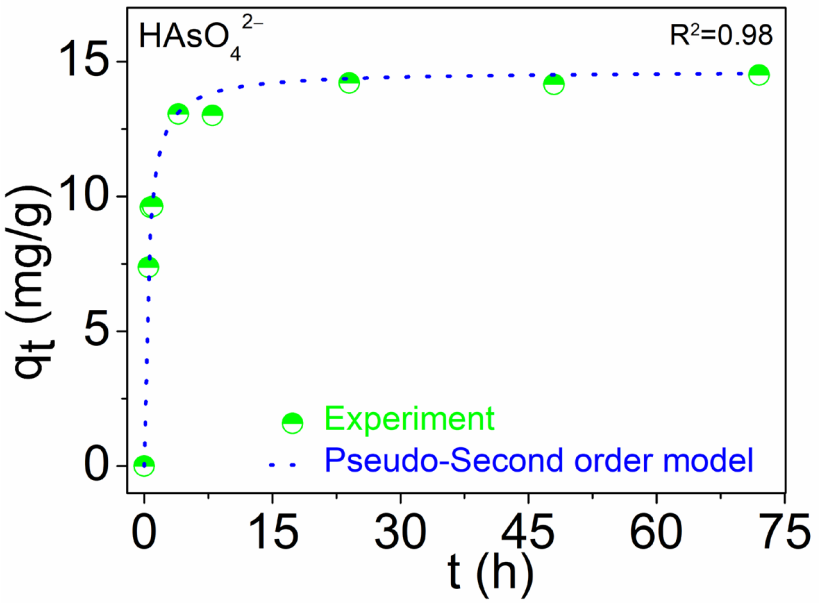
Appendix 4.13: Packing diagram of iMOF-1C-SeO_4^{2-} along *c*-axis.



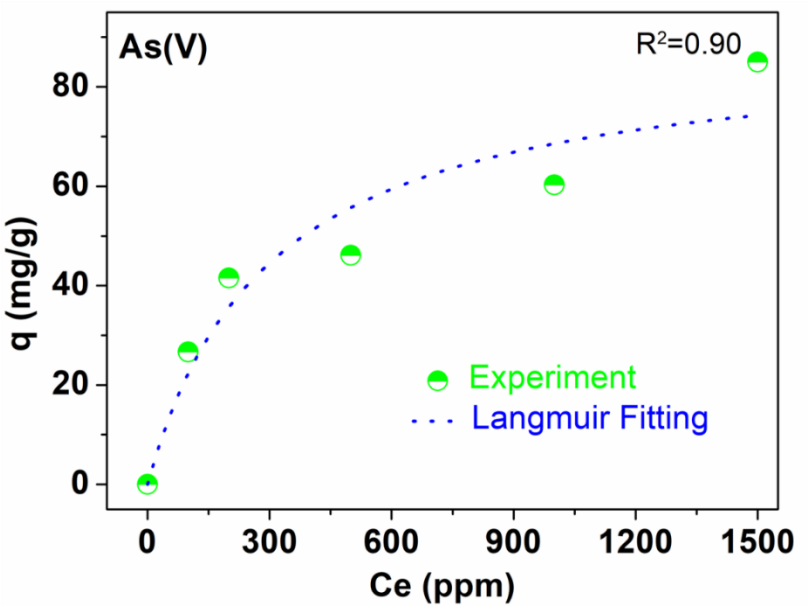
Appendix 4.14: a) FESEM images, b) EDX spectra and c) EDX mapping profile for iMOF-1C exposed to an aqueous solution of $HAsO_4^{2-}$



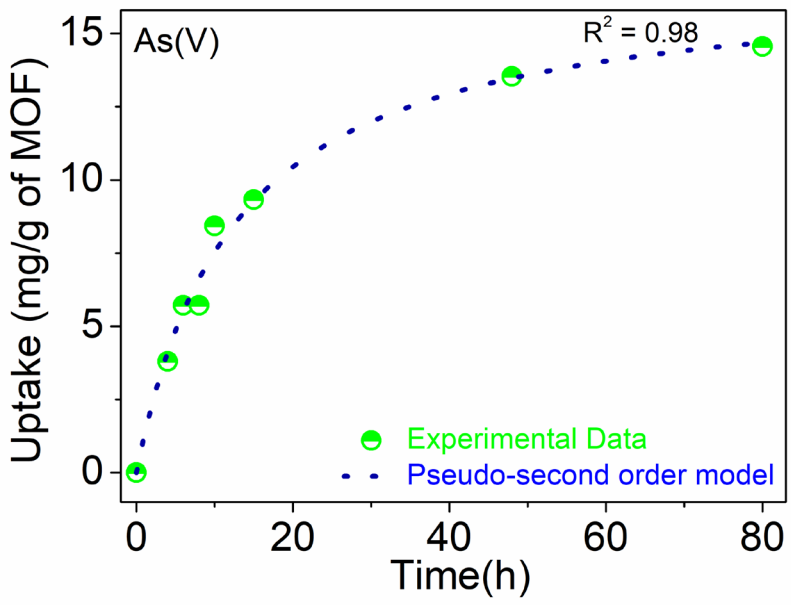
Appendix 4.15: XPS spectra of iMOF-1C after dipping in aqueous solution of $HAsO_4^{2-}$ anion



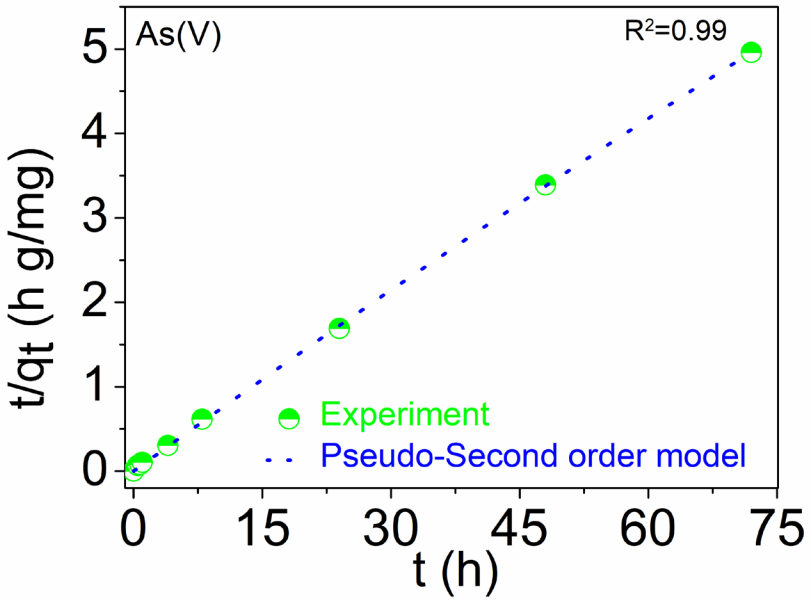
Appendix 4.16: Time dependent uptake profile of $HAsO_4^{2-}$ by iMOF-1C at 100 ppm.



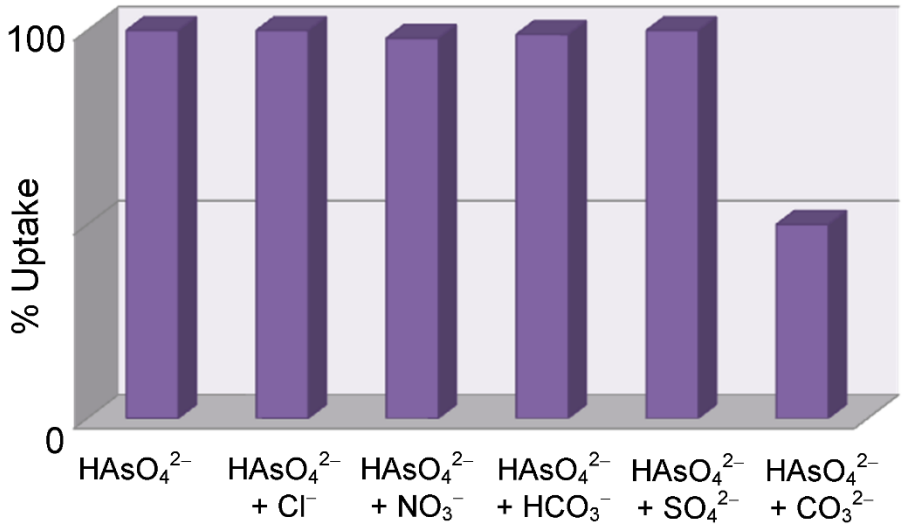
Appendix 4.17: Concentration dependent sorption isotherm for $HAsO_4^{2-}$ oxoanion capture by iMOF-1C fit with Langmuir model.



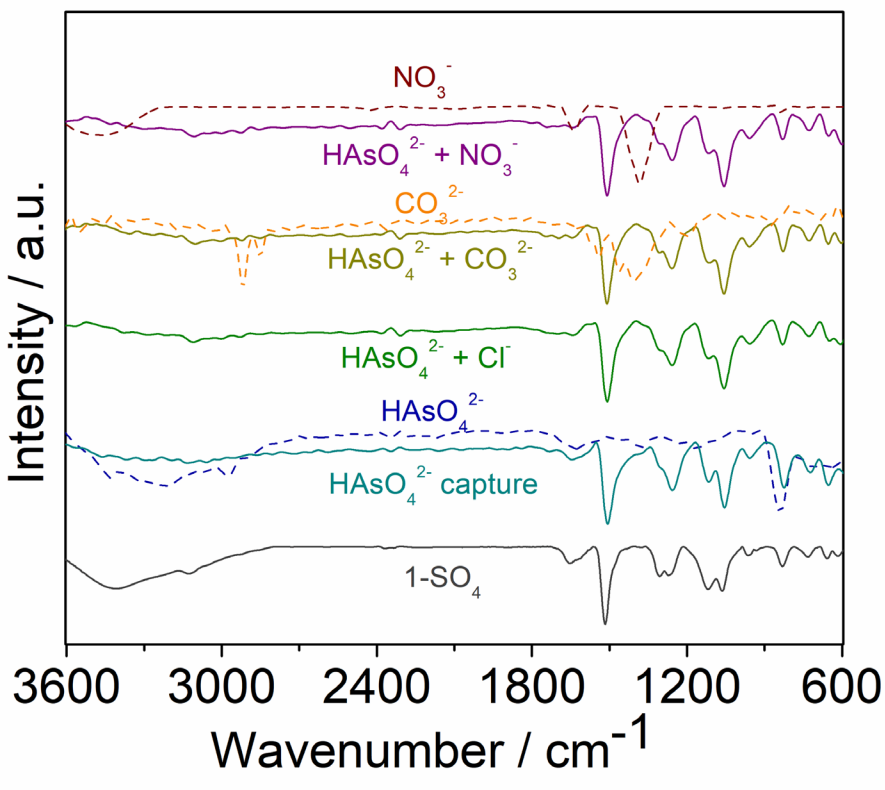
Appendix 4.18: Time dependent uptake profile of $HAsO_4^{2-}$ by iMOF-1C at low concentration 20 ppm.



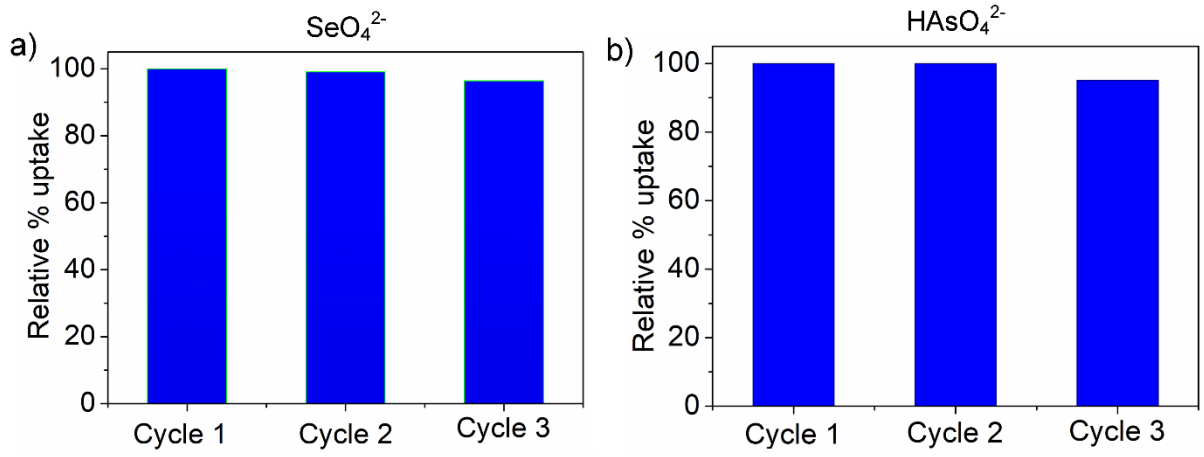
Appendix 4.19: Pseudo-second order kinetics profile for uptake of $HAsO_4^{2-}$ by iMOF-1C at higher concentration of 100 ppm of Se(VI).



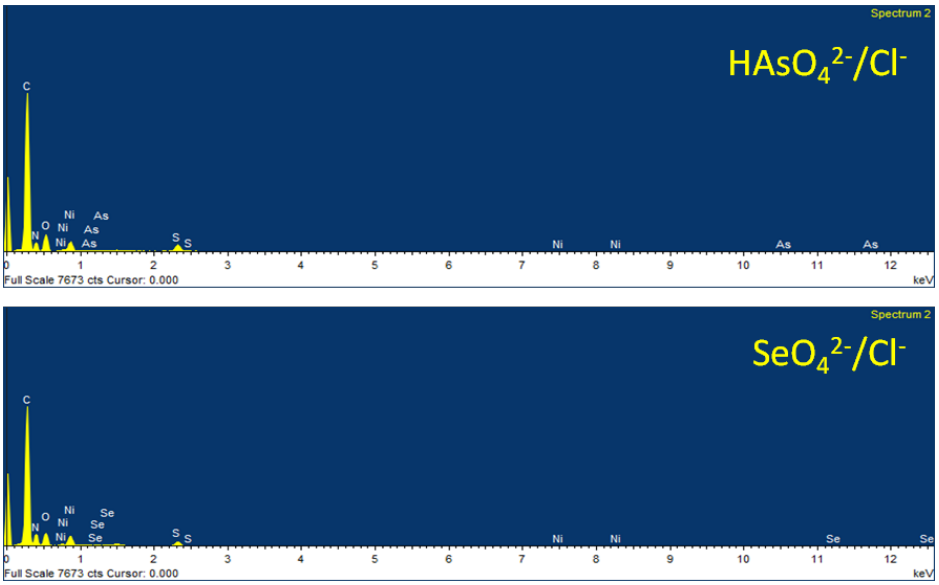
Appendix 4.20: Comparative percentage uptake profiles showing $HAsO_4^{2-}$ capture by iMOF-1C in presence of equimolar ratio of NO_3^- ,Cl^-, HCO_3^-, SO_4^{2-}, CO_3^{2-}.



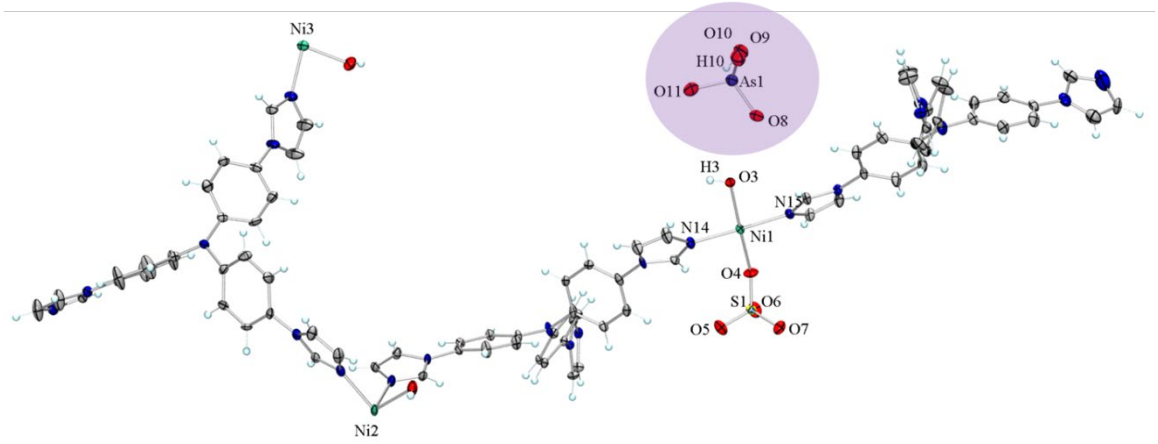
Appendix 4.21: FT-IR spectra for as-synthesized (iMOF-1C), iMOF-1C exposed to $HAsO_4^{2-}$ oxoanion, binary mixture of anions (continuous line) and individual anions (dotted line).



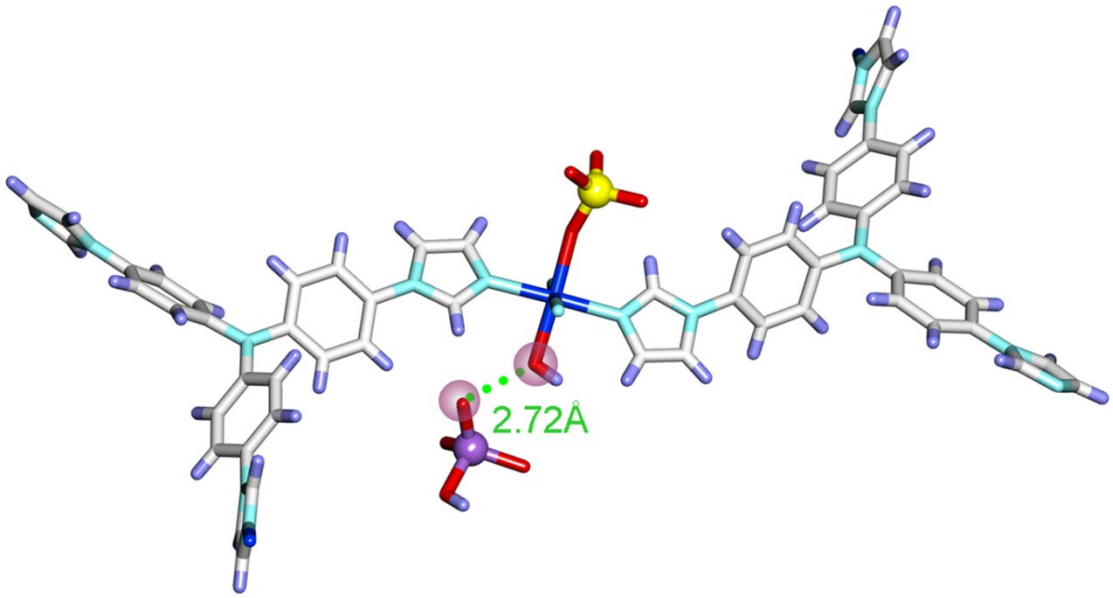
Appendix 4.22: Plot depicting cycling experiment for capture of oxoanions a) SeO_4^{2-} and b) $HAsO_4^{2-}$ by iMOF-1C.



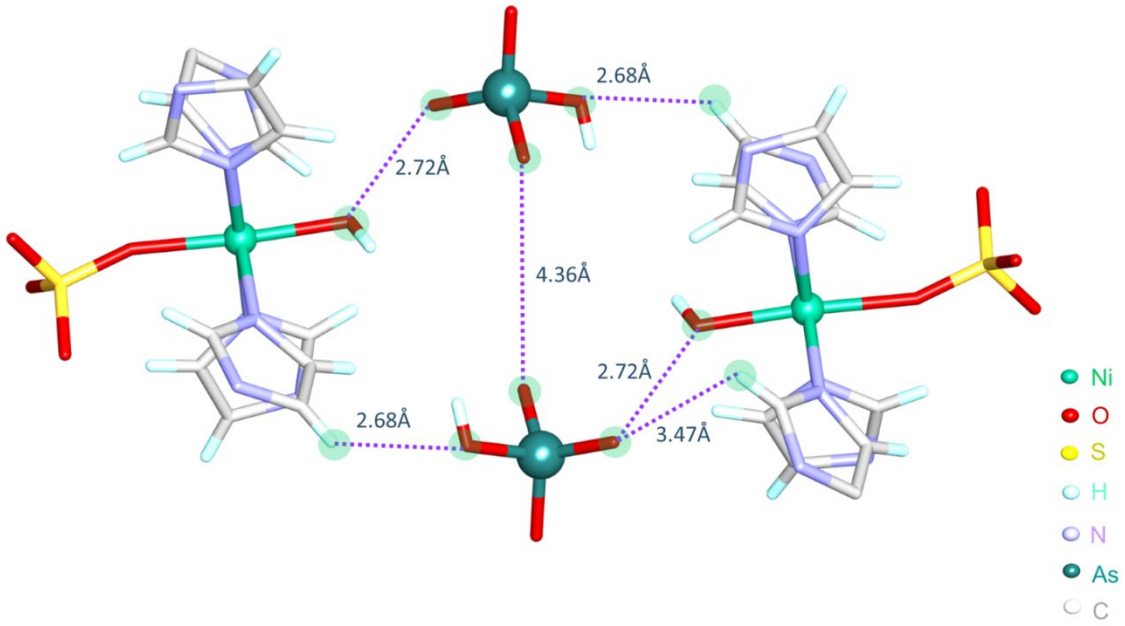
Appendix 4.23: FESEM-EDX data for binary mixtures ($HAsO_4^{2-}$ /Cl^- and SeO_4^{2-} / Cl^-).



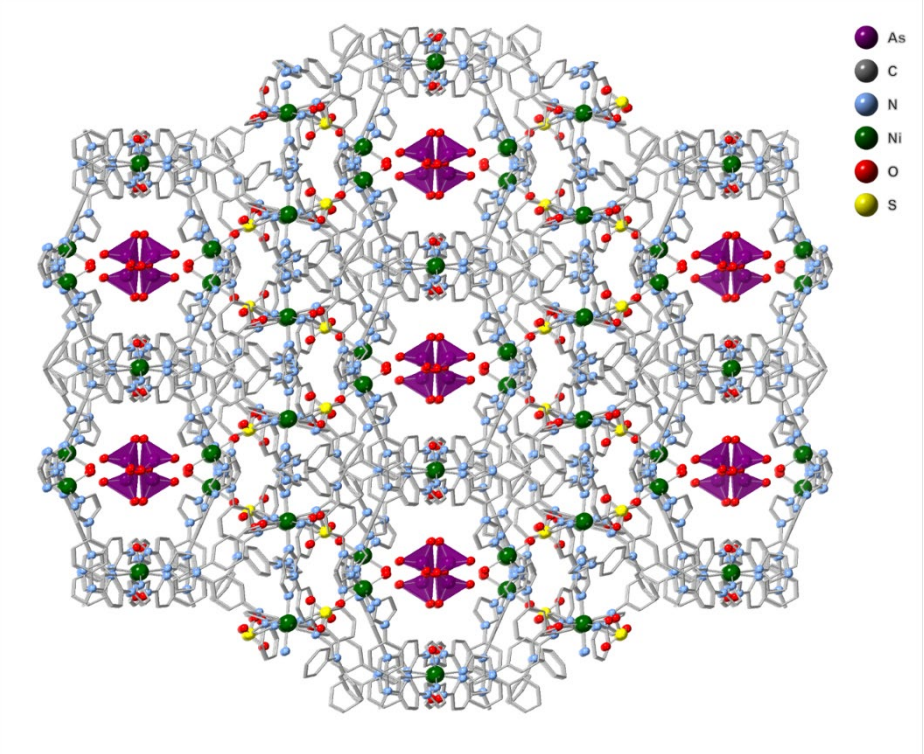
Appendix 4.24: ORTEP diagram of asymmetric unit of iMOF-1C-$HAsO_4^{2-}$ in thermal ellipsoids (50% probability).



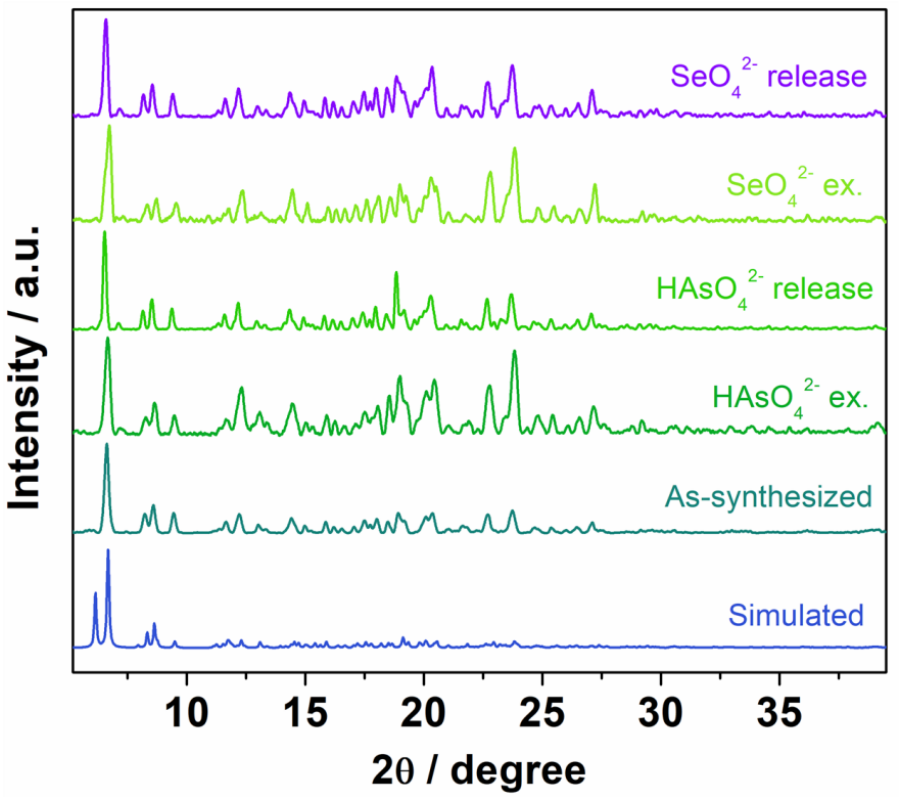
Appendix 4.25: Hydrogen bond interaction between $HAsO_4^{2-}$ and framework backbone. Colour code (H, purple; C, grey; N, blue; Ni, dark blue; O, red; S, yellow; As, violet)



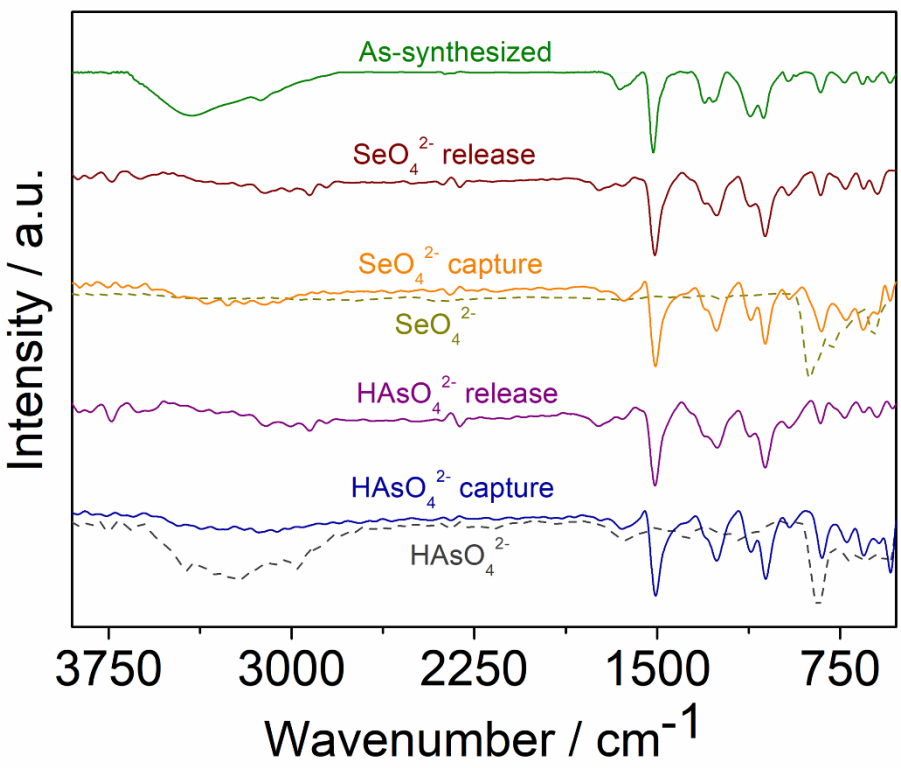
Appendix 4.26: Different non-covalent interactions between $HAsO_4^{2-}$ and framework.



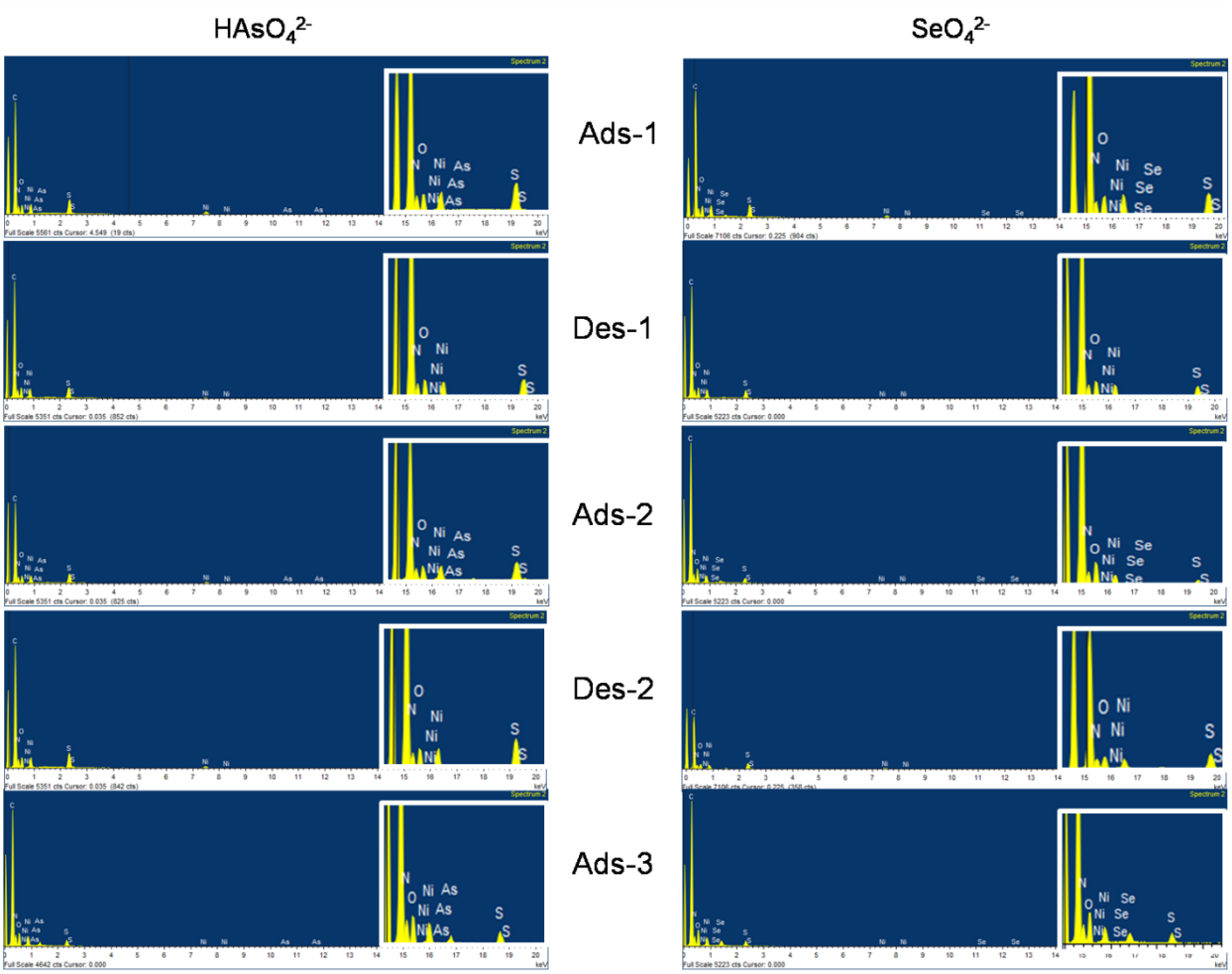
Appendix 4.27: Packing diagram of iMOF-1C-$HAsO_4^{2-}$ along *c*-axis.



Appendix 4.28: PXRD patterns for simulated, as-synthesized, capture and release phases for $HAsO_4^{2-}$ and SeO_4^{2-}.



Appendix 4.29: FT-IR spectra for as-synthesized, $SeO_4^{2-}$and $HAsO_4^{2-}$ capture and release phase.



Appendix 4.30: EDX spectra for capture and release of respective anions for 3 adsorption cycles. (Inset: zoomed view)

Appendix Table 1 | MOFs reported for the capture of Se(VI) oxoanions.

Adsorbent	**Type of MOF**	**Capacity (mg/g)**	**Reference**
iMOF-1C	Ionic (Cationic)	100	**This work**
NU-1000	Neutral	85.5	10b
CAU-17	Neutral	20.3	11k
MOF-808	Neutral	118	25

Appendix Table 2 | MOFs reported for the capture of As(V) oxoanions.

Adsorbent	**Type of MOF**	**Capacity (mg/g)**	**Reference**
iMOF-1C	Ionic (Cationic)	85 in water	**This work**
MOF-808	Neutral	24.83	26
UiO-66	Neutral	147.71 at pH=7 303.4 at pH=2	8
Fe-BTC	Neutral	12.3	27
MIL-53 (Al)	Neutral	106.5	28
MIL-53 (Fe)	Neutral	21.27	29
MIL-100 (Fe)	Neutral	116	30
MIL-100 (Al)	Neutral	128	30
ZIF-8	Neutral	50.5 in water 72.33 in MeOH	31
ZIF-8	Neutral	76.5	32
AUBM-1	Neutral	103.1	33
RT-Zn-MOF-74	Neutral	99.0	34
HT-Zn-MOF-74	Neutral	48.7	34
NH2-MIL-88(Fe)	Neutral	125	35

Appendix Table 3 | Comparison of unit-cell parameters for iMOF-1C, iMOF-1C-$HAsO_4$ and iMOF-1C-SeO_4.

Unit Cell parameters	iMOF-1C	iMOF-1C-$HAsO_4$	iMOF-1C-SeO_4
a (Å)	46.61 (8)	46.51 (6)	46.79 (20)
b (Å)	15.15 (2)	15.27 (19)	15.16 (7)
c (Å)	27.70 (4)	27.29 (3)	27.47 (12)
α (°)	90	90	90
β (°)	107.72 (5)	107.62 (5)	107.65 (12)
γ (°)	90	90	90
Volume ($Å^3$)	18649	18486.1	18575.4

Appendix Table 4 | Stability studies of iMOF-1C.

Concentration of Ni(II) in the supernatant solution during recyclability experiment.

Sample	Concentration of Ni(II) (ppm)
$HAsO_4^{2-}$ uptake Cycle 1	0.22
$HAsO_4^{2-}$ uptake Cycle 2	*NA
$HAsO_4^{2-}$ uptake Cycle 3	*NA
SeO_4^{2-} uptake cycle 1	0.34
SeO_4^{2-} uptake cycle 2	0.20
SeO_4^{2-} uptake cycle 3	0.17

*NA : Less than detection limit via <10ppb.

Appendix Table 5. Crystal data and structure refinement for iMOF-1C-$HAsO_4$.

Identification code	iMOF-1C-$HAsO_4$ (CCDC - 1959430)	
Empirical formula	C81 H67 As N21 Ni2 O11 S	
Formula weight	1734.95	
Temperature	150(2) K	
Wavelength	0.71073 Å	
Crystal system	Monoclinic	
Space group	*C* 2/c	
Unit cell dimensions	a = 46.512(6) Å	a= 90°.
	b = 15.2774(19) Å	b= 107.627(5)°.
	c = 27.297(3) Å	g = 90°.
Volume	18486(4) $Å^3$	
Z	8	
Density (calculated)	1.247 Mg/m^3	
Absorption coefficient	0.850 mm^{-1}	
F(000)	7144	
Crystal size	0.17 x 0.12 x 0.10 mm^3	
Theta range for data collection	2.196 to 28.388°.	
Index ranges	-62<=h<=61, -20<=k<=20, -36<=l<=36	
Reflections collected	223303	
Independent reflections	23137 [R(int) = 0.1602]	
Completeness to theta = 25.242°	99.9 %	
Absorption correction	Semi-empirical from equivalents	
Max. and min. transmission	0.7457 and 0.6744	
Refinement method	Full-matrix least-squares on F^2	
Data / restraints / parameters	23137 / 24 / 1061	
Goodness-of-fit on F2	1.095	
Final R indices [I>2sigma(I)]	R1 = 0.0916, wR2 = 0.2688	
R indices (all data)	R1 = 0.1790, wR2 = 0.3286	
Extinction coefficient	n/a	
Largest diff. peak and hole	2.538 and -2.095 e.$Å^{-3}$	

Appendix Table 6. Crystal data and structure refinement for iMOF-1C-SeO_4.

Identification code	iMOF-1C-SeO_4 (CCDC - 1959440)	
Empirical formula	C81 H66 N21 Ni2 O11 S Se	
Formula weight	1737.98	
Temperature	150(2) K	
Wavelength	0.71073 Å	
Crystal system	Monoclinic	
Space group	C 2/c	
Unit cell dimensions	a = 46.793(20) Å	a= 90°.
	b = 15.160(7) Å	b= 107.651(12)°.
	c = 27.479(12) Å	g = 90°.
Volume	18576(14) $Å^3$	
Z	8	
Density (calculated)	1.243 Mg/m^3	
Absorption coefficient	0.884 mm^{-1}	
F(000)	7144	
Crystal size	0.16 x 0.14 x 0.12 mm^3	
Theta range for data collection	2.205 to 25.259°.	
Index ranges	-55<=h<=54, -17<=k<=17, -32<=l<=32	
Reflections collected	101891	
Independent reflections	16232 [R(int) = 0.1161]	
Completeness to theta = 25.242°	96.5 %	
Absorption correction	Semi-empirical from equivalents	
Max. and min. transmission	0.899 and 0.868	
Refinement method	Full-matrix least-squares on F^2	
Data / restraints / parameters	16232 / 24 / 1060	
Goodness-of-fit on F^2	1.676	
Final R indices [I>2sigma(I)]	R1 = 0.1727, wR2 = 0.4324	
R indices (all data)	R1 = 0.2124, wR2 = 0.4596	
Extinction coefficient	n/a	
Largest diff. peak and hole	2.400 and -2.798 $e.Å^{-3}$	

4.6 References

1. www.epa.gov/eg/toxic-and-priority-pollutants-under-clean-water-act

2. D. Ashworth, John Wiley & Sons Ltd. 2011, doi: 10.1002/9781119951438.eibc0420.

3. Guidelines for drinking-water quality, 4th ed., World Health Organization, 2011, ISBN: 9789241548151.

4. K. Tokunaga and Y. Takahashi, *Environ. Sci. Technol.*, 2017, **51**, 9194-9201.

5. P. Bienvenu, P. Cassette, G. Andreoletti, M.-M. Be, J. Comte and M.-C. Lepy, *Appl. Radiat. Isot.*, 2007, **65**, 355-364.

6. a) M. F. Hughes, *Toxicology Lett.*, 2002, **133**, 1-16; b) J. C. Ng, *Environ. Chem.*, 2005, **2**, 146-160; c) S. Wei, H. Zhang and S. Tao, *Toxicol. Res.*, 2019, **8**, 319-327.

7. J.-Y. Chung, S.-D. Yu and Y.-S. Hong, *J. Prev. Med. Public Health*, 2014, **47**, 253-257.

8. C. Wang, X. Liu, J. P. Chen and K. Li, *Sci. Rep.*, 2015, **5**, 16613.

9. a) L. Ma, S. M. Islam, C. Xiao, J. Zhao, H. Liu, M. Yuan, G. Sun, H. Li, S. Ma and M. G. Kanatzidis, *J. Am. Chem. Soc.*, 2017, **139**, 12745-12757; b) L. Zhu, L. Zhang, J. Li, D. Zhang, L. Chen, D. Sheng, S. Yang, C. Xiao, J. Wang, Z. Chai, T. E. Albrecht-Schmitt and S. Wang, *Environ. Sci. Technol.*, 2017, **51**, 8606-8615; c) V. K. Sharma, M. Sohn and T. J. McDonald, Advances in Water Purification Techniques, Chapter-8: Remediation of Selenium in Water: A Review, 2019, 203-218; d) Y. He, Y. P. Tang and T. S. Chung, *Ind. Eng. Chem. Res.*, 2016, **55**, 12929-12938; e) L. Ma, S. M. Islam, H. Liu, J. Zhao, G. Sun, H. Li, S. Ma and M. G. Kanatzidis, *Chem. Mater.*, 2017, **29**, 3274-3284; f) J. Wang, T. Zhang, M. Li, Y. Yang, P. Lu, P. Ning and Q. Wang, *RSC Adv.*, 2018, **8**, 22694-22709.

10. a) T. Yu, B. Liu and J. Liu, *J. Anal. Testing*, 2017, 1:2, doi: 10.1007/s41664-017-0001-0; b) A. J. Howarth, M. J. Katz, T. C. Wang, A. E. Platero-Prats, K. W. Chapman, J. T. Hupp and O. K. Farha, *J. Am. Chem. Soc.*, 2015, **137**, 7488-7494.

11. a) S. Horike, S. Shimomura and S. Kitagawa, *Nat. Chem.*, 2009, **1**, 695-704; b) H. Furukawa, K. E. Cordova, M. O'Keeffe and O. M. Yaghi, *Science*, 2013, **341**, 1230444; c) S.-L. Li and Q. Xu, *Energy Environ. Sci.*, 2013, **6**, 1656-1683; d) A. J. Howarth, Y. Liu, J. T. Hupp and O. K. Farha, *CrystEngComm*,

2015, **17**, 7245-7253; e) B. Li, H.-M. Wen, Y. Cui, W. Zhou, G. Qian and B. Chen, *Adv. Mater.*, 2016, **28**, 8819-8860; f) C. O. Audu, H. G. T. Nguyen, C.-Y. Chang, M. J. Katz, L. Mao, O. K. Farha, J. T. Hupp and S. T. Nguyen, *Chem. Sci.*, 2016, **7**, 6492-6498; g) K. Wang, X.-L. Lv, D. Feng, J. Li, S. Chen, J. Sun, L. Song, Y. Xie, J.-R. Li and H.-C. Zhou, *J. Am. Chem. Soc.*, 2016, **138**, 914-919; h) G. Maurin, C. Serre, A. Cooper and G. Ferey, *Chem. Soc. Rev.*, 2017, **46**, 3104-3107; i) P. Kumar, A. Pournara, K.-H. Kim, V. Bansal, S. Rapti and M. J. Manos, *Prog. Mater. Sci.*, 2017, **86**, 25-74; j) A. Kirchon, L. Feng, H. F. Drake, E. A. Joseph and H.-C. Zhou, *Chem. Soc. Rev.*, 2018, **47**, 8611-8638; k) H. Ouyang, N. Chen, G. Chang, X. Zhao, Y. Sun, S. Chen, H. Zhang and D. Yang, *Angew. Chem. Int. Ed.*, 2018, **57**, 13197-13201; l) P. A. Kobielska, A. J. Howarth, O. K. Farha and S. Nayak, *Coord. Chem. Rev.*, 2018, **358**, 92-107; m) J. Li, X. Wang, G. Zhao, C. Chen, Z. Chai, A. Alsaedi, T. Hayat and X. Wang, *Chem. Soc. Rev.*, 2018, **47**, 2322-2356; n) A. J. Reith, A. M. Wright, G. Skorupskii, J. L. Mancuso, C. H. Hendon and M. Dinca, *J. Am. Chem. Soc.*, 2019, **141**, 13858-13866; o) Q. Gao, J. Xu and X.-H. Bu, *Coord. Chem. Rev.*, 2019, **378**, 17-31; p) O. T. Qazvini, R. Babarao, Z.-L. Shi, Y.-B. Zhang and S. G. Telfer, *J. Am. Chem. Soc.*, 2019, **141**, 5014-5020; q) H. Wang and J. Li, *Acc. Chem. Res.*, 2019, **52**, 1968-1978; r) Metal-organic frameworks (MOFs) for environmental applications, 1st edition, (Ed.: S. K. Ghosh), Elsevier, 2019, doi: 10.1016/C2017-0-01721-4.

12. a) H. Fei, M. R. Bresler and S. R. J. Oliver, *J. Am. Chem. Soc.*, 2011, **133**, 11110-11113; b) H. R. Fu, Z.-X. Xu and J. Zhang, *Chem. Mater.*, 2015, **27**, 205-210; c) C.-P. Li, H. Zhou, S. Wang, H.-H. Yuan, S.-Z. Zhang and M. Du, *Chem. Commun*., 2017, **53**, 4767-4770; d) H.-R. Fu, N. Wang, J.-H. Qin, M.-L. Han, L.-F. Ma and F. Wang, *Chem. Commun.*, 2018, **54**, 11645-11648; e) Y.-H. Zou, J. Liang, C. He, Y.-B. Huang and R. Cao, *Dalton Trans.*, 2019, **48**, 6680-6684; f) E. Soe, B. Ehlke and S. R. J. Oliver, *Environ. Sci. Technol.*, 2019, **53**, 7663-7672.

13. a) T. K. Maji, R. Matsuda and S. Kitagawa, *Nat. Mater.*, 2007, **6**, 142-148; b) H. Fei, D. L. Rogow and S. R. J. Oliver, *J. Am. Chem. Soc.*, 2010, **132**, 7202-7209; c) X. Li, H. Xu, F. Kong and R. Wang, *Angew. Chem. Int. Ed.*, 2013, **52**, 13769-13773; d) X. Zhao, X. Bu, T. Wu, S.-T. Zheng, L. Wang and P. Feng, *Nat. Commun.*, 2013, **4**, 2344; e) Q. Zhang, J. Yu, J. Cai, L. Zhang, Y. Cui, Y. Yang, B. Chen and G. Qian, *Chem. Commun.*, 2015, **51**, 14732-14734; f) I. R. Colinas, R. C. Silva and S. R. J. Oliver, *Environ. Sci. Technol.*, 2016, **50**, 1949-1954; g) A. V. Desai, B. Manna, A. Karmakar, A. Sahu and S. K. Ghosh, *Angew. Chem. Int. Ed.*, 2016, **55**, 7811-7815; h) L. Zhu, D. Sheng, C. Xu, X. Dai, M. A. Silver, J. Li, P. Li,

Y. Wang, Y. Wang, L. Chen, C. Xiao, J. Chen, R. Zhou, C. Zhang, O. K. Farha, Z. Chai, T. E. Albrecht-Schmitt and S. Wang, *J. Am. Chem. Soc.*, 2017, **139**, 14873-14876; i) D. Sheng, L. Zhu, C. Xu, C. Xiao, Y. Wang, Y. Wang, L. Chen, J. Diwu, J. Chen, Z. Chai, T. E. Albrecht-Schmitt and S. Wang, *Environ. Sci. Technol.*, 2017, **51**, 3471-3479; j) D. Sheng, L. Zhu, X. Dai, C. Xu, P. Li, C. I. Pearce, C. Xiao, J. Chen, R. Zhou, T. Duan, O. K. Farha, Z. Chai and S. Wang, *Angew. Chem. Int. Ed.*, 2019, **58**, 4968-4972; k) D. Zhang T. K. Ronson, J. Mosquera, A. Martinez, L. Guy and J. R. Nitchske, *J. Am. Chem. Soc.*, 2017, **139**, 6574-6577.

14. a) A. Karmakar, A. V. Desai and S. K. Ghosh, *Coord. Chem. Rev.*, 2016, **307**, 313-341; b) Y. Li, Z. Yang, Y. Wang, Z. Bai, T. Zheng, X. Dai, S. Liu, D. Gui, W. Liu, M. Chen, L. Chen, J. Diwu, L. Zhu, R. Zhou, Z. Chai, T. E. Albrecht-Schmitt and S. Wang, *Nat. Commun.*, 2017, **8**, 1354; c) C. Xiao, A. Khayambashi and S. Wang, *Chem. Mater.*, 2019, **31**, 3863-3877.

15. a) P. Li, N. A. Vermeulen, X. Gong, C. D. Malliakas, J. F. Stoddart, J. T. Hupp and O. K. Farha, *Angew. Chem. Int. Ed*., 2016, **55**, 10358-10362; b) A. V. Desai, A. Roy, P. Samanta, B. Manna and S. K. Ghosh, *iScience*, 2018, **3**, 21-30; c) A. V. Desai, S. Sharma, S. Let and S. K. Ghosh, *Coord. Chem. Rev*., 2019, **395**, 146-192; d) S.-Q. Deng, X.-J. Mo, S.-R. Zheng, X. Jin, Y. Gao, S.-L. Cai, J. Fan and W.-G. Zhang, *Inorg. Chem.*, 2019, **58**, 2899-2909.

16. SAINT Plus, Bruker AXS Inc.: Madison, WI, 2004.

17. L. Krause, R. Herbst-Irmer, G. M. Sheldrick and D. Stalke, *J. Appl. Cryst*., 2015, **48**, 3-10.

18. G. M. Sheldrick, SHELXTL, Reference Manual, version 5.1; Bruker AXS Inc.: Madison, WI, 1997.

19. G. M. Sheldrick, *Acta. Cryst*. 2008, **A64**, 112-122.

20. G. M. Sheldrick, *Acta. Cryst*. 2015, **C71**, 3-8.

21. L. Farrugia, WinGX, 2009, University of Glasgow: Glasgow, Scotland.

22. A. L. Spek, *Acta. Cryst*. 2015, **C71**, 9-18.

23. H. Pulin, R. Crane, D. Morgan and T. Scott, *J. Environ. Chem. Eng.*, 2017, **5**, 1166.

24. W. H. Baur and A. A. Khan, *Acta Cryst*., 1970, **B26**, 1584-1596.

25. R. J. Drout, A. J. Howarth, K.-i. Otake, T. Islamoglu and O. K. Farha, *CrystEngComm.*, 2018, **20**, 6140–6145.

26. Z.-Q. Li, J.-C. Yang, K.-W. Sui and N. Yin, *Mater. Lett.*, 2015, **160**, 412-414.

27. B.-J. Zhu, X.-Y. Yu, Y. Jia, F.-M. Peng, B. Sun, M.-Y. Zhang, T. Luo, J.-H. Liu and X.-J. Huang. *J. Phys. Chem. C*, 2012, **116**, 8601-8607.

28. J. Li, Y.-N. Wu, Z. Li, M. Zhu and F. Li, *Water Sci. Tech.*, 2014, **70**, 1391-1397.

29. T. A. Vu, G. H. Le, C. D. Dao, L. Q. Dang, K. T. Nguyen, Q. K. Nguyen, P. T. Dang, H. T. K. Tran, Q. T. Duong, T. V. Nguyen and G. D. Lee, *RSC Adv.*, 2015, **5**, 5261–5268.

30. J. Cai, X. Mao and W.-G. Song, Mater. *Chem. Front.*, 2018, **2**, 1389-1396.

31. Y.-N. Wu, M. Zhou, B. Zhang, B. Wu, J. Li, J. Qiao, X. Guan and F. Li, *Nanoscale*, 2014, **6**, 1105-1112.

32. J. Li, Y.-n. Wu, Z. Li, B. Zhang, M. Zhu, X. Hu, Y. Zhang and F. Li, *J. Phys. Chem. C*, 2014, **118**, 27382-27387.

33. H. Atallah, M. E. Mahmoud, A. Jelle, A. Lough and M. Hmadeh, *Dalton Trans.*, 2018, **47**, 799-806.

34. B. J. A. Tarboush, A. Chouman, A. Jonderian, M. Ahmad, M. Hmadeh and M. Al-Ghoul, *ACS Appl. Nano Mater.*, 2018, **1**, 3283-3292.

35. D. Xie, Y. Ma, Y. Gu, H. Zhou, H. Zhang, G. Wang, Y. Zhang and H. Zhao, *J. Mater. Chem. A*, 2017, **5**, 23794-23804.

Chapter 5

Rapid, selective capture of toxic oxo-anions of Se(IV), Se(VI) and As(V) from water by an ionic metal-organic framework (iMOF)

5.1 Introduction

To achieve global fresh water security through detoxification of wastewater presents as a contemporary strategy.[1] A recent report by United Nations states that in 2017, ~80% of world's wastewater is released without any pre-treatment.[1] Additionally, the global fresh water requirements are projected to increase ~20-55% by 2050, and bearing in mind the strain on present fresh water resources, detoxification of waste water appears as efficient way to tackle this problem.[2] To this end, the United States Environmental Protection Agency (US EPA) has enlisted few compounds based on their severe toxicity, hazardous nature and this includes several inorganic elements such as selenium, arsenic, etc. which need immediate addresal. The anthropogenic sources of selenium and arsenic include mining plants, industrial effluents, core fire plants ore processing, etc.[3] Yet another source of selenium production include nuclear power plants that generate radioactive isotope of selenium (^{79}Se) during the fission process which has a long half-life (3.77×10^5 years) thereby demanding immediate containment.[3] Typically, exposure to these elements is known to induce various defects and diseases including neurodegeneration, skin diseases, cardiovascular diseases, cancer, gene mutation, defects etc. therefore posing as severe environmental and health hazard.[4] Notably, in aqueous medium (oxic conditions), these elements prevail in their oxo-anionic form with selenium existing as Se(VI) (SeO_4^{2-})/Se(IV) (SeO_3^{2-}),($HSeO_3^-$) while arsenic as As(V) ($HAsO_4^{2-}$)/As(III)($HAsO_3^{2-}$) depending on pH.[5] The selective sequestration of these toxic oxoanions from waste water is a tortuous task pertaining to their extremely low binding affinity, presence of competing ions, and high solubility in water i.e. 58.5 g, 89.8 g, 39 g per 100 mL of water at room temperature, for the sodium salts of SeO_4^{2-}, SeO_3^{2-}, $HAsO_4^{2-}$ anions respectively.[6] With the current rate of growth and development it becomes imperative to maintain certain standards as issued by World Health Organization (WHO) and EPA wherein safe permissible concentration of selenium and arsenic in drinking water is as low as 50 ppb and 10 ppb respectively.[7]

The state-of-the-art materials tested for sequestering such toxic oxoanions include carbonaceous materials, metal oxides, resins, etc. via the efficient ion-exchange/adsorption based route.[8] Though offering tremendous potential, these materials are typically limited by low capacity, slow kinetics, low selectivity, etc. therefore offering tremendous scope for the development of novel materials to address the existing impediments.[9] Recently, Layered Double Hydroxides (LDHs) have emerged showing great potential toward toxic oxoanionssequestration.[10] With this background, it was envisioned that a highly suited material targeting mitigation of these aforementioned anions should encompass the following features (a) high binding affinity, (b) fast kinetics, (c) superior selectivity to sustain in real-time conditions, (d) appreciable

capacity, (e) high chemical stability and (f) efficient uptake at industrially relevant concentrations i.e ~10 ppm and at lower concentrations ~1 ppm etc.

In an effort to design a better sorbent material with aforementioned features, supramolecular coordination chemistry offers a fine control at the molecular level via imparting crucial non-covalent interaction sites between host and guest moieties.[11] These key interactions are known to govern fundamental properties such as selectivity, binding strength, etc., which are the prime factors in determining the efficiency of a sorbent material. Porous materials especially metal-organic frameworks (MOFs) offer such modular level engineering, rendering precise control over functionalities and properties, providing an edge in various applications including pollutant capture, separation, sensing, catalysis etc.[12] In recent years, ionic MOFs (iMOFs), particularly cationic MOFs have sparked significant interest toward the sequestration and trapping of major anionic pollutants.[13] A combination of desired features including modular porosity, guest template effect, active interacting sites in synergy with strong electrostatic forces at play, cationic MOFs can afford multi-level tunability to the system. Although presenting various prominent features, development of cationic MOFs targeted for capturing oxoanions of Se(VI), Se(VI), As(V), As(III) is still in its infancy owing to the weak binding nature of these anions to the host framework. Our group has recently demonstrated a water stable cationic MOF i.e. iMOF-1C as a selective scavenger for toxic oxoanions viz. $HAsO_4^{2-}$ and SeO_4^{2-} by tapping guest template effect.[13k] Though offering high selectivity and appreciable exchange capacity, this material lacks real-time application on account of its slow kinetics, limited chemical stability, low capacity owed to a smaller number of exchangeable anions. Inspired by this study, existing impediments were targeted via superior design of sorbent. Our efforts were directed toward the fabrication of a chemically stable cationic porous network integrated with template effect to achieve much desired selectivity, fast kinetics for oxo-anion capture. One of the recent report from our group highlights the rationale for constructing chemically stable cationic network based on the principles of HSAB, efficient utilization of smaller five membered imidazole rings as terminal moiety to achieve maximum coordination thereby shielding the metal center.[13l] In this work, our design strategy underscores the efficient utilization of guest template effect in synergy with HSAB principles/metal center shielding for constructing chemically stable positively charged nano-space with multiple guest binding sites which may result in efficient and rapid stabilization of toxic oxoanions via ion-exchange. Herein, remarkable efficacy towards selective, rapid sequestration of toxic oxoanions of Se(IV)/Se(VI) and As(V) was demonstrated, via a novel chemically stable cationic framework, iMOF-3C $[\{Ni(L)_2\}\cdot(SO_4)\cdot xG]_n$ wherein L=tris(4-(1H-imidazol-1-yl)phenyl)amine (TIPA), G = DMF, H_2O(Appendix 5.1). The material exhibited record high K_d values with appreciable uptake capacity along with fast kinetics. iMOF-3C underscores the potential of cationic MOFs

for selective removal of toxic oxoanions from complex solutions with concurrent anions including Cl^-/ NO_3^-/ SO_4^{2-}/ CO_3^{2-} even at higher concentrations. iMOF-3C exhibited successful capture of oxoanions of selenium and arsenic from complicated systems such as river water, mixtures of oxoanions at ultralow concentration and reduce it to acceptable limits in drinking water as specified by EPA. The host-guest chemistry of oxo-anion trapping has been investigated in detail with both density functional theory and Monte Carlo simulation which provide useful insights on the preferential location of anions within the framework as well as the interaction energy. The results display relevance of careful design of host-guest systems to develop more suited sorbents for this application.

5.2 Experimental

5.2.1 Materials

All solvents and reagents were commercially available and used without further purification. All experiments were performed at ambient temperature and Milli-Q water was utilized. Linker (L) (Appendix 5.1) was synthesized utilizing previous reported protocol.[13k]

5.2.2 Synthesis of iMOF-3C

Solvothermal reaction of linker L (8.86 mg, 0.02 mmol) and $NiSO_4.xH_2O$ (8.42 mg, 0.03 mmol) in a solvent combination of DMF:Water (2:1) was performed in a teflon lined vessel and heated at 130 °C for 48 h and then was cooled down to ambient temperature over 12 h. Hexagonal shaped crystals were separated from mother liquor by filtration and washed with DMF, water to remove any unreacted precursors followed by drying in air. Yield ~8.8 mg; % yield with respect to linker ~62%. Elemental Analysis: Calc. - C/H- 15.31 ; C/N- 3.30 ; C/S - 10.11 ; Found C/H- 15.18; C/N- 3.23; C/S- 10.1

For capture studies, the pristine MOF was exchanged with MeOH for 24 h and thereafter activated in vacuum and was utilized as it is for capture experiments.

5.2.3 Stability studies of iMOF-3C

For PXRD, FT-IR studies 30 mg of iMOF-3C was exposed 30 mL of different pH solution conditions including pH = 7, pH = 9 and pH =10 for 12 h. The solid samples were filtered and were used for measurements. For ICP spectroscopic analysis: 2 mg compound was exposed to 2 mL solution of various pH conditions including pH = 7, pH = 9 and pH =10. After 12 h, dispersed solutions were centrifuged and solution was taken out and Ni(II) content was analyzed by ICP spectroscopy which would correspond to any decomposition.

5.2.4 Uptake of oxoanions of Se(IV)/Se(VI)/As(V)

All sorption experiments of iMOF-3C for oxoanions of Se(IV)/Se(VI)/As(V) were performed at room temperature. Aqueous solutions of oxoanions (50 ppm-1000 ppm) of Se(VI)/ Se(IV)/As(V) were prepared by dissolving their corresponding salts Na_2SeO_3, Na_2SeO_4, $Na_2HAsO_4.7H_2O$ in milli-Q water. The uptake studies were performed by batch experiments wherein 2 mg of iMOF-3C was dispersed in 2 mL (V/m = 1000 mL/g) aqueous solution of oxoanions of Se(VI)/Se(IV)/As(V) and the mixture was stirred in vortex to ensure maximum contact. After 24 h, the solutions were centrifuged and solutions were diluted further with 2-3% HNO_3 acid solution for ICP spectroscopic analysis.

The adsorption capacity was determined by the following formula[12a]: $Q = (C_o - C_f) \times V/m$ where C_o and C_f are the initial and final concentration of elements in solution, V is the volume of solution and m is the mass of sorbent material. The sorption isotherm was fitted using Langmuir isotherm model[16] with the following equation:

(1) Langmuir adsorption Model: Mathematical equation: $q_e = q_m (K_L C_e/(1+ K_L C_e)$ wherein q_e represents equilibrium sorption capacity in mg/g, q_m represents theoretical maximum sorption capacity with monolayer coverage, K_L represents langmuir constant (L/mg), C_e represents the equilibrium concentration.

Sorption kinetics of iMOF-3C towards oxoanions of Se(IV)/Se(VI)/As(V)

Sorption kinetics experiments was performed by exposing 5 mg of iMOF-3C to 5 mL of 10 ppm aqueous solution of oxoanions of Se(IV)/Se(VI)/As(V). The solutions were stirred on vortex to ensure sufficient contact time. At specific intervals ranging from 10 min to 1800 min, suspensions were centrifuged for 2 mins at 7800 rpm and were diluted with 2-3% HNO_3 acid solution for further analysis by ICP spectroscopy.

The kinetics data was fitted with different kinetic model using the following equations:

(1) Pseudo first order kinetic model:

$\ln(q_e - q_t) = \ln q_e - k_1 t.$

(2) Pseudo Second order kinetic model:

$t/q_t = 1/K_2 q_e^2 + t/q_e$

wherein q_e is the amount adsorbed by sorbent after equilibration, q_t is the amount adsorbed by sorbent at time t, K_1 (min^{-1}) and K_2 ($g/mg\ min^{-1}$) is the equilibrium rate constants of pseudo first order and second order rate constant.

Low concentration (1 ppm) kinetic experiments were performed by exposing 6 mg of iMOF-3C to 6 mL aqueous solution of Se(IV)/Se(VI)/As(V) respectively. The solutions were stirred on vortex to ensure sufficient contact time and at specific time intervals ranging from 2 min-180 min, and 24 h. Further, the suspensions were centrifuged for 2 min at 7800 rpm. The solution were taken out and were analyzed further using ICP spectroscopy.

The % removal was calculated by the following equation: 100 % X (C_o - C_f)/ C_o. The distribution coefficient (Kd) was calculated based on the following equation[14] [{(C_o - C_f) / C_f) X V}/m].

5.2.5 Low concentration kinetics of iMOF-3C towards mixture of oxoanions of Se(IV)/Se(VI)/As(V)

Stock solution was prepared with effective concentration of Se(IV)/Se(VI)/As(V) ~1 ppm and ~10 ppm each. 6 mg of iMOF-3C was exposed to 6 mL aqueous solution containing mixture of Se(IV)/Se(VI)/As(V). The solutions were stirred on vortex to ensure sufficient contact time and after 24 h, the suspensions were centrifuged for 2 min at 7800 rpm. The solution was taken out and analysed further using ICP spectroscopy.

5.2.6 Competing ion studies of iMOF-3C towards capture of oxoanions of Se(IV)/Se(VI)/As(V) in presence of Cl^-, NO_3^-, SO_4^{2-}, CO_3^{2-}

Competing ion experiments was performed by exposing 2 mg of iMOF-3C to 2 mL solution containing 1 mL of 20 ppm aqueous solution of oxoanions of Se(IV)/Se(VI)/As(V) and 1 mL 20 ppm solution of Cl^-, NO_3^-, SO_4^{2-}, CO_3^{2-} with an effective concentration ~ 10 ppm. The solutions were stirred on vortex to ensure sufficient contact time and after 24 h, suspensions were centrifuged for 2 min at 7800 rpm and were diluted with 2-3% HNO_3 acid solution for further analysis by ICP spectroscopy.

For higher concentrations of competing ion, 2 mg of iMOF-3C was exposed to 1 mL of 10 ppm solution of respective aqueous solution of Se(IV)/Se(VI)/As(V) and 1 mL aqueous solution of SO_4^{2-}, CO_3^{2-} at higher concentration ratios of 100 ppm ,1000 ppm and 10000 ppm. After 24 h, the solutions were centrifuged and were diluted with 2-3% HNO_3 acid solution for further analysis by ICP spectroscopy.

5.2.7 Uptake towards oxoanions of Se(IV), Se(VI) and As(V) in real-time conditions

For real-time analysis, Mutha river water (From Pune, India) was spiked with 1000 ppb of Se(IV)/Se(VI)/As(V) each. 6 mg of iMOF-3C to 6 mL of this spiked solution. The solutions were stirred on vortex for 24 h to ensure sufficient contact time and after 24 h, suspensions were centrifuged for 2 min at 7800 rpm and solution was further analysis by ICP spectroscopy.

5.2.8 Physical Measurements

Powder X-ray diffraction patterns were recorded on Bruker D8 Advanced X-Ray diffractometer using Cu Kα radiation (λ= 1.5406 Å) in 5° to 40° 2θ range with a scan speed of 1.2° min^{-1}. The IR Spectra were acquired by using NICOLET 6700 FT-IR spectrophotometer using KBr pellet in 400-4000 cm^{-1} range. Transmission electron microscopy (TEM) images and high resolution TEM (HRTEM) images are captured by using a UHR FEG-TEM, JEOL JEM 2200FS field emission transmission electron microscope operated at 200 kV. The SEM images & EDX data were obtained using FEI Quanta 3D dual beam ESEM. Thermogravimetric analysis profiles were recorded on Perkin-Elmer STA6000, TGA analyzer under N_2 atmosphere with heating rate of 10 °C/min. ICP-AAS analysis were performed on Thermo Scientific iCE 3000 Series. ICP-MS was performed on Quadrupole inductively coupled plasma mass spectrometry (Q-ICP MS; Thermo Scientific iCAP Q) instrument. ICP-AES analysis was performed on ARCOS, Simultaneous ICP Spectrometer. Multi-element standards were purchased from in-organic ventures. X-ray Photoelectron Spectroscopy (XPS) studies were performed using K-Alpha+ model (Thermo Fischer Scientific, UK) with Al Kα source (λ = 1486.7 eV). The XPS spectra were corrected considering carbon C1s spectrum as standard. The standard peak position of C1s was taken at 284.6 eV and accordingly each element specific scans (short/high – resolution scans) were corrected. The data fitting was done using XPSPEAK41 software. During fitting Shirley background was considered and peak shape was optimized by appropriately adjusting Gaussian to Lorentzian ratio.

5.2.9 X-ray Structural Studies

Single-crystal X-ray data of compound iMOF-3C was collected at 100 K on a Bruker D8 Venture Duo X-ray diffractometer equipped with Microfocus X-ray source (operated at 50 W; 50 kV/1 mA), graded multilayer optics for monochromatic Mo Kα radiation (λ = 0.71073 Å) focused X-ray beam and Photon 100 CMOS chip based detector system. Crystal was mounted on nylon CryoLoops (Hampton Research) with Paraton-N (Hampton Research). The data integration and reduction were processed with SAINT soft-ware.[15] A multi-scan absorption correction was applied to the collected reflections.[16] The structure was solved by the direct method using SHELXTL[17-18] and was refined on F^2 by full-matrix least-squares technique using the SHELXL-2014/7[19] program package within the WINGX[20] programme. All non-hydrogen atoms were refined anisotropically. All hydrogen atoms were located in successive difference Fourier maps and they were treated as riding atoms using SHELXL default parameters. The structures were examined using the Adsym subroutine of PLATON to assure that no additional symmetry could be applied

to the models. The SQUEEZE option[21] was used to eliminate the contribution of disordered guest molecules and sulphate anions.

CCDC 1990643 (iMOF-3C) contains the supplementary crystallographic data.These data can be obtained free of charge from The Cambridge Crystallographic Data Centre via www.ccdc.cam.ac.uk/data_request/cif.

5.2.10 DFT calculations

Periodic geometric optimization and the static binding energies for each anion in iMOF-3C frameworks were calculated using density functional theory (DFT) as implemented in the software package VASP 5.4.4.[22] It is well-known that standard DFT methods based on generalized gradient approximation do not fully account for the long-range dispersion interactions between the framework and the bound adsorbates. To accurately estimate static binding energies for each ani-on with the framework, dispersion corrections using DFT-D3 method was done.[23] Electron exchange and correlation were described using the generalized gradient approximation Perdew, Burke, and Ernzerhof (PBE)[24] form and the projector-augmented wave potentials were used to treat core and valence electrons.[25] In all cases, plane-wave kinetic energy cutoff of 800 eV was used and a Gamma-point mesh for sampling the Brillouin zone. The ionic coordinates were relaxed until the Hellman-Feynman ionic forces were less than 0.01 eV/Å. The lattice parameters were fixed at the experimental values.

5.2.11 Electrostatic Potential Surface (ESP)

Density functional theory (DFT) computations were performed using the Gaussian program[26] to derive the ESP surface of iMOF-C3 cluster model. Based on the periodic DFT optimized structure of iMOF-C3, two different cluster models which contains one Ni^{2+} cation and six linkers were constructed. Each linker contains one imidazole ring and one benzene ring and the terminal sp^3 carbon atom of each linker was saturated by H atoms. Geometry optimization of fragment were carried out in the liquid phase at (SMD)B3LYP-D3/SDD~6-31G(d) level. The SMD implicit solvent model[27] with water as the solvent was used to include the solvation effects. The hybrid B3LYP exchange-correlation functional[28-29] combined with the D3 version of Grimme's dispersion[30] were employed. The Stuttgart/Dresden relativistic effective core potential and the associated valence basis set (SDD) were applied for Ni[31-32], while the 6-31G(d) basis sets were used for C, H, O, and N.[33] During optimizations, the Ni^{2+} cations, the N and C atoms of the imidazole rings, and the terminal sp^3 carbons were fixed. The electrostatic potential (ESP) on the van der

Waals (VDW) surfaces (isodensity = 0.001 a.u.) of iMOF-3C fragment was derived based on its ground state electron density.

5.2.12 Simulated Annealing:

The lowest energy configuration of each anions in the primitive cell of iMOF-C3 MOF structure was obtained from the classical simulated annealing technique using classical force field as implemented in sorption module in Materials Studio.[34] The framework atoms are kept frozen during simulation. The interactions of gas-adsorbent and gas-gas were modeled as a combination of pairwise site-site Lennard-Jones (LJ) and Coulombic potentials. The LJ potential parameters of both the framework atoms and the adsorbates are adopted from the Universal force field (UFF).[35] The charges for the framework atoms were as-signed based on the Qeq charges as implemented in Materials Studio package. DFT optimization was per-formed on each anion using Dmol3[34] module. The Becke exchange plus Lee-Yang-Parr correlation functional and all-electron core potentials were used. The double-ξ numerical polarization (DNP) basis set was adopted, which is comparable to the 6-31G(d,p) Gaussian type basis set. The DNP basis set incorporates d-type polarization into heavier atoms and p-type polarization into hydrogen atoms. Electrostatic potential charges were assigned to each anion based on the DFT optimised model.

In the simulated annealing method, the temperature was lowered stepwise, allowing the gas molecule to reach a desirable configuration based on different moves such as rotation, translation and repositioning with pre-set probabilities of occurrence. This process of heating and cooling the system was repeated in several heating cycles to find the local minima. Forty heating cycles were performed where the maximum temperature and the final temperature were 10^5 K and 100 K, respectively.

Binding Energies:

The initial location of the anion in the primitive cell of iMOF-C3 was obtained from the classical simulated annealing technique as described above. Static binding energies (ΔE) at 0 K in vacuum were calculated using the following expression -

$$\Delta E = E(MOF+Anion) - E(MOF+) - EAnion$$

where Ex refers, respectively, to the total energies of the MOF + Anion complex, the charged MOF+ alone, and the anion molecule respectively.

5.3 Results and Discussion

iMOF-3C was synthesized solvothermally by mixing linker (L), $NiSO_4 \cdot xH_2O$ in a solvent combination of DMF: H_2O (2:1) (Figure 5.1a, Appendix 5.1). Hexagonal-shaped single crystals of iMOF-3C were characterized via single crystal X-ray diffraction (SC-XRD) analysis and the cationic part of the framework was found to be isostructural to IPM-201[131] (Figure 5.1a, Appendix 5.2-5.3). SC-XRD analysis revealed that iMOF-3C crystallizes in trigonal crystal system with space group, *R*-3 (Appendix Table 13). Detailed structural analysis unveiled the two-dimensional layered structure (Figure 5.1b, Appendix 5.4), similar to LDHs materials reported in literature[36] which have been successfully utilized as scavengers for toxic pollutants. Further, structural analysis revealed basic building unit as six coordinated Ni(II) metal nodes with terminal nitrogen atom of imidazole as binding moiety (Appendix 5.5). The tridentate linker (L) with sp3 nitrogen atom at the center extends the network further[37] via forming coordination bond to three distinct metal centers, thereby creating inherent porosity as revealed by in depth structural analysis (Appendix 5.6). The one-dimensional (1D) porous channels with dimensions 6.6 X 4.89 $Å^2$ (excluding van der Waals radii) (Appendix 5.7), were occupied by disordered charge balancing sulphate (SO_4^{2-}) anions as confirmed by various experimental techniques including X-ray photoelectron spectroscopy (XPS), and Fourier-transform infrared spectroscopy (FTIR). XPS analysis of pristine MOF showed peak at 170.3 eV which matches well with the literature value[38] corresponding to sulphur in context of SO_4^{2-} anions (Appendix 5.8).

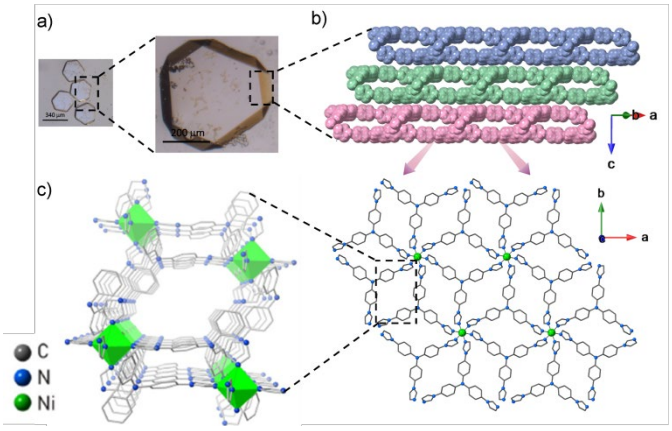


Figure 5.1. (a) Single crystals of iMOF-3C. (b) Layered structure of iMOF-3C with zoomed view of single net. (c) Packing diagram of iMOF-3C showing one dimensional porous voids. (Disordered guests, H atoms and solvent molecules have been omitted for clarity). Scale Bar: 340 µm and 200 µm.

FTIR exhibited peak at 1070 cm^{-1} and 1134 cm^{-1} corresponding to presence of SO_4^{2-} anions present within the voids (Appendix 5.9). The bulk phase purity was confirmed by powder X-ray diffraction (PXRD) analysis which showed identical diffraction pattern as calculated from pristine MOF (Appendix 5.10). Thermogravimetric analysis revealed negligible weight loss prior to 400 °C after vacuum treatment of MeOH exchanged phase (Appendix 5.11). Further, towards understanding the chemical stability of iMOF-3C, compound was exposed to solution of varied pH (7-10) and obtained solids as well as the filtrate was characterized thoroughly. Optical microscopic images of solid compounds revealed retention of hexagonal-shape of the crystals; while FESEM analysis confirmed analogous morphology with the pristine MOF (Appendix 5.12-5.14). PXRD data analysis lucidly confirmed retention of long-range order with identical diffraction pattern to the pristine MOF (Appendix 5.15). The filtrate was analyzed by Inductively coupled plasma mass spectroscopy (ICP-MS) which showed negligible concentration of Ni(II) ions in the filtrate solution thereby affirming stability of iMOF-3C in various media (Appendix Table 5.2).

Further, prior to oxoanion capture studies, the preliminary investigation for analyzing stability of iMOF-3C towards aqueous solution of oxoanions viz. $HSeO_3^-$, SeO_3^{2-}, SeO_4^{2-}, $HAsO_4^{2-}$ was performed. Optical microscopy images confirmed that crystals maintained hexagonal-shape while unit cell parameters were found similar to parent framework (Appendix 5.16, Appendix Table 5.1). PXRD data analysis showed similar peak pattern hence establishing stability of material towards aforementioned toxic oxoanions (Appendix 5.17). FESEM analysis of exposed solid compounds revealed similar morphology while the EDX spectra substantiated presence of Se(IV)/Se(VI)/As(V) in the exchanged samples while the %weight of sulphur decreased (Appendix 5.18-5.21). ICP spectroscopy of the supernatant showed negligible concentration of Ni(II) thus confirming framework integrity (Appendix Table 5.3). Enthused from these observation, detailed investigation towards the capture of oxoanions of Se(IV)/Se(VI)/As(V) was performed.

5.3.1 Low concentration studies towards oxoanions of Se(IV), Se(VI) and As(V)

Capture studies at low concentrations viz. at 1000 ppb, 10 ppm hold high relevance as these represent industrially relevant waste water concentrations. iMOF-3C was evaluated for its ability to capture trace concentrations (~1000 ppb) of oxoanions viz. Se(IV)/ Se(VI)/As(V). Time dependent kinetics studies were performed and the samples were analyzed by ICP spectroscopy. The results demonstrated iMOF-3C as efficient sorbent towards capturing trace amounts of Se(IV)/Se(VI)/As(V), as ~ 99.9 % removal within ~ 5 mins was observed (Appendix 5.22). iMOF-3C could successfully reduce the concentration of these toxic anions in water < 10 ppb thereby successfully fulfilling the guidelines provided by US-EPA and WHO (<

10 ppb for arsenic and < 50 ppb for selenium) for potable water.[7] The efficiency of the sorbent was further confirmed due to lack of leaching, as the adsorbed amount remained constant after 30 mins (Appendix 5.22). This exceptional performance can be ascribed to the high affinity of the cationic framework towards toxic oxoanions of Se(IV)/Se(VI)/As(V).

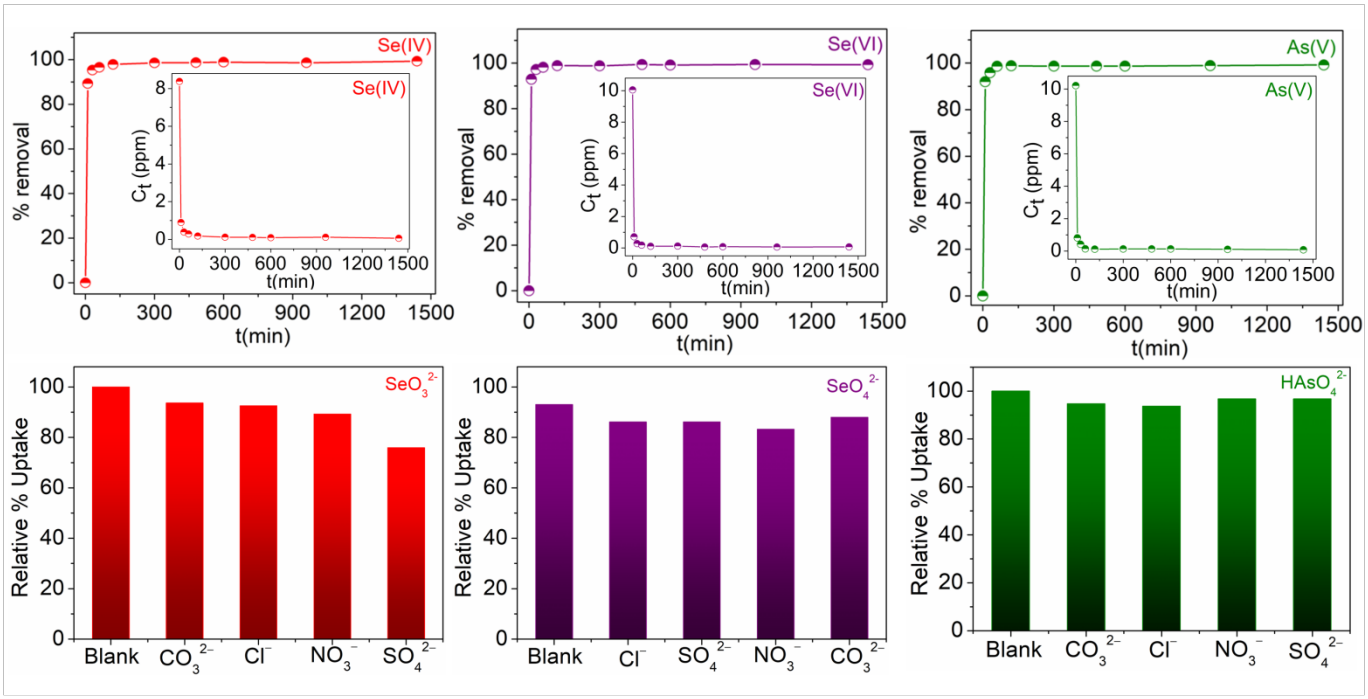


Figure 5.2: (Upper row) Kinetics sorption profile for uptake of oxo anions of Se(IV)/Se(VI)/As(V) at 10 ppm. (Inset: Concentration Vs time plot.) (Bottom Row): Relative percentage uptake of oxoanions of Se(IV)/Se(VI)/As(V) in presence of binary mixture of competing ions.

To further probe the material, the capture performance towards mixture of oxoanions of Se(IV)/Se(VI)/As(V) at trace concentrations (~1000 ppb) was done. The results established that iMOF-3C can simultaneously reduce the concentration of oxoanions of Se(IV)/Se(VI)/As(V) to < 10 ppb, thereby by meeting the demands for drinking water (Appendix 5.23). These experiments reveal the remarkable ability of iMOF-3C to capture oxoanions of Se(IV)/Se(VI)/As(V) at trace concentrations with fast kinetics. For further evaluating sorbent performance and pathway of capture, iMOF-3C was exposed to an aqueous solution consisting oxoanions of Se(IV)/Se(VI)/As(V) at 10 ppm respectively, and the concentrations were monitored by ICP spectroscopy after certain time intervals. The results indicate fast kinetic performance as the sorption equilibrium reached within 30 mins (Appendix 5.24-5.28) with > 95% removal observed for oxoanions of Se(IV)/Se(VI)/As(V). Further, iMOF-3C showed ~ 99.9%, ~ 99.4%, ~ 99.9% removal

towards oxo-anion of Se(VI), Se(IV) and As(V) respectively upon prolonged exposure (Appendix Table 5.4-5.6). The performance of iMOF-3C towards aqueous solution of As(III) was also checked, but to our surprise negligible uptake was observed, as compared to Se(IV)/Se(VI)/As(V) (Appendix 5.29). It is noteworthy to mention that at pH= 7, Se(IV) exists in equilibrium between $HSeO_3^-$/ SeO_3^{2-}, while at pH>2 Se(VI) exists majorly as SeO_4^{2-} and As(V) dominates as $HAsO_4^{2-}$ at neutral pH, all existing in anionic form.[5,39] This unique behaviour of iMOF-3C toward As(III) capture can be explained on the basis of the speciation of As(III) present at pH=7, which is neutral form, devoid of any negative charge thereby lacking affinity towards iMOF-3C. This experiment affirms the ability of the cationic network to selectively sequester anionic pollutants and ion-exchange as modus operandi during the capture of oxoanions of Se(IV)/Se(VI)/As(V).

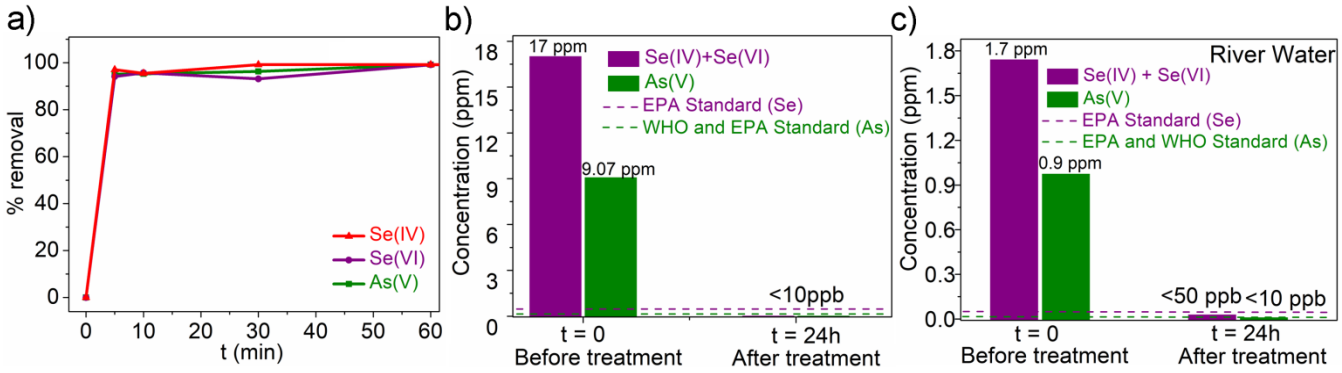


Figure 5.3: (a) Kinetics sorption profile of iMOF-3C at ultralow concentration ~1000 ppb of Se(IV)/Se(VI)/As(V). Bar diagram showing decrease in concentration of oxoanions of Se(IV)/ Se(VI)/ As(V) after treatment with iMOF-3C in (b) mixture of oxoanions containing Se(IV)+Se(VI)+As(V). (c) River Water spiked with a mixture of 1000 ppb each of Se(IV)+Se(VI)+As(V).

Further, the ability of the compound to capture mixture of oxoanions at higher concentration (~10 ppm) was analysed and the results reveal that iMOF-3C can simultaneously reduce the concentration of selenium and arsenic below the permissible limit specified by EPA and WHO for drinking water (Figure 5.3b, Appendix 5.23a). It is noteworthy to mention that the inherent binding affinity of oxoanions of selenium depends upon the speciation, wherein oxoanions of Se(VI) are weakly adsorbing while Se(IV) oxoanions adsorb strongly. Notably, iMOF-3C performs well in sequestering both species i.e for Se(IV)/Se(VI) oxoanions from aqueous solution. Typically, the efficacy of any sorbent material is assessed on the basis of distribution coefficient value (K_d values) and typically sorbents having K_d values > 10^4 mL/g are considered as outstanding.[40] The physical interpretation of K_d can be understood in terms of the ability of

sorbent material to efficiently separate sorbate (in this case of oxoanions) from aqueous medium onto the sorbent (MOF). In this regard, iMOF-3C performs well as it achieved K_d value for Se(VI), Se(IV), As(V) capture as 1.0 X 10^6 mL/g, 0.8 X 10^6 mL/g, 1.2 X 10^6 mL/g respectively (Appendix Table 5.1, Appendix 5.4-5.7), thus making this material as an exceptional host to capture oxoanions of Se(IV)/Se(VI)/As(V) which can rationalize the observed kinetic data. The sorption kinetics performance was evaluated with standard kinetic rate equations (Experimental section) and fitting parameters were calculated from the rate equations (Appendix Table 5.8). The experimental kinetics data fits well with the pseudo second order theoretical kinetic model with $R^2 \sim 1$ indicating chemisorption process.[36a] From the fitting, the k_2 values for Se(VI), Se(IV), As(V) were determined as 9.3 X 10^{-2} g mg^{-1} min^{-1}, 3.9 X 10^{-2} g mg^{-1} min^{-1}, 5.7 X 10^{-2} g mg^{-1} min^{-1} indicating differential rate of adsorption (Appendix 5.8). It is noteworthy to mention that k_2 value for Se(VI)/Se(IV) adsorption was found to be an order of magnitude higher than the commercially available resins/activated alumina, making iMOF-3C an efficient sorbent.[41]

5.3.2 Maximum uptake capacity studies towards oxoanions of Se(IV), Se(VI) and As(V)

The maximum uptake performance was evaluated for iMOF-3C towards oxoanions of Se(IV)/Se(VI)/As(V) by performing concentration dependent sorption isotherm. The experimental data showed complete saturation of iMOF-3C around ~ 300 ppm for Se(VI), Se(IV), As(V) which can be correlated to the high affinity of the material to these oxoanions (high K_d value) and its ability to perform in extremely contaminated sites. The sorption isotherm revealed a maximum adsorption capacity for Se(IV)/Se(VI)/As(V) as 140 mg/g, 72 mg/g and 75 mg/g (Appendix 5.30). Further, the sorption isotherm curve was fitted with Langmuir model with $R^2 \sim 1$ which confirms monolayer sorption (Appendix 5.30). The theoretical maximum q_m values estimated from the fitting for Se(IV)/ Se(VI)/ As(V) are 140.5 mg/g, 73 mg/g, 75.5 mg/g respectively and were found to be in close agreement with the experimental values. A comparison with the state-of-the-art materials revealed that these uptake amount represents among the highest values reported in literature (Appendix Table 5.10-5.12). Specifically, in the domain of cationic MOFs these uptake capacities represent among the highest and especially for Se(IV) its uptake capacity was found to be highest in the domain of cationic MOFs (ionic MOFs).

5.3.3 Selectivity studies towards oxoanions of Se(IV), Se(VI) and As(V)

Selectivity is an inherent property of material which governs the effectiveness of capture in real-time scenario. Porous materials targeting applications in waste water remediation needs to be thoroughly assessed for solid state sorbents with potential for any real-time application. The performance of iMOF-3C

was tested towards the capture of oxoanions of Se(IV)/Se(VI)/As(V) in presence of commonly encountered competing ions[42] including CO_3^{2-}, SO_4^{2-}, Cl^-, NO_3^- (1:1 equivalent).

	C_0 (ppm)	C_f	% removal	K_d (mL/g)
Se(IV)+ Se(VI)	17	<10 ppb	>99.94	$> 1.6 \times 10^6$
As(V)	9.07	<10 ppb	>99.8	$> 0.9 \times 10^6$

Table 1: Sorption Data of iMOF-3C for mixture of oxoanions of Se(IV)+Se(VI)+As(V).

iMOF-3C exhibited excellent selectivity towards oxoanions of Se(VI), As(V), Se(IV) with negligible effect on uptake performance in presence of competing ion (Figure 5.2, Appendix 5.31). Further, the selectivity studies was extended to check the performance at higher concentrations (100, 1000 equivalent) of competing ions (CO_3^{2-}, SO_4^{2-}) which are more prone to interfere. A decrease in the uptake performance for iMOF-3C was found, but it showed successful capture of oxoanions from such complicated system (Appendix 5.32). It is noteworthy to mention that materials exhibiting such selectivity for oxoanions of As(V) in presence of competing ions viz. SO_4^{2-}, CO_3^{2-}, Cl^-, NO_3^- are extremely rare and it should be emphasized that commercially available resins functioning as ion-exchangers fail to achieve such selective behaviour.[43]

5.3.4 Uptake towards oxoanions of Se(IV), Se(VI) and As(V) in real-time conditions

For any sorbent material designed for sequestration of oxoanions, the performance should be checked in real-time conditions. For this, the performance of compound was checked especially in basic conditions, as waste water pH lies within this range (at pH 7-9). The experiment revealed that compound maintains ~90% of uptake performance observed at pH=7 which makes this material extremely attractive for testing in real-time scenario (Appendix 5.33). For real time study in batch scale, the Mutha river waste (Pune, India) was utilized and initially the stability of iMOF-3C was tested in the river water. The PXRD analysis showed that iMOF-3C retains its framework integrity in such complex solution and FESEM showed similar hexagonal morphology thus can serve as a sorbent (Appendix 5.34-5.35). Further, the Mutha river water which contains many competing anions and organic waste was spiked with 1 ppm of Se(VI)/Se(IV)/As(V) and exposed this solution to iMOF-3C. After 24 h, ICP spectroscopic analysis of the supernatant revealed that iMOF-3C could successfully decrease the concentration of selenium and arsenic to < 10 ppb which is well below the permitted values of EPA and WHO, thus making iMOF-3C as a potential sorbent material to entrap these oxoanions from complex solutions (Figure 5.3C, Appendix 5.36).

5.3.5 Solid state characterization of iMOF-3C post adsorption of oxoanions of Se(IV), Se(VI) and As(V)

The oxoanions exposed solids were thoroughly characterized post ion-capture via various techniques including PXRD, ICP, FESEM, TEM, XPS. PXRD analysis indicated complete retention of long-range order with peak pattern analogous to pristine iMOF-3C (Appendix Table 5.1, Appendix 5.17). In addition, the stability of iMOF-3C was also affirmed after ion-exchange by monitoring concentration of Ni(II) through ICP spectroscopy. The experiment revealed almost negligible concentration of Ni(II) in the filtrate thus indicative of exceptional stability of network (Appendix Table 5.3). The exchanged solids were further characterized for confirming the inclusion of toxic oxoanions within the framework via FESEM-EDX, STEM-EDS mapping, XPS, FTIR. FT-IR analysis of post-adsorption samples revealed peaks corresponding to the presence of oxoanions of Se(VI), Se(IV) and As(V) at 876 cm^{-1} , 836 cm^{-1}, 726 cm^{-1} respectively (Appendix 5.37). These values correspond to the stretching frequencies of Se-O and As-O bond and corroborated with the literature.[10, 14d] XPS analysis showed peaks corresponding to the respective elements Se(IV), Se(VI), As(V) at 58.9 eV, 59.7 eV and 45 eV which match well to the reported values for corresponding oxoanions (Appendix 5.39-541).[10,14] Additionally, STEM-EDS mapping showed homogenous distribution of these toxic elements in iMOF-3C while maintaining two dimensional nature of the crystals (Figure 5.4, Appendix 5.38).

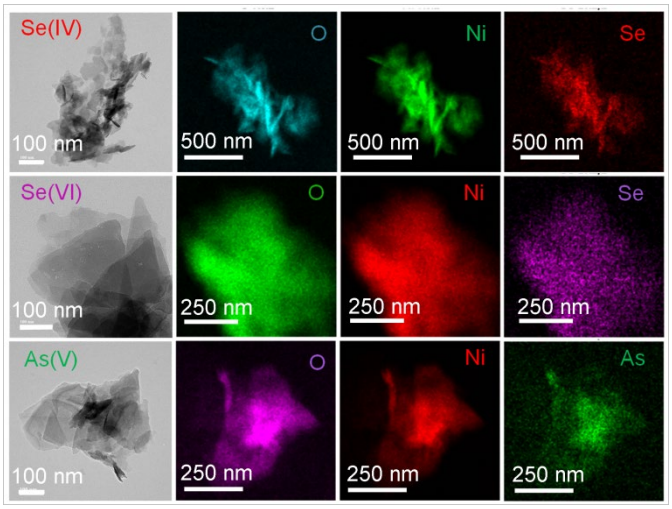


Figure 5.4: Post ion-exchange analysis for iMOF-3C exposed to oxoanions of Se(IV)/Se(VI)/As(V) showing STEM-EDS mapping profile.

5.3.6 Mechanistic insights of the capture process

Firstly, based on the DFT optimised model of iMOF-3C, NVT simulated annealing using Monte Carlo approach were performed to recognize the most preferable site of various anions within the porous framework. Secondly, the binding energies between iMOF-3C structure and different anions were calculated based on periodic model using the dispersion corrected DFT method (DFT-D3) as implemented in the software package VASP 5.4.4. Figure 5.5 shows the optimized location of oxoanions and their calculated binding energies. Furthermore, the location of anions identified from DFT correlates well with the electrostatic potential distribution of iMOF-3C cluster model which contains one Ni^{2+} cation and six linkers (Appendix 5.42). In this model, the positive charges on the Ni^{2+} is uniformly transferred to the linkers, particularly to the imidazole moiety; the region where the anions are preferably located (Figure.5. 5, Appendix 5.43).The site of stabilization of oxoanions includes hydrogen bonding interaction between the hydrogen atoms of imidazole moiety of the linker in iMOF-3C and oxygen atoms of the toxic anions i.e. C-H(imidazole)...O(oxoanion) (Figure 5.5, Appendix 5.43) which highlights the role of imidazole moiety in the overall distribution of positive charge and is also observed in other porous materials as site of stabilization.[44]

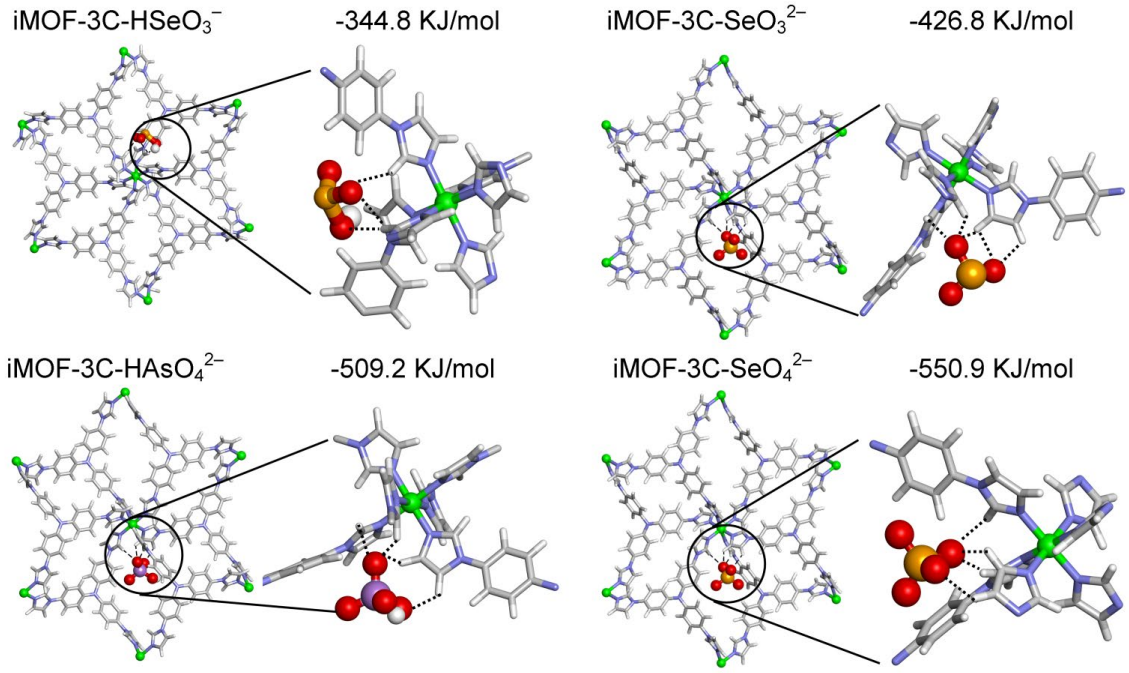


Figure 5.5: DFT optimized structures and corresponding zoomed view showing hydrogen bonding interactions of iMOF-3C with different oxoanions and binding energies.

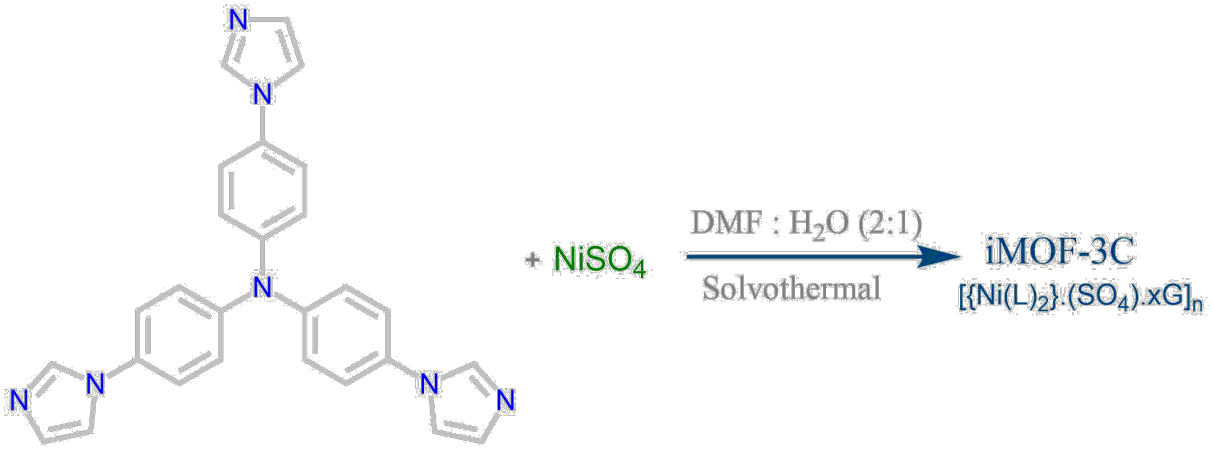
As shown in Figure 5.5, the calculated static binding energy of iMOF-3C_SeO_4^{2-} (-550.9 kJ/mol) and iMOF-3C_$HAsO_4^{2-}$ (-509.2 kJ/mol) are higher than those of iMOF-3C_SO_4^{2-} (-477.9 kJ/mol) and iMOF-3C_CO_3^{2-} (-354.7 kJ/mol) (Appendix 5.43). Also, they are considerably higher than those of other anions such as iMOF-3C_Cl^- (-296.8 kJ/mol) and iMOF-3C_NO_3^- (-277.2 kJ/mol) (Appendix 5.44 and Appendix Table 5.9). This shows that iMOF-3C framework exhibit exceptional selectivity towards oxo anions when compared to other anions. The observed trend in binding energies i.e. SeO_4^{2-}> $HAsO_4^{2-}$>SO_4^{2-}~ SeO_3^{2-}>>> CO_3^{2-}> Cl^-> NO_3^- may be rationally explained on account of multiple factors including shape and size of oxoanion, matching fit of anions within the binding pockets of the framework. The trend suggests favored stabilization of toxic oxoanions with tetrahedral geometry as compared to non-tetrahedral Se(IV) oxoanions and competing ions (Cl^-, NO_3^-, CO_3^{2-}). It is noteworthy to mention that although selenate [Se(VI)] dominates as the inorganic form of Selenium in natural environment along with higher mobility, materials such as oxides and clays have greater preference for selenite [Se(IV)], and selenate is only weakly adsorbed.[39] A reverse effect in case of iMOF-3C was observed wherein stabilization of selenate (SeO_4^{2-}) oxoanion is favored over selenite anion as clearly evidenced from the binding energies. Furthermore, consistent with the binding energy calculations, the concentration dependent sorption profile of both oxo anions Se (VI) and As (V) show a steep increase in uptake when compared to Se(IV) oxo anion (Appendix 5.30). Thus, the current findings wherein the iMOF-3C demonstrates higher affinity (in terms of binding energies) for oxoanions of selenium and arsenic, is a paramount advancement for solid state sorbents developed toward environmental remediation of toxic inorganic pollutants. These results underscore the utility and potency of iMOFs as tunable, solid materials for addressing pressing concerns of trapping priority environmental pollutants.

5.4 Conclusion

In this work, a novel chemically stable cationic MOF viz. iMOF-3C was reported that act as an efficient, selective scavenger toward oxoanions of selenium and arsenic viz. $HSeO_3^-$, SeO_3^{2-}, SeO_4^{2-}, $HAsO_4^{2-}$. By rational choice of building blocks, selectivity for toxic anions as well high chemical stability was realised. The material affords drinking quality water within minutes by reducing concentration of toxic elements Se(IV), Se(VI), As(V) (1000 ppb) to <10 ppb, meeting the permissible limit set by WHO and EPA for consumption. The observed ultrafast kinetics could be explained on the basis of remarkable affinity (K_d > 10^6 mL/g) of cationic network towards these oxoanions which is the among highest value in the field of MOFs. The sorbent also displayed high affinity towards toxic oxoanions even in the presence of large excess of competing ions with an appreciable sorption capacity. The excellent sequestration ability of

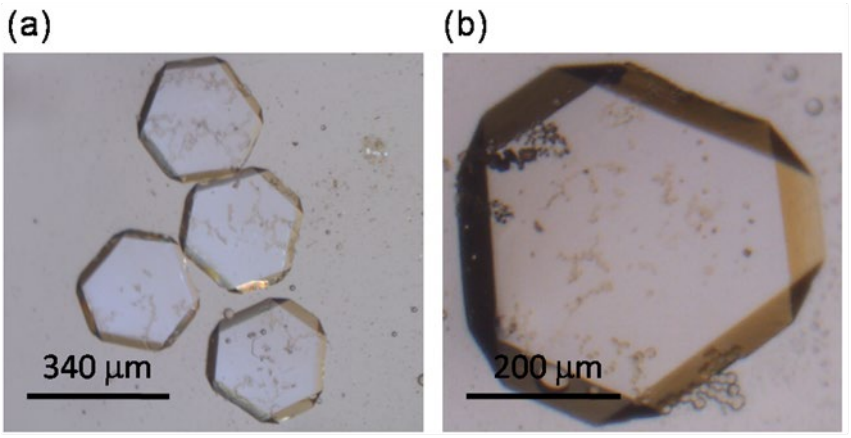
iMOF-3C was further highlighted in real time waste water, such as river water wherein the material performed remarkably well in meeting the EPA standards specified for drinking water. The experimental finding were strongly supported by DFT studies which shed significant light on the location and the binding energies of various anions with the adsorbent. The relatively high binding energy values as obtained for the framework and oxoanions ($HSeO_3^-$, SeO_3^{2-}, SeO_4^{2-}, $HAsO_4^{2-}$), when compared against the energies obtained for the competing ions and parent framework, complements the observed selectivity resulting in efficient stabilization of toxic oxoanions in the porous voids. This detailed investigation will enhance the basic understanding toward developing sorbent targeting oxoanions of arsenic and selenium, hitherto known for their weaker affinity in literature, and underscore the utility and potency of MOFs as tunable, solid materials for real-time applications. With such promising results, this report will propel the development of solid-state sorbents targeted towards the capture of oxoanions of selenium and arsenic.

5.5 Appendix

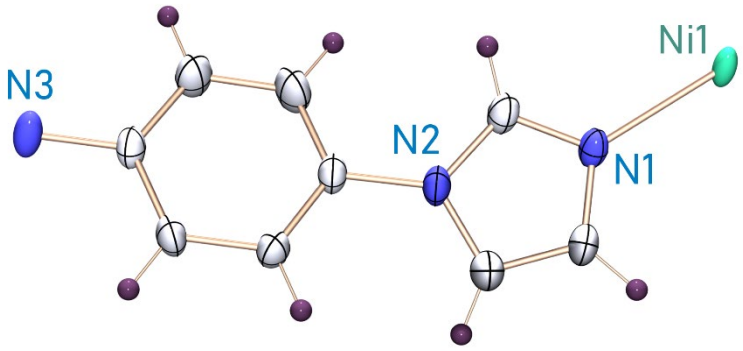


Appendix 5.1: Schematic representation showing synthesis for iMOF-3C.

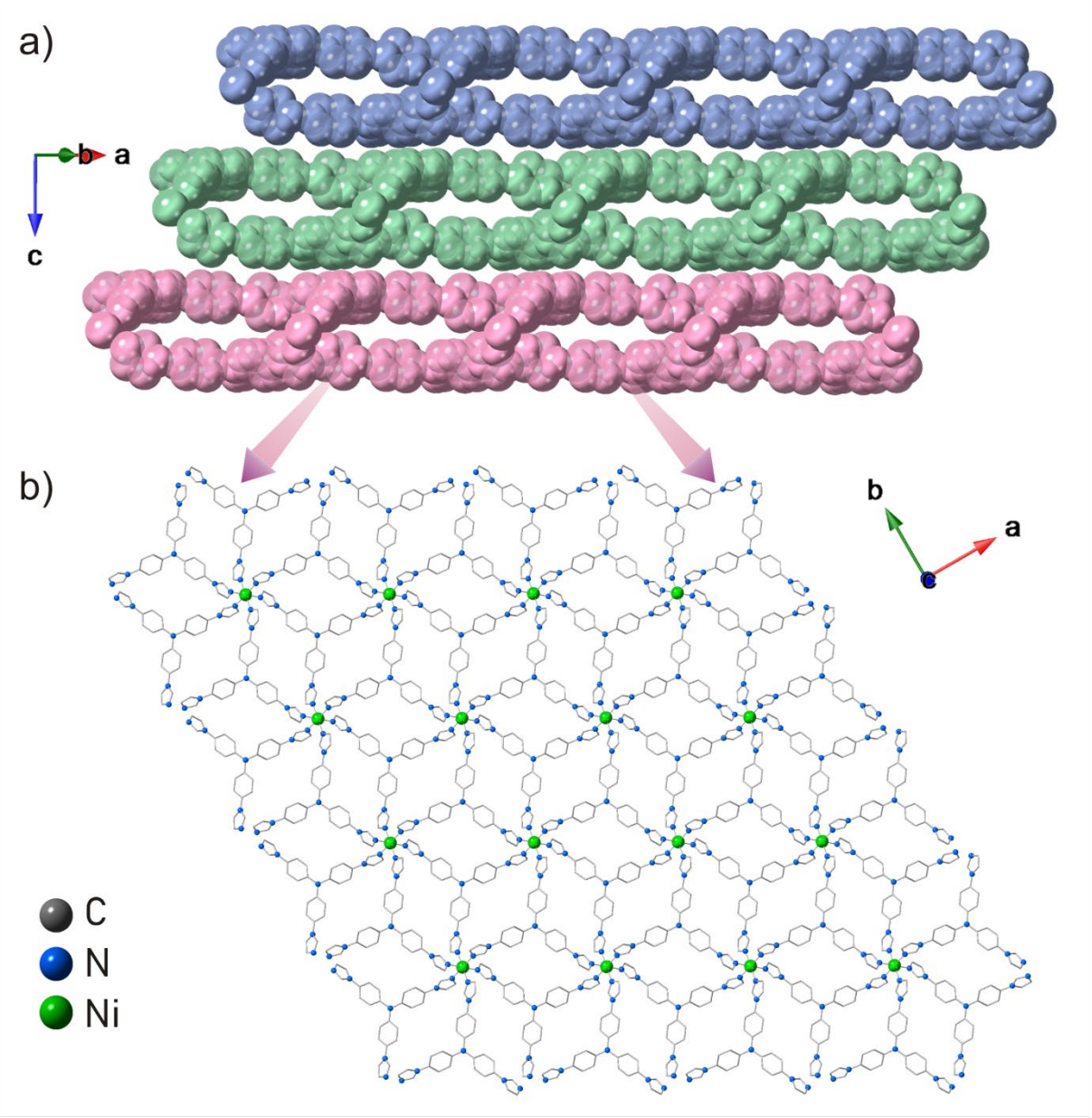
-



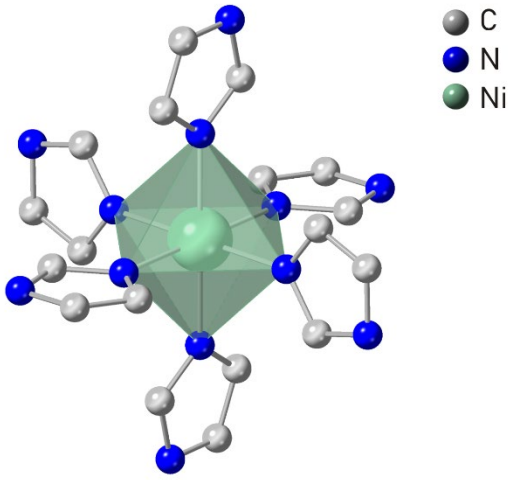
Appendix 5.2: Photographs of parent framework viz. iMOF-3C, a) Bulk and b) single crystal under optical microscope.



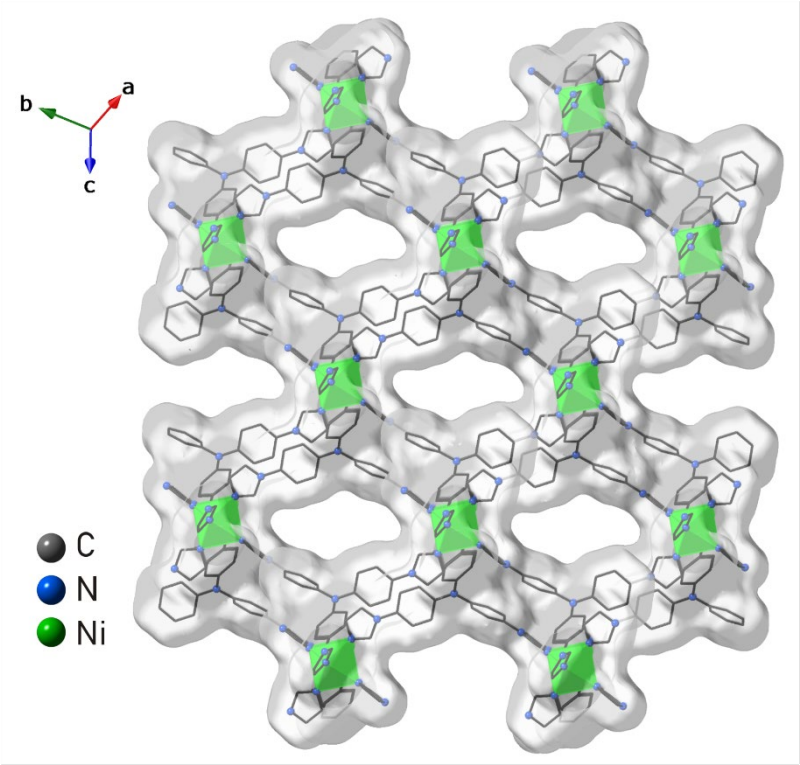
Appendix 5.3: ORTEP diagram of asymmetric unit of pristine MOF.



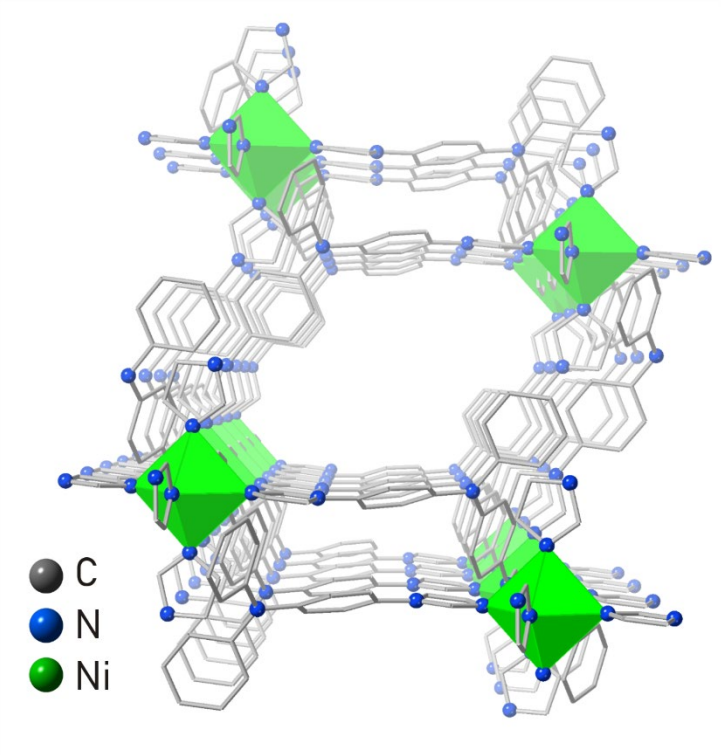
Appendix 5.4: Packing diagram showing two dimensional layered structure of iMOF-3C and a single net showing coordination of linker(L) with Ni(II) nodes.(H-atoms omitted for clarity).



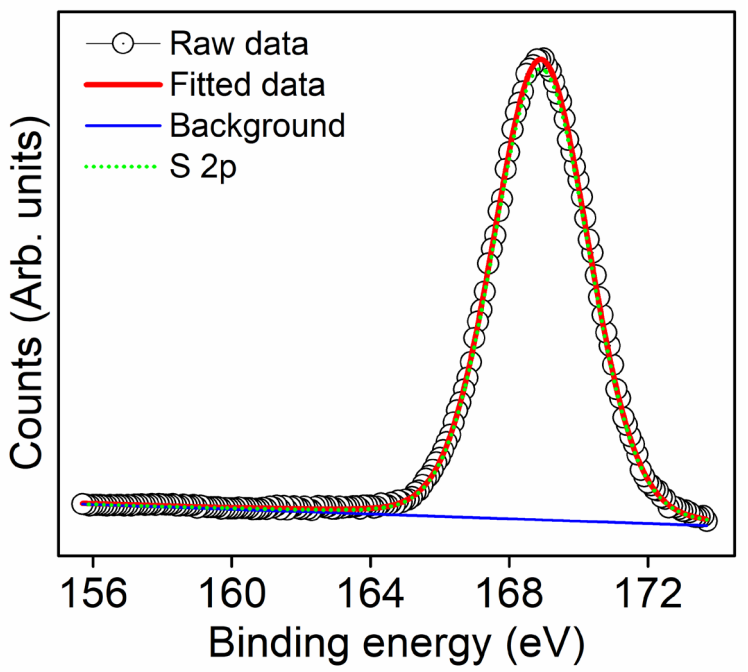
Appendix 5.5: Coordination environment of the Ni(II) metal center.



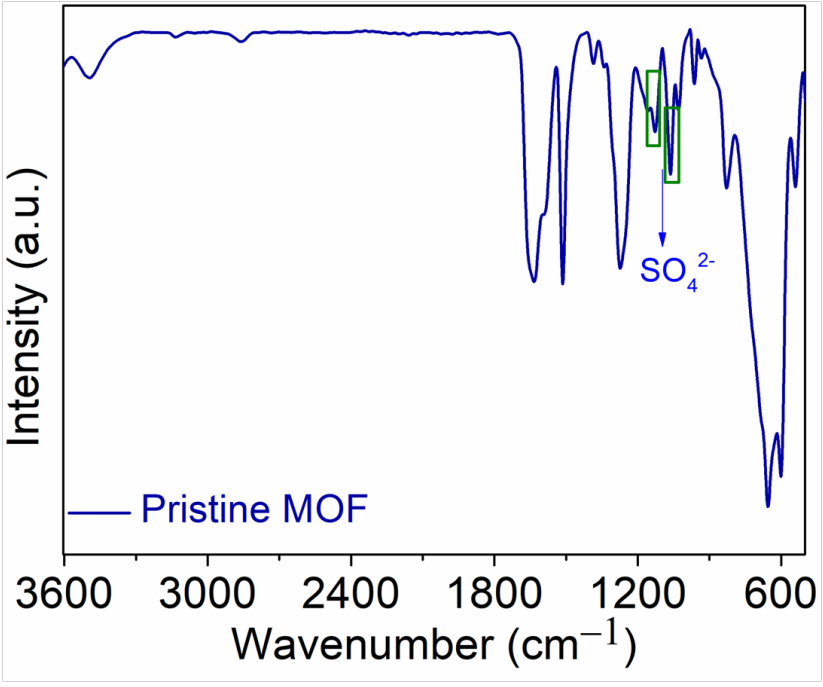
Appendix 5.6: Packing diagram depicting one dimensional porous voids.(Disordered SO_4^{2-} anions, hydrogen atoms and solvent have been omitted for clarity).



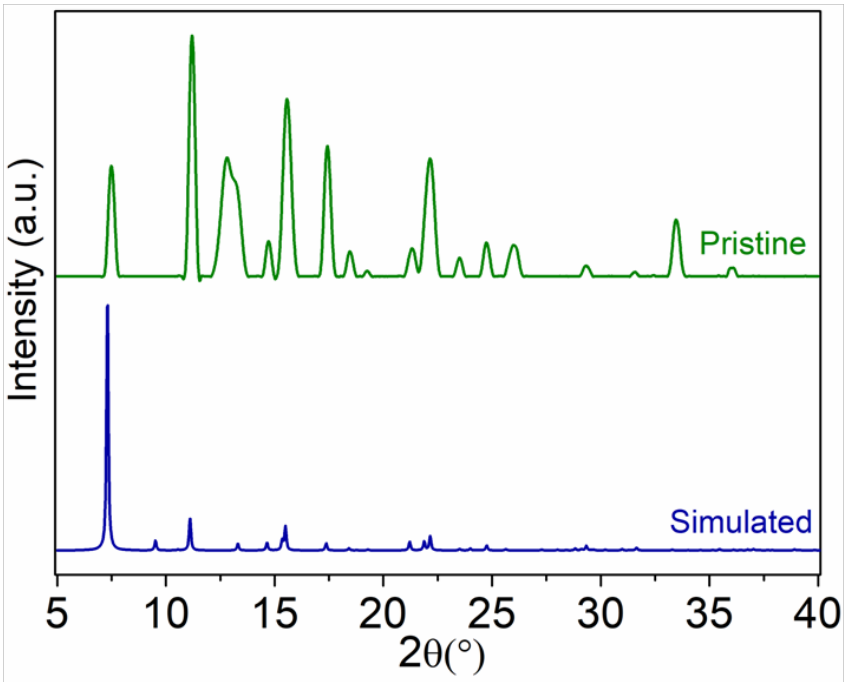
Appendix 5.7: Packing diagram showing aperture of the porous channels.(Disordered SO_4^{2-} anions, hydrogen atoms and solvent have been omitted for clarity). The dimension of the voids excluding the Van der Walls radii is 6.6×4.89 $Å^2$.



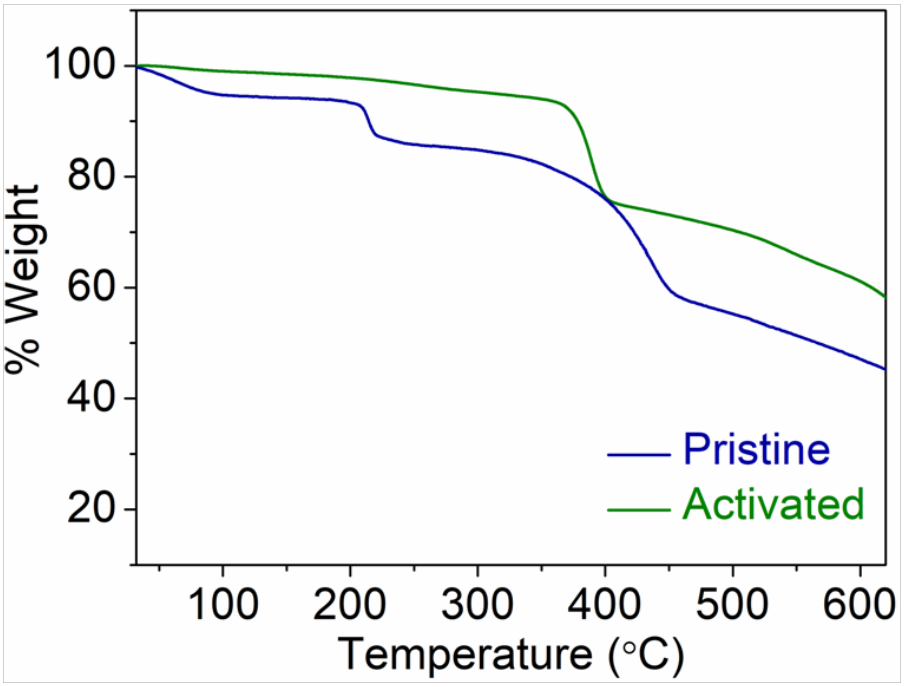
Appendix 5.8: XPS fitting profile for sulphur (S 2p) in iMOF-3C.



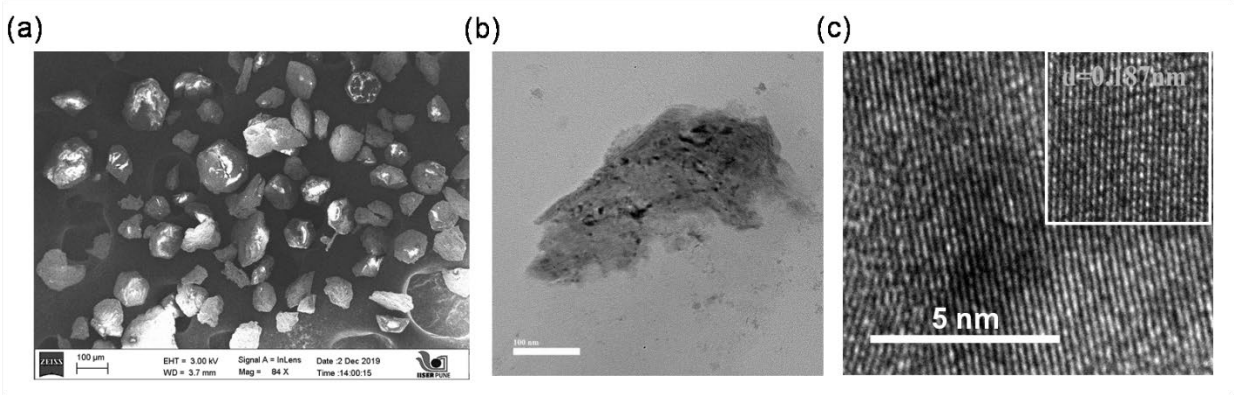
Appendix 5.9: FT-IR spectra for pristine iMOF-3C showing peak corresponding to SO_4^{2-} anion.



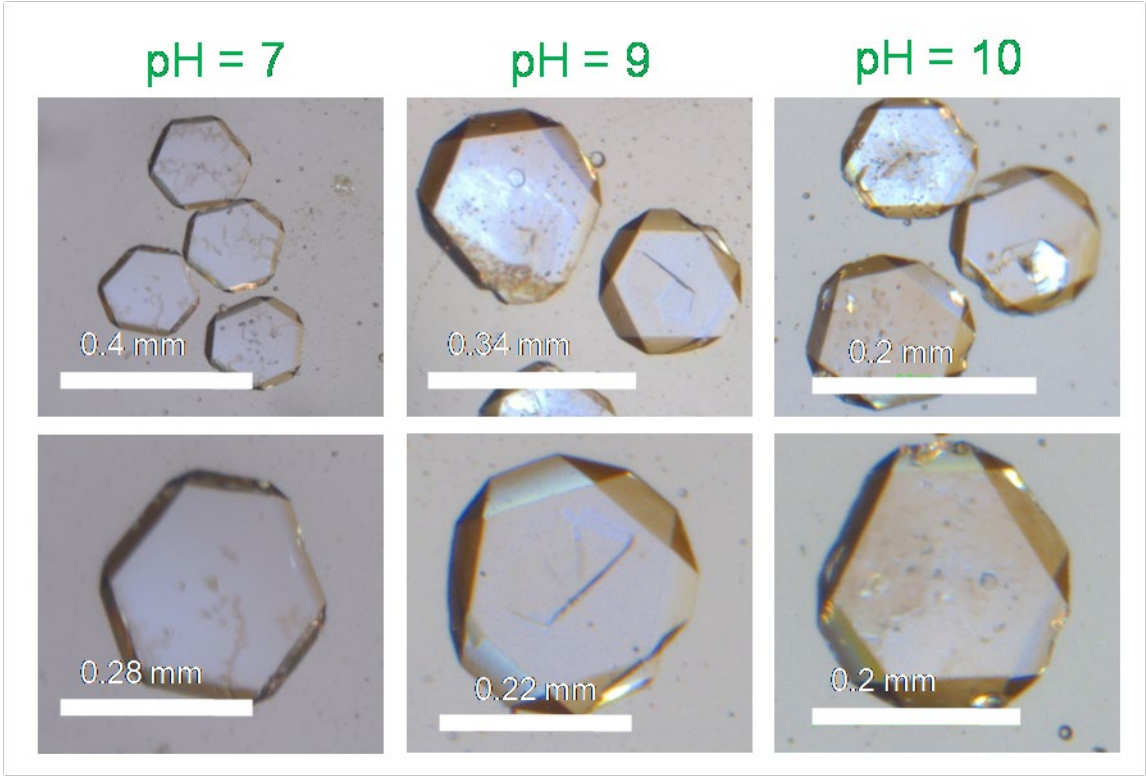
Appendix 5.10: PXRD spectra for simulated and pristine iMOF-3C.



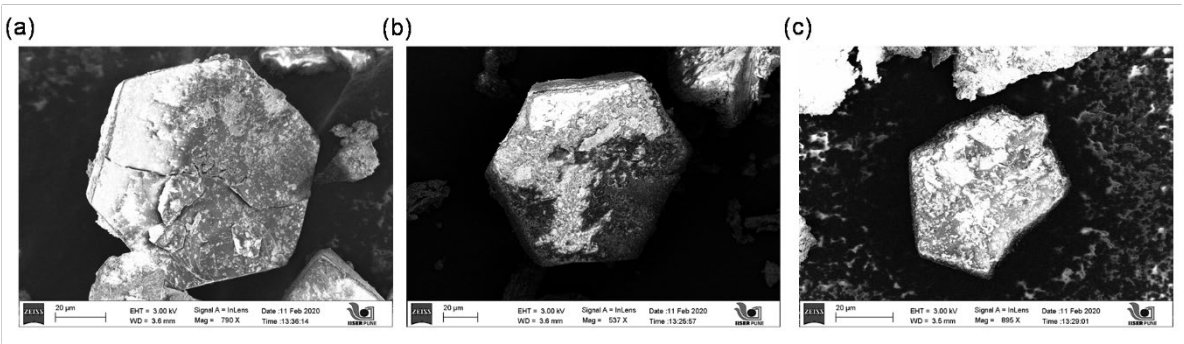
Appendix 5.11: Thermogravimetric analysis for pristine iMOF-3C.



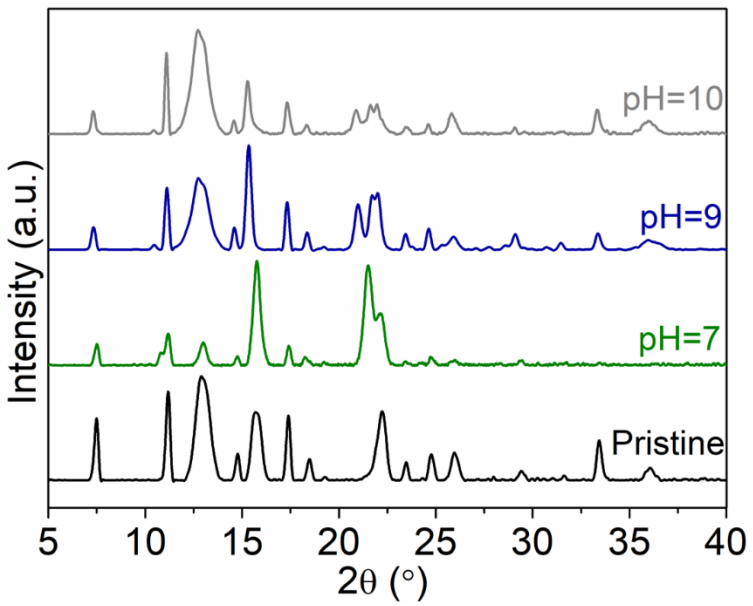
Appendix 5.12: FESEM, TEM, HRTEM (Lattice fringes) images for pristine iMOF-3C.



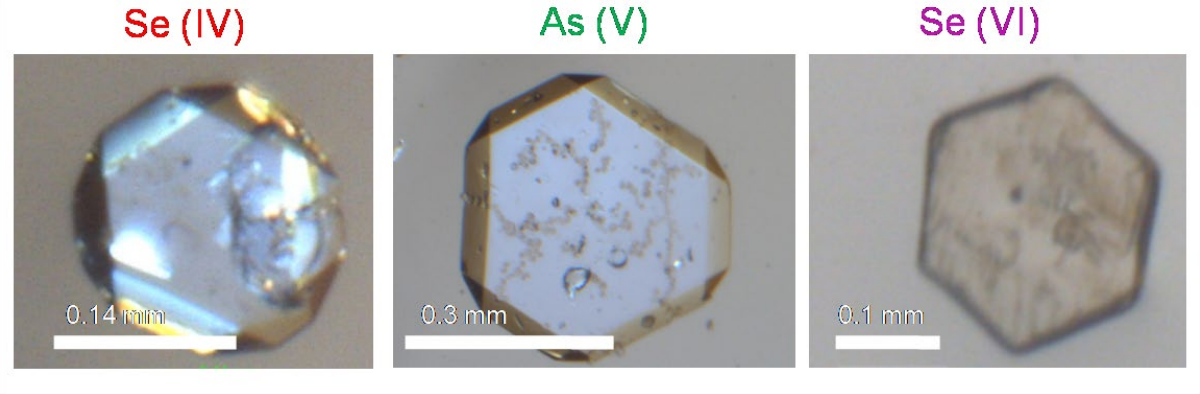
Appendix 5.13: Optical microscopy images of pristine iMOF-3C dipped in various media.



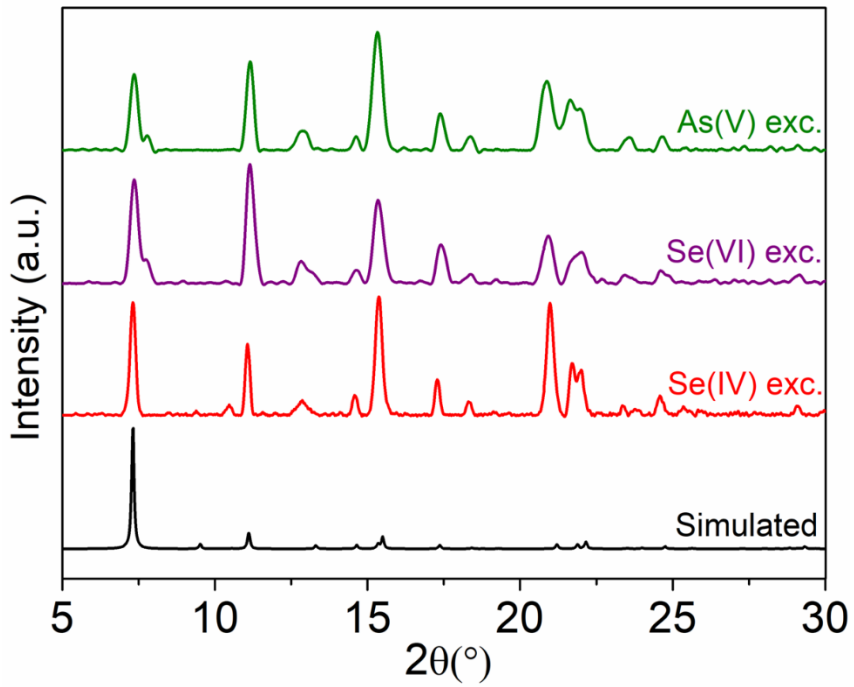
Appendix 5.14: FESEM images of pristine iMOF-3C post-treatment in various media (a) pH=7, pH=9, pH=10.



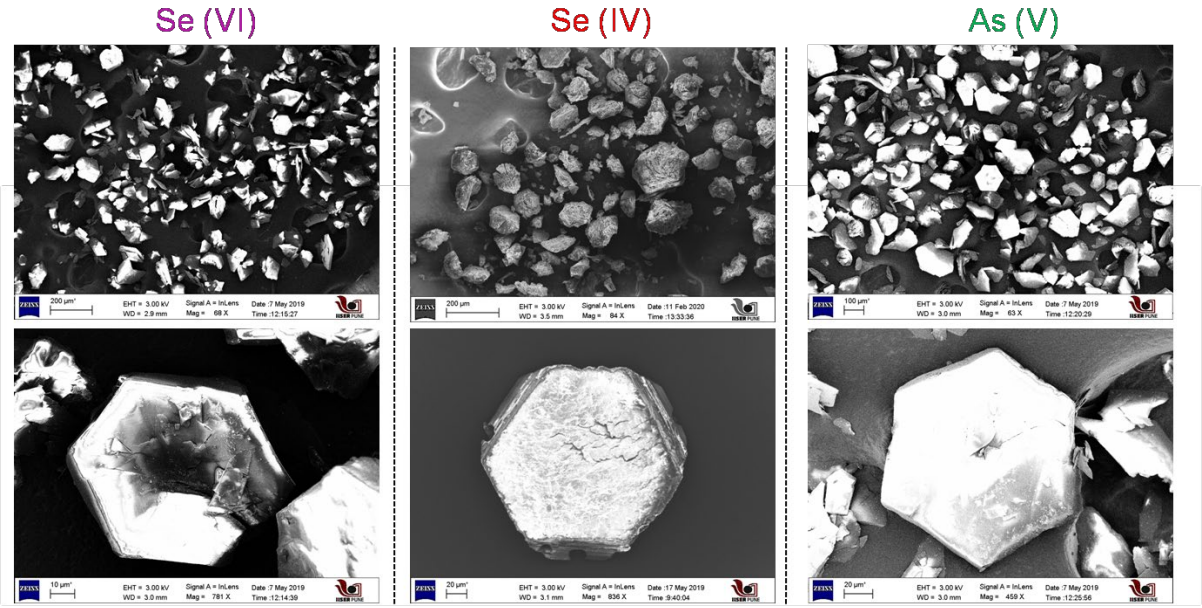
Appendix 5.15: PXRD spectra of pristine iMOF-3C post-treatment in various media.



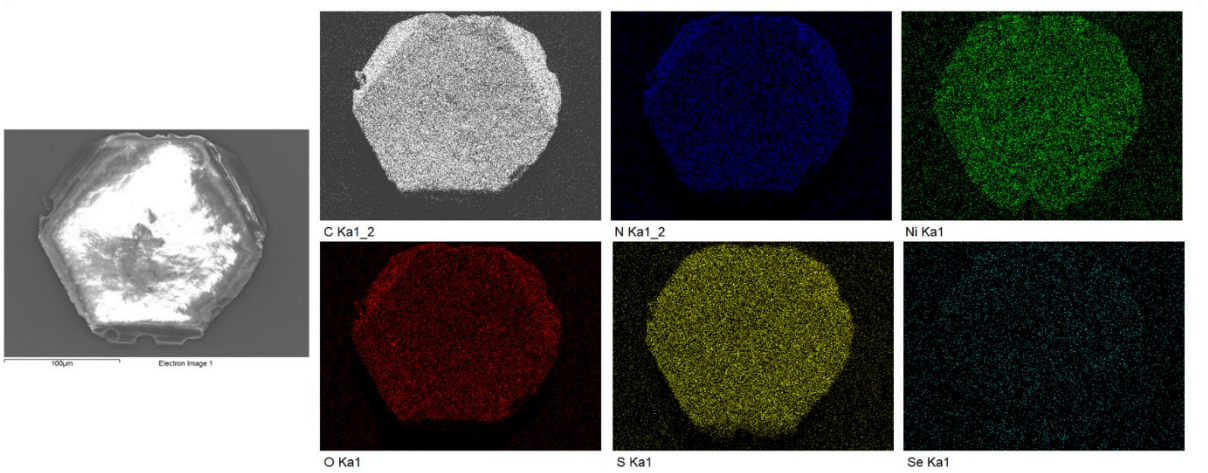
Appendix 5.16: Optical microscopy images of pristine iMOF-3C dipped in aqueous solution of toxic oxo-anions viz. SeO_3^{2-}, SeO_4^{2-}, $HAsO_4^{2-}$.

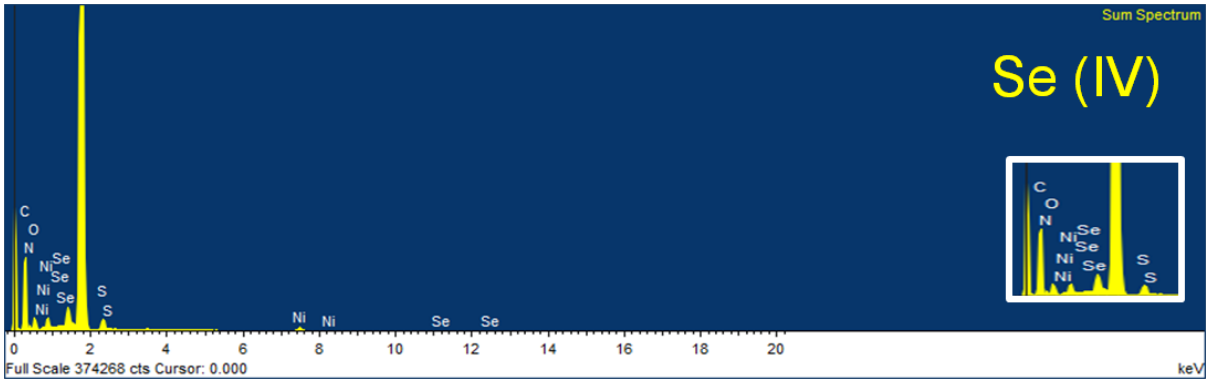


Appendix 5.17: PXRD spectra for simulated iMOF-3C, pristine and SeO_3^{2-}, SeO_4^{2-}, $HAsO_4^{2-}$exchanged phases.



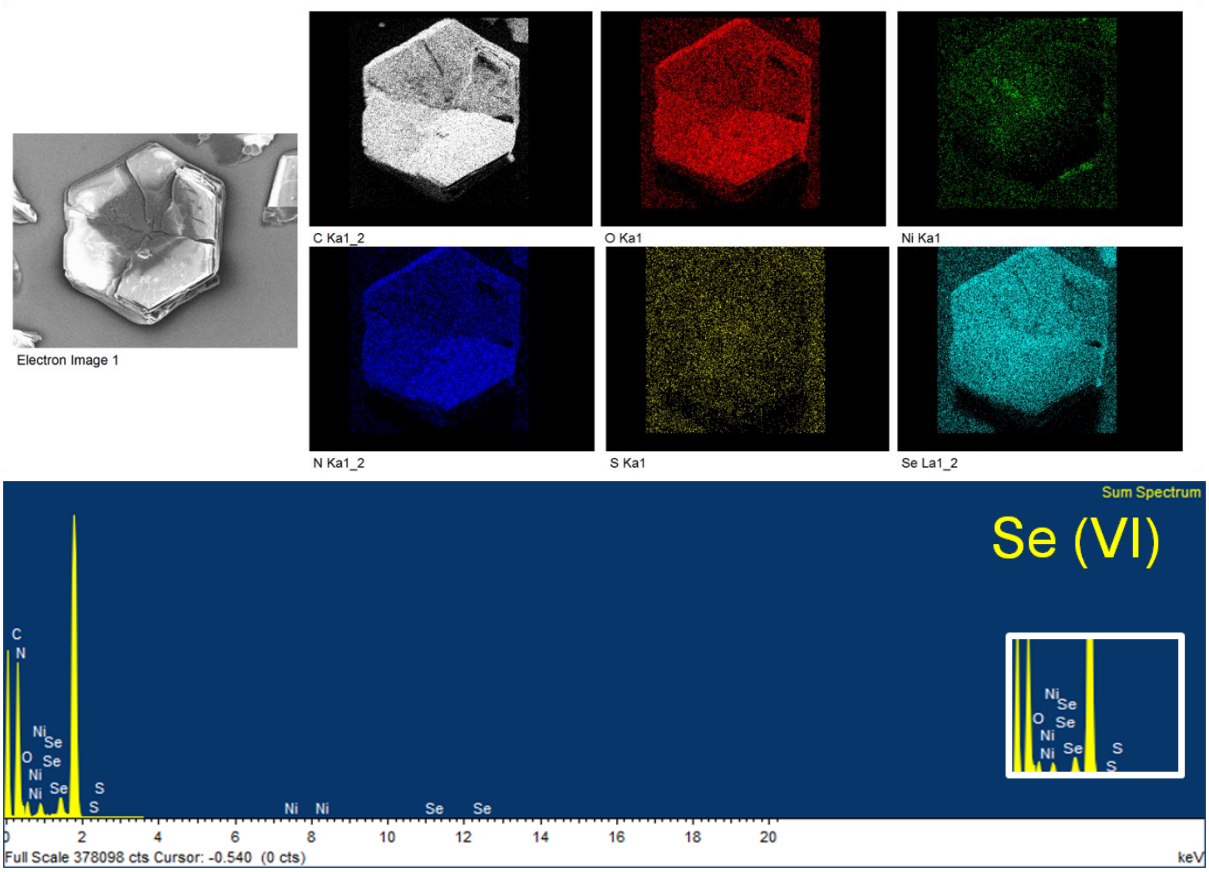
Appendix 5.18: FESEM images for pristine MOF exposed to an aqueous solution of SeO_3^{2-}, SeO_4^{2-}, $HAsO_4^{2-}$.





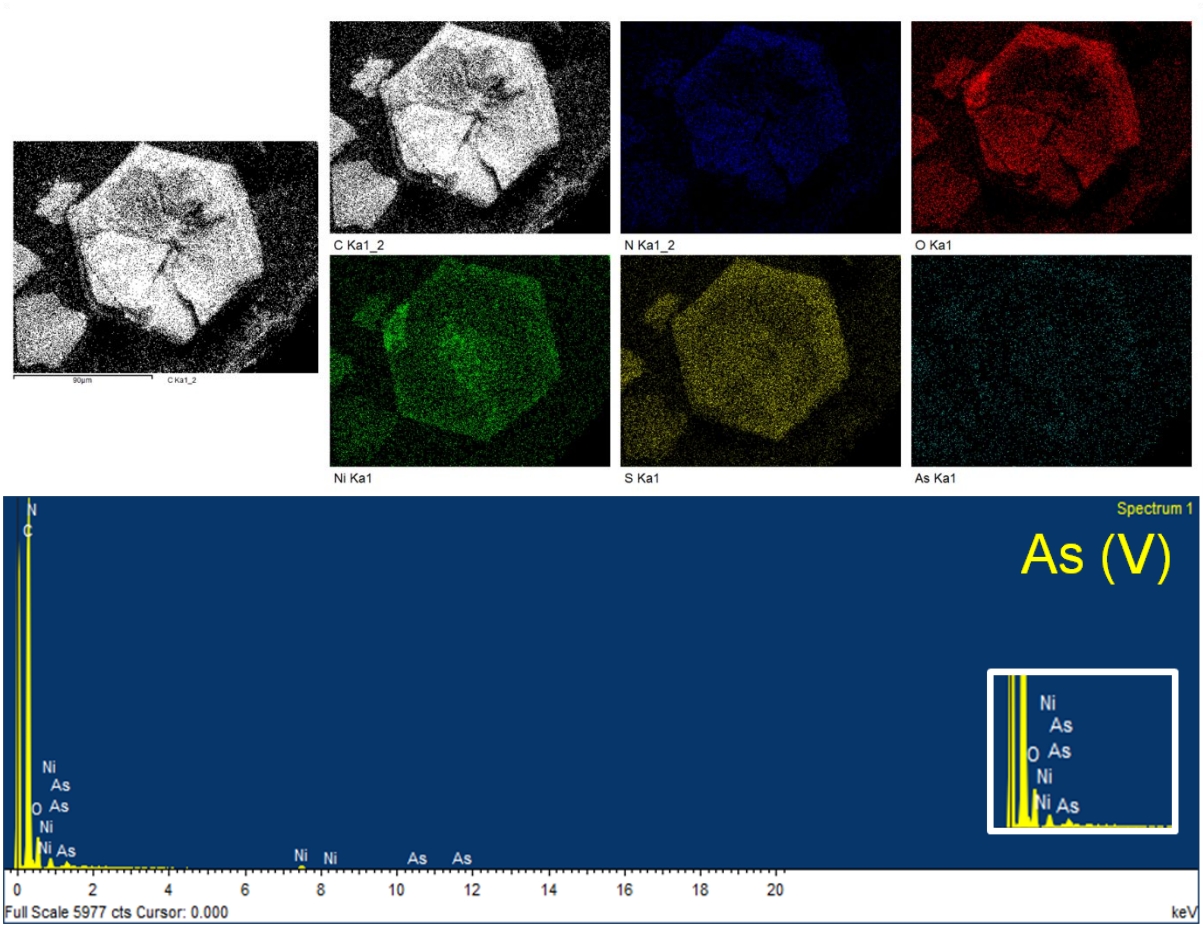
Element	Atomic %
C	65.32
N	17.12
O	14.91
S	0.86
Ni	0.88
Se	0.91

Appendix 5.19: EDX mapping profile and spectra for pristine MOF exposed to an aqueous solution of SeO_3^{2-}.



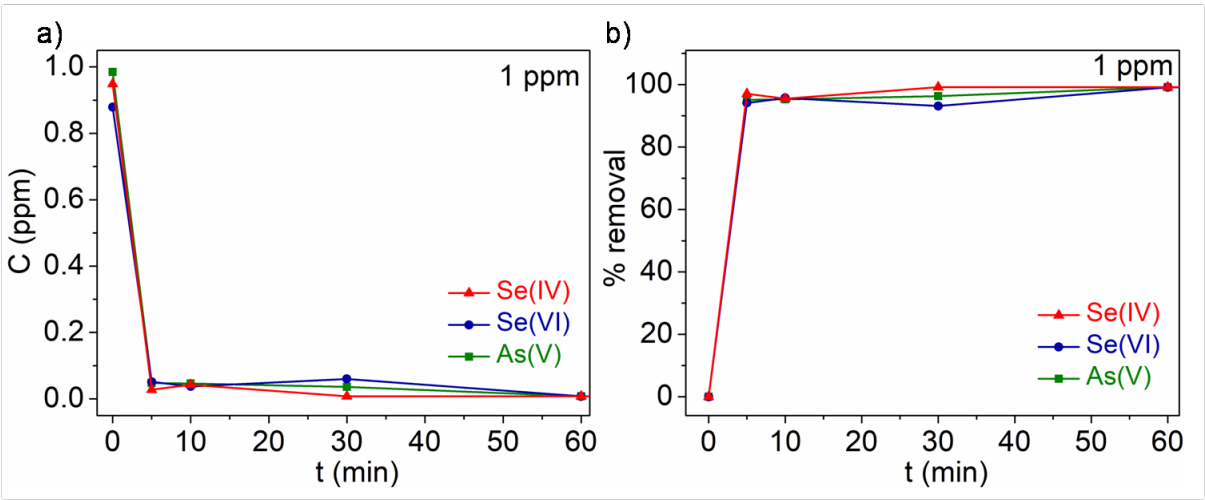
Element	Atomic %
C	64.08
N	22.54
O	12.08
S	0.06
Ni	0.47
Se	0.78

Appendix 5.20: EDX mapping profile and spectra for pristine MOF exposed to an aqueous solution of SeO_4^{2-}.

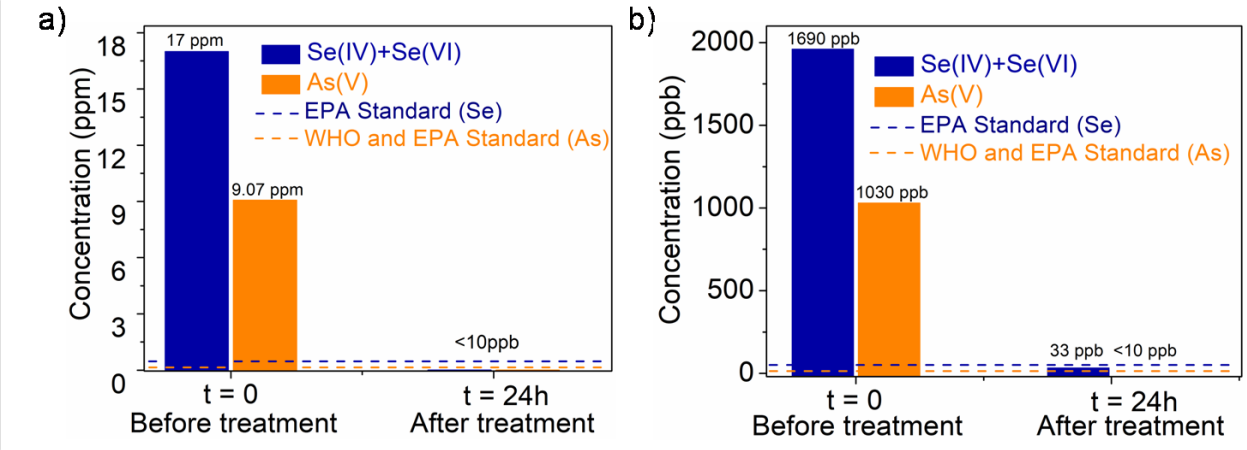


Element	Atomic %
C	63.53
N	17.25
O	16.83
S	0.81
Ni	0.99
As	0.60

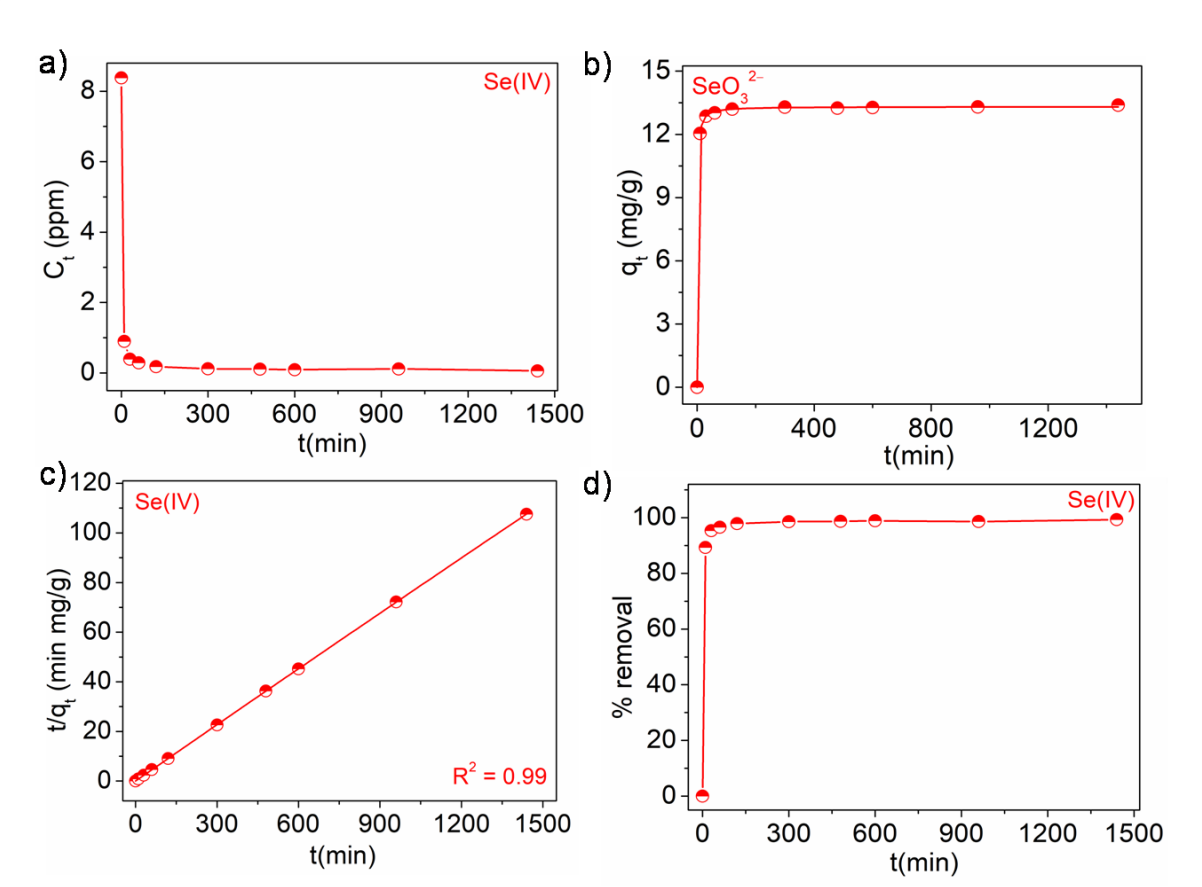
Appendix 5.21: EDX mapping profile and spectra for pristine MOF exposed to an aqueous solution of $HAsO_4^{2-}$.



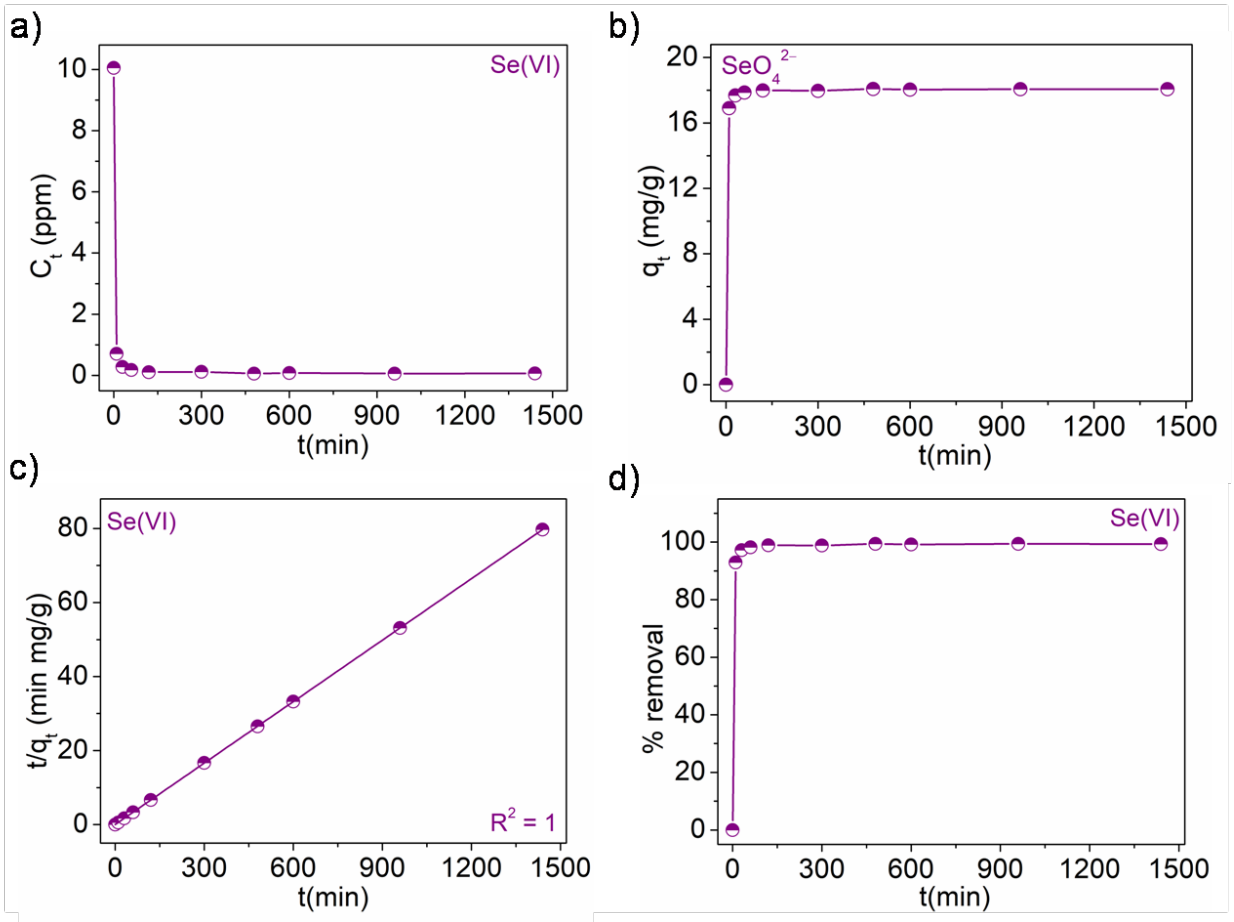
Appendix 5.22: Kinetic profiles of iMOF-3C towards of oxo-anion of Se(IV), Se(VI), As(V) at 1 ppm. (a) Concentration of Se(IV), Se(VI), As(V) as a function of time. (b) % removal plot as a function of time.



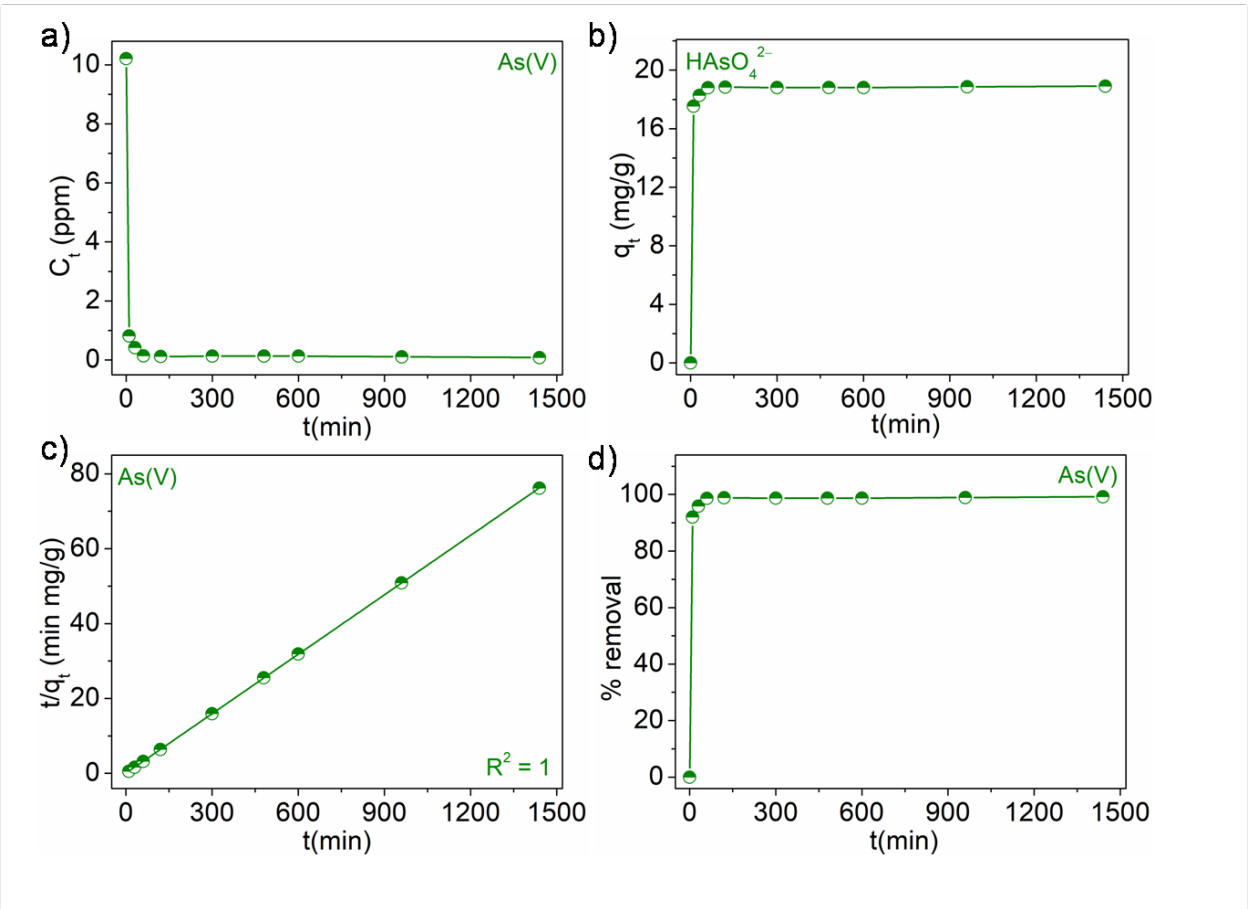
Appendix 5.23: Bar diagram depicting removal of mixture of oxo-anions of Se(IV)/Se(VI)/As(V) at (a) High concentration ~10 ppm. (b) Low concentration ~1000 ppb.



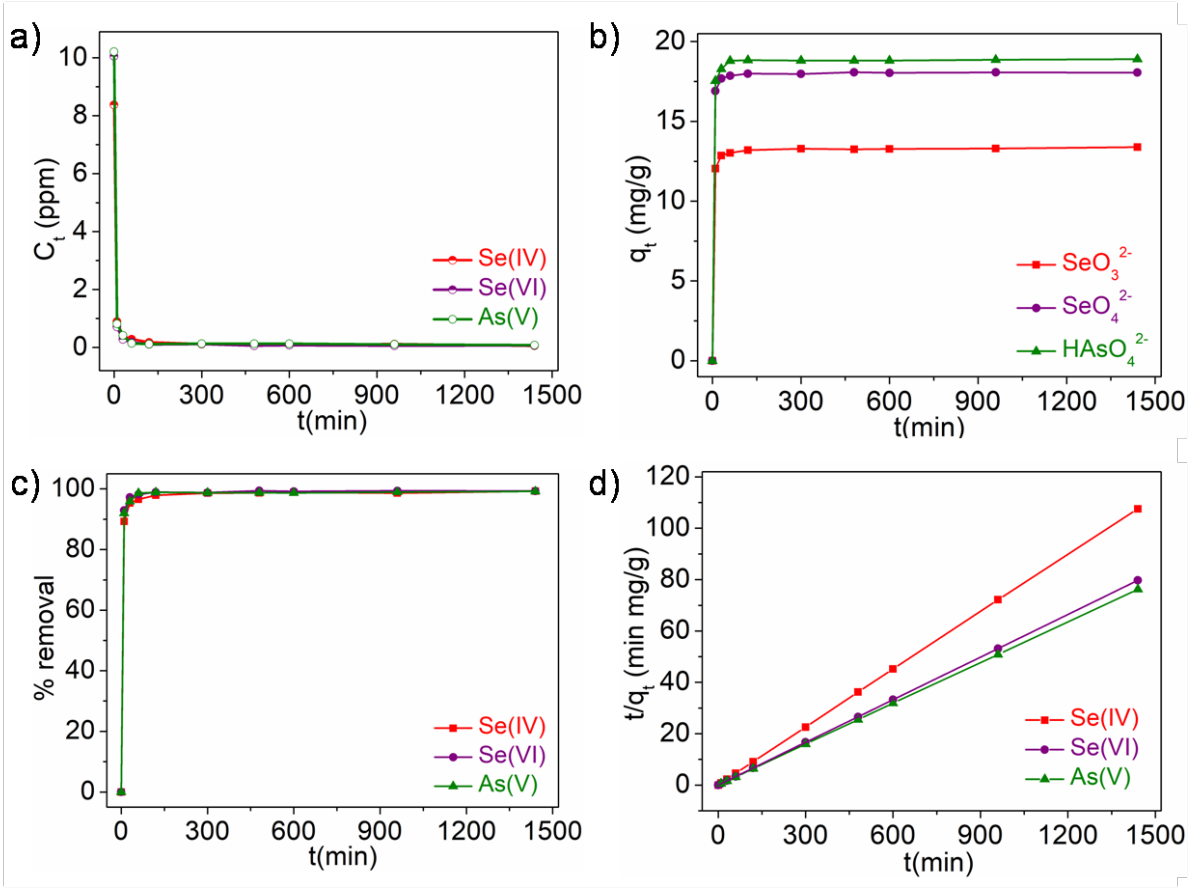
Appendix 5.24: Kinetic profiles of iMOF-3C towards of oxo-anion of Se(IV) at 10 ppm. (a) Concentration of Se(IV) as a function of time. (b) % removal plot as a function of time. (c) Sorption capacity with respect to time. (d) Pseudo-second order fitting model.



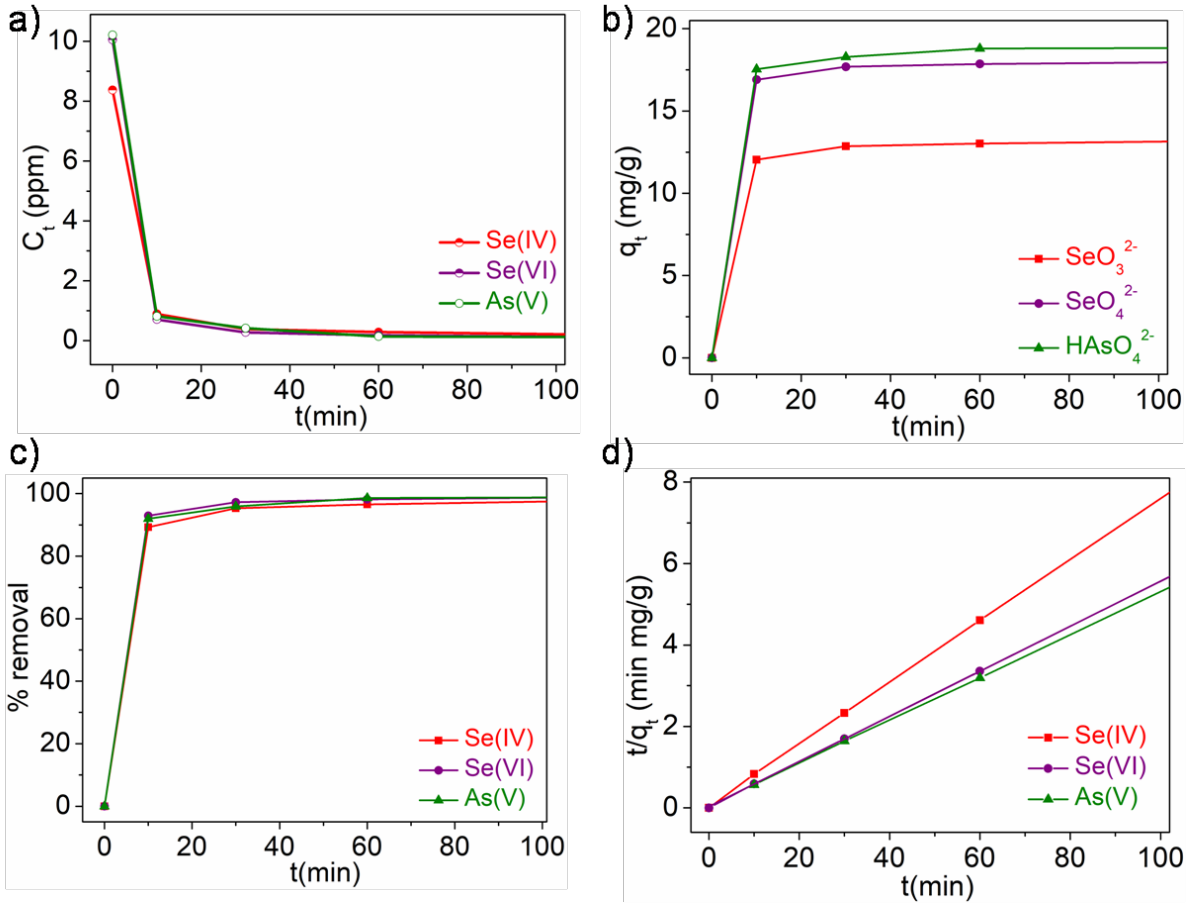
Appendix 5.25: Kinetic profiles of iMOF-3C towards of oxo-anion of Se(VI) at 10 ppm. (a) Concentration of Se(IV) as a function of time. (b) % removal plot as a function of time. (c) Sorption capacity with respect to time. (d) Pseudo-second order fitting model.



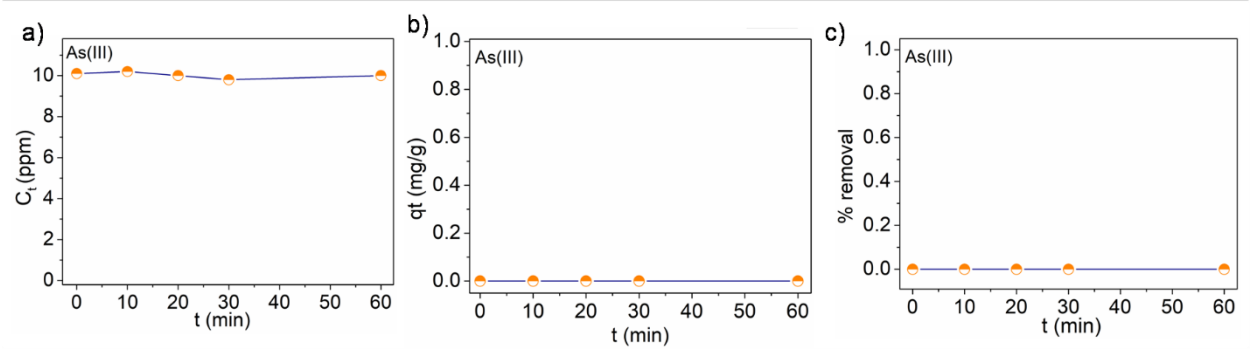
Appendix 5.26: Kinetic profiles of iMOF-3C towards of oxo-anion of As(V) at 10 ppm. (a) Concentration of Se(IV) as a function of time. (b) Sorption capacity with respect to time. (c) Pseudo-second order fitting model. (d) % removal plot as a function of time.



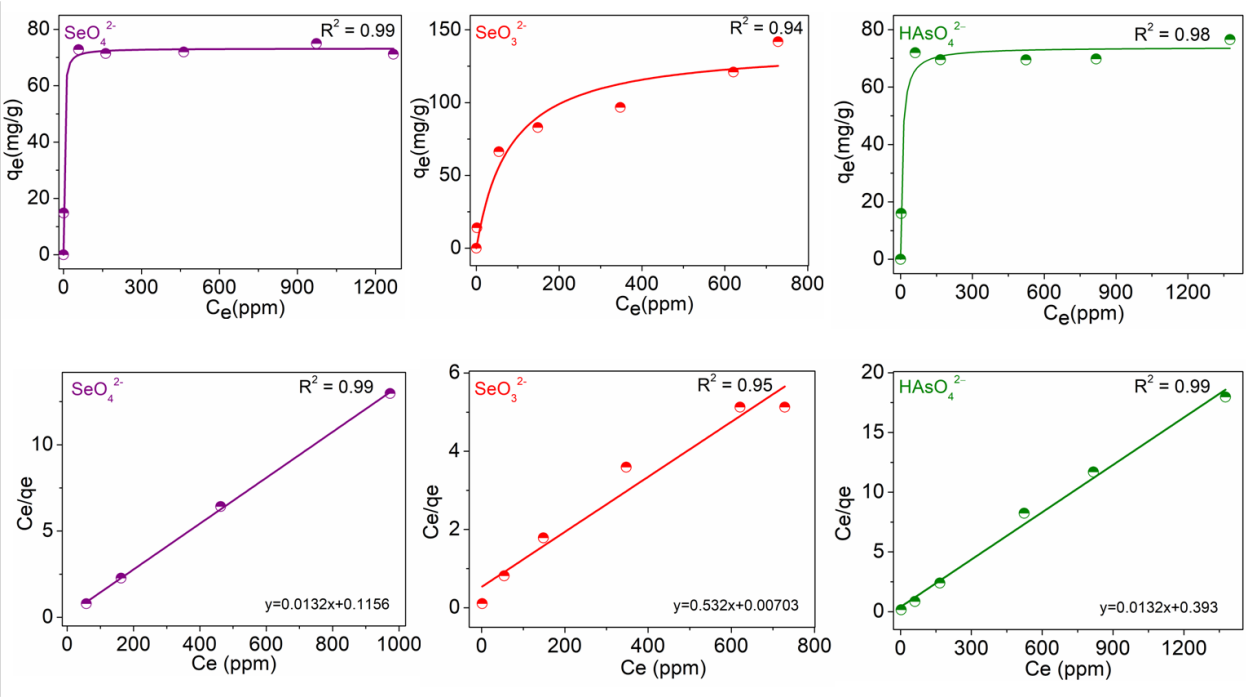
Appendix 5.27: Comparative Kinetic profiles of iMOF-3C towards of oxo-anion of Se(VI), Se(IV), As(V) at 10 ppm. (a) Change in concentration of oxo-anions as a function of time. (b) Sorption capacity with respect to time. (c) % removal plot as a function of time. (d) Pseudo-second order fitting model.



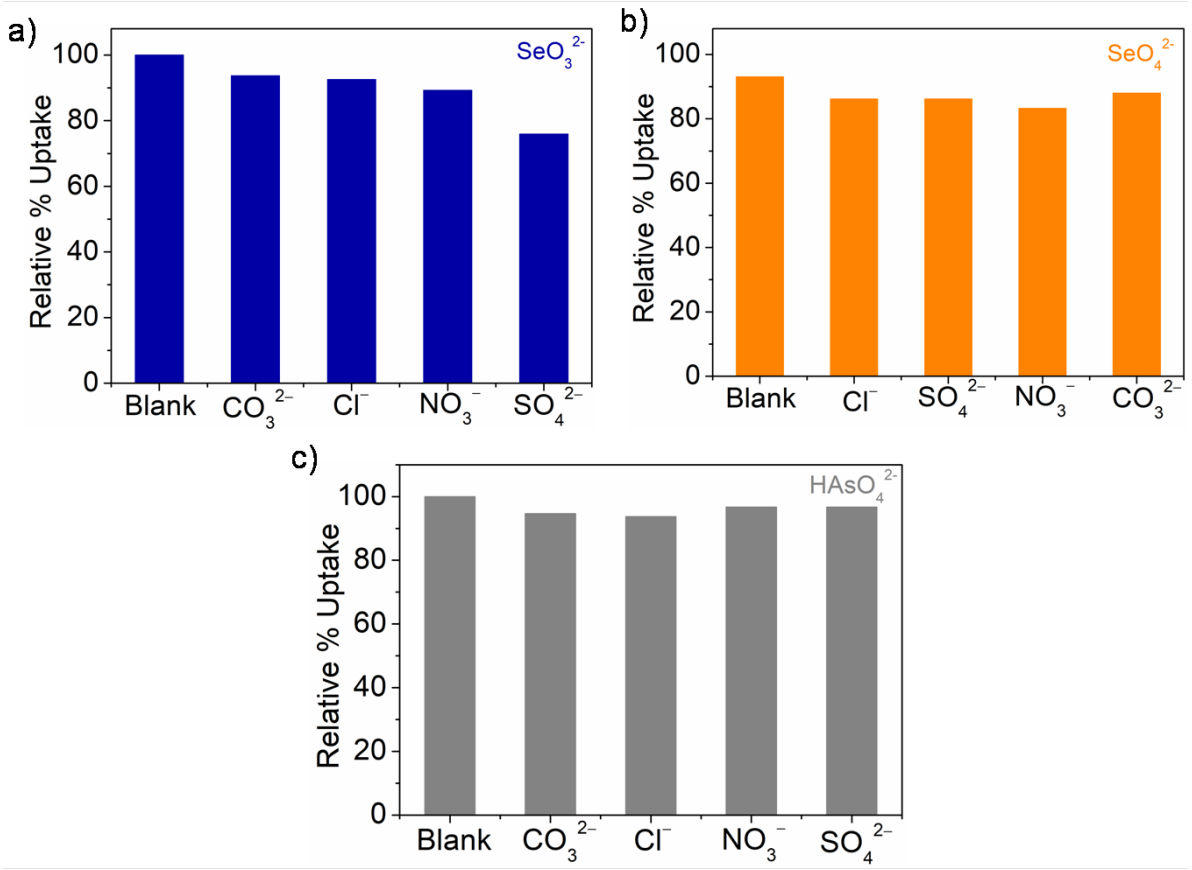
Appendix 5.28: Zoomed View of Comparative Kinetic profiles of iMOF-3C towards of oxo-anion of Se(VI), Se(IV), As(V) at 10 ppm. (a) Change in concentration of oxo-anions as a function of time. (b) Sorption capacity with respect to time (c) .% removal plot as a function of time. (d) Pseudo-second order fitting model.



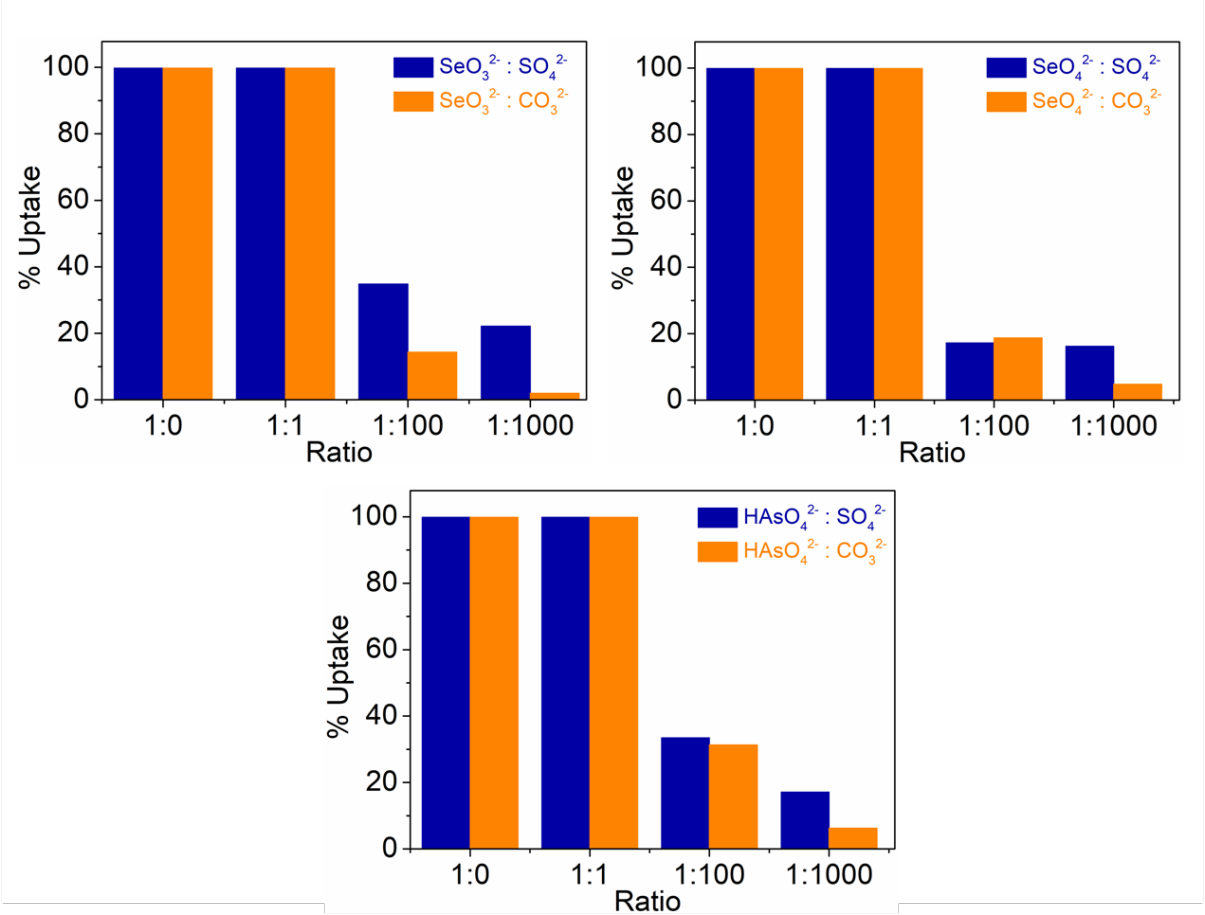
Appendix 5.29: Kinetic profiles of iMOF-3C towards of oxo-anion of As(III). (a) Concentration of As(III) as a function of time. (b) Sorption capacity with respect to time. (c) % removal plot as a function of time (y-axis is divided by 100).



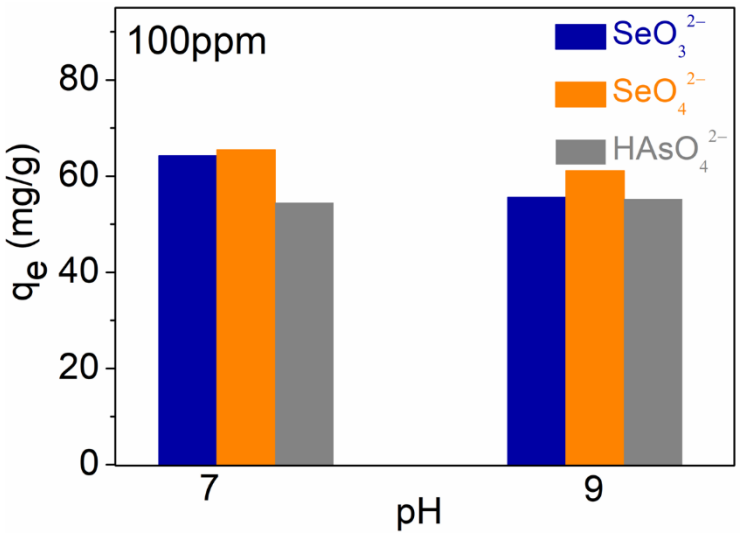
Appendix 5.30: Concentration dependent sorption profiles of iMOF-3C towards of oxo-anion of Se(VI), Se(IV), As(V) and corresponding Langmuir linear fitting model.



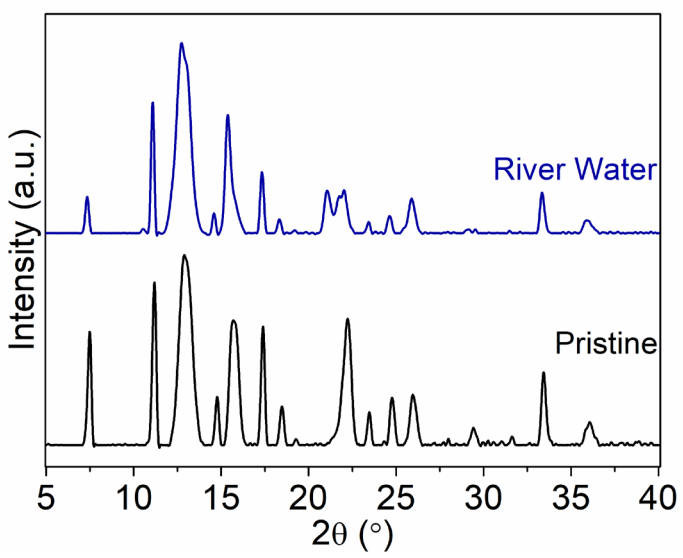
Appendix 5.31: Comparative uptake profiles for capture of oxo-anions viz. Se(IV)/Se(VI)/As(V) in binary mixture of oxo-anions. {Blank: Compound exposed to only anion}.



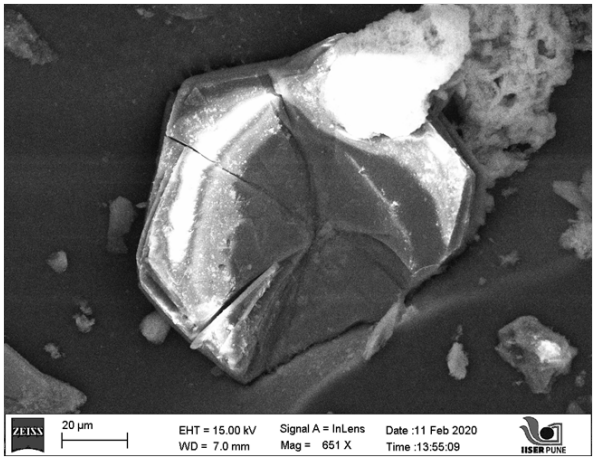
Appendix 5.32: Comparative uptake profiles for capture of oxo-anions viz. Se(IV)/Se(VI)/As(V) in presence of higher concentration of competing ions.



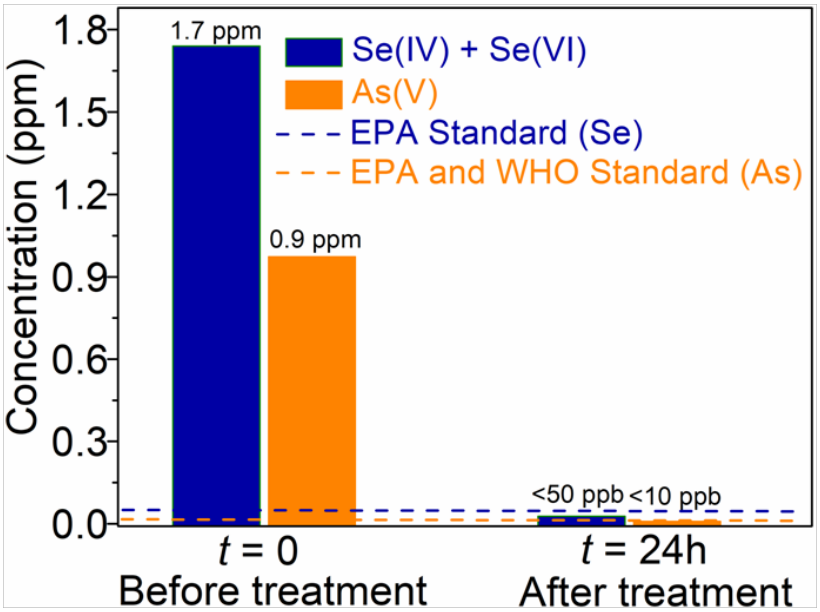
Appendix 5.33: Comparative uptake profiles for capture of oxo-anions viz. Se(IV)/Se(VI)/As(V) at different pH by iMOF-3C.



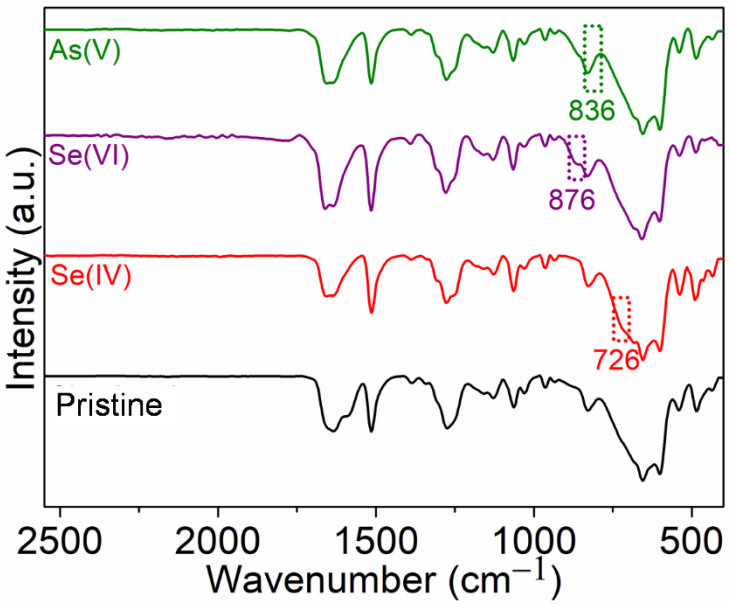
Appendix 5.34: Comparative PXRD spectra for pristine iMOF-3C dipped in River Water.



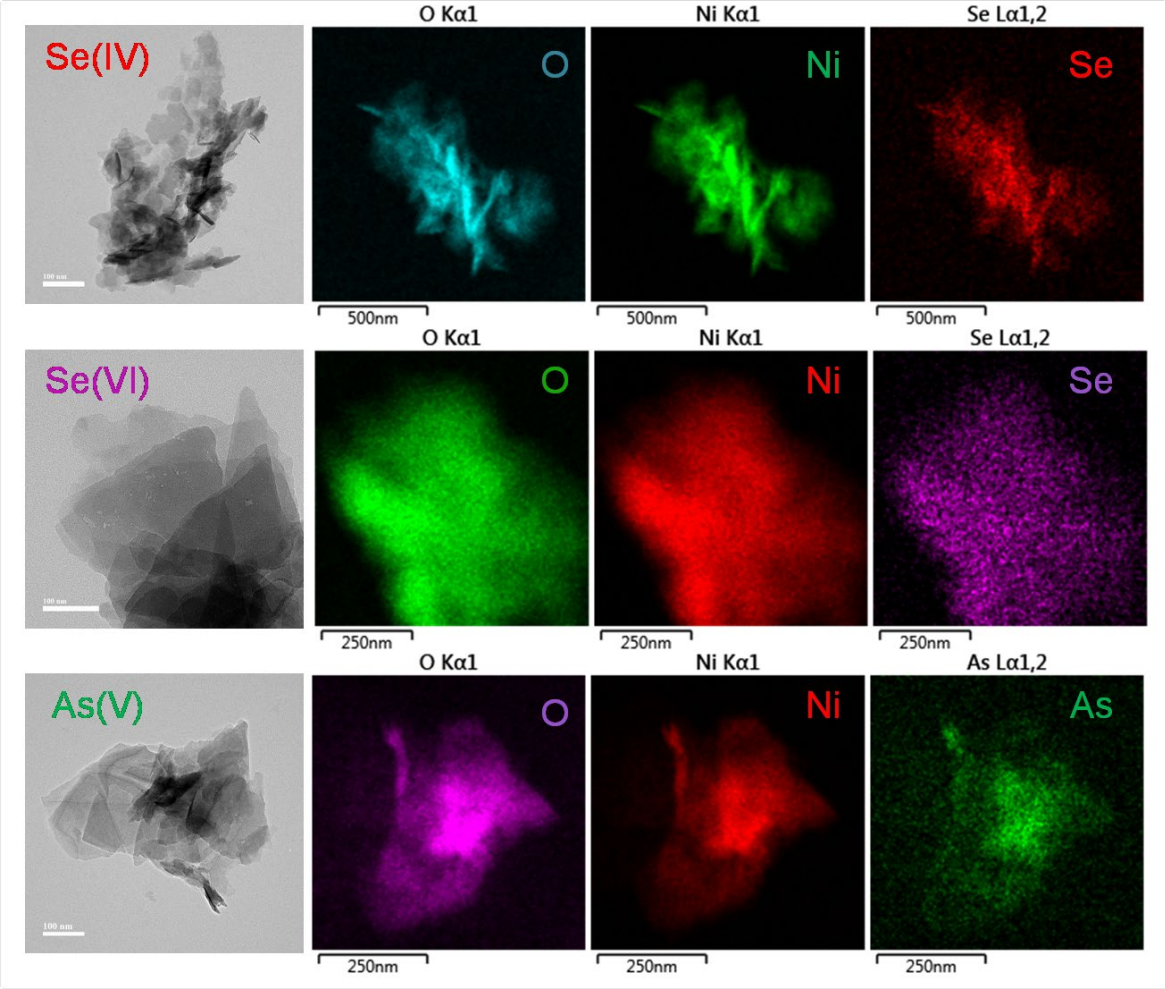
Appendix 5.35: FESEM spectra for pristine iMOF-3C dipped in River Water.



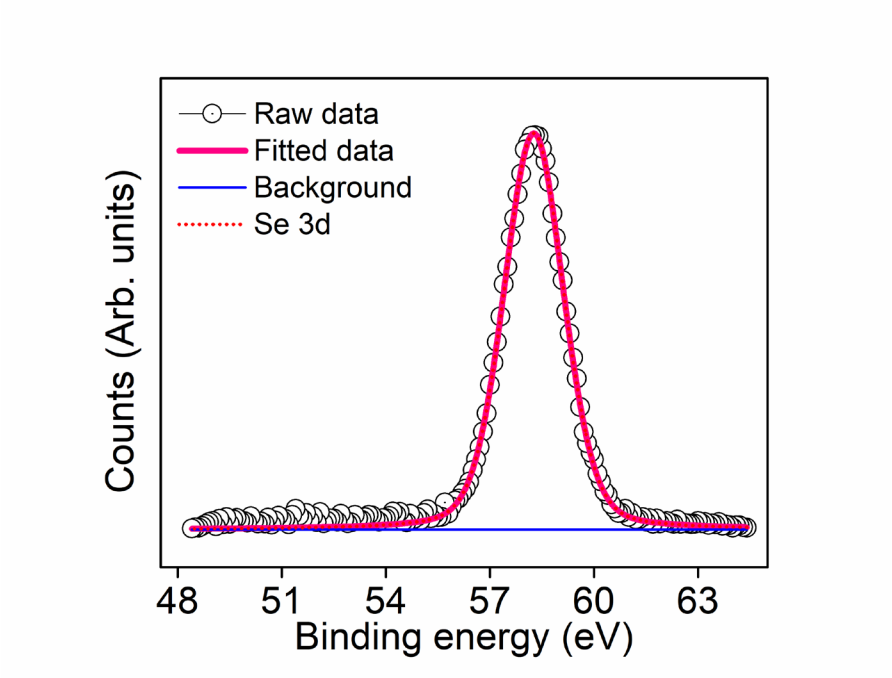
Appendix 5.36: Bar diagram depicting removal of mixture of oxo-anions of Se(IV)/Se(VI)/As(V) at ~1000 ppb in river water.



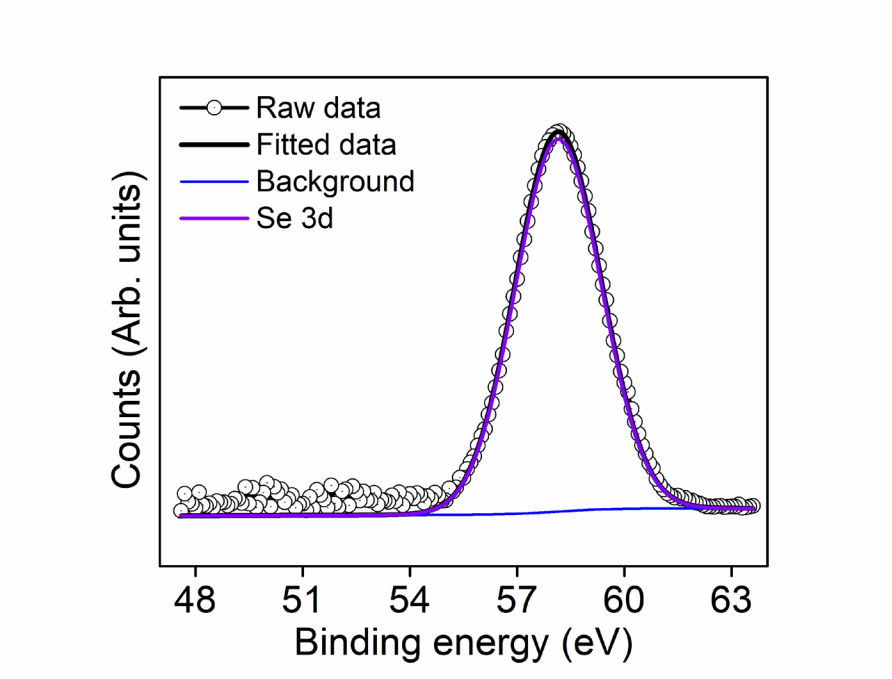
Appendix 5.37: FT-IR spectra for pristine MOF exposed to an aqueous solution of oxo-anions viz. SeO_3^{2-}, SeO_4^{2-}, $HAsO_4^{2-}$.



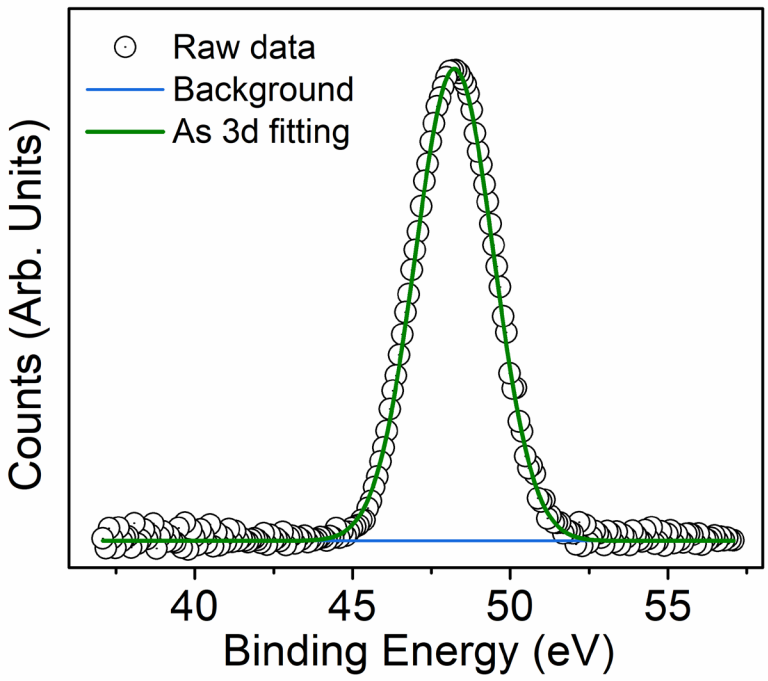
Appendix 5.38: TEM images and TEM-EDS spectra for pristine MOF exposed to an aqueous solution of SeO_3^{2-}. SeO_4^{2-}, $HAsO_4^{2-}$ (1000ppm).



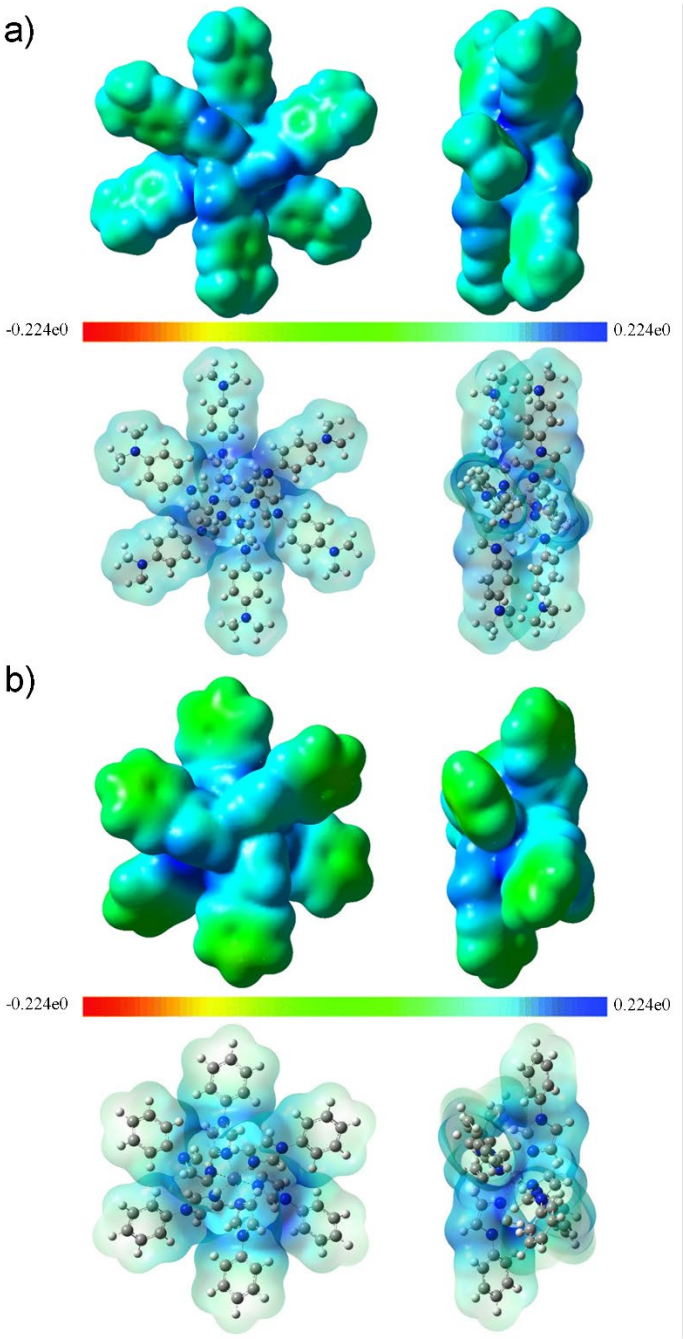
Appendix 5.39: XPS spectra for pristine MOF exposed to an aqueous solution of oxo-anions viz. SeO_3^{2-}.



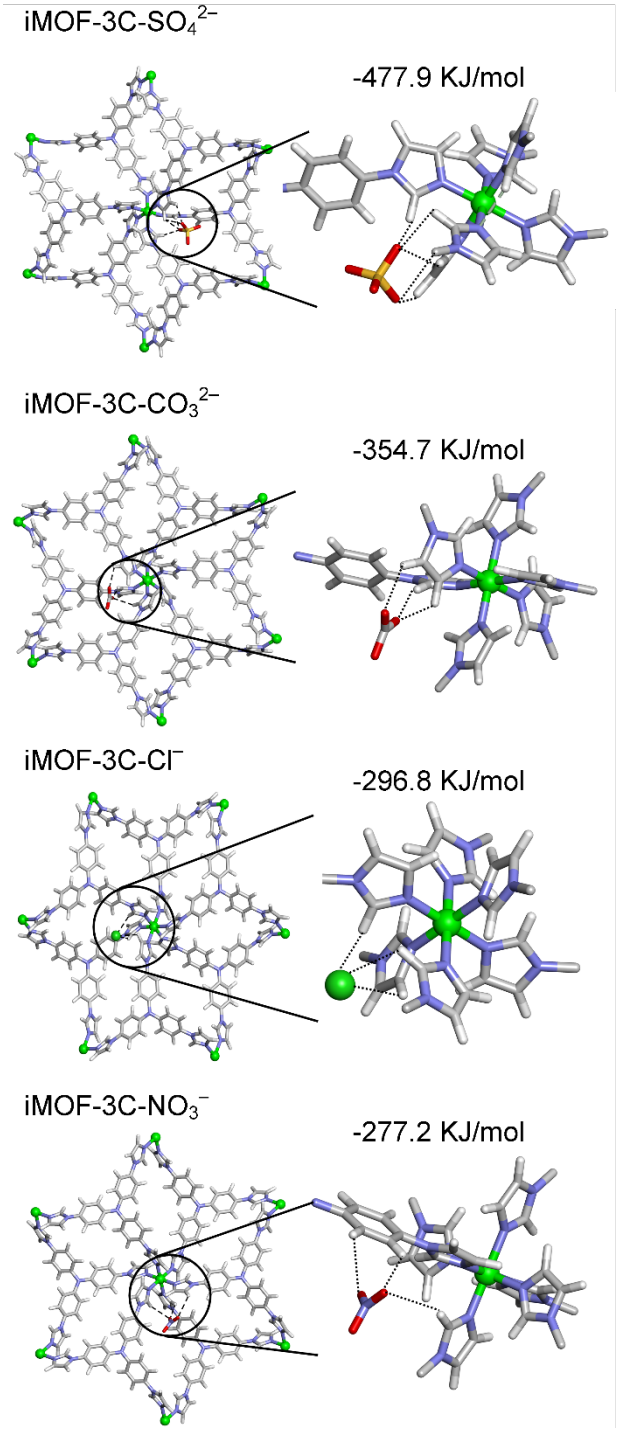
Appendix 5.40: XPS spectra for pristine MOF exposed to an aqueous solution of oxo-anions viz. SeO_4^{2-}.



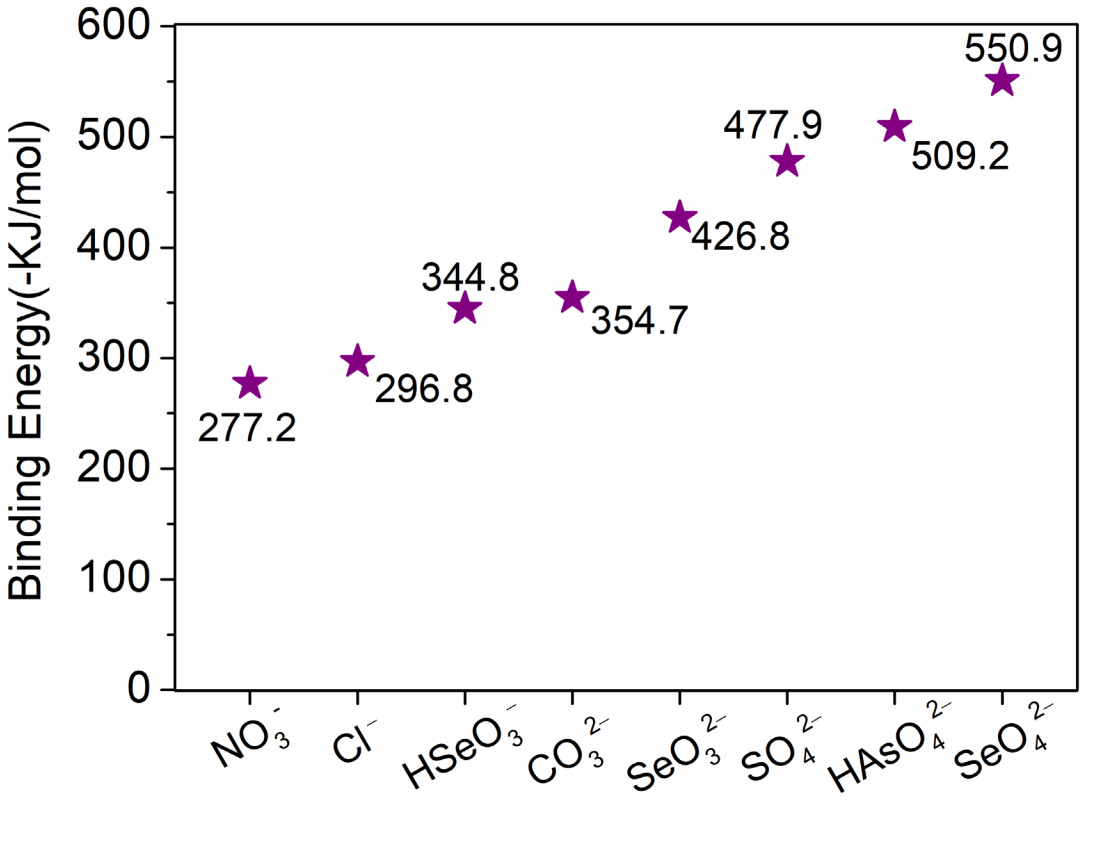
Appendix 5.41: XPS spectra for pristine MOF exposed to an aqueous solution of oxo-anions viz. $HAsO_4^{2-}$.



Appendix 5.42: Electrostatic Potential (ESP) diagram of two different part of framework in iMOF-3C.



Appendix 5.43: Optimized structures and corresponding zoomed view showing hydrogen bonding interactions of iMOF-3C with different anions and binding energies.



Appendix 5.44: Static binding energies for various anions in iMOF-3C framework calculated using density functional theory (DFT).

Appendix Table 1: Comparison of unit-cell parameters for pristine iMOF-3C and corresponding anion exchanged products viz. iMOF-3C-SeO_3^{2-}, iMOF-3C-SeO_4^{2-}, iMOF-3C-$HAsO_4^{2-}$.

Unit cell parameters	iMOF-C3	iMOF-C3-SeO_3^{2-}	iMOF-C3-SeO_4^{2-}	iMOF-C3-$HAsO_4^{2-}$
a (Å)	16.01(3)	16.06(5)	15.97(3)	16.06(6)
b (Å)	16.01(3)	16.06(5)	15.97(3)	16.06(6)
c (Å)	25.63(5)	25.79(7)	25.97(7)	24.79(8)
$\alpha^{(o)}$	90	90	90	90
$\beta^{(o)}$	90	90	90	90
$\gamma^{(o)}$	120	120	120	120
Volume ($Å^3$)	5691(2)	5967(30)	5550(20)	5540(30)

Appendix Table 2: Concentration of Ni(II) ion in the supernatant of various media as recorded by ICP-MS.

pH	Concentration of Ni (ppm)
7	0.48
9	0.54
12.45	0.18

Appendix Table 3: Concentration of Ni(II) ion in the supernatant of iMOF-3C exposed to toxic oxo-anions of Se(IV)/Se(VI)/As(V)/As(III) as recorded by ICP-MS.

	Concentration of Ni (ppm)
Se(IV)	N.D.
Se(VI)	0.27
As(V)	0.26
As(III)	0.51

Appendix Table 4: Sorption kinetics data for uptake of Se(IV) by iMOF-3C at low concentration.

C_o(ppm) Se(IV)	Time(min)	C_f	Removal (%)	K_d (mL/g)	q_t (SeO_3^{2-}) (mg/g)
8.37	10	0.895	89.31	8.4×10^3	12.04
	30	0.388	95.36	2.0×10^4	12.86
	60	0.287	96.57	2.8×10^4	13.02
	120	0.177	97.88	4.6×10^4	13.20
	300	0.118	98.59	6.9×10^4	13.28
	480	0.11	98.68	7.5×10^4	13.24
	600	0.0925	98.89	8.9×10^4	13.27
	960	0.116	98.61	7.1×10^4	13.29
	1440	0.06	99.28	1.3×10^5	13.38
	1800	<10ppb	>99.40	$>8.3 \times 10^5$	>13.38

Appendix Table 5: Kinetics Sorption kinetics data for uptake of Se(VI) by iMOF-3C at low concentration.

C_o (ppm) Se(VI)	Time(min)	C_f	Removal (%)	K_d (mL/g)	q_t (SeO_4^{2-}) (mg/g)
10.05	10	0.71	92.93	1.3×10^4	16.9
	30	0.28	97.23	3.5×10^4	17.68
	60	0.18	98.19	5.4×10^4	17.86
	120	0.10	98.91	9.1×10^4	17.99
	300	0.12	98.8	8.2×10^4	17.97
	480	0.06	99.39	1.63×10^5	18.08
	600	0.08	99.19	1.22×10^5	18.04
	960	0.06	99.37	1.56×10^5	18.07
	1440	0.07	99.3	1.42×10^5	18.06
	1800	<10ppb	>99.90	1.0×10^6	>18.17

Appendix Table 6: Sorption kinetics data for uptake of As(V) by iMOF-3C at low concentration.

C_o (ppm) As(V)	Time(min)	C_f	Removal (%)	K_d (mL/g)	q_t ($HAsO_4^{2-}$) (mg/g)
10.21	10	0.81	92.01	1.1×10^4	17.54
	30	0.42	95.9	2.3×10^4	18.28
	60	0.14	98.62	7.1×10^4	18.8
	120	0.12	98.84	8.5×10^4	18.84
	300	0.13	98.71	7.7×10^4	18.81
	480	0.13	98.72	7.7×10^4	18.81
	600	0.13	98.7	7.7×10^4	18.81
	960	0.11	98.94	9.3×10^4	18.86
	1440	0.083	99.18	1.22×10^5	18.91
	1800	<10ppb	>99.90	1.02×10^6	>19.04

Appendix Table 7: Uptake performance of iMOF-3C towards oxo-anion of Se(IV)+Se(VI), As(V) at 10ppm.

	C_o (ppm)	C_f (ppm)	% removal	K_d (mL/g)
Se(IV) + Se(VI)	17	<10ppb	>99.94	$>1.6 \times 10^6$
As(V)	9.07	<10ppb	>99.8	$> 0.9 \times 10^6$

Appendix Table 8: Listing kinetic fitting parameters as obtained by pseudo-second order fitting model for oxo-anions of Se(IV)/Se(VI)/As(V) by iMOF-3C.

	q_e (exp.) mg/g	q_e (cal.) mg/g	k_2	R^2
Se(IV)	13.38	13.37	0.039	0.99
Se(VI)	18.06	18.08	0.093	1
As(V)	18.9	18.89	0.057	1

Appendix Table 9: Comparative analysis of static binding energies in iMOF-3C framework calculated using density functional theory (DFT) and hydration energy from literature values.

Anion	Cl^-	NO_3^-	CO_3^{2-}	SO_4^{2-}	SeO_4^{2-}	SeO_3^{2-}	$HSeO_3^-$	$HAsO_4^{2-}$
Binding energy (-KJ/mol)	296.89	277.29	354.7	477.9	550.9	426.8	344.8	509.2
Hydration Energy (-KJ/mol)	340	300	1315	1080	900	937-1025	NA	NA
Reference	45	45	45	45	45	46	-	-

Appendix Table 10: Comparison for state-of-the-art materials available for capture of Se(IV) oxo-anion.

Adsorbent	Oxo-anion	Method	Selectivity	Capacity (mg/g)	Time (min)	Reference
iMOF-3C	Se(IV)	Ion-exchange	vs. NO_3^-, Cl^-, CO_3^{2-}, SO_4^{2-}	140	5	This work
NU-1000	Se(IV)	Adsorption	NA	95	1	12a
CAU-17	Se(IV)	Irreversible Chemical Bond	vs. CO_3^{2-}, Cl^-, NO_3^-, SO_4^{2-}etc	255.3	360	47
MgAl-MoS4-LDH	Se(IV)	Ion-exchange	NA	294	10	14
LDH	Se(IV)	Ion-exchange	vs. CO_3^{2-}, Cl^-, NO_3^-, HPO_4^{2-}, SO_4^{2-}	207	100	36c
MgO Nanosheets	Se(IV)	Adsorption	NO_3^-, Cl^-, F^-, PO_4^{3-}	103.52	300	48
Iron Oxide on SiO_2	Se(IV)	Adsorption	NA	20.4	120	49

Appendix Table 11: Comparison for state-of-the-art materials available for capture of Se(VI) oxo-anion.

Adsorbent	Oxo-anion	Method	Selectivity	Capacity (mg/g)	Time (min)	Reference
iMOF-3C	Se(VI)	Ion-exchange	vs. NO_3^-, Cl^-, CO_3^{2-},SO_4^{2-}	73	5	This work
iMOF-1C	Se(VI)	Ion-exchange	vs. NO_3^-, Cl^-, SO_4^{2-}, HCO_3^-, CO_3^{2-}	100	4320	13k
NU-1000	Se(VI)	Adsorption	NA	85	1	12a
CAU-17	Se(VI)	Irreversible Chemical Bond	vs. NO_3^-, NO_2^-, SO_4^{2-}, F^-, Cl^-, HCO_3^- ,CO_3^{2-}, Ac^-, PO_4^{3-}, LAS^-, $B_4O_7^{2-}$	20.3	600	47
MOF-808	Se(VI)	Adsorption	NA	118	5	50
MgAl-MoS4-LDH	Se(VI)	Ion-exchange	NA	85	30	14
MgO Nanosheets	Se(VI)	Adsorption	NO_3^-, Cl^-, F^-, PO_4^{3-}	10.28	300	48
Iron oxide on chitosan	Se(VI)	Adsorption	vs. SO_4^{2-}	17	1440	51
Cu^{2+}-anchored diamino functionalized MCM-41	Se(VI)	Adsorption	vs SO_4^{2-}	83	600	52
Polyamine-type ion-exchange resin	Se(VI)	Adsorption	vs. SO_4^{2-}, Cl^-	243	180	53

Appendix Table 12: Comparison for state-of-the-art materials available for capture of As(V) oxo-anion.

Adsorbent	Oxo-anion	Method	Selectivity	Capacity (mg/g)	Time (min)	Reference
iMOF-3C	As(V)	Ion-exchange	vs. NO_3^-, Cl^-, CO_3^{2-}, SO_4^{2-}	75.5	5	This work
iMOF-1C	As(V)	Ion-exchange	vs. NO_3^-, Cl^-, CO_3^{2-}, HCO_3^-, SO_4^{2-}	85	4320	13k
UiO-66	As(V)	Adsorption	NA	303 at pH=2	2880	54
Mg/Al-LDH	As(V)	Ion-exchange	vs. SO_4^{2-}, NO_3^-, Cl^-	56	5	10
Fe-BTC	As(V)	Adsorption	NA	12.3	10	55
MIL-53(Al)	As(V)	Adsorption	vs. CO_3^{2-}, Cl^-, NO_3^-, SO_4^{2-}	106.5	660	56
MIL-53(Fe)	As(V)	Adsorption	NA	21.27	90	56
ZIF-8 (prepared in MeOH)	As(V)	Adsorption	NA	72.33	90	57

Appendix Table 13. Crystal data and structure refinement for iMOF-3C

Identification code	iMOF-3C (CCDC - 1990643)	
Empirical formula	C54 H42 N14 Ni	
Formula weight	945.72	
Temperature	150(2) K	
Wavelength	0.71073 Å	
Crystal system	Trigonal	
Space group	R -3 :H	
Unit cell dimensions	a = 16.012(3) Å	α= 90°.
	b = 16.012(3) Å	β= 90°.
	c = 25.633(5) Å	γ = 120°.
Volume	5691(2) $Å^3$	
Z	3	
Density (calculated)	0.828 Mg/m3	
Absorption coefficient	0.289 mm-1	
F(000)	1476	
Crystal size	0.13 x 0.12 x 0.10 mm^3	
Theta range for data collection	2.384 to 28.368°.	
Index ranges	-21<=h<=21, -21<=k<=21, -34<=l<=29	
Reflections collected	30467	
Independent reflections	3159 [R(int) = 0.123]	
Completeness to theta = 25.242°	99.9 %	
Refinement method	Full-matrix least-squares on F2	
Data / restraints / parameters	3159 / 0 / 105	
Goodness-of-fit on F2	0.907	
Final R indices [I>2sigma(I)]	R1 = 0.07, wR2 = 0.26	
Extinction coefficient	n/a	
Largest diff. peak and hole	2.246 and -0.779 e.Å-3	

5.6 References

1. WWAP [United Nations World Water Assessment Programme]. 2017. The United Nations World Water Development Report 2017: Wastewater, The Untapped Resource. Paris, UNESCO.

2. (a) R. P. Schwarzenbach, B. I. Escher, K. Fenner, T. B. Hofstetter, C. A. Johnson, U. v. Gunten and B. Wehril, *Science*, 2006, **313**, 1072-1077; (b)The United Nations World Water Development Report 2019. [ISBN: 978-92-3-100309-7]; (c) OECD Environmental Outlook to 2050: The Consequences of Inaction - ISBN 978-92-64-122161; (d) A. Boretti and L. Rosa, *npj Clean Water*, 2019, **2**, 15; (e) United States Environmental Protection Agency. National Primary Drinking Water Regulations. EPA, 816-F-09-004, MAY 2009.

3. (a) J.-Y. Chung, S.-D. Yu and Y. S. Hong, *J. Prev. Med. Public Health*, 2014, **47**, 253-257; (b) Y. He, Y. Xiang, Y. Zhou, Y. Yang, J. Zhang, H. Huang, C. Shang, L. Luo, J. Gao and L. Tang, *Environ. Res.*, 2018, **164**, 288-301.

4. (a) M. F. Hughes, Toxicology Lett., 2002, 133, 1-16; (b) S. Wei, H. Zhang and S. Tao, *Toxicol. Res.*, 2019, **8**, 319-327; (c) K. A. See, P. S. Lavercombe, J. Dillon and R. Ginsberg, *Med. J. Aust.*, 2006, **185**, 388-389; (d) J. K. MacFarquhar, D. L. Broussard, P. Melstrom, R. Hutchinson, A. Wolkin, C. Martin, R. F. Burk, J. R. Dunn, A. L. Green, R. Hammond, W. Schaffner and T. F. Jones, *Arch. Intern Med.*, 2010, **170**, 256-261.

5. (a) G. Shaw, Selenium in Encyclopedia of Inorganic Chemistry, 2010, John-Wiley & Sons Ltd. doi: 10.1002/9781119951438.eibc0420; (b) N. Ben Issa, V. N. Rajakovic-Ognjanovic, B. M. Jovanovic and L. V. Rajakovic, *Anal. Chim. Acta*, 2010, **673**, 185-193.

6. (a) D. R. Lide, CRC Handbook of Chemistry and Physics, 88th Edition, 2007-2008. CRC Press, Taylor & Francis, Boca Raton, FL 2007, 4-91; (b) ILO International Chemical Safety Cards [ICSC]. ICSC: 0326. Disodium Arsenate Heptahydrate www.ilo.org/dyn/icsc/showcard.display?p_version=2&p_card_id=0326].

7. (a) Selenium in Drinking-water. Background document for development of WHO Guidelines for Drinking-water Quality. [apps.who.int/iris/handle/10665/75424]; (b) Arsenic in Drinking-water. Background document for development of WHO Guidelines for Drinking-water Quality. [apps.who.int/iris/handle/10665/75375]; (c) United States Environment Protection Agency [USEPA]. 2018

Edition of the Drinking Water Standards and Health Advisories Tables. EPA 822-F-18-001. (www.epa.gov/sdwa/2018-drinking-water-standards-andadvisory-tables).

8. (a) E. Weidner and F. Ciesielczyk, *Materials*, 2019, **12**, 927; (b) K.-H. Goh, T.-T. Lim and Z. Dong, *Water Res.*, 2008, **42**, 1343-1368; (c) K. Z. Elwakeel, A. A. Atia and A. M. Donia, *Hydrometallurgy*, 2009, **97**, 21-28; (d) B. Gierczyk, M. Ceglowski and M. Zala, *PLOS ONE*, 2015, **10**(5), e0122891.

9. P. Kumar, A. Pournara, K.-H. Kim, V. Bansal, S. Rapti and M. J. Manos, *Prog. Mater. Sci*., 2017, **86**, 25-74.

10. L. Ma, S. M. Islam, H. Liu, J. Zhao, G. Sun, H. Li and S. Ma, *Chem. Mater.*, 2017, **29**, 3274-3284.

11. (a) P. H. Dinolfo and J. T. Hupp, *Chem. Mater*., 2001, **13**, 3113-3125; (b) K. Ariga, A. Vinu, J. P. Hill and T. Mori, *Coord. Chem. Rev.*, 2007, **251**, 2562-2591; (c) P. J. Lusby, *Annu. Rep. Prog. Chem., Sect. A: Inorg. Chem.*, 2013, **109**, 254-276; (d) R. Chakrabarty, P. S. Mukherjee and P. J. Stang, *Chem. Rev.*, 2011, **111**, 6810-6918; (e) T. R. Cook, Y.-R. Zheng and P. J. Stang, *Chem. Rev.*, 2013, **113**, 734-777.

12. (a) A. J. Howarth, M. J. Katz, T. C. Wang, A. E. Platero-Prats, K. W. Chapman, J. T. Hupp and O. K. Farha, *J. Am. Chem. Soc.*, 2015, **137**, 7488-7494; (b) R. J. Drout, L. Robison, Z. Chen, T. Islamoglu and O. K. Farha, *Trends Chem.*, 2019, **1**, 304-317; (c) J. Li, X. Wang, G. Zhao, C. Chen, Z. Chai, A. Alsaedi, T. Hayat and X. Wang, *Chem. Soc. Rev.*, 2018, **47**, 2322-2356; (d) C. Xiao, A. Khayambashi and S. Wang, *Chem. Mater.*, 2019, **31**, 3863-3877; (e) Metal-organic frameworks for environmental applications. Ed. Sujit K. Ghosh. 2019. ISBN: 978-0-12-814633-0. doi: 10.1016/C2017-0-01721-4. (f) L.-H. Xie, X.-M. Liu, T. He and J.-R. Li, *Chem*, 2018, **4**, 1911-1927; (g) Z. Bao, G. Chang, H. Xing, R. Krishna, Q. Ren and B. Chen, *Energy Environ. Sci.*, 2016, **9**, 3612-3641; (h) X. Zhao, Y. Wang, D.-S. Li, X. Bu and P. Feng, *Adv. Mater.*, 2018, **30**, 1705189; (i) R.-B. Lin, S. Xiang, H. Xing, W. Zhou and B. Chen, *Coord. Chem. Rev.*, 2019, **378**, 87-103; (j) H. Wang and J. Li, *Acc. Chem. Res.*, 2019, **52**, 1968-1978; (k) W. P. Lustig, S. Mukherjee, N. D. Rudd, A. V. Desai, J. Li and S. K. Ghosh, *Chem. Soc. Rev.*, 2017, **46**, 3242-3285; (l) D. T. Sun, L. Peng, W. S. Reeder, S. M. Moosavi, D. Tiana, D. K. Britt, E. Oveisi and W. L. Queen, *ACS Cent. Sci.*, 2018, **4**, 349-356; (m) H. Wang, W. P. Lustig and J. Li, *Chem. Soc. Rev.*, 2018, **47**, 4729-4756; (n) W. P. Lustig and J. Li, *Coord. Chem. Rev.*, 2018, **373**, 116-147; (o) E. M. Dias and C. Petit, *J. Mater. Chem. A*, 2015, **3**, 22484-22506; (p) A. J. Howarth, Y. Liu, J. T. Hupp and O. K. Farha, *CrystEngComm*, 2015, **17**, 7245-7253; (q) A. Evans, R. Luebke and C. Petit, *J. Mater. Chem. A*, 2018, **6**, 10570-10594; (r) M. C. Wasson, C. T. Buru, Z. Chen, T. Islamoglu and O. K. Farha, *Appl. Catalysis A: General*, 2019, **586**, 117214; (s) L. Jiao and H.-L. Jiang, *Chem*, 2019, **5**, 786-804; (t) W.-G. Cui, G.-Y. Zhang, T.-L. Hu and X.-H. Bu,

Coord. Chem. Rev., 2019, **387**, 79-120; (u) A. V. Desai, S. Sharma, S. Let and S. K. Ghosh, *Coord. Chem. Rev.*, 2019, **395**, 146-192.

13. (a) J. A. Johnson, X. Zhang, X. Zhang and J. Zhang, *Curr. Org. Chem.*, 2014, **18**, 1973-2001; (b) P. Li, N. A. Vermeuleun, X. Gong, C. D. Malliakas, J. F. Stoddart, J. T. Hupp and O. K. Farha, *Angew. Chem. Int. Ed.*, 2016, **55**, 10358-10362; (c) A. Karmakar, A. V. Desai and S. K. Ghosh, *Coord. Chem. Rev.*, 2016, **307**, 313-341; (d) I. R. Colinas, R. C. Silva, S. R. J. Oliver, *Environ. Sci. Technol.*, 2016, **50**, 1949-1954; (e) A. V. Desai, B. Manna, A. Karmakar, A. Sahu and S. K. Ghosh, *Angew. Chem. Int. Ed.*, 2016, **55**, 7811-7815; (f) Y. Li, Z. Yang, Y. Wang, Z. Bai, T. Zheng, X. Dai, S. Liu, D. Gui, W. Liu, M. Chen, L. Chen, J. Diwu, L. Zhu, R. Zhou, Z. Chai, T. E. Albrecht-Schmitt and S. Wang, *Nat. Commun.*, 2017, **8**, 1354; (g) L. Zhu, D. Sheng, C. Xu, X. Dai, M. A. Silver, J. Li, P. Li, Y. Wang, Y. Wang, L. Chen, C. Xiao, J. Chen, R. Zhou, C. Zhang, O. K. Farha, Z. Chai, T. E. Albrecht-Schmitt and S. Wang, *J. Am. Chem. Soc.*, 2017, **139**, 14873-14876; (h) J. Pang, S. Yuan, J.-S. Qin, C. T. Lollar, N. Huang, J. Li, Q. Wang, M. Wu, D. Yuan, M. Hong and H.-C. Zhou, *J. Am. Chem. Soc.*, 2019, **141**, 3129-3136; (i) D. Sheng, L. Zhu, X. Dai, C. Xu, P. Li, C. I. Pearce, C. Xiao, J. Chen, R. Zhou, T. Duan, O. K. Farha, Z. Chai and S. Wang, *Angew. Chem. Int. Ed.*, 2019, **58**, 4968-4972; (j) E. Soe, B. Ehlke and S. R. J. Oliver, *Environ. Sci. Technol.*, 2019, **53**, 7663-7672; (k) S. Sharma, A. V. Desai, B. Joarder and S. K. Ghosh, *Angew. Chem. Int. Ed.*, 2020, **59**, 7788-7792; (l) A. V. Desai, A. Roy, P. Samanta, B. Manna and S. K. Ghosh, *iScience*, 2018, **3**, 21-30.

14. L. Ma, S. M. Islam, C. Xiao, J. Zhao, H. Liu, M. Yuan, G. Sun, H. Li, S. Ma and M. G. Kanatzidis *J. Am. Chem. Soc.*, 2017, **139**, 12745−12757.

15. SAINT Plus, Bruker AXS Inc.: Madison, WI, 2004.

16. L. Krause, R. Herbst-Irmer, G. M. Sheldrick, D. J. Stalke, *Appl. Cryst.*, 2015, **48**, 3-10.

17. G. M. Sheldrick, SHELXTL, Reference Manual, version 5.1; Bruker AXS Inc.:Madison, WI, 1997.

18. G. M. Sheldrick, *Acta. Cryst.*, 2008, **A64**, 112-122.

19. G. M. Sheldrick, *Acta. Cryst.*, 2015, **C71**, 3-8.

20. L. Farrugia, WinGX, 2009, University of Glasgow: Glasgow, Scotland.

21. A. L. Spek, *Acta. Cryst.*, 2015, **C71**, 9-18.

22. G. Kresse and *J.* Hafner, *Phys. Rev. B*, 1993, **48**, 13115-13118.

23. S. Grimme, S. Ehrlich and L. Goerigk, *J. Comp. Chem.*, 2011, **32**, 1456-1465.

24. J. P. Perdew, K. Burke and M. Ernzerhof, *Phys. Rev. Lett.*, 1996, **77**, 3865-3868.

25. G. Kresse and D. Joubert, *Phys. Rev. B*, 1999, **59**, 1758-1775.

26. Gaussian 09, Revision E.01, M. J. Frisch, G. W. Trucks, H. B. Schlegel, G. E. Scuseria, M. A. Robb, J. R. Cheeseman, G. Scalmani, V. Barone, B. Mennucci, G. A. Petersson, H. Nakat-suji, M. Caricato, X. Li, H. P. Hratchian, A. F. Izmaylov, J. Bloino, G. Zheng, J. L. Sonnenberg, M. Hada, M. Ehara, K. Toyota, R. Fukuda, J. Hasegawa, M. Ishida, T. Nakajima, Y. Honda, O. Kitao, H. Nakai, T. Vreven, J. A. Montgomery Jr., J. E. Peralta, F. Ogliaro, M. Bearpark, J. J. Heyd, E. Brothers, K. N. Kudin, V. N. Staroverov, R. Kobayashi, J. Normand, K. Raghavachari, A. Rendell, J. C. Burant, S. S. Iyengar, J. Tomasi, M. Cossi, N. Rega, J. M. Millam, M. Klene, J. E. Knox, J. B. Cross, V. Bakken, C. Adamo, J. Jaramillo, R. Gomperts, R. E. Stratmann, O. Yazyev, A. J. Austin, R. Cammi, C. Pomelli, J. W .Ochterski, R. L. Martin, K. Morokuma, V. G. Zakrzewski, G. A. Voth, P. Salvador, J. J. Dannenberg, S. Dapprich, A. D. Daniels, Ö.Farkas, J. B. Foresman, J. V. Ortiz, J. Cioslowski and D. J. Gaussian Fox, , Inc., Wallingford CT, 2009.

27. A. V. Marenich, C. J. Cramer and D. G. Truhlar, *J. Phys. Chem. B.*, 2009, **113**, 6378-6396.

28. A. D. Becke, *J. Chem. Phys.*, 1993, **98**, 5648-5652.

29. C. T. Lee, W. T. Yang and R. G. Parr, *Phys. Rev. B.*, 1988, **37**, 785-789.

30. S. Grimme, J. Antony, S. Ehrlich and H. *J.* Krieg, *Chem. Phys.*, 2010, **132**, 154104-154123.

31. M. Dolg, U. Wedig, H. Stoll, and H. J. Preuss, *Chem. Phys.*, 1987, **86**, 866-872.

32. D. Andrae, U. Haeussermann, M. Dolg, H. Stoll and H. Preuss, *Theor. Chim. Acta*, 1990, **77**, 123-141.

33. W. J. Hehre, R. Ditchfie, and J. A. Pople, *J. Chem. Phys.*, 1972, **56**, 2257-2261.

34. Dassault Systèmes BIOVIA, Material Studio, San Diego: Dassault Systèmes, 2019.

35. A. K. Rappe, C. J. Casewit, K. S. Colwell, W. A. Goddard and W. M. Skiff, *J. Am. Chem. Soc.*, 1992, **114**, 10024-10035.

36. (a) L. Ma, Q. Wang, S. M. Islam, Y. Liu, S. Ma and M. G. Kanatzidis, *J. Am. Chem. Soc.*, 2016, **138**, 2858-2866; (b) A. Jawad, Z. Liao, Z. Zhou, A. Khan, T. Wang, J. Ifthikar, A. Shahzad, Z. Chen and Z. Chen, *ACS Appl. Mater. Interfaces* 2017, **9**, 28451-28463; (c) L. Zhu, L. Zhang, J. Li, D. Zhang, L.

Chen, D. Sheng, S. Yang, C. Xiao, J. Wang, Z. Chai, T. E. Albrecht-Schmitt and S. Wang, *Environ. Sci. Technol.*, 2017, **51**, 8606-8615; (d) Y.-J. Gao, H.-Y. Sun, J.-L. Li, X.-H. Qi, K.-Z. Du, Y.-Y. Liao, X.-Y. Huang, M.-L. Feng and M. G. Kanatzidis, *Chem. Mater.*, 2020, **32**, 1957-1963.

37. (a) H.-R. Fu, Z.-X. Xu and J. Zhang, *Chem. Mater.*, 2015, **27**, 205-210; (b) H.-R. Fu, Y. Zhao, Z. Zhou, X.-G. Yang and L.-F. Ma, *Dalton Trans.*, 2018, **47**, 3725-3732; (c) A. V. Desai, S. Sharma, A. Roy and S. K. Ghosh, *Cryst. Growth Des.*, 2019, **19**, 7046-7054.

38. M. Wahlqvist and A. Shchukarev, *J. Electron Spect. Related Phenomena*, 2007, **156-158**, 310-314.

39. J. A. Plant, D. G. Kinnibugh, P. L. Smedley, F. M. Fordyce and B. A. Klinck, Treatise on Geochemistry, 2003, **9**, 17-66.

40. G. E. Fryxell, Y. Lin, S. Fiskum, J. C. Birnbaum, H. Wu, K. Kemner and S. Kelly, *Environ. Sci. Technol.*, 2005, **39**, 1324-1331.

41. (a) N. Rajamohan, R. Rajesh Kanna and M. Rajasimman, *Engg. Technol. Appl. Sci. Res.*, 2016, **6**, 1045-1049; (b) C.-G. Lee, P. J. J. Alvarez, A. Nam, S.-J. Park, T. Do, U.-S. Choi and S.-H. Lee, *J. Hazard. Mater.*, 2017, **325**, 223-229; (c) L. Hongtao, L. Shuxia, Z. Hua, Q. Yanling, Y. Daqiang, Z. Jianfu and Z. Zhiliang, *RSC Adv.*, 2018, **8**, 33301-33313; (d) L. C. Tan, E. M. Calix, E. R. Rene, Y. V. Nancharaiah, E. D. van Hullebusch and P. N. L. Lens, *J. Environ. Eng.*, 2018, **144**, 04018110.

42. H. Pullin, R. A. Crane, D. J. Morgan and T. B. Scott, *J. Environ. Chem. Engg.*, 2017, **5**, 1166-1173.

43. (a) www.dupont.com/water/periodic-table/arsenic.html; (b) L. Wang, A. Chen and K. Fields, US Environmental Protection Agency, 2000. [EPA/600/R-00/088].

44. J. Li, X. Dai, L. Zhu, C. Xu, D. Zhang, M. A. Silver, P. Li, L. Chen, Y. Li,D. Zuo, H. Zhang, C. Xiao, J. Chen, J. Diwu, O. K. Farha, T. E. Albrecht-Schmitt, Z. Chai and S. Wang, *Nat. Commun.*, 2018, **9**, 3007.

45. Y. Marcus, *J. Chem. Soc. Faraday Trans.*, 1991, **87**, 2995-2999.

46. A. Meleshyn and H. Wicke, *J. Phys. Chem. A*, 2010, **114**, 8948–8960.

47. H. Ouyang, N. Chen, G. Chang, X. Zhao, Y. Sun, S. Chen, H. Zhang and D. Yang, *Angew. Chem. Int. Ed.*, 2018, **57**, 13197– 13201.

48. W. Cui, P. Li, Z. Wang, S. Zheng and Y. Zhanga, *J. Hazard. Mat.*, 2018, **341**, 268-276.

49. Y. T. Chana, W. H. Kuanb, T. Y. Chenc and M. K. Wanga, *Water Res.*, 2009, **43**, 4412–4420.

50. R. J. Drout, A. J. Howarth, K. -i. Otake, T. Islamoglu and O. K. Farha, *CrystEngComm*, 2018, **20**, 6140.

51. N. Bleiman and Y. G. Mishael, *J. Hazard. Mat.*, 2010, **183**, 590-595.

52. T. Yokoi, T. Tatsumi, and H. Yoshitake, *Bull. Chem. Soc. Jpn.*, 2003, **76**, 2225–2232.

53. H. Hashimoto, M. Nakayama and T. Nishimura, *Sep. Sci. Technol.*, 2007, **42**, 3155–3167.

54. C. Wang, X. Liu, J. P. Chen and K. Li, *Sci. Rep.*, 2015, DOI: 10.1038/srep16613.

55. B. J. Zhu, X. Y. Yu, Y. Jia, F. M. Peng, B. Sun, M.-Y. Zhang, T. Luo, J.-H. Liu and X.-J. Huang, *J. Phys. Chem. C.*, 2012, **116**, 8601-8607.

56. J. Li, Y.-n. Wu, Z. Li, M. Zhu and F. Li, *Water Sci. Technol.*, 2014, **70**, 1391- 1397.

57. Y.-n. Wu, M. Zhou, B. Zhang, B. Wu, J. Li, J. Qiao, X. Guan and F. Li, *Nanoscale*, 2014, **6**, 1105-1112.